Università degli studi di Genova
Facoltà di scienze Matematiche, Fisiche e Naturali
Scuola di Dottorato in Scienze e Tecnologie
per l'informazione e la conoscenza
XX Ciclo, A.A. 2005 - 2008

A Thesis submitted for the degree of
Dottore di Ricerca in
Fisica Nucleare e Subnucleare

Characterization of cryogenic bolometers and data acquisition system for the CUORE experiment

School Coordinator
Prof. Pierantonio Zanghì
Università e sezione INFN di Genova

Author
Dott. Andrea Giachero
Università di Genova e
Laboratori Nazionali del Gran Sasso

Advisors
Prof. Marco Pallavicini
Università e sezione INFN di Genova

Dott. Carlo Bucci
Laboratori Nazionali del Gran Sasso

Area 02 - Scienze Fisiche
Settore Scientifico-Disciplinare: FIS/04

Contents

Introduction

Our knowledge of the neutrino properties has grown steadily and significantly in the last ten years. The existence of the neutrino oscillations, discovered in 1998 by Super-KamiokaNDE in the atmospheric neutrino spectrum and confirmed in 2001 by the SNO experiment in the solar neutrino spectrum, proves that at least two out of three neutrino flavors have a non zero mass and that lepton number is not a good quantum number. Nevertheless, while precision measurements of the oscillation parameters are planned for the near future, there are still two important missing pieces in the neutrino puzzle: the understanding of the nature of the mass term (Dirac or Majorana) and the measurement of the absolute mass scale. In fact, neutrino oscillations are sensitive only to the squared mass differences between neutrino flavors, yielding no information at all concerning the absolute mass scale. Besides, the oscillation process does not depend on the Majorana or Dirac nature of the mass terms.

Neutrinoless double beta decay has long been recognized as a useful avenue for the study of electron neutrinos properties, and particularly for the measurement of the absolute mass scale and for the determination of the nature of the electron neutrino effective mass. In fact, the detection of such a very rare nuclear decay mode would set a lower limit on the mass of the electron neutrino, as well as prove that the neutrino is a Majorana particle. Moreover, characteristics of this mode such as lepton number violation have repercussions that constitute evidence for physics beyond the Standard Model, and impact cosmology as well.

The data obtained by the neutrino oscillation experiments put limits on possible value of neutrino masses. There are three possible scenarios: the so called *quasi degenerate* scenario foresees three almost equal values of the neutrino masses below but not much below 1 eV; the so called *inverted hierarchy* and the *direct hierarchy* scenarios allow a much lighter electron neutrino mass, of the order of 10 meV and 1 meV respectively. The *quasi degenerate* scenario is being investigated right now by the current generation of double beta decay using different and complementary techniques with various nuclei. A new generation of detectors is now rising up with the claim to look inside the *inverted hierarchy* mass region. The bolometric detectors, which this thesis is all about, are based on tellurium dioxide (TeO_2) crystals and play a leading role in this new generation of experiments.

This Ph.D. work has been performed in the framework of the CUORE (*Cryogenic Underground Observatory for Rare Events*) experiment, a tellurium dioxide array of 988 detectors with the aim to search the double beta decay. The expected sensitivity on the neutrino mass is supposed to be better than 50 meV. A prototype of CUORE, CUORICINO, is already running at the Gran Sasso National Laboratory of INFN (*Istituto Nazionale di Fisica Nucleare*): the data it collected in the last five years demonstrated the feasibility of CUOREsetting, at the same time, the best current upper limit for the 130-tellurium neutrinoless double beta decay half-life

During the past three years, two of which entirely spent at the Gran Sasso National Laboratory, I have worked in the CUORE collaboration dealing with different aspects of the experiment. My research activity was focused manly on two tasks: the R&D activity aimed at the reduction of the detector background, and the design and development of the data acquisition system for the CUORE experiment.

The background reduction is the most important task in view of CUORE. Background is the only parameter that can be reduced by orders of magnitude thus allowing a sizeable improvement of the experimental sensitivity. The CUORE background reduction program foresees a reduction from the present CUORICINO level of 0.18 counts/keV/kg/years to about 0.01 counts/keV/kg/years. The performed tests during my Ph.D work was devoted to a reduction of the surface radioactive contaminations of the detector main components: the copper holders and the tellurium dioxide crystals. These contaminations, due to the alpha particle contributions, are believed to be at the origin of the flat continuous background in the neutrinoless double beta decay region. The results of these tests showed a relevant reduction for the crystal surface contribution. Unfortunately, only a smaller improvement was reached for the copper surfaces. The last two tests regarded the background analysis but also the validation of the final protocol for the CUORE crystals production and treatment. The aim of these two final tests was to check ten crystals produced with a controlled procedure completely processed in China.

The second part of my work was devoted to the development of the data acquisition and control system of the experiment. In these years I continually cooperated with the CUORE DAQ Working Group in order to design and test the best hardware configuration and to develop the software necessary to operate it. A first prototype was installed at the Gran Sasso Underground Laboratory and several tests were performed exploiting the set-ups, quoted above, achieved for background measurements.

The thesis is composed of three parts: the first is a short theoretical overview on the neutrino physics, the double beta decay and the bolometric techniques for double beta decay detection. The second part reviews the experimental approach to study the neutrinoless double beta decay by using sources of 130-Tellurium and bolometric techniques for the detection. In this part I illustrate the next generation experiment CUORE, the status of CUORICINO and the results about the CUORE background reducing program which is the main activity of my Ph.D work. The third part deals with the technical aspects of the experiments. In this last part I explain how the CUORE electronics works, its interface with the data acquisition system, the data acquisition system design status and its performances at the Hall C R&D facility.

PART I

THEORETICAL OVERVIEW

Chapter 1

The massive neutrino

1.1 Introduction

Neutrinos are spin-half, left-handed chirality, electrically neutral particles introduced by W. E. Pauli in 1930 as a "*desperate remedy*" to the long standing problems related to angular momentum and energy conservation in nuclear beta decay. After Pauli suggestion, Enrico Fermi wrote the first theory of nuclear beta decay in 1934[1]. He formulates a quantitative theory of weak particle interactions in which the neutrino played a fundamental role.

In the same year, using Fermi's theory, H. A. Bethe and R. E. Peierls calculated the neutrino-nucleon scattering cross-section[2]. They obtained a value smaller than 10^{-44} cm^2 and the scientific community concluded that there was no practical way to detect these particles. In 1942 K. C. Wang first proposed to use beta-capture to experimentally detect neutrinos[3]. In 1956 C. Cowan, F. Reines and co-workers detected neutrinos for the first time and published the article "*Detection of the Free Neutrino: a Confirmation*"[4]. This result was rewarded with the 1995 Nobel Prize [5]. They placed three tanks with inorganic liquid scintillator (cadmium chloride, $CdCl_2$) 11 m far from the Savannah River reactor's core, each of them equipped with 110 photomultiplier tubes. The neutrinos created in the nuclear reactor by beta decay were detected by neutrino capture ($\overline{\nu}_e + p \rightarrow e^+ + n$). We now know that the observed particles were antineutrinos.

In 1957 Lee and Yang[6] suggested that the neutrinos could be massless Dirac particles. This hypothesis was confirmed in 1958 by the experiment at *Brookhaven National Laboratory* (BNL) performed by M. Goldhaber *et al.*, that showed clearly how neutrinos were produced with negative helicity[7]. In the same year Bruno Pontecorvo proposed the hypothesis that the existence of neutrino masses could allow for *neutrino* ↔ *antineutrino* transitions[8, 9].

In 1962 L. M. Lederman, M. Schwartz and J. Steinberger showed that more than one type of neutrino exists by first detecting interactions of the muon neutrino[10], which earned them the 1988 Nobel Prize. They installed a 10 tons spark chamber at the new *Brookhaven Alternating Gradient Synchrotron* and demonstrated the presence of muon tracks (rather than electrons) produced by neutrinos emitted in pion decay. Due to its different nature, this particle was labeled *muon neutrino* (ν_μ), as opposed to the *electron neutrino* (ν_e) emitted in β-decay.

When a third type of lepton, the tau (τ), was discovered in 1975 at the *Stanford Linear Accelerator Center* (SLAC) by M. L. Perl and co-workers[11], an associated neutrino was also expected. The first evidence for this third neutrino type came from the observation of missing energy and momentum in τ-decays. This led to the discovery of the τ neutrino. The first observation of tau neutrino interactions was announced in summer of 2000 by the DONUT (*Direct Observation of NU Tau*) collaboration[12] at the *Fermi National Accelerator Laboratory* (FNAL, Fermilab). It was the last missing particle in the *Standard Model* and its existence had already been inferred both based on theoretical consistency and from experimental data of the LEP collider (*Large Electron-Positron Collider* at CERN).

In the late 1960's the *Homestake Experiment*, headed by the astrophysicists R. Davis Jr. and J. N. Bahcall, collected and counted neutrinos emitted in nuclear fusion reactions taking place in the Sun (*solar neutrino*). Bahcall did the theoretical calculations and Davis designed the experiment. The discrepancy between the expected number of solar neutrinos and the detected one originated the *Solar Neutrino Problem*: only one-third of the expected neutrinos was detected.

The Homestake Experiment (1968-1994) was followed by other experiments with the same purpose, such as KamiokaNDE (*Kamioka Nucleon Decay Experiment*, Mozumi Mine, Japan), SAGE (*Sovietic American Gallium Experiment*, *Baksan Neutrino Observatory*, Soviet Union), GALLEX/GNO (*GALLium European EXperiment/Gallium Neutrino Observatory*, *Laboratori Nazionali del Gran Sasso*, Italy) and *Super-Kamiokande* (Super-K, also in Japan).

The experiments SAGE (1990-1994[13, 14]) and GALLEX/GNO (1991-1997[15, 16, 17] and 1998-2002[18, 19]) confirmed the deficit in the measured solar neutrino flux. Super-K (1983-1998) detected neutrinos from SN 1987A, a supernova which was observed in the Large Magellanic Cloud in February 1987, and observed solar neutrinos in 1988. In 1998 the experiment also showed a deficit in the *atmospheric neutrino*[1] flux. An anomalous number of muon neutrino events compared to electron neutrino events was measured: it was the first evidence for neutrino oscillations [20, 21, 22].

In 1985 S. Mikheyev and A. Smirnov[23] (expanding on 1978 work by L. Wolfenstein [24]) noted that flavor oscillations can be modified when neutrinos propagate through matter. This so-called MSW effect is important to understand neutrinos emitted by the Sun, which traverse its dense atmosphere on their way to detectors on Earth.

The SNO (*Sudbury Neutrino Observatory*) experiment was the first detector able to detect neutrino oscillations, solving the solar (and atmospheric) neutrino problem. The results of the experiment, published in 2002[25], revealed the three neutrino *flavors* (ν_e,

---

[1] neutrinos produced in the collision of primary cosmic rays (typically protons) with nuclei in the upper atmosphere

ν_μ and ν_τ) can oscillate into each other. The precedent detectors were sensitive to only one. In the 2003 the KamLAND experiment (*Kamioka Liquid Scintillator Antineutrino Detector*, Kamioka Observatory, Japan) detected the *disappearance* of the electron antineutrinos produced by nuclear reactors[26, 27].

In 2002 Raymond Davis Jr. and Masatoshi Koshiba were jointly awarded the Nobel Prize in Physics. Ray Davis for his pioneer work on solar neutrinos and Koshiba for the first real time observation of supernova neutrinos.

The discovery of neutrino oscillations implies a non-vanishing neutrino mass, and this calls for a physics beyond the Standard Model. Neutrino oscillation experiments can only measure the differences between the neutrino mass-values. The absolute scale of neutrino masses can be obtained from direct mass measurements. The Troitsk[28, 29] and Mainz[30] ^{3}H single β-decay experiments have placed upper limits of 2.2 eV on the mass of the electron neutrino. KATRIN, a greatly enlarged ^{3}H decay experiment in preparation, is designed to have a sensitivity of 0.2 eV[31]. In the case of Majorana neutrinos[2], a greater sensitivity is needed. To achieve this goal the next generation of the neutrinoless double-beta decay will be able to test the $(0.02 \div 0.05)$ eV region.

1.2 Majorana and Dirac Neutrino

Majorana particles are identical to their own antiparticles whereas Dirac particles can be distinguished from their antiparticles. As it is well known from the study of the Dirac equation a spin-half massive fermion is described by a four-component wave function (two *Weyl spinor*). Two spin state for the particle and two spin state for the antiparticle, all encoded in the same wave function. In the case of Majorana character (*particle* $\equiv$ *antiparticle*) the needed wave function could have only two components (one *Weyl spinor*). However for many calculation purposes, it is convenient to use the four-component form. For more details see [32, 33] and [34, 35].

The Lagragian mass terms describe transitions between *right* (R) and *left* (L)-*handed* states. A Dirac mass term, which conserves lepton number, involves transition between two different *Weyl neutrinos*, named ν_L and N_R, where the right-handed state N_R is different from ν_R, the CPT partner of the ν_L[36]. The form is:

$$-\mathcal{L}_{\text{Dirac}} = M_D[\overline{\nu}_L N_R + \overline{N}_R \nu_L] = M_D \overline{\nu}\nu \quad \text{with} \quad \nu = \nu_L + N_R \tag{1.1}$$

The Dirac field has four component

---

[2] it is still possible that the neutrino and antineutrino are in fact the same particle, a hypothesis first proposed by the italian physicist Ettore Majorana.

$$\nu = \begin{pmatrix} \overline{\nu}_L \\ \nu_R^c \\ N_R \\ N_L^c \end{pmatrix} \tag{1.2}$$

where N_L^c is the CPT partner of N_R. This mass term allows a conserved lepton number $L = L_\nu + L_N$. For an ordinary Dirac neutrino the ν_L is active whereas the N_R is sterile[3].

In the case of Majorana mass, which violates lepton number by two units ($\Delta L = 2$), is used a single right-handed antineutrino ($N_R = \nu_R^c$) rather than a two separate Weyl neutrino. This it can be viewed as the creation or annihilation of two neutrinos, and, if present, it can therefore lead to *neutrinoless double beta decay* ($0\nu\beta\beta$). The form of a Majorana mass term is:

$$-\mathcal{L}_{\text{Majorana}} = \frac{1}{2}M_M[\overline{\nu}_L\nu_R^c + \overline{\nu}_R^c\nu_L] = \frac{1}{2}M_M[\overline{\nu}_L C\overline{\nu}_L^T + \text{h.c}] = \frac{1}{2}M_M\overline{\nu}\nu \tag{1.3}$$

where $\nu = \nu_L + \nu_R^c$ is a two-component state satisfying the self-charged-conjugated condition $\nu = \nu^c = C\overline{\nu}^T$, where the unitary matrix $C = \imath\gamma^2\gamma^0$ represents the charge conjugation operator with the property $C\gamma_\lambda C^{-1} = -\gamma^{\lambda T}$.

It is also possible to consider mixed models in which both Majorana and Dirac mass terms are present. In this case in the neutrino Lagrangian the Lorentz-invariant mass term can appear in three forms[37]:

$$\begin{array}{lcl} \text{Majorana} & \Rightarrow & \begin{cases} M_{M,T}\text{: triplet Majorana mass matrix (Higgs triplet)} \\ \\ M_{M,S}\text{: Dirac mass matrix (Higgs doublet)} \end{cases} \\ \\ \text{Dirac} & \Rightarrow & \quad M_D\text{: singlet Majorana mass matrix (Higgs singlet)} \end{array} \tag{1.4}$$

The *Dirac mass term* (with the mass parameter M_D) requires the existence of both chirality eigenstates ν_R and ν_L and conserves the lepton quantum number. The *Majorana mass terms* violate the lepton number and can be present even without ν_R (for the term with mass parameter $M_{M,T}$) or ν_L (for the term with mass parameter $M_{M,S}$). Assuming that the states are respectively active and sterile, these terms transform as weak triplets ($M_{M,T}$) and singlets ($M_{M,S}$).

The most general Lorentz-invariant mass term of the neutrino Lagrangian has the form:

---

[3] a sterile neutrino is a hypothetical neutrino that does not interact via any of the fundamental interactions of the Standard Model.

$$\mathcal{L}_m = -\frac{1}{2}\Big[\overline{\nu}_L^c \overline{N}_L^c\Big]\mathcal{M}\begin{pmatrix}\nu_R^c \\ N_R\end{pmatrix} + \text{h.c} \quad \text{where} \quad \mathcal{M} = \begin{pmatrix} M_L & M_D^T \\ M_D & M_R \end{pmatrix} \tag{1.5}$$

where $\nu_L \leftrightarrow \nu_R^c$ and $N_L^c \leftrightarrow N_R$ are two Weyl states and where $\mathcal{M}$ is the *Dirac-Majorana neutrino mass matrix*. Rewriting the Lagrangian in terms of two new field χ_L and χ_R:

$$\chi_L = \frac{\nu_L + N_L^c}{\sqrt{2}} \quad , \quad \chi_R = \frac{\nu_R + N_R^c}{\sqrt{2}} \tag{1.6}$$

arranged in a doublet $\chi = \binom{\chi_L}{\chi_R}$ one obtains:

$$-\mathcal{L} = \overline{\chi}\gamma_\mu \delta_\mu \chi + \overline{\chi}\mathcal{M}\chi \tag{1.7}$$

In general, the terms M_D, M_R and M_L might coexist, and then the mass Lagrangian must be diagonalized, resulting in two generally non-degenerate mass eigenvalues for each flavor. Diagonalizing the mass matrix by a rotation in the two-dimensional space of the vector χ one obtains the usual free Lagrangian for two particles ν_1 and ν_2, with masses m_1 and m_2, respectively.

Considering the *Seesaw mechanism*[36, 38] the Majorana mass is comparable to the GUT scale ($M_{\text{GUT}} \simeq (10^{11} \div 10^{16})$ GeV) whereas the Dirac mass is of order of the electroweak scale. Under this hypothesis one has $M_R >> M_D$ (electroweak symmetry breaking)) and $M_L \simeq 0$ (from phenomenological constraint). This model produces two Majorana neutrinos, the former corresponds to the three known neutrino flavors while the latter is a very heavy undiscovered neutrino not interacting. Their respective masses are:

$$\begin{cases} m_1 \simeq \dfrac{M_D^2}{M_R} << M_D & \Rightarrow \quad \text{light neutrino (left-handed)} \\ \\ m_2 \simeq M_R & \Rightarrow \quad \text{heavy neutrino (right-handed)} \end{cases}$$

Thus, there is one heavy neutrino and one neutrino much lighter than the typical Dirac scale. Such model represent the popular and natural way of generating neutrino masses much smaller than the other fermion masses. The *Seesaw mechanism* is used to explain why the neutrino masses are so small.

1.3 Neutrino Oscillations

A phenomenological consequence of neutrino mass is the possibility of neutrino flavor oscillations. This phenomenon was first predicted by Bruno Pontecorvo in 1957 [8, 9] while the possibility of arbitrary mixing between two massive neutrino states was first introduced by Z. Maki, M. Nakagawa, S. Sakata in 1962[39]. If neutrinos have masses the neutrino state produced by electroweak interactions is generally not a mass eigenstate. The weak eigenstates ν_α with $\alpha = e, \mu, \tau$, produced in weak interactions are, in general, linear combinations of the mass eigenstates ν_i with $i = 1, 2, 3$:

$$|\nu_\alpha\rangle = \sum_{i=1}^{n=3} U^*_{\alpha i} |\nu_i\rangle \tag{1.8}$$

where U represents the *PMNS matrix* (*Pontecorvo-Maki-Nakagawa-Sakata matrix* also called *MNS matrix*, *Neutrino Mixing Matrix*), a mixing matrix analogue of the *CKM matrix* for quarks[40, 41]. Using the L. L. Chau *et al.*[42] parameterization one has:

$$\begin{pmatrix} \nu_e \\ \nu_\mu \\ \nu_\tau \end{pmatrix} = \begin{pmatrix} U_{e1} & U_{e2} & U_{e3} \\ U_{\mu 1} & U_{\mu 2} & U_{\mu 3} \\ U_{\tau 1} & U_{\tau 2} & U_{\tau 3} \end{pmatrix} \cdot \begin{pmatrix} \nu_1 \\ \nu_2 \\ \nu_3 \end{pmatrix} \tag{1.9}$$

where:

$$\begin{aligned} U \; = & \begin{pmatrix} c_{12}c_{13} & s_{12}c_{13} & s_{13}e^{-i\delta} \\ -s_{12}c_{23} - c_{12}s_{23}s_{13}e^{i\delta} & c_{12}c_{23} - s_{12}s_{23}s_{13}e^{i\delta} & s_{23}c_{13} \\ s_{12}s_{23} - c_{12}c_{23}s_{13}e^{i\delta} & -c_{12}s_{23} - s_{12}c_{23}s_{13}e^{i\delta} & c_{23}c_{13} \end{pmatrix} \cdot \\ \cdot & \begin{pmatrix} 1 & 0 & 0 \\ 0 & e^{i\alpha_2/2} & 0 \\ 0 & 0 & e^{i\alpha_3/2} \end{pmatrix} = \\ = & \begin{pmatrix} 1 & 0 & 0 \\ 0 & c_{23} & s_{23} \\ 0 & -s_{23} & c_{23} \end{pmatrix} \begin{pmatrix} c_{13} & 0 & s_{13}e^{-i\delta} \\ 0 & 1 & 0 \\ -s_{13}e^{-i\delta} & 0 & c_{13} \end{pmatrix} \begin{pmatrix} c_{12} & s_{12} & 0 \\ -s_{12} & c_{12} & 0 \\ 0 & 0 & 1 \end{pmatrix} \cdot \\ \cdot & \begin{pmatrix} 1 & 0 & 0 \\ 0 & e^{i\alpha_2/2} & 0 \\ 0 & 0 & e^{i\alpha_3/2} \end{pmatrix} \quad , \quad c_{ij} = \cos\theta_{ij} \quad , \quad s_{ij} = \sin\theta_{ij} \end{aligned} \tag{1.10}$$

The mixing is a function of three *mixing angles* (θ_{12}, θ_{23} and θ_{13}). The phase factors α_2 and α_3 are no-zero only if neutrinos are Majorana particles, and do not enter into oscillation phenomena regardless. The phase factor δ is no-zero only if neutrino oscillation violates the CP symmetry. If experiment shows this 3 × 3 matrix to be not unitary, a sterile neutrino or some other new physics is required.

After travelling a distance L (or, equivalently for relativistic neutrinos, a time t), a neutrino originally produced with flavour α evolves as follows[43, 44]:

$$|\nu_i(t)\rangle = \mathrm{e}^{-\imath(E_i t - \vec{p}_i\cdot\vec{x})}|\nu_i(0)\rangle \tag{1.11}$$

In the ultra-relativistic limit ($|\vec{p}_i| = p_i \gg m_i$) one can approximate the energy as:

$$E_i = \sqrt{p_i^2 + m_i^2} \simeq p_i + \frac{m_i^2}{2p_i} \approx E + \frac{m_i^2}{2E} \tag{1.12}$$

assuming $p_i \simeq p_j \equiv p \simeq E$. Using $t \simeq L$ and also dropping the phase factors, the wave function becomes:

$$|\nu_i(t \simeq L)\rangle = \mathrm{e}^{-\imath m_i^2 \frac{L}{2E}}|\nu_i(0)\rangle \tag{1.13}$$

Considering this last relation, the probability that a neutrino originally of flavor α will later be observed as having flavor β is given by:

$$P_{\alpha\to\beta} = |\langle\nu_\beta|\nu_\alpha(t)\rangle|^2 = \left|\sum_i U_{\alpha i}^* U_{\beta i} e^{-\imath m_i^2 \frac{L}{2E}}\right|^2 \tag{1.14}$$

or in more convenient form:

$$P_{\alpha\to\beta} = \delta_{\alpha\beta} - 4\sum_{i>j} \Re\Big(U_{\alpha i}^* U_{\beta i} U_{\alpha j} U_{\beta j}^*\Big) \sin^2\left(\frac{\Delta m_{ij}^2 L}{4E}\right) \tag{1.15}$$

$$+2\sum_{i>j} \Im\Big(U_{\alpha i}^* U_{\beta i} U_{\alpha j} U_{\beta j}^*\Big) \sin\left(\frac{\Delta m_{ij}^2 L}{2E}\right) \tag{1.16}$$

where $\Delta m_{ij}^2 \equiv m_i^2 - m_j^2$ with $i, j = 1, 2, 3$. Restoring c and $\hbar$ the *oscillation phase*, that is responsible for oscillation, is often written as[45]:

$$\Phi_{ij} = 1.27\Delta m_{ij}^2[\mathrm{eV}^2]\,\frac{L[\mathrm{Km}]}{E[\mathrm{GeV}]} \tag{1.17}$$

where $L = ct \simeq t$ is the distance between the source of ν_α and the detector (i.e. the detection point of ν_β). The transition probability $P_{\alpha\to\beta}$ has an oscillatory behavior, with *oscillation length*:

$$L^{\mathrm{osc}} = \frac{4\pi E}{\Delta m_{ij}^2}. \tag{1.18}$$

The transition amplitude is proportional to the elements present in the mixing matrix. Thus, in order to have oscillations, neutrinos must have different masses ($\Delta m^2_{ij} \neq 0$) and they must mix ($U_{\alpha i} U_{\beta i} \neq 0$), since flavor oscillation is due to interference between different mass eigenstates.

In order to be sensitive to a given value of Δm^2_{ij}, an experiment has to be set up with $E/L \simeq \Delta m^2_{ij}$ (where L is the source-detector distance, table 1.1). If $E/L >> \Delta m^2_{ij}$ ($\Rightarrow L << L^{\text{osc}}$) the oscillation does not have time to give an appreciable effect because $\sin^2 x_{ij} << 1$. For $E/L << \Delta m^2_{ij}$ ($\Rightarrow L >> L^{osc}$), the oscillating phase goes through many cycles before detection and, since in general neutrino beams are not monochromatic, the phase is averaged to $< sin^2\theta_{ij} >= 1/2$ and the oscillation pattern is vanished.

Experiment	**L** [m]	**E** [MeV]	$\mathbf{\Delta m^2}$ [eV^2]
Solar	10^{11}	1	10^{-11}
Atmospheric	$10^4 \div 10^7$	$10^2 \div 10^5$	$10^{-1} \div 10^{-4}$
Reactor	$10^2 \div 10^6$	1	$10^{-2} \div 10^{-3}$
Accelerator	10^2	$10^3 \div 10^4$	$\gtrsim 0.1$
Long Baseline Accelerator	$10^5 \div 10^6$	10^4	$10^{-2} \div 10^{-3}$

Table 1.1: Characteristic values of L and E for various neutrino sources and experiments.

For a two neutrino case, the mixing matrix depends on a single parameter θ and there is a single mass-squared difference Δm^2.

$$U = \begin{pmatrix} \cos\theta & \sin\theta \\ -\sin\theta & \cos\theta \end{pmatrix} \Rightarrow P_{\alpha\rightarrow\beta} = \delta_{\alpha\beta} - (2\delta_{\alpha\beta} - 1)\sin^2 2\theta \sin^2\left(\frac{\Delta m^2 L}{4E}\right) \quad (1.19)$$

1.4 Neutrino mass hierarchy

The combined information on neutrino oscillations and the upper mass limit from tritium decays show that the heaviest active neutrino state is nine to eleven orders of magnitude lighter than the other fermions in the third family[46]. The oscillations experiments measure only mass squared differences and the mixing parameters (table 1.2), so cannot give information about the absolute neutrino mass. The *hierarchy scale* among the eigenvalues m_i is still unknown.

Neutrino oscillation data are compatible with three types of neutrino mass spectra (figure 1.1):

Parameter	Best fit	2σ	3σ	4σ
Δm^2_{21} $[10^{-5}$ eV$^2]$	7.9	$7.3\div 8.5$	$7.1\div 8.9$	$6.8\div 9.3$
Δm^2_{31} $[10^{-3}$ eV$^2]$	2.6	$2.2\div 3.0$	$2.0\div 3.2$	$1.8\div 3.5$
$\sin^2\theta_{12}$	0.30	$0.26\div 0.36$	$0.24\div 0.40$	$0.22\div 0.44$
$\sin^2\theta_{23}$	0.50	$0.38\div 0.63$	$0.34\div 0.68$	$0.31\div 0.71$
$\sin^2\theta_{13}$	0.000	≤ 0.025	≤ 0.040	≤ 0.058

Table 1.2: Best-fit values, 2σ, 3σ, and 4σ intervals for the three-flavour neutrino oscillation parameters from global data including solar, atmospheric, reactor (KamLAND and CHOOZ) and accelerator (K2K and MINOS) experiments[47]. The values are updated at 2006.

1) **Normal Hierarchy** (NH)

$$m_1 \ll (<) m_2 \ll m_3 \;\; : \;\; \begin{cases} \Delta^2_{21} = \Delta m^2_{\odot} \\ \Delta^2_{32} = \Delta m^2_{\mathrm{atm}} \\ m_1 = m_{\min} << \sqrt{\Delta m^2_{\odot}} \\ m_2 = \sqrt{m^2_{\min} + \Delta m^2_{\odot}} \simeq \sqrt{\Delta m^2_{\odot}} \\ m_3 = \sqrt{m^2_{\min} + \Delta m^2_{\mathrm{atm}}} \simeq \sqrt{\Delta m^2_{\mathrm{atm}}} \end{cases} \tag{1.20}$$

where $m_{\min}$ is the lightest neutrino mass.

2) **Inverted Hierarchy** (IH)

$$m_3 \ll m_1 \lesssim m_2 \;\; : \;\; \begin{cases} \Delta^2_{21} = \Delta m^2_{\odot} \\ \Delta^2_{32} = \Delta m^2_{\mathrm{atm}} \\ m_3 = m_{\min} << \sqrt{\Delta m^2_{\mathrm{atm}}} \\ m_1 = \sqrt{m^2_{\min} + \Delta m^2_{\mathrm{atm}} - \Delta m^2_{\odot}} \simeq \sqrt{\Delta m^2_{\mathrm{atm}}} \\ m_2 = \sqrt{m^2_{\min} + \Delta m^2_{\mathrm{atm}}} \simeq \sqrt{\Delta m^2_{\mathrm{atm}}} \end{cases} \tag{1.21}$$

3) **Quasi-Degenerated Hierarchy** (QDH)
In this third possibility the lightest neutrino mass is much larger than $\sqrt{\Delta m^2_{atm}}$ and one has $m_1 \simeq m_2 \simeq m_3$.

As it will shown in the next chapters the study of the *double-beta decay* could distinguish neutrino mass hierarchies setting a limit on the neutrino mass.

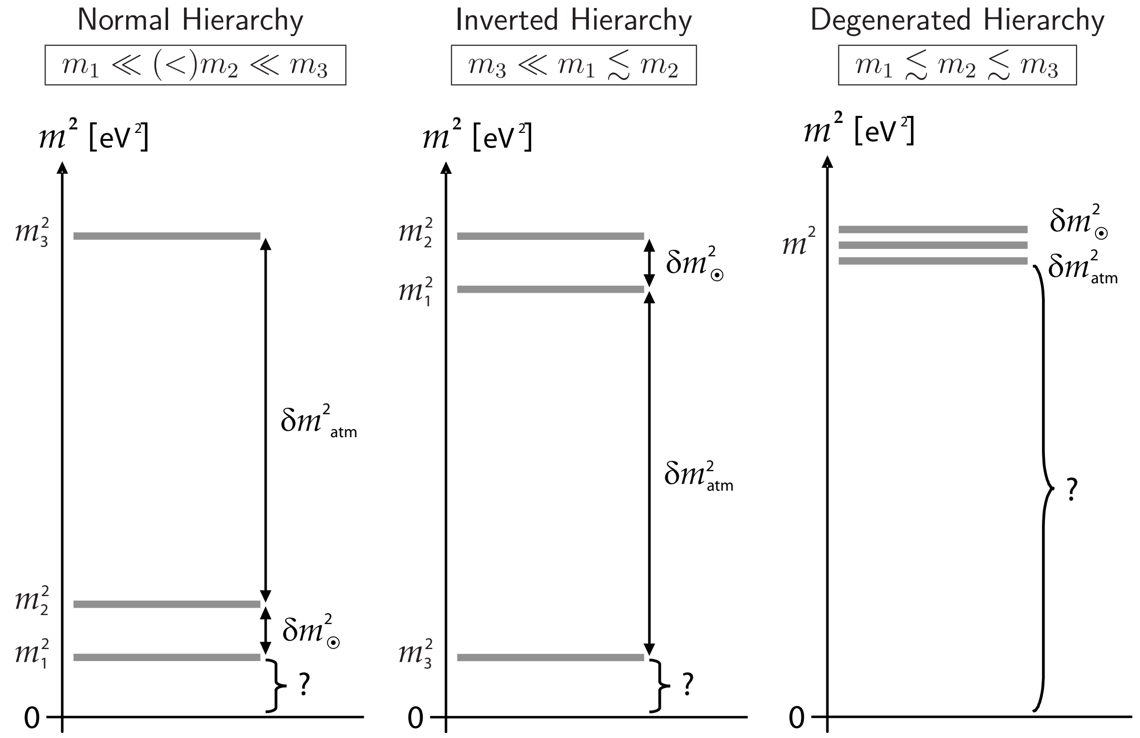

$\delta m^2_{\odot} = \delta m^2_{21}$
$\delta m^2_{\mathrm{atm}} = \delta m^2_{31} \simeq \delta m^2_{32}$
$\sin^2 \delta = |U_{e3}|^2$
$(\boldsymbol{a})$

$\delta m^2_{\odot} = \delta m^2_{21}$
$\delta m^2_{\mathrm{atm}} = \delta m^2_{31} \simeq \delta m^2_{32}$
$\sin^2 \delta = |U_{e1}|^2$
$(\boldsymbol{b})$

$\delta m^2_{\odot}$, $\delta m^2_{\mathrm{atm}}$ and $\sin^2 \delta$
not important for the
$\langle m_\nu \rangle$ estimation
$(\boldsymbol{c})$

Figure 1.1: *Normal*, *inverted* and *quasi-degenerated* mass hierarchies schemes

Chapter 2

Double Beta Decay

2.1 Introduction

Double Beta Decay (DBD) is a rare spontaneous transition in which the nuclear charge changes by two units while the mass number remains the same (two neutrons simultaneously transmute into two proton). This decay may occur with the emission of two neutrinos (*two neutrino double beta decay*, $2\nu\beta\beta$) or without (*neutrinoless double beta decay*, $0\nu\beta\beta$). The latter hasn't been officially observed yet .

In 1935 paper M. Goeppert-Meyer first calculated the probability for the $2\nu\beta\beta$-decay, using the new Fermi theory of weak decays and predicted half-life time in excess of 10^{20} years[48]. In the 1937 Ettore Majorana proposed that the neutrino particle might be indistinguishable from its antiparticle[49]. In the same year G. Racah, following the fundamental suggestion of Majorana, discussed the possibility of a neutrinoless transformation of two neutrons into two protons plus two electrons[50]. W. Furry in 1939 realized that $0\nu\beta\beta$-decay could be mediated by virtual neutrino and predicted the half-life on the level of $T^{0\nu}_{1/2} = (10^{12} \div 10^{15})$ years [51].

The first laboratory search for double-beta decay was made in 1948 by E.L. Fireman[52]. The experiment involved a search for coincident pulses in Geiger counters in proximity to a source ^{124}Sn. A limit of $T_{1/2} \simeq (3 \div 9) \cdot 10^{15}$ was assigned to the two neutrino decay mode. The existence of double-beta decay was first confirmed in a series of geochronological experiments by M.C. Inghram and J. H. Reynolds[53] in 1950 using ^{130}Te. These results were confirmed by Takaoka and Ogata[54] in 1966 and again by T. Kirsten *et al.*[55] in 1968. T. Kirsten and co-workers also reported measurement of double beta decay for ^{82}Se in 1967. These experiments relied on mass-spectrometric measurements of the noble gas daughters entrained in very old ores. Excesses of ^{130}Xe and ^{82}Kr were used to determine the double-beta decay half-lives from ores that were independently dated by other techniques. While these measurements unequivocally demonstrated that double-beta decay was a real phenomenon, nothing could be inferred about the particular mode of double-beta decay (*two neutrinos* or *neutrinoless*) responsible of the daughter products.

The discovery by C.S. Wu (1957) of parity violation in weak interaction[56] opened the Dirac-Majorana question, since the long $0\nu\beta\beta$-decay half-life limits could be explained by parity alone, a virtual antineutrino had a wrong helicity to be absorbed as a neutrino. Modern theories allow for the helicity reversal of Majorana neutrinos due to non-zero neutrino mass or for contribution from right-handed weak processes.

The utilization of a high-resolution germanium diode gamma-ray spectrometer as both the source and detector for a double-beta decay experiment was introduced by Fiorini and colleagues[57] in 1967. They were able to assign a limit to the ^{76}Ge neutrinoless double-beta decay mode of $T_{1/2} > 2 \cdot 10^{20}$ years.

The double beta decay, and in particular the neutrinoless mode, has been long recognized as a powerful tool to study lepton number conservation in general, and neutrino properties in particular. Since 1950 many experiments have been realized using different techniques and different $\beta\beta$-candidate nuclei.

2.2 Possible decays

The $\beta\beta$ decay can proceed only if the initial nucleus (A, Z) is less bound than the final one $(A, Z \pm 2)$, but more bound than the intermediate nucleus $(A, Z \pm 1)$. These conditions are realized in nature for a number of even-even nuclei and never for nuclei with an odd number of protons or neutrons. Since the lifetime of $\beta\beta$-decay is always much longer than the age of the Universe (the half-lives is normally in excess of 10^{18} years) both the initial and the final nuclei exist in nature.

An excellent parametrization of the binding energies of nuclei in their ground state is given by the *Semi-Empirical Mass Formula* (SEMF, also called *Bethe-Weizsäcker's formula*) proposed in 1935 by H. Bethe and C. F. von Weizsäcker[58]. This formula relies on *Liquid Drop Nuclear Model*[1] but also incorporates two quantum term: the *asymmetry energy* and the *pairing energy*. The analytic expression is:

$$B(Z,A) = a_{\mathrm{v}}A - a_{\mathrm{s}}A^{\frac{2}{3}} - a_{\mathrm{c}}\frac{Z^2}{A^{\frac{1}{3}}} - a_{\mathrm{a}}\frac{(N-Z)^2}{A} + \delta(Z,A) \tag{2.1}$$

$$\text{where} \quad \delta(Z,A) = \begin{cases} +33.6A^{1/2} & \text{MeV} \quad A \text{ even} \quad Z, N \text{ even} \\ 0 & \text{MeV} \quad A \text{ odd} \\ -33.6A^{1/2} & \text{MeV} \quad A \text{ even} \quad Z, N \text{ odd} \end{cases}$$

where $\delta(Z, A)$ is the *pairing energy term* and where the parameters a_{i} with $\mathrm{i} = \mathrm{v}, \mathrm{s}, \mathrm{c}, \mathrm{a}$ (volume, surface, Coulomb repulsion and asymmetry) are determined empirically. The

---

[1] The liquid drop model is a model in nuclear physics which treats the nucleus as a drop of incompressible nuclear fluid, first proposed by George Gamow. The fluid is made of nucleons, and is held together by the strong nuclear force.

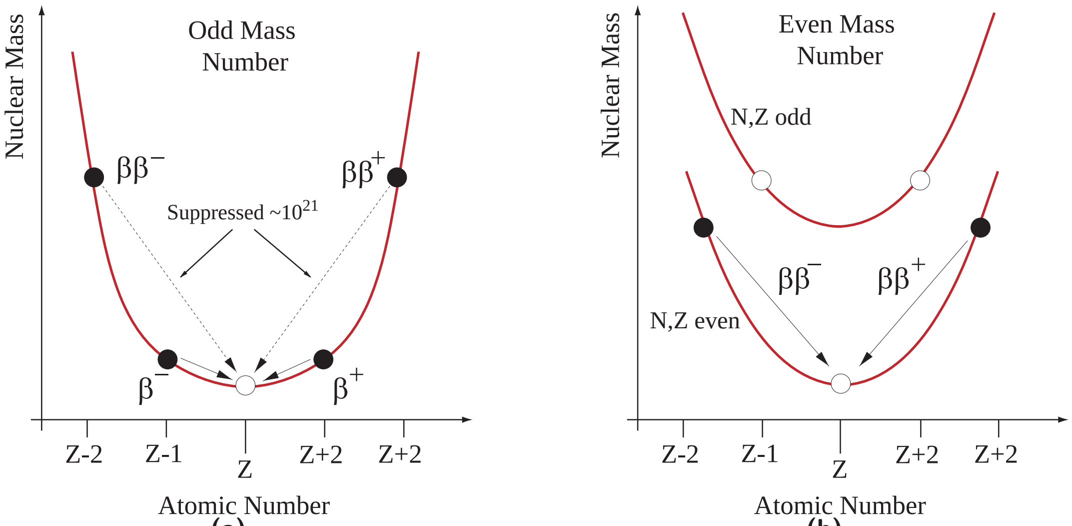

(a) **(b)**

Figure 2.1: Atomic mass as a function of the atomic number Z in the case of a isobar multiplet with A even (left) and A odd (right).

pairing term is a correction that arises from the tendency of proton pairs and neutron pairs to occur. An even number of particles is more stable than an odd number[59, 58].

For a given value of A the nuclear masses follows a parabolic behavior (figure 2.1. For odd-A the binding energy follows a parabola in Z and only one stable nucleus results. The other isobars decay $\beta^{\pm}$, or by electronic capture, towards the only stable nucleus (figure 2.1(a)). For even-A, both even-even and odd-odd occur so two parabolas are implied by the mass equation. The two parabolas are shifted by 2δ and, usually, more than one stable nuclei result. These are cases where double-beta decay can occur (figure 2.1(b)). Double beta decay can occur at the bottom part of the mass valley where a given nucleus ${}^{A}_{Z}\mathrm{X}_{N}$ has an adjacent nucleus ${}^{A}_{Z+1}\mathrm{Y}_{N-1}$ with higher mass while the nucleus ${}^{A}_{Z+2}\mathrm{Y}_{N-2}$ has a lower mass.

For these reasons a possible $\beta\beta$-decay can be observed, in a given nucleus in the initial state (A, Z), only if one of the two following conditions is satisfied:

a) The single-β decay in any state of $(A, Z \pm 1)$ is not allowed energetically;

b) The single-β is allowed energetically but strongly inhibited by an associated large spin change so that the double-β decay in the final state $(A, Z \pm 2)$ is more probable.

These condition are fulfilled in nature for the elements given in table 2.1. In table 2.2 are shown double beta-decay candidates with Q-value of at least 2 MeV.

The two-neutrino double beta decay mode ($2\nu\beta\beta$, figure 2.2(a)) is expected in the Standard Model as a second order weak semileptonic process, and it imposes no special

Decay			Ab. [%]
^{46}Ca	→	^{46}Ti	.004
^{48}Ca	→	^{48}Ti	.187
^{70}Zn	→	^{70}Ge	.6
^{76}Ge	→	^{76}Se	7.8
^{80}Se	→	^{80}Kr	50
^{82}Se	→	^{82}Kr	9
^{86}Kr	→	^{86}Sr	17.3
^{94}Zr	→	^{94}Mo	17.4
^{96}Zr	→	^{96}Mo	2.8
^{98}Mo	→	^{98}Ru	24.1
^{100}Mo	→	^{100}Ru	9.6
^{104}Ru	→	^{104}Pd	18.6
^{110}Pd	→	^{110}Cd	11.7
^{114}Cd	→	^{114}Sn	28.7
^{116}Cd	→	^{116}Sn	7.5
^{122}Sn	→	^{122}Te	4.6
^{124}Sn	→	^{124}Te	5.8
^{128}Te	→	^{128}Xe	31.7
^{130}Te	→	^{130}Xe	33.9
^{134}Xe	→	^{134}Ba	10.4
^{136}Xe	→	^{136}Ba	8.9
^{142}Ce	→	^{142}Nd	11.1
^{146}Nd	→	^{146}Sm	17.2
^{148}Nd	→	^{148}Sm	5.8
^{150}Nd	→	^{150}Sm	5.6
^{154}Sm	→	^{154}Gd	22.1
^{160}Gd	→	^{160}Dy	21.9
^{170}Er	→	^{170}Yb	14.9
^{176}Yb	→	^{176}Hf	12.7
^{186}W	→	^{186}Os	26.6
^{192}Os	→	^{192}Pt	41.0
^{198}Pt	→	^{198}Hg	7.2
^{204}Hg	→	^{204}Pb	6.8
^{232}Th	→	^{232}U	100
^{238}U	→	^{238}Pu	99.

Decay			Ab. [%]
^{36}Ar	→	^{36}S	.34
^{40}Ca	→	^{40}Ar	97
^{50}Cr	→	^{50}Ti	4.3
^{54}Fe	→	^{54}Cr	5.9
^{58}Ni	→	^{58}Fe	68.3
^{64}Zn	→	^{64}Ni	48.6
^{74}Se	→	^{74}Ge	.9
^{78}Kr	→	^{78}Se	.35
^{92}Mo	→	^{92}Zr	15
^{96}Ru	→	^{96}Mo	5.5
^{102}Pd	→	^{102}Ru	1
^{106}Cd	→	^{106}Pd	1.25
^{108}Cd	→	^{108}Pd	.9
^{112}Sn	→	^{112}Cd	.1
^{120}Te	→	^{120}Sn	.1
^{124}Xe	→	^{124}Te	.1
^{126}Xe	→	^{126}Te	.1
^{130}Ba	→	^{130}Xe	.1
^{132}Ba	→	^{132}Xe	.1
^{136}Ce	→	^{136}Ba	.2
^{138}Ce	→	^{138}Ba	.25
^{152}Gd	→	^{152}Sm	.2
^{156}Dy	→	^{156}Gd	.06
^{158}Dy	→	^{158}Gd	.1
^{162}Er	→	^{162}Dy	.14
^{164}Er	→	^{164}Dy	1.6
^{168}Yb	→	^{168}Er	.13
^{174}Hf	→	^{174}Yb	.16
^{184}Os	→	^{184}W	.02
^{196}Hg	→	^{196}Pt	.15

Table 2.1: Double beta decay (left) and double electronic capture (right), with positron emission, candidates.

Decay			Q [keV]			i.a [%]	$(G^{0\nu})^{-1}$ [yr·eV^2]	$(G^{2\nu})^{-1}$ [yr]
^{48}Ca	→	^{48}Ti	4274.0	±	4.0	0.187	4.10E24	2.52E16
^{76}Ge	→	^{76}Se	2039.0	±	0.05	7.800	4.09E25	7.66E18
^{82}Se	→	^{82}Kr	2995.5	±	1.9	9.000	9.27E24	9.27E24
^{96}Zr	→	^{96}Mo	3347.7	±	2.2	2.800	4.46E24	5.19E16
^{100}Mo	→	^{100}Ru	3035.0	±	6.0	9.600	5.70E24	1.06E17
^{110}Pd	→	^{110}Cd	2004.0	±	11.0	11.800	1.86E25	2.51E18
^{116}Cd	→	^{116}Sn	2809.0	±	4.0	7.500	5.28E24	5.28E24
^{124}Sn	→	^{124}Te	2287.8	±	1.5	5.640	9.48E24	5.93E17
^{130}Te	→	^{130}Xe	2530.3	±	2.0	34.500	5.89E24	2.08E17
^{136}Xe	→	^{136}Ba	2462.0	±	7.0	8.900	5.52E24	2.07E17
^{150}Nd	→	^{150}Sm	3367.7	±	2.2	5.600	1.25E24	8.41E15

Table 2.2: Double Beta-Decay candidates with Q-value of at least 2 MeV[60]. The Q-values with errors are deduced from [61], the natural abundances and the phase-space factor for $0\nu\beta\beta$ and $2\nu\beta\beta$ are taken from [62].

requirements on the properties of the neutrino. It will occur independently of whether the neutrino is a Majorana or a Dirac particle and also independently of whether it has mass or not. Its lifetime is proportional to $(G_{\mathrm{F}}\cos\theta_c)^{-4}$, where $G_{\mathrm{F}} = 1.166\cdot 10^{-5}$ GeV^{-2} is the *Fermi coupling constant* and θ_c is the *Cabibbo angle*. The possible 2ν decay modes are:

$$
\begin{array}{rcllc}
(A,Z) & \rightarrow & (A,Z+2)+2e^{-}+2\overline{\nu}_e & \beta\beta^{-} & (i) \\
(A,Z) & \rightarrow & (A,Z-2)+2e^{+}+2\nu_e & \beta\beta^{+} & (ii) \\
(A,Z)+2e^{-} & \rightarrow & (A,Z-2)+2\nu_e & \mathrm{ECEC} & (iii) \\
(A,Z)+e^{-} & \rightarrow & (A,Z-2)+e^{+}+2\nu_e & \mathrm{EC}\beta^{+} & (iv)
\end{array}
\tag{2.2}
$$

It is simply to see that in all processes the *lepton number* is conserved ($\Delta L = 0$). The nuclear transition accompanied by positron or electron capture processes (2.2, (*ii*), (*iii*), (*iv*)) are characterized by poorer experimental sensitivities.

The first direct laboratory observation of $2\nu\beta\beta$ decay was reported by Elliott, Hahn, and Moe[63] in 1987. They used a Time Projection Chamber to measure the two-neutrino double-beta events from a source consisting of 14g of 97% isotopically enriched ^{82}Se contained between thin aluminized Mylar® sheets. Their value of $T_{1/2} = 1.1\cdot 10^{20}$ years was in excellent agreement with the *geochronological half-life* reported earlier for this isotope. Afterwards this decay was observed in more than ten nuclei [64, 65].

More interesting is the *neutrinoless* double beta decay ($0\nu\beta\beta$, figure 2.2(b)), first suggest by G. Racah in 1939[50], with the emission of a neutrino from one neutron and its absorption on another.

$$
(A,Z) \;\rightarrow\; (A,Z+2)+2e^{-} \tag{2.3}
$$

This process violates the lepton number conservation ($\Delta L = 2$) and is therefore forbidden in the standard electroweak theory. For this reason it could be a possible window into a physics "*beyond the Standard Model*". In fact the $0\nu\beta\beta$ decay can occur only if two requirements are satisfied:

a) the neutrino exchanged has to be a Majorana particle. This means that antineutrino and neutrino are actually the same particle ($\overline{\nu} = \nu$);

b) the neutrino has to have a non-vanishing mass and/or the neutral current has to have a right handed (V+A) component. This condition is needed because of the helicity of the neutrino. Due to the V-A nature of the weak interaction, the neutrino emitted in the first vertex (figure 2.2(b)) is right-handed, while in order to be absorber in the second one, it needs to change its helicity. This is possible only if the neutrino has a finite mass and, in this case, the decay amplitude is proportional to m_ν.

If the global symmetry associated with lepton number[2] is broken spontaneously, the model imply the existence of a Goldstone boson, called *Majoron* (χ), which couples to neutrinos. The possible process is the following:

$$(A, Z) \quad \rightarrow \quad (A, Z+2) + 2e^- + \chi \tag{2.4}$$

Double beta decay with majoron emission, the $\beta\beta\chi$ mode (eq. 2.4 and figure 2.2(c)), is classified in the category of *lepton-number-violating* decays, even though the lepton number is formally conserved when χ is assigned the lepton number $L_\chi = -2$[66].

It is easy to distinguish the three decay modes by the shape of the electron sum energy spectra, which are determined by the phase space of the outgoing light particles. In the 2ν decay (figure 2.3), the summed kinetic energy K_e of the two electrons displays a broad maximum below half the endpoint energy. In contrast, in the 0ν mode, the two electrons carry the full available kinetic energy (the nuclear recoil is negligible for all practical purposes) and the spectrum is therefore a single peak at the endpoint. In the majoron decay the electron spectrum is again continuous, but the maximum is shifted higher, above the halfway point, as required by the *three-light-particle* phase space.

From a Particle Physics point of view the neutrinoless double beta decay is a very important process insofar as representing a unique tool to establish the absolute neutrino mass scale, its nature (Dirac/Majorana) and the values of the Majorana CP phase. Starting from experimental results on $0\nu\beta\beta$ decay lifetimes it's possible to determinate the very important quantity $\langle m_\nu \rangle$ called *effective neutrino mass*. In order to extrapolate this parameter a precise knowledge of the nuclear transition matrix elements is required.

The experimental study of $0\nu\beta\beta$ decay presents a formidable challenge. This decay must be detected in the presence of an inevitable background of similar energy caused

---

[2] the *B-L symmetry*, baryon number minus the lepton number.

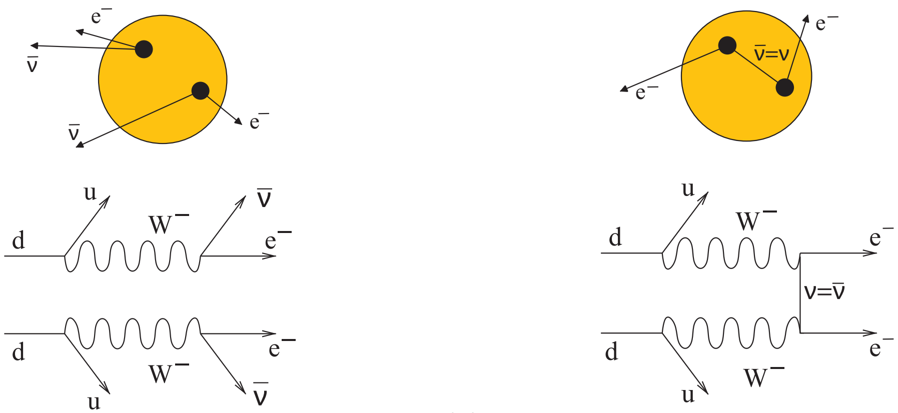

(a) Feynman diagram for $2\nu\beta\beta$ decay. The lepton number is conserved ($\Delta L = 0$), this transition is expected in the standard electroweak theory

(b) Feynman diagram for $0\nu\beta\beta$ decay. The lepton number is violated ($\Delta L = 2$), this transition is forbidden in the standard electroweak theory.

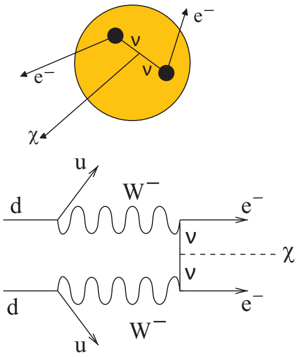

(c) Feynman diagram for $2\nu\beta\beta$ decay with the emission of a Majoron χ.

Figure 2.2: The three possible $\beta\beta$ transitions.

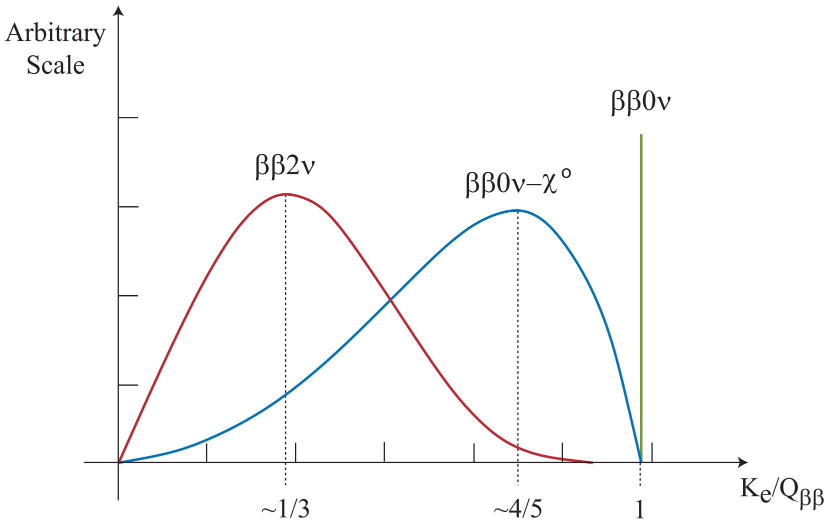

Figure 2.3: Schematic electron sum-energy of the three $\beta\beta$ decay modes. Each is normalized arbitrarily and independently of the others. The abscissa is the ratio $K_e/Q_{\beta\beta}$ of the sum of the electron kinetic energies divided by its maximum value.

by trace radioisotopes with half-lives 15 or more orders of magnitude shorter. Thus the present-day experiments are characterized by an optimum separation of the signal from the background combined with the requirement of kilogram quantities of the source isotopes.

2.3 Decay rate and Majorana Mass

Considering only the case of left-handed V-A weak current and light massive Majorana neutrinos, the *differential decay rate* (*inverse half-time*) for the $\beta\beta0\nu$ transition can be written as:

$$\begin{aligned}\Gamma^{0\nu}_{1/2} = [T^{0\nu}_{1/2}(0^+ \rightarrow 0^+)]^{-1} &= G^{0\nu}(E_{\max}, Z)\left| M^{0\nu}_{\mathrm{GT}} - \frac{g_V^2}{g_A^2} M^{0\nu}_{\mathrm{F}} \right|^2 |\langle m_\nu \rangle|^2 \\ &= G^{0\nu}(E_{\max}, Z)|M^{0\nu}|^2 \; |\langle m_\nu \rangle|^2 \\ &= F_N \, \frac{|\langle m_\nu \rangle|^2}{m_e^2} \end{aligned} \tag{2.5}$$

$$\text{with} \quad |M^{0\nu}|^2 = \left| M^{0\nu}_{\mathrm{GT}} - \frac{g_V^2}{g_A^2} M^{0\nu}_{\mathrm{F}} \right|^2 \quad \text{and} \quad \frac{F_N}{m_e^2} = G^{0\nu}(E_{\max}, Z)|M^{0\nu}|^2 \tag{2.6}$$

$G^{0\nu}$ is the exactly calculable[67, 68] *phase space* integral ($G^{0\nu} \propto Q^5_{\beta\beta}$ where $Q_{\beta\beta}$ represents the Q-value of the decay), $|M^{0\nu}|^2$ is the specific *nuclear matrix element* of the nucleus undergoing the decay (M_{GT} and M_{F} are, respectively, the Gamow-Teller and Fermi matrix elements), g_V and g_A are the *vector* and the *axial-vector* coupling constant and, at last, the parameter m_e is the electron mass. The *nuclear structure factor* F_N is calculable using different nuclear models.

The parameter $|\langle m_\nu \rangle|$ is the *effective electron neutrino mass* (often written $|\langle m_{ee} \rangle|$) also called *effective Majorana mass.* This mass is directly derivable from the measured half-life of the decays as follows:

$$|\langle m_\nu \rangle| \equiv |\langle m_{ee} \rangle| = m_e \, \frac{1}{\sqrt{F_N \; T^{0\nu}_{1/2}}} \tag{2.7}$$

The value of $|\langle m_\nu \rangle|$ is derived from nuclear structure calculation and, for this reason, is model dependent. In table 5.2 is reported the case of the ^{130}Te. Using the oscillation parameters the *effective Majorana mass* is given by:

$$|\langle m_\nu \rangle|^2 = \left| \sum_{i=1}^{n=3} U_{ei} m_i \right|^2 = \left| |U_{e1}|^2 m_1 + |U_{e2}|^2 m_2 \mathrm{e}^{\imath\alpha_2} + |U_{e3}|^2 m_3 \mathrm{e}^{\imath\alpha_3} \right|^2 \tag{2.8}$$

where $\mathrm{e}^{\imath\alpha_2}$ and $\mathrm{e}^{\imath\alpha_3}$ are the *Majorana CP Phase* (±1 for CP conservation), m_i with $i = 1, 2, 3$ are the mass eigenvalues. The parameters U_{ei} are the elements of the mixing matrix PMNS, they are given by:

$$\begin{cases} |U_{e1}| = \cos^2\theta_{13}\cos^2\theta_{12} \\ |U_{e2}| = \cos^2\theta_{13}\sin^2\theta_{12} \\ |U_{e3}| = \sin^2\theta_{13} \end{cases} \tag{2.9}$$

The presence of the phases $\mathrm{e}^{\imath\alpha_i}$ implies that the CP cancellations are, unfortunately, possible. Such cancellations are complete for a Dirac neutrino, since it is equivalent to two degenerate Majorana neutrinos with opposite CP phases. This stresses once more the fact that $0\nu\beta\beta$ can occur only through the exchange of Majorana neutrinos.

From a Particle Physics point of view, the neutrinoless double-beta decay represents a unique tool in order to measure the neutrino Majorana phases and to estimates the absolute scale of the neutrino masses. As in evidence from eq. 2.5, the derivation of the crucial parameter $|\langle m_\nu \rangle|$ from the experimental results on the lifetime requires a precise knowledge of the Nuclear Matrix Elements (NME) of the transition. Many, often conflicting, evaluations are available in the literature and it is unfortunately not easy to judge their correctness or accuracy (table 2.3).There are two well established approaches for the calculation of the double-beta decay nuclear matrix elements: the *Shell Model* (SM, [69]) and the *Quasi-particle Random Phase Approximation* (QRPA, [70, 71, 72, 73]).

The values of $|\langle m_\nu \rangle|$ also depends on the neutrino mass spectrum. According with the mass hierarchies scenario (presented in section 1.4) three mass scheme are possible:

1) **Normal Hierarchy**

$$\langle m_\nu \rangle \simeq |\cos^2\theta_{13}\left[\Delta m^2_\odot e^{2\imath\phi_2} sin^2\theta_\odot\right] + \sqrt{\Delta m^2_{\text{atm}}} e^{2\imath\phi_3} \sin^2\theta_{13}\sqrt{\Delta m^2_{\text{atm}}}| \qquad (2.10)$$

From this expression we can also derive an upper and a lower bound for $< m_\nu >$:

$$\begin{cases} \langle m_\nu \rangle \leq |\cos^2\theta_{13}\sin^2\theta_\odot\sqrt{\Delta m^2_\odot} + \sin^2\theta_{13}\sqrt{\Delta m^2_{atm}}| \\ \\ \langle m_\nu \rangle \geq |\cos^2\theta_{13}\sin^2\theta_\odot\sqrt{\Delta m^2_\odot} - \sin^2\theta_{13}| \end{cases} \qquad (2.11)$$

2) **Inverted Hierarchy**
By Neglecting the small correction due to $|U_{e3}|^2$ one obtains:

$$\langle m_\nu \rangle \simeq \sqrt{\Delta m^2_{\text{atm}}}|\cos^2\theta_{13}(\cos^2\theta_\odot + e^{2\imath\alpha_{23}} sin^2\theta_\odot)| \qquad (2.12)$$

where $\alpha_{23} = \alpha_2 - \alpha_3$ is a Majorana CP-phase difference. In the case of HI the value of the $\langle m_\nu \rangle$ can lay in the range (in the case of CP conservation):

$$\begin{cases} \langle m_\nu \rangle \leq \sqrt{\Delta m^2_{\text{atm}}} \\ \\ \langle m_\nu \rangle \geq \cos 2\theta_\odot\sqrt{\Delta m^2_{\text{atm}}} \end{cases} \qquad (2.13)$$

3) **Quasi-Degenerated Hierarchy**
By Neglecting the small correction due to $|U_{e3}|^2$ one obtains:

$$\langle m_\nu \rangle \simeq m_1|\cos^2\theta_{13}(\cos^2\theta_\odot + e^{2\imath\alpha_3}\sin^2\theta_\odot)| \qquad (2.14)$$

thus in the case of QDH the value of $< m_\nu >$ can lay in the range:

$$\begin{cases} \langle m_\nu \rangle \leq m_1 \\ \\ \langle m_\nu \rangle \geq \cos 2\theta_\odot m_1 \end{cases} \qquad (2.15)$$

From the previous equations it is simple to see that unless $\langle m_\nu \rangle$ depends on the unknown phases α_i, the upper and lower limits for effective mass depend only on the absolute value of the mixing angles. Thus, if the search for $0\nu\beta\beta$ is successful and the value of $\langle m_\nu \rangle$ is determined, and, at the same, time the mixing angles $|U^2_{ei}|$ and the mass square differences Δm^2_{ij} are known from oscillation experiments[74, 47], a range of absolute values of the neutrino masses can be deduced (figure 2.4). Using

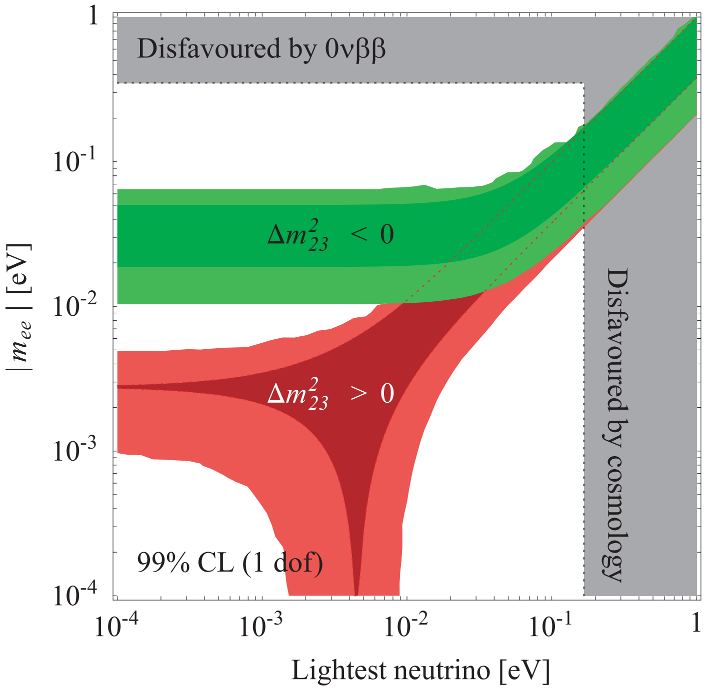

Figure 2.4: The effective Majorana mass $\langle m_\nu \rangle$ as a function of the lightest neutrino mass [34, 75, 76]. The disfavored regions are given by the present limits on double-beta decay experiments (table 2.5[77]) and by cosmological bounds.[78, 79, 80]

other constraint, for example a successful determination of the neutrino mass square $\langle m_\nu \rangle \equiv \langle m_e \rangle = \sum_i |U^2_{ei}| m_i^2$ in single-beta decay experiments, it's possible to use the knowledge of $\langle m_\nu \rangle$ to determine or constrain the phases α_i.

It is also possible to constrain the Majorana neutrino contribution to the to the sum of neutrino masses[81, 82] $\Sigma = \Sigma_j m_j$ (cosmic microwave fluctuations):

$$2|\langle m_\nu \rangle| + \sqrt{|\langle m_\nu \rangle|^2 \pm \Delta m^2_{\text{atm}}} \leq \Sigma \leq \frac{2|\langle m_\nu \rangle| + \sqrt{|\langle m_\nu \rangle|^2 \pm \Delta m^2_{\text{atm}} \cos^2(2\theta_{13})}}{|\cos 2\theta_{13}|} \tag{2.16}$$

where the plus sign is for NH and the minus sign is for IH. In the case $\Delta m^2_{\text{atm}} << \Sigma^2$ the above inequality can be simplified as follow:

$$|\langle m_\nu \rangle| \leq \frac{\Sigma}{3} \leq 2|\langle m_\nu \rangle| \tag{2.17}$$

The $\beta\beta$-experiments developed up to now, often called *First Generation Experiments*, were designed to explore only the degenerate mass scenario. The proposed *Second Generation Experiments* are designed to explore the inverted hierarchy scenario, with an expected sensitivity on $|m_{ee}|$ of the order of $(10 \div 50)$ meV.

Finally, in the case of double-beta decay with emission of two neutrinos and in the case of neutrinoless double-beta decay with Majoron emission, the inverse half-time is given by:

$$\begin{aligned}
\Gamma^{2\nu}_{1/2} &= [T^{2\nu}_{1/2}(0^+ \to 0^+)]^{-1} = G^{2\nu}(E_{\max}, Z)|M^{2\nu}_{\rm GT}|^2 && 2\nu\beta\beta \\
\Gamma^{0\nu,\chi}_{1/2} &= [T^{2\nu}_{1/2}(0^+ \to 0^+)]^{-1} = G^{0\nu,\chi}\left|M^{0\nu}_{\rm GT} - \tfrac{g_V^2}{g_A^2}M^{0\nu}_{\rm F}\right|^2 \langle g_{\nu\chi}\rangle && 0\nu\beta\beta\chi
\end{aligned} \tag{2.18}$$

where $g_{\nu\chi}$ is the effective majoron-neutrino coupling constant[67].

2.4 Nuclear matrix elements

As shown in 2.5 and 2.6 for the $0\nu\beta\beta$ mode (but also for $2\nu\beta\beta$ and $0\nu\beta\beta\chi$ modes) one can separate the phase space and nuclear parts of the rate formula. All nuclear structure effects are then represented by the nuclear matrix elements. These values have become an important issue because they play a central role when one starts to extract quantitative neutrino properties. The matrix elements are weak spots of the double-beta decay research for the neutrino mass determination. In fact, the uncertainty in the elements calculation determines the spread width for the neutrino effective mass.

In the case of two neutrinos double-beta decay mode the nuclear matrix elements are given by[83]:

$$M^{2\nu}_{\rm GT} = \sum_{\rm m} \frac{\langle {\rm f}|\vec{\sigma}\cdot\vec{\tau}|{\rm m}\rangle\langle {\rm m}|\vec{\sigma}\cdot\vec{\tau}|{\rm i}\rangle}{E_{\rm m} - \frac{M_{\rm m}+M_{\rm f}}{2}} \tag{2.19}$$

where $|{\rm f}\rangle$ ($|{\rm i}\rangle$) are the 0^+ ground states of the final (initial) even-even nuclei of masses $M_{\rm f}$ ($M_{\rm i}$), and $|{\rm m}\rangle$ are the 1^+ states in the intermediate odd-odd nucleus of energy $E_{\rm m}$. Owing to the isospin conservation there is only the Gamow-Teller contribution ($M^{2\nu}_{\rm GT}$) without the Fermi part ($M^{2\nu}_{\rm F} = 0$).

The individual factors in equation 2.19 have straightforward physical meaning; the last factor in the numerator is the amplitude of the β^- decay (or of the forward-angle (p , n) reaction) of the initial nucleus, and the first factor is the amplitude of the β^+ decay (or of the (n , p) reaction) of the final nucleus.

Considering the neutrinoless double-beta decay mode, the process can proceed via exchange of a light virtual Majorana neutrino the nuclear matrix elements are defined as:

$$\begin{aligned} M_{\mathrm{F}}^{0\nu} &= \sum_{\mathrm{m,n}} \langle \mathrm{f}||h_{\mathrm{F}}(|\vec{r}_{\mathrm{m}} - \vec{r}_{\mathrm{n}}|)||\mathrm{i}\rangle \\ M_{\mathrm{GT}}^{0\nu} &= \sum_{\mathrm{m,n}} \langle \mathrm{f}||h_{\mathrm{GT}}(|\vec{r}_{\mathrm{m}} - \vec{r}_{\mathrm{n}}||)(\vec{\sigma}_m \cdot \vec{\sigma}_n)|\mathrm{i}\rangle \end{aligned} \tag{2.20}$$

where the summation runs over all the intermediate states and the integration is taken over the relative coordinate $|\vec{r}_{\mathrm{m}} - \vec{r}_{\mathrm{n}}|$ between the nucleus m and n. The term $h_{\mathrm{k}}(|\vec{r}_{\mathrm{m}} - \vec{r}_{\mathrm{n}}|)$, with $\mathrm{k} = \mathrm{F}, \mathrm{GT}$, is the neutrino potential[83].

There are two basic approaches to the evaluation of the nuclear matrix elements for both the $0\nu\beta\beta$ and $2\nu\beta\beta$ decays: the *Quasi-particle Random Phase Approximation* (QRPA) and the *Nuclear Shell Model* (NSM).

NSM attempts to solve the nuclear many body problem as exactly as possible. Hence, it is the best choice for the calculation of the nuclear matrix elements. Despite of the advantages of calculation techniques up to now only a limited set of single particle states can be used.

QRPA is the nuclear much body method most widely used to deal with the nuclear structure aspects of the double-beta decay process. This method has been found successful in explaining the quenching of the $0\nu\beta\beta$-decay nuclear matrix element and bring them into closer agreement with experimental values. But despite this success the QRPA approach to double-beta decay has some defects. The main problem is that results are extremely sensitivity to the renormalization of the attractive particle-particle component of residual interaction, which is large part responsible for suppressing calculated two neutrino decay rate. Including proton-neutron pairing, several alternations have been made in QRPA (RQRPA[72, 73], pnQRPA[84]).

Alternative models, as the *Operator Expansion Method* (OEM), the broken $SU(4)$ symmetry, the pseudo $SU(3)$ and *Single State Dominance Hypothesis* (SSDH) have their own problems. Recently, deformation structure in nuclei has been taken into account in calculation of nuclear matrix element.

Unfortunately, at the present time, the calculated matrix elements are far away from the experimental results. This is a very strong limitation for the neutrino effective mass determination using the double-beta decay search.

2.5 Experimental overview

Up to now, in order to measure double beta decays, there are two main experimental approaches:

1) **Indirect** (or *Inclusive*): These techniques, which had an important role in the past, measure the anomalous concentration of daughter nuclei in samples with a

	Ref.	**Authors**	**Method**	$\mathbf{F_N}(^{\mathbf{130}}\mathrm{Te})$ $[10^{-13}\ \mathrm{y}^{-1}]$	$\mathbf{F_N}(^{\mathbf{76}}\mathrm{Ge})$ $[10^{-13}\ \mathrm{y}^{-1}]$
QRPA	[85]	Staudt *et al.* (1992)	pairing (Paris)	29-34	5.9-10
		pairing (Bonn)	24-29	4.5-8.9	
	[86]	Pantis *et al.* (1996)	no p-n pairing	3.0	0.73
		p-n pairing	1.24	0.14	
	[87]	Vogel, (1986)		3.96	0.19
	[88]	Civitarese, (1987)		5.0	1.2
	[89]	Tomoda, (1991)		5.03	1.2
	[90]	Barbero *et al.* (1999)		7.77	0.84
	[91]	Simkovic (1999)	pn-RQRPA	1.79	0.62
	[70]	Suhonen *et al.* (1992)		3.13	0.72
	[92]	Muto et *al.* (1989)		5.34	1.1
	[93]	Stoica *et al.* (2001)	large basis	2.44	0.65
			short basis	2.66	0.9
	[71]	Faessler *et al.* (1998)		2.78	0.83
	[68]	Engel *et al.* (1989)	generalized seniority	10.9	1.14
	[94]	Aunola *et al.* (1998)	WS	5.72	0.9
			AWS	5.06	1.33
	[95]	Rodin *et al.* (2003)		0.95	0.45
SM	[96]	Haxton *et al.* (1984)	weak coupling	16.3	1.54
	[97]	Caurier *et al.* (1996)	large basis	0.45	0.15
OEM	[98]	Hirsh *et al.* (1995)		7.3	3.6

Table 2.3: Example of $0nu\beta\beta$-nuclear structure factor F_N for ^{130}Te and ^{76}Ge according to different evaluation methods. QRPA: Quasi Random Phase Approximation, SM: Shell Model and OEM: Operator Expansion Method).

long accumulation time. They have been used to give indirect evaluations of the $0\nu\beta\beta$ and $2\nu\beta\beta$ lifetimes. This category includes two of measurements:

(a) **Geochemical measurement**: determination of the total decay time through the measurement of the daughter nuclei $(A, Z+2)$ produced by the parent nuclei $(A, Z+2)$ in a sample of *old* geological rocks (for example by extraction of Kr and Xe from very old Se and Te minerals).

(b) **Radiochemical measurement**: determination of the total decay time by extraction of the radioactive daughter nuclei from the parent nuclei. For example the double-beta decay rate of ^{238}U (also an alpha emitter) has been measured radiochemically; ^{238}Pu is produced by this type of radioactivity.

2) **Direct** (or *Counter*): these are the presently most diffuse techniques, and are

based on the direct observation of electrons emitted in the process. These detectors can identify the double-beta reaction modes: $0\nu\beta\beta$ process should be easily identified because of a mono-energetic line at the Q value. The better the detector energy resolution, the stronger the signal. Two technical approaches are possible:

(a) **Passive source**: the source is external to the detector: the experimental configuration usually consists of foil shaped sources with two detectors (e.g. scintillators, TPCs, drift chambers, etc) analyzing the electrons emerging from the foil. Using tracking detectors a background rejection is possible studying the event topology. The limits of this approach are the energy resolution and the small source mass.

(b) **Active source**: the source is internal to the detector (*calorimeter*): only the sum energy of the two electrons is measured and the signature for $0\nu\beta\beta$ decay is therefore a peak at the transition energy $Q_{\beta\beta}$. The detector can be a scintillator, a bolometer, a semiconductor diode or a gas chamber. Calorimeters can have large mass and high efficiency. Depending on the technique, high energy resolution and also some tracking are possible.

Geochemical and radiochemical experiments, a mainstay of double beta decay physics through the 1970s and 1980s, do not distinguish the different $\beta\beta$-decay. Thus, there is little interest in pursuing these techniques further. Instead, relatively new technologies such as bolometers and scintillating crystals are receiving attention. Using these it is also possible to search for the decay without neutrinos, which represents the most interesting process.

Neutrinoless double beta decays of interest to experimentalists are typically resulting in an energy release of around 2 MeV (^{48}Ca has, with 4.274 MeV, the largest decay energy, table 2.2). Many forms of natural, cosmogenic and anthropogenic radioactivity result in a similar low energy signature constituting potential background.

In order to compare the performances of different detectors, it's convenient to introduce a parameter that work like a figure of merit called *Neutrinoless Sensitivity* and denoted by $S^{0\nu\beta\beta}$ or $S^{0\nu}$. It is defined as the process' half life corresponding to the maximum number of signals (N_{bkg}) that could be hidden by background fluctuation, at a given statistical confidence level[99]. It's an experimental parameter expressed, at 1σ level, as:

$$S^{0\nu\beta\beta} \equiv T^{0\nu}_{1/2} = \ln 2 \cdot \epsilon \, \frac{N_{\text{nuclei}}}{N_{\text{bkg}}} \, t \tag{2.21}$$

where:

$$N_{\text{bkg}} = \sqrt{B \cdot \Gamma \cdot M \cdot t} \quad , \quad N_{\text{nuclei}} = \frac{M \cdot \text{i.a.}}{A} \tag{2.22}$$

N_{nuclei} is the number of atoms candidates for the decay present in the source, i.a. their isotopic abundance, M the mass of the $\beta\beta$-emitter, ϵ the efficiency of the detector, Γ the energy resolution (around the $Q_{\beta\beta}$-value), B is the background expressed in counts per unit per energy per unit time, A the molecular mass and, at last, t the measurement time (or live time). Replacing the 2.22 in the 2.21 one obtains:

$$S^{0\nu\beta\beta} = \ln 2 \cdot \epsilon \, \frac{\text{i.a.}}{A} \sqrt{\frac{M \cdot t}{\Gamma \cdot B}} \tag{2.23}$$

This factor emphasises the role of the essential experimental parameter: mass, live time, isotopic abundance, background level, energy resolution and detection efficiency. By the equation 2.8, it is also possible to deduce the experimental sensitivity to the neutrino mass:

$$F^{\langle m_\nu \rangle} \equiv |\langle m_\nu \rangle| = m_e \, \frac{1}{\sqrt{S^{0\nu\beta\beta} \cdot F_N}} = m_e \, \sqrt{\frac{A}{\text{i.a.} \cdot \ln 2 \cdot \epsilon \cdot F_N}} \, \left(\frac{\Gamma \cdot B}{M \cdot t} \right)^{\frac{1}{4}} \tag{2.24}$$

Because the number of background counts increases linearly with time (`eq.` 2.22), the decay rate sensitivity scales as the square root of time (`eq.` 2.23). In turn, the neutrino effective mass scales as the square root of the decay rate, and therefore as the fourth root of the counting time (`eq.` 2.24).

According to `eq` 2.23 and `eq` 2.24, it is straightforward to conclude that to obtain the best sensitivity to $|\langle m_\nu \rangle|$, a $0\nu\beta\beta$ experiments must have the following characteristics:

- a very large mass (approximately a ton of isotope will be required);
- a good resolution and high efficiency around the $Q_{\beta\beta}$-value;
- a very low background. Any radioactive isotope with Q-value greater than the $0\nu\beta\beta$ endpoint may be a potential background. To suppress the background contribution it is desirable to select a double-beta candidate with a large $Q_{\beta\beta}$ as possible performing the experiment in a low activity environment and, eventually, using event topology reconstruction;
- a long measurements time;
- a chosen $\beta\beta$-emitter isotope with a high natural isotopic abundance is preferred. If enrichment is not necessary the result is a significant cost savings.

A sensitivity of $\simeq$ 0.01 eV is required in order to check inverse hierarchy. The background is a fundamental issue: to reduce it, all passive (e.g. heavy shielding in underground sites, material selection and purification) and active (e.g. Pulse Shape Discrimination, topology analysis through granularity and segmentation) expedients must be taken. However the background caused by the high energy tail of the continuous $2\nu\beta\beta$ spectrum cannot be avoided and must be minimized by improving the energy resolution.

2.5.1 Past and existing experiments

Optimal neutrinoless sensitivities have been reached in a series of experiments based on the active source approach. In particular, the best limit on $0\nu\beta\beta$ comes from the Heidelberg-Moscow (HM) experiment[100, 101] on ^{76}Ge even if similar results have been obtained also by the IGEX experiment[102, 103]. In the following a selection of the most sensitive past and running experiments is presented (table 2.5).

1) **Calcium-48**
^{48}Ca is the most favorable isotope among other potential $0\nu\beta\beta$ nuclei because it has the largest Q-value (4274 keV), hence the possibility of the occurrence is highest, and the expected background should be lower than in remaining candidate nuclei. A CaF$_2$ scintillation detector system (ELEGANTS VI), which consists of 6.6 Kg of CaF$_2$ crystals as sensitive mass, has been developed at the Oto Cosmo observatory, near Nara in Japan. The obtained energy spectrum after all cuts gives a lower limit for the half life of $T^{0\nu}_{1/2} > 1.4 \cdot 10^{22}$ y.

2) **Germanium-76**
Two experiments have looked for the double-beta decay of ^{76}Ge nucleus.

   (a) The Heidelberg-Moscow (HM): this experiment searched the $0\nu\beta\beta$ decay of ^{76}Ge using five *High Purity Ge* (HPGe) semiconductor detectors enriched to 86-88% in ^{76}Ge[100, 101]. It run in the Gran Sasso Underground Laboratory (Italy) from 1990 to 2003, totalling an exposure of 71.7 $\text{Kg} \cdot \text{y}$. It is by far the longest running $0\nu\beta\beta$ decay experiment with the largest exposure. The final background at the Q-value is about (0.113 ± 0.007) counts/keV/kg/y and it is attributed mainly to ^{238}U and ^{232}Th contaminations in the set-up materials.

   After the conclusion of the experiment, part of the collaboration (hereafter KKDC) has reanalyzed the data[104] claiming a 4.2σ evidence for ^{76}Ge $0\nu\beta\beta$ decay with a lifetime $T^{0\nu}_{1/2} \simeq 1.2 \cdot 10^{25}$ y, corresponding to a neutrino effective mass of about 0.44 eV[101]. This claim has sparked a debate in the neutrino physics community[105, 106, 107, 108, 109, 110] because the signal is indeed faint and close to other unexplained peaks (figure 2.5).

   (b) IGEX (*International Germanium EXperiment*): the detector[102, 103], which is homed at the Spanish laboratory of Canfranc, consists of three HPGe detectors enriched in ^{76}Ge up to 88%, with a total active mass of at least 6 Kg.

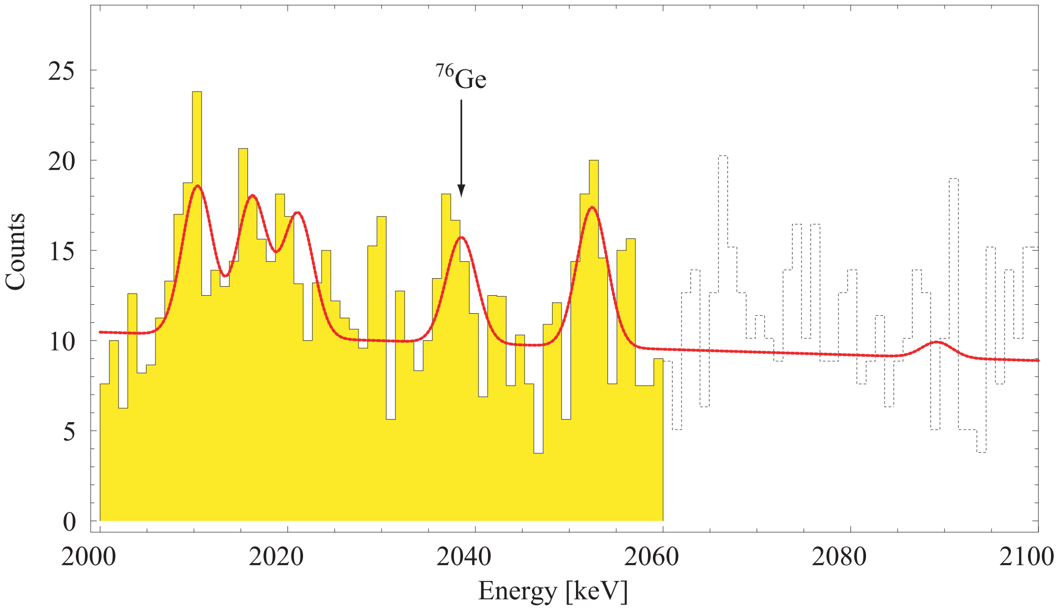

Figure 2.5: The latest HM data (71.7 $\mathrm{Kg \cdot y}$, from November 1990 to May 2003) used to claim a 4.2σ evidence for ^{76}Ge $0\nu\beta\beta$. The claimed $0\nu\beta\beta$-peak is at (2038.07 ± 0.44) KeV.
x

After pulse shape discrimination analysis, the background rate (about 0.17 counts/keV/kg/y) is as great as in HM experiment in the energy interval between 2.0 and 2.5 MeV, while the energy resolution is 4 KeV. Analysis on 8.87 Kg(76Ge) · y of data gives a lower bound $T^{0\nu}_{1/2} > 1.57 \cdot 10^{25}$ y. Its sensitivity is not enough to check the KKDC claim.

3) **Molybdenum-100**
Several collaborations have worked on ^{100}Mo isotope, in particular

(a) NEMO *Neutrino Ettore Majorana Observatory*: NEMO-3 experiment[111, 112], which started its data taking in February 2003, is homed at Fréjus Underground Laboratory. It uses a cylindrical tracking detector (drift chamber) to analyze the electrons emitted by foils of different enriched material. Interesting $0\nu\beta\beta$ decay sensitivities are expected only for the ^{100}Mo and ^{82}Se sources. It analyzes also the $0\nu\beta\beta$ reactions of ^{82}Se, ^{96}Zr, ^{100}Mo, and ^{116}Cd. After measures taken in 2004 to suppress radon, the background is now about 0.5 count/kg/y. The data analysis using a maximum likelihood gives the following 90%C.L. lower limits:

$$\begin{cases} {}^{100}\mathrm{Mo}: & T^{0\nu}_{1/2} \simeq 5.8 \cdot 10^{23}\ \mathrm{y} \quad \Rightarrow \quad |\langle m_\nu \rangle| = (0.6 \div 2.4)\ \mathrm{eV} \\ \\ {}^{82}\mathrm{Se}: & T^{0\nu}_{1/2} \simeq 2.1 \cdot 10^{23}\ \mathrm{y} \quad \Rightarrow \quad |\langle m_\nu \rangle| = (1.2 \div 3.2)\ \mathrm{eV} \end{cases} \tag{2.25}$$

In 2009, the expected 90%C.L. sensitivity on ^{100}Mo will be $T^{0\nu}_{1/2} \simeq 2 \cdot 10^{24}$ y corresponding to $|\langle m_\nu \rangle| \simeq (0.3 \div 1.3)$ eV.

(b) ELEGANT V: the most stringent half-life limit on ^{100}Mo is obtained by a spectrometer at the Oto Cosmo Observatory by Osaka University. The detector consists of three drift chambers and the passive source consists of two foils enriched in ^{100}Mo up to 95%. The lower limit thus obtained is $T^{0\nu}_{1/2} > 5.5 \cdot 10^{22}$ y[113].

4) **Cadmium-116**
Experiments with ^{116}Cd have been made by the Ukrainian Institute of Nuclear Research INR-Kiev in collaboration with a italian group (INFN Firenze). The apparatus was housed in the salt mine of Solotvina (Ukraina). The lower limit is $T^{0\nu}_{1/2} > 1.7 \cdot 10^{23}$ y[114]

5) **Tellurium-130**
^{130}Te isotope (and also ^{128}Te) has been investigated by the Milano WIG Group (*Weak Interactions Group*), within the project MiBETA (or MiDBD), by developing low temperature thermal detectors in the form of TeO_2 crystals (bolometers).

The detector was homed at Gran Sasso Laboratories, and consists of an array of 20 TeO_2 crystals, with a total mass of 6.8 Kg, which operate at a temperature of about 12 mK; its resolution is 8 KeV in the $0\nu\beta\beta$ region (2530.3 KeV). The background level in the same region is about 0.5 counts/KeV/Kg/y. The lower limit is $T^{0\nu}_{1/2} > 2.1 \cdot 10^{23}$ y corresponding to $|\langle m_\nu \rangle| \simeq (1.1 \div 2.6)$ eV[115, 116].

As it will illustrated afterwards (chapter 5), since April 2003 a prototype called CUORICINO, which consists of an array of TeO_2 bolometers for a total mass of 40.7 Kg, is running at the Gran Sasso Laboratories.

6) **Xenon-136**
The $0\nu\beta\beta$ decay of ^{136}Xe has been studied by the Caltech-Neuchatel-PSI collaboration and the Italian DAMA collaboration.

(a) Gotthard Double Beta Decay Experiment: the Caltech-Neuchatel-PSI detector consisted of a time projection chamber with a total active volume of $\simeq 180$ liters, containing 3.3 Kg of Xe gas enriched in ^{136}Xe to 62.5% at a pressure of 5 atm. The detector was located in the Gotthard Underground Laboratory in the Swiss Alps. The background rejection is assured by the time projection chamber track reconstruction, and its value is $\simeq 0.02$ counts/Ke/Kg/y in the $Q_{2\beta}$ region (within a FWHM interval energy). The obtained lower limit is $T^{0\nu}_{1/2} > 4.4 \cdot 10^{23}$ y[117].

(b) DAMA-LXe: the best result using ^{136}Xe has been obtained by the Roma group at Gran Sasso Underground Laboratories, by using $\simeq 6.5$ Kg of high

	HM	**IGEX**	**Cuoricino**
Nucleus	^{76}Ge	^{76}Ge	^{130}Te
Q value of $0\nu\beta\beta$	2039.0 KeV	2039.0 KeV	2530.3 KeV
Exposure in 10^{25} nuclei·yr	25	7	0.14
Isotopic fraction f	0.86	0.86	0.34
Efficiency ϵ	0.5	0.7	0.84
Energy resolution σ_E	1.6 KeV	1.7 KeV	3 KeV
Total events n	21	9.6	24
Expected background bkg	20.4 ± 1.6	17.2 ± 2	35.2 ± 2
Predicted signal s	$76 \cdot \lvert m_{ee} h^{-1}\ \mathrm{eV}\rvert^2$	$23.5 \cdot \lvert m_{ee} h^{-1}\ \mathrm{eV}\rvert^2$	$21.5 \cdot \lvert m_{ee} h^{-1}\ \mathrm{eV}\rvert^2$

Table 2.4: The main present $0\nu\beta\beta$ experiments are HM, IGEX and CUORICINO. In figure is shown the number of events and expected background in a $\pm 3\sigma$ region around the Q-value of the $0\nu\beta\beta$[34]. IGEX and Cuoricino observe a number of events slightly below the expected background, while the opposite happens for HM. The scale factor h depends on the chosen nuclear model; in the case of [85] $h = 1$.

purity liquid Xenon scintillator filled with (Kr-free) Xe gas enriched in ^{136}Xe (68.8%), and in ^{134}Xe (17.1%). The statistics is 1.1 Kg · y for ^{134}Xe, and 4.5 Kg · y ^{136}Xe, and the 90%C.L. lower limits obtained for half-life are[118]:

$$\begin{cases} ^{136}\mathrm{Xe}: \quad T^{0\nu}_{1/2} \simeq 1.2 \cdot 10^{24}\ \mathrm{y} \\[2ex] ^{134}\mathrm{Xe}: \quad T^{0\nu}_{1/2} \simeq 5.8 \cdot 10^{22}\ \mathrm{y} \end{cases} \tag{2.26}$$

At the present moment, only NEMO-3 and CUORICINO detectors are running.

2.5.2 Future experiments

The recently running experiment will not be able to confirm or rule out the KKDC positive result; a *second generation experiments* is need. For a reliable confirmation, $0\nu\beta\beta$ decay must be observed for different isotopes with similar $|\langle m_\nu \rangle|$. The KKDC claim rejection requires a negative result from either a more sensitive ^{76}Ge experiment or a much more sensitive experiment on a different isotope.

All proposed next generation experiments aim at sensitivities of about 0.01 eV. The large sensitivity improvement will be obtained by scaling up to 1 ton mass experiments and by further reducing the background. A strong effort is also demanded to nuclear theory to reduce the uncertainties in the nuclear matrix evaluation.

Table 2.6 gives some informations about the more well-defined projects. Most of the projects presented here are at a very early R&D stage. In the following a selection of the these future experiments is presented (table 2.6).

1) **Calcium-48**
The experiment CANDLES (*CAlcium fluoride for studies of Neutrino and Dark matters by Low Energy Spectrometer*) is based on the use of CaF_2 immersed liquid scintillator at the Oto Cosmo Observatory (Japan). The upgraded setup, called CANDLES IV, consisting of 1000 crystals (3.2 Kg each) for a total mass of $\simeq 3.2$ tons. The limit on the sensitivity will be 10^{26} y ($|\langle m_\nu \rangle| \simeq 0.03$ eV) for neutrinoless double beta decay of ^{48}Ca (i.a. = 0.187%)[119, 120]. It's also scheduled a next phase (called CANDLES V) with enriched calcium-48 (i.a. = 2.0%)

2) **Germanium**
Several Ge detector are proposed:

   (a) Majorana (*Majorana Neutrinoless Double-Beta Decay Experiment*): the final aim is a 1 ton experiment using HPGe crystals (as segmented diodes) in a ultra low background cryostats. It will start in 2010 and will be installed in the DUSEL (*Deep Underground Science and Engineering Laboratory*) or SNOlab underground laboratories.

   The background model ($\simeq 0.00025$ counts/KeV/Kg/y) is motivated in part from early IGEX data and predicts an achievable $0\nu\beta\beta$ half-life limit of over $(4 \div 7) \cdot 10^{27}$ y within 5 years of initial receipt of the enriched material[121]. The main component of the background reduction will be the granularity of the detector. Its expected energy resolution at the $Q_{\beta\beta}$-value is 4 KeV. The expected sensitivity for an experimental running time of 10 years is the range $|\langle m_\nu \rangle| \simeq (30 \div 40)$ meV

   (b) GENIUS (*GErmanium NItrogen Underground Setup*): this experiment, proposed by part of the HM collaboration, would consists of 400 enriched (86-88%) HPGe naked crystals, for a total mass of about 1 ton, suspended in a 12 m diameter liquid nitrogen tank. The use of naked crystals should move the external radioactivity to outside the liquid nitrogen region.

   The quoted energy resolution is 6 KeV, while the expected background, which should be maximally due to the external component, is $\simeq 0.0002$ counts/KeV/Kg/y). After 10 years, the estimated sensitivity on mass is $|\langle m_\nu \rangle| \simeq (15 \div 45)$ meV[122].

   A test, performed at the Gran Sasso Underground Laboratories, on 10 Kg of a naked crystal operating in a liquid nitrogen (GENIUS - Test Facility) filled dewar was successful[123].

   (c) GEM (*Gamma, Electron and Muon Experiment*): this project should use 1 ton of naked HPGe detectors operating in super-high purity liquid nitrogen contained in a copper vacuum cryostat. The detector is within a 5 m diameter sphere placed in a water shield. The first GEM-I phase will employ natural germanium, the GEM-II step will be enriched in ^{76}Ge at 86%[124].

Similar to GENIUS, the main difference is the reduction of the amount of liquid nitrogen obtained by adding an external layer of pure water.

(d) GERDA (*GERmanium Detector Array*): it is similar to GENIUS and GEM but has more compact dimensions. The driving idea is to scrutinize the KKDC evidence in a short time using the existing ^{76}Ge enriched detectors of the HM and IGEX collaborations. The set-up consists of a liquid argon cryostat (4 m diameter) immersed in pure water tank (10 m diameter) at the LNGS.

The Phase-I aims to reduce the background to about 0.01 counts/keV/kg/y and reach an exposure of about 15 $\mathrm{Kg}\cdot\mathrm{y}$. If the KKDC evidence is correct, GERDA would detect a 5σ signal.

In Phase-II other 20 Kg of enriched and segmented Ge detectors will be added. A further reduction of the background to 0.001 counts/keV/kg/y and an exposure of 100 $\mathrm{Kg}\cdot\mathrm{y}$ would give a 90%C.L. sensitivity of $T^{0\nu}_{1/2} \simeq 2\cdot 10^{23}$ y corresponding to $|\langle m_\nu \rangle| \simeq (0.09 \div 0.29)$ eV[125].

3) **Molybdenum-100**

In Japan, the MOON (*MOlybdenum Observatory of Neutrinos*) experiment will use ^{100}Mo as active target. The setup will be a huge sandwich made by foils of natural molybdenum interleaved with a specially designed plastic scintillator. The molybdenum total mass will be large[126, 127]. High purity levels for the scintillator are needed, and a great effort is required in this sector, because of the large surface. The resolution at the Q-value (3.035 MeV) should be about the 7%. MOON would be also a solar neutrino experiment.

4) **Cadmium**

The planned experiments are:

(a) COBRA (*Cadmium-Telluride O-neutrino double Beta Research Apparatus*): the apparatus[128] uses new generation of semiconductors. These ionization detectors, which operate at 300 K with an energy resolution of $\simeq 1\%$ at the 661 KeV line, are quite small in size, and allow systematic studies on Cd and Te isotopes, and rare beta decays of ^{113}Cd and ^{123}Te. Up to now, four 1 cm^3 CdZnTe semiconductor detectors are operating the Gran Sasso National Laboratory. Half-life limits (90% C.L.) are presented for decays to ground and excited states[129]. Four improved lower limits have been obtained, including zero neutrino double electron capture transitions of ^{64}Zn and ^{120}Te to the ground state, which are $1.19\cdot 10^{17}$ years and $2.68\cdot 10^{15}$ years respectively.

(b) CAMEO: this is an upgraded version of the experiment on ^{116}Cd performed in Solotvina underground laboratory. The initial step will use 24 enriched cylindrical ^{116}CdWO$_4$ crystals, with a total mass of 65 Kg, and will be placed in the middle of the Counting Test Facility (CTF), at LNGS. After a measuring time of more than 5 years a half-life limit of more than 10^{26} y will be reached, corresponding to a mass of $\simeq 0.060$ eV[130]. In a second possible step, 370 crystals will be placed within the Borexino apparatus.

5) **Tellurium-130**
To date, the CUORE (*Cryogenic Underground Observatory for Rare Events*) is the only fully approved next generation 1 ton size $0\nu\beta\beta$ decay experiment: it is being built in the Gran Sasso Underground Laboratory where it is due to start data taking in 2011. CUORE is the subject of this Ph.D work.

6) **Xenon-136**
Two main projects plan to look for ^{136}Xe:

   (a) EXO (*Enriched Xenon Observator*): this experiment[131] should use a new approach that combines quantum optics techniques with radiation detectors, aiming to detect single Ba^{+} ions, via resonant excitation with a set of lasers, in the final state of ^{136}Xe double beta decay.

   Running for 5 years a 10 ton Xe detector with an energy resolution of 1% and with just the $2\nu\beta\beta$ tail background, a sensitivity on $|\langle m_\nu \rangle|$ of about $(11 \div 15)$ meV could be reached. Presently a 200 Kg enriched liquid Xe TPC prototype without tagging is being installed at WIPP (*Waste Isolation Pilot Plant*, New Mexico, USA). Running for 2 years the expected sensitivity for EXO-200 is $6.4 \cdot 10^{25}$ y corrinsponing to $|\langle m_\nu \rangle| \simeq (0.27 \div 0.38)$ eV[132].

   (b) XMASS (*Xenon neutrino MASS detecto*): this experiment will take place at the Kamioka Underground Laboratory, Japan. The detector will use liquid Xenon viewed by photomultipliers. Liquid Xenon is a good scintillator, and has a high Z value, density and boiling point. Moreover, Xenon allows purification to take place during the operations.

   After an R&D 100 Kg prototype a 800 Kg detector is currently under construction. The final step will be a 10 ton detector, which should reach a sensitivity of about $8 \cdot 10^{21}$ y for $2\nu\beta\beta$ and about $3.3 \cdot 10^{26}$ y for $0\nu\beta\beta$, which implies a neutrino mass limit of $(0.03 \div 0.09)$ eV without enriched materials[133].

7) **Neodymium-150**
The SuperNEMO experiment will be based on the NEMO-3 concept. The preliminary SuperNEMO design is based on a planar, modular geometry with 20 modules each containing about 5 Kg of enriched isotopes.

   The main candidate isotopes have emerged to be ^{82}Se and ^{150}Nd. A sample of 4 Kg of ^{82}Se has been enriched and is currently undergoing purification. The collaboration is investigating the possibility of enriching large amounts of ^{150}Nd via the method of atomic laser isotope separation[134].

Isotope	Experiment	Latest	$Q_{\beta\beta}$	i. a.		Exposure	Technique	Material	$T^{0\nu}_{1/2}$	$\langle m_\nu \rangle$
		Result	[KeV]	Nat.	Enrich.	[kg×y]			[10^{23} y]	[eV]
^{48}Ca	Elegant VI	2004[135]	4274	0.19	–	4.2	scintillator	CaF_2	0.14	7.2÷44.7
^{76}Ge	Heidelberg/Moscow	2004[100, 101]	2039	7.8	87	71.7	ionization	Ge	120.0	0.44
^{82}Se	NEMO-3	2007[112]	2995	9.2	97	1.8	tracking	Se	2.1	1.2÷3.2
^{100}Mo	NEMO-3	2007[112]	3034	9.6	95÷99	13.1	tracking	Mo	5.8	0.6÷2.4
^{116}Cd	Solotvina	2003[114]	2805	7.5	83	0.5	scintillator	$CdWO_4$	1.7	1.7
^{130}Te	Cuoricino	2007[136]	2529	33.8	–	11.8	bolometer	TeO_2	30.0	0.16÷0.84
^{136}Xe	DAMA	2002[118]	2476	8.9	69	4.5	scintillator	Xe	12.0	1.10÷2.9
^{150}Nd	Irvine TPC	1997[137]	3367	5.6	91	0.01	tracking	Nd_2O_3	0.012	3.0
^{160}Gd	Solotvina	2001[138]	1791	21.8	–	1.0	scintillator	Gd_2SiO_5	0.013	26.0

Table 2.5: A selection of the past and present experiments giving the best result per isotope to date. All given $T^{0\nu}_{1/2}$ ($\langle m_\nu \rangle$) are lower (upper) limits with the exception of the Heidelberg-Moscow experiment where the 99.9973% CL value is given. The spread in $\langle m_\nu \rangle$ is due to the uncertainties on the nuclear factor F_N.

Experiment	Isotope	$Q_{\beta\beta}$	Tech.	i.a.	Mass	t_M	σ_E	*bkg*	$T^{0\nu}_{1/2}$	$\langle m_\nu \rangle$	Project
		[keV]		[%]	[kmol]	[y]	[KeV]	[c/y]	[10^{28} y]	[meV]	Status
CANDLES IV+ [120]	^{48}Ca	4271	scint.	2	1.8	5	73	0.35	0.3	30	R&D (III: 5 mol)
Majorana 120 [121]	^{76}Ge	2039	ion.	86	1.6	4.5	2	0.1	0.07	90	R&D - reviewing
GERDA II [125]	^{76}Ge	2039	ion.	86	0.5	5	2	0.1	0.02	90÷290	funded/R&D (I: 0.3 kmol)
MOON III [126, 127]	^{100}Mo	3034	track.	85	8.5	10	66	3.8	0.17	15	R&D (I: *small*)
CAMEO III [130]	^{116}Cd	2805	scint.	83	2.7	10	47	4	0.1	20	proposed
CUORE [139]	^{130}Te	2529	bol.	33.8	1.7	10	2	7.5	0.07	11÷57	construction
EXO [131]	^{136}Xe	2476	track.	65	60.0	10	25	1	4.1	11÷15	R&D (1.5 kmol)
SuperNEMO [134]	^{150}Nd	3367	track.	90	0.7	–	57	10	0.01	50	R&D
DCBA-F [140]	^{150}Nd	3367	track.	80	2.7	–	85	–	0.01	20	R&D (T2: *small*)
GSO [138]	^{160}Gd	22	scint.	22	2.5	10	83	200	0.02	65	proposed

Table 2.6: A selection of the proposed experiments. Except for CUORE and GSO all experiments use isotopically enriched material. Background *bkg* is calculated on an energy interval equal to σ_E. For all tracking experiments the quoted background is due only to the $\beta\beta$-2ν tail.

Chapter 3

Bolometric Technique

3.1 Introduction

The expression *bolometer* is normally used to indicate a *Low Temperature Detector* (LTD) in which the energy of particle interactions is converted into phonons and measured through temperature variation.

Convectional techniques, used to measure energy deposition caused by interactions, are based on the detection of energy released in form of ionization and excitation of the detector's atoms. Unfortunately the amount of energy lost to channels differing from the ones of interest is quite large. In particular most of the energy is converted to phonon excitation of the detector's lattice volume. This lost energy, together with the energy needed for atom excitation or ionization (namely the *elementary detected event*), increases the statistical fluctuations of the number of elementary excitations, with a consequent worsening of the intrinsic resolution of these convectional techniques. Bolometric Techniques, on the other hand, measure the portion of the deposited energy converted into phonons by means of the related temperature rise. As it will be shown in this chapter this guarantees a better intrinsic energy resolution.

In the year 1935 S. Simon[141] was the first to propose the use of temperature detectors to study nuclear phenomena. In 1949 H.D. Andrews, for the first time, detected alpha particles using superconductive bolometers[142]. In the following years the possibility of using thermal detectors for various research topics (such as solar neutrino and X-ray spectroscopy, material contamination analysis, dark matter detection and rare processes), was a strong motivation for the development of this technique. However the use of large bolometric sensors is quite recent for rare event physics and was first suggested by E. Fiorini and T.O. Niinikoski in 1983[143].

Presently the bolometric technique finds one of their best applications in rare events physics, particularly in *Double Beta Decay* and *Dark Matter*[144]. The typical time evolutions of the pulses do not allow high radiation rates on the detector, for this reason bolometers are intrinsic rare events detector. Besides this time limitation however there are many advantages. The most important are:

1) the energy resolution is better than of most of the other particle detectors[145];

2) bolometer offers a wide choice of different materials that can be used as absorber.

This last feature is very important since in the case of DBD research it can allow to cross check a possible evidence on different isotopes whereas in the case of DM it allows to probe different mass region.

In this chapter I will show the working principles of the *bolometric technique* with particular attention about its application in the double-beta research.

3.2 General principles

From a very basic approach a bolometer consists of two main components:

1) **Energy absorber**: this is the sensitive part of the detector, where the interactive particles deposit their energies. The absorber material can be chosen quite freely, as long as it is characterized by a low specific heat at the working temperature. Its mass can range from a few hundred micrograms (such as for X-ray spectroscopy or direct neutrino measurements) up to a few kilograms (such as for Dark Matter or Double Beta Decay searches).

2) **Phonon sensor**: this is a crucial element; it converts the excitation produced by particle interaction into an electrical signal. For this purpose different kinds of thermometers exist, depending on the material and on the process through which the temperature signal is converted into an electric signal.

Bolometers are LTDs sensitive to phonons. These devices are therefore named *Phonon Mediated particles Detectors* (PMDs) where the sensitive element is consequently the *phonon sensor*. In Figure 3.2 a simple scheme of a TeO_2 (Tellurium dioxide) bolometric detector is shown.

A PMD can be schematized as a calorimeter with a heat capacity C connected to a heat sink, with constant temperature (T_0), through a thermal conductance G (the monolithic model of figure 3.1(b)). The heat capacity contains all the contribution of the elements which compose the detector: the lattice heat capacity of the absorber (C_A) and the lattice heat capacity of the sensor (C_T). The conductance G represents the thermal connection between the detector and the heat sink and its heat capacity is considered negligible. For a given absorber with temperature $T(t)$ one can assume that:

$$\Delta T = \left| T(t) - T_0 \right| << T_0 \quad \forall t \quad \Rightarrow \quad G, C = \text{const} \tag{3.1}$$

so that one can treat G and C as constant. An instantaneous deposition of energy ΔE in the absorber gives rise to a temperature pulse:

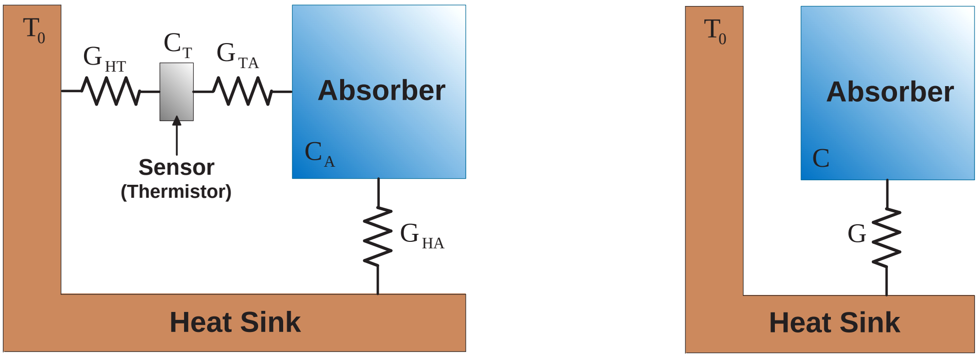

(a) A two-stage thermal model: G_{HA} describes the conductance between the heat sink and the absorber (Teflon thermal coupling), G_{TA} describes the conductance between the absorber and the sensor (a two-component epoxy resin), and, at last, G_{HT} describes the conductance between the sensor and the heat sink (a gold wire needed to bias the sensor)

(b) A monolithic thermal model: here the detector is modeled as a single object weakly coupled to the heat sink. The heat capacity C contains all the contribution of the elements which compose the detector. G describes the thermal conductance between the detector and the heat sink.

Figure 3.1: Two models of thermal detector.

$$\Delta T(t) = \frac{\Delta E}{C}\, e^{\left(-\frac{t}{\tau}\right)} \quad \text{where} \quad \tau = \frac{C}{G} \tag{3.2}$$

One can easily see from equation 3.2 that the heat capacity is a very crucial parameter for this kind of device, as a smaller C will increase the amplitude of the signals.
The heat capacity at the temperature T is given by:

$$C(T) = c(T) \cdot n \tag{3.3}$$

where $c(T)$ is the specific heat with temperature T and n the number of moles in the absorber. In order to minimize this, one has to use a suitable material (such as dielectric crystals or superconductors below the transition phase) and, most importantly, operate the detector at a very low temperature. In fact a 1 MeV particle impinging on a 1 mole absorber at room temperature generates a variation of the order of $\Delta T \simeq (10^{-18} \div 10^{-15})$K, which is impossible to measure. For bolometers the typical operating temperature is in the range of $\simeq (10 \div 100)$mK.

The PMDs can be classified as *fast* or *slow* bolometric detectors. This classification depends on which type of phonon sensor is used. In the former case, these phonon sensors have a response time of the order of a few microseconds. If this response time is not larger than the thermalization time of the non-equilibrium phonons produced by interaction, then these sensors could become sensitive to athermal phonons[1]. In

---

[1] phonons out of equilibrium.

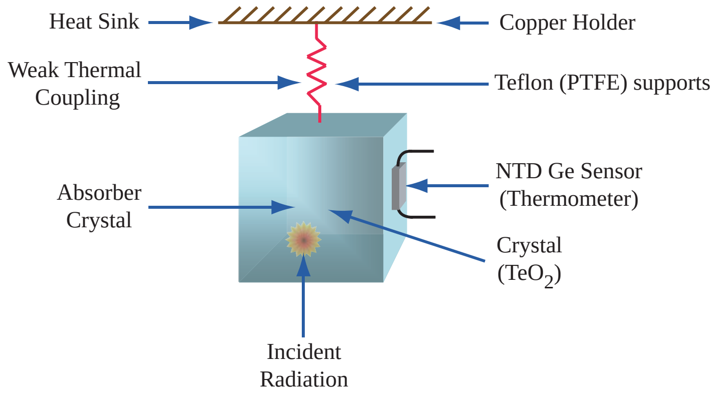

Figure 3.2: Simple schematic of Bolometric Detector: an absorber is connected to a heat sink through an insulating link (made of Teflon); a sensor is attached to the absorber.

the latter case their response time is larger; thus they are only sensitive to thermal phonons measuring the temperature of the detector. The sensor is a thermometer in all respects and thus the PMD works as a perfect calorimeter.

3.3 The energy absorber

As described in the above section, the most important parameter of the detector is its heat capacity, which needs to be kept small in order to achieve large and fast signals. To fulfill this requirement, low temperatures are needed.

At low temperatures the specific heat of the crystal can be expressed as:

$$c(T) = c_{\mathrm{r}}(T) + c_{\mathrm{e}}(T) + c_{\mathrm{m}}(T) \tag{3.4}$$

where c_{r}, c_{e} and c_{e} represent, respectively, the lattice, electron and magnetic contributions to the specific heat. The lattice contribution for a dielectric solid can be expressed looking at the Debye Model in the low temperature approximation:

$$c_{\mathrm{r}}(T) = \frac{12\pi^4 \mathcal{N}_{\mathcal{A}} k_B}{5} \left(\frac{T}{\Theta_D} \right)^3 \tag{3.5}$$

where k_b and $\mathcal{N}_{\mathcal{A}}$ are, respectively, the *Boltzmann constant* and *Avogadro's number*. The constant Θ_D represents the *Debye temperature*, a parameter intrinsic to the material, which can be expressed as follows[146]:

$$\Theta_D = \frac{\hbar}{k_B} \omega_D = \frac{\hbar}{k_B} c_s \left(\frac{6\pi^2 NK}{V} \right)^{\frac{1}{3}} = \frac{\hbar}{k_B} \sqrt{E} \left(\frac{6\pi^2}{A\rho^2} \right)^{\frac{1}{3}} \tag{3.6}$$

$$\text{where} \quad c_s = \sqrt{\frac{E}{\rho}} \quad , \quad \frac{KN}{V} = n = \frac{\rho}{A}$$

where $V = L_x L_y L_z$ is the volume of the solid, c_s is the speed of sound in the material, ρ is the density, N is the number of unit cell, K is the number of atoms per unit cell and, at last, E is Young's modulus. The corresponding heat capacity (from equation 3.5) can be written as:

$$C(T) = \beta \frac{m}{M} \left(\frac{T}{\Theta_D} \right)^3 \quad \text{with} \quad T < \Theta_D \tag{3.7}$$

where $\beta = 1944$ J K^{-1} mol^{-1}, m is the absorber mass and M is the molecular weight. As one can easily see, the heat capacity is proportional to the mass and, for $T < \Theta_D$, to the temperature cubed.

The electronic contribution c_{e} depends on the conductive or superconductive nature of the material, as follows:

$$c_{\mathrm{e}}(T) = \begin{cases} \dfrac{\pi^2}{\Theta_D} Z R \dfrac{T}{\Theta_F} & \Rightarrow \text{ conductive} \qquad (3.8\text{a}) \\[2ex] K_s \, \mathrm{e}^{-2\frac{T_c}{T}} & \Rightarrow \text{ superconductive} \qquad (3.8\text{b}) \end{cases} \tag{3.8}$$

where Z,R and Θ_F are, respectively, the conduction electron number for each atom, the gas constant and the Fermi temperature. T_c is the critical temperature[2] while K_s is a constant which depends on the characteristics of the superconductive material. For conductors c_{e} is proportional to T; for superconductors however, with $T < T_c$, c_{e} decreases exponentially with the temperature. The eventual magnetic nature of the material gives rise to the last term in equation 3.4, inversely proportional to T^2.

Finally it is easily seen that in order to minimize the global heat capacity, one has to work at very low temperatures and avoid conductor and magnetic materials. One of the two optimal choices is to work with superconductive materials, characterized by a critical temperature higher than the working temperature. Another choice is to work with dielectric diamagnetic materials characterized by a maximized Debye temperature. In this case only the lattice contribution is present, while the electron and magnetic contributions can be ignored. Furthermore, since the Debye temperature depends on the mass number A and on the material density (according to $\Theta_D \propto A^{-\frac{1}{3}} \cdot \rho^{-\frac{1}{6}}$, 3.6) low atomic mass and low density would provide lower heat capacity, even one has to keep in mind that higher atomic number guarantees a higher detection efficiency for electrons and gammas.

---

[2] in superconducting materials, the characteristics of superconductivity appear when the temperature T is lowered below a critical temperature T_c.

3.3.1 Thermalization processes

When a particle interacts with the detector it releases its energy into the absorber. This deposited energy is afterwards downgraded through two main channel: nuclear and electronic[147].

- **Nuclear channel**: the energy released into the nuclear branch (E_{N}) in part is converted in vibrational excitations (phonons) and in part it could produce structural defects in the absorber's lattice. Because of the low temperature these defect are stable and could constitute energy traps. The statistical fluctuations of the number of the produced defects can worsen the energy resolution of the detector. The fraction of this lost energy depends on the incident particle; for electrons and photons it's negligible, whereas for alpha particle having some MeV of energy it can cause a FWHM resolution of some eV.

- **Electronic channel**: the energy released in the electronic channel (E_e) is spent to excite electron-hole pairs (e/h pairs). The impinging particle is slowed down in few μm (heavy particles) or mm (electrons) after its interaction into the crystal absorber. Along its path it produces many e/h pairs, with, at the beginning, very spatial density and energy. These charge carriers interact with each other and spread very quickly in the crystal. As soon as an the equilibrium is reached, they undergo their final degradation interacting with the lattice: these produce phonons. In this process a large fraction of the initial pairs energy is transferred to the lattice as vibrational phonons but also undesirable processes could occur. In fact a fraction of this energy instead of being converted into crystal lattice excitations can leave the crystal or can be stored in stable or metastable states. It's possible to have:

  i) *radiative recombinations*, where the e/h couples generated interact with the escape emitted photons;

  ii) *non-radiative recombinations*, where the e/h couples generated interact with the other carriers;

  iii) *trapping* (also called *Shockley-Read-Hall Recombination*) of electrons and holes in the states created by an impurity defects in the lattice.

In order to understand the phonons thermalization processes inside the crystal absorber it's useful to consider the mono-dimensional representation of the phonon dispersion curves (figure 3.3). The e/h pair recombination process across conduction and valence bands, produces high energy and low momentum phonons on the optical branch. Then these primary phonons turn from the particle interaction region. One *optical phonons* decay in the *LA-Branch* in a very short time ($10 \div 100$) ps. The energy and momentum are conserved and two phonons, each having half of the energy of the initial particle (of the order of the Debye energy) and opposite momentum, are produced. Therefore the final result is a phonon system, mainly belonging to the LA-Branch, and having the energy of the order of $E_{\mathrm{D}} = \hbar\omega_{\mathrm{D}}$ (where ω_{D} is the Debye cutoff frequency of the crystal). This energy is much higher than the average energy of thermal phonons at the bolometer working temperature (@$T = 10$ mK, the average energy is $< E > \simeq \mu$eV) so that new phenomena of phonon energy degradation can occur and the two produced phonons become thermal phonons.

These processes (thermalization of the athermal phonons) can be classified in three channels:

1) **Phonon-phonon scattering**: it is due to the anharmonic terms of the lattice potential and can only behave as a decay. The LA-phonons decay are responsible for the *transverse acoustic* TA-phonons production, differently the decay of the TA-phonons is forbidden by the momentum conservation law. The decays allowed are: $LA \rightarrow LA + TA$, $LA \rightarrow TA + TA$ and $TA \rightarrow TA + TA$. It is clear that this degradation mechanisms is not enough to permit, in a reasonable time, the thermalization of the energy trapped in the athermal phonons. Other mechanisms must exist and must be able to degrade phonon energy, and also to induce the conversion of the TA-phonons, otherwise stable, into LA-phonons so that they can be thermalized. The following two processes owns these features.

2) **Mass defect or impurity scattering**: it is a Rayleigh-Like scattering (elastic and isotropic) but it is irrelevant for the thermalization process.

3) **Reflection on crystal surfaces** (or **boundary scattering**): this phenomenon is composed by two terms: *diffuse* (due to the surface roughness) and *specular scattering*. After a certain number of $TA \rightarrow TA + TA$ decays the mean free path of the phonons becomes larger than crystal dimensions. In a pure crystal this means that there is a ballistic propagation of phonons until they reach the crystal surfaces[148]. Here a fraction f of them are *diffuse* and directly thermalized. The $(1 - f)$ fraction of the phonons is reflected *specularly* in a way depending on their incident direction and polarization. These phonons can suffer other decay processes and, at the end, interact with the background thermal phonons with a final thermalization.

   In the case of the superconductor material the thermalization processes can be long, in particular when the Debye temperature Θ_D is large and the critical temperature T_c is low. Indeed, under this conditions, phonons generated by particle interaction can break the Cooper pairs and cause an energy storage in the quasi-particle system. For this reason diamagnetic dielectric material are to be preferred.

Since fast (ballistic) and thermal phonon have separated development times, two kind of phonon sensor have been conceived[149]:

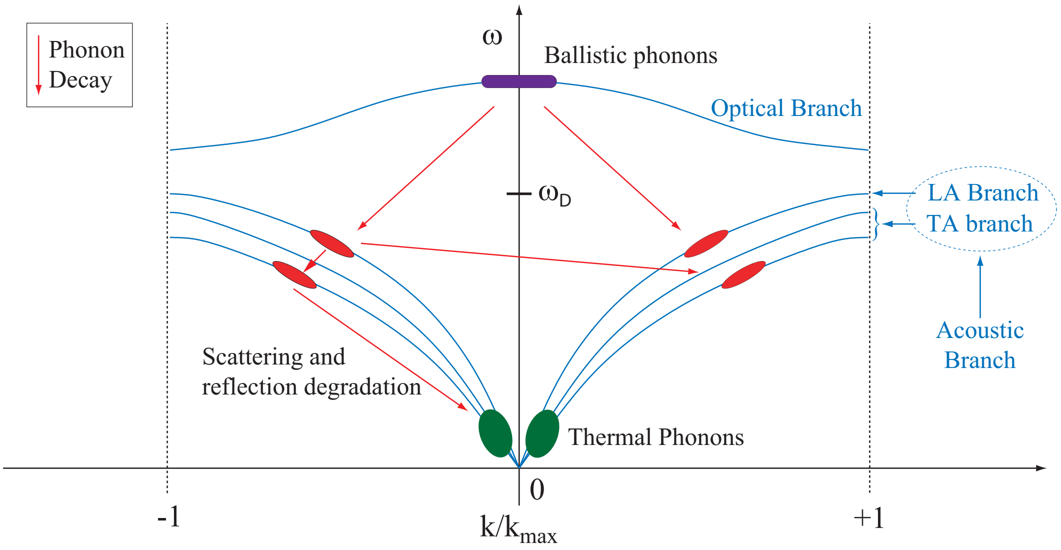

Figure 3.3: Athermal model for the phonons thermalization. The abscissa k is the module of the *Crystal momentum*, a *momentum-like* vector quantum number associated with electrons in a crystal. There are two types of phonons: *acoustic* and *optical*[150]. The *acoustic phonons* correspond to sound waves in the lattice. *Longitudinal* and *transverse* acoustic phonons are often abbreviated as *LA* and *TA phonons*, respectively. The *optical phonons* are so called because they are excited very easily by electromagnetic radiation. The optical modes are responsible of much of the characteristic optical behavior of the crystal.

i) *ballistic phonon sensor*, used to detected (athermal) phonons at their first interaction with the the crystal surface interface and used for spatial event reconstruction (determination of the interaction point);

ii) *thermal phonon sensor*, used to detected thermalized phonons.

3.3.2 Energy Resolution

The energy resolution of a given detector is related to the statistical fluctuation of the number of elementary events contributing to the signal[151]. Every elementary event is associated to activation threshold energy ε. This energy is the minimum amount required to produce an elementary excitation (ionization for the conventional detectors, phonons for thermal detector). In reality the actual amount is generally higher than ε because of the loss energy lost in channels different from the detected one, and it can change event by event. One can considers its average value as ε_a. For an energy release E the number of generated elementary events is:

$$N = \frac{E}{\varepsilon_a} \quad \Rightarrow \quad E = \varepsilon_a N \quad \Rightarrow \quad \sigma_E = \varepsilon_a \Delta N \tag{3.9}$$

There are a number of potential sources of fluctuations in the response of the detector which get worse the energy resolution. The main responsible are:

1) any drift of the operating characteristics of the detector during the course of the measurements;

2) sources of random noise within the detector;

3) statistical noise arising from the discrete nature of the measured signal itself.

By assuming that these fluctuation are a Poisson process with $\Delta N = \sqrt{N}$, the theoretical energy resolution (FWHM) is:

$$R\Big|_{\substack{\text{Poisson}\\ \text{Limit}}} := \frac{\text{FWHM}}{E} = \frac{2\sqrt{2\ln 2}\sigma_E}{E} = \frac{2.35\ \varepsilon_a\sqrt{N}}{\varepsilon_a N} = \frac{2.35}{\sqrt{N}} \tag{3.10}$$

where R depends only on the number of the elementary processes generated. To take into account possible correlation effect among the events one can introduce the *Fano factor* defined as[152, 153, 151]:

$$F = \frac{\text{observed variance}}{\text{predicted variance}} \quad \Rightarrow \quad 0 < F < 1 \tag{3.11}$$

Because the variance is given by σ^2 the equivalent expression to `eq.` 3.10 is now:

$$R\Big|_{\substack{\text{Statistical}\\ \text{Limit}}} = \frac{2.35\ \sqrt{N}\sqrt{F}}{N} = 2.35\ \sqrt{\frac{F}{N}} = 2.35\ \sqrt{F\frac{\varepsilon_a}{E}} \propto \sqrt{\varepsilon_a} \tag{3.12}$$

As it is shown in the `eq.` 3.12 the resolution is proportional to $\sqrt{\varepsilon_a}$, so lower is the activation threshold energy of the detector and lower is its intrinsic energy resolution.

For a thermal detector at a given temperature T one has:

$$E(T) = C(T)T \quad , \quad \varepsilon_a = k_b T \quad \Rightarrow \quad N = \frac{C(T)T}{k_b T} = \frac{C(T)}{k_b} \tag{3.13}$$

and assuming again the Poisson statistic for intrinsic energy resolution one obtains:

$$R = \frac{\Delta E}{E} = 2.35\ \sqrt{\frac{F}{N}} = 2.35\ \sqrt{F\frac{k_b}{C(T)}} \quad \Rightarrow \quad \Delta E = 2.35\ \sqrt{F k_b C(T) T^2} \tag{3.14}$$

According to this last equation (`eq.` 3.14), the resolution for a bolometer is independent of the energy E, so, for example 1 Kg of TeO_2 crystal operating at 10 mK could measure energy deposition of the order of few MeV with a resolution of in the range (20÷100) eV, more than two order of magnitudes than conventional detectors.

In the case of bolometers the effective energy resolution could be got worse because of other energy fluctuations (metastable e/h states o long-lived non thermal phonons) which combine themselves with the statistical ones, taking part to the energy deposition process.

3.4 The phonon sensor

The phonon sensor is a devices able to collect the phonon produced inside the absorber and able to generate an electrical signal proportional to the energy contained in the collected phonons. A simple realization of this devices can be filled using a thermistor whose resistance, as a function of temperature, has a steep slop. In this way a little variation of temperature could generate a significant and measurable variation of resistance.

There are two main classes of thermistor with the best performances: *semiconductor thermistors* (STs) and *transition edge sensors*(TESs). These type of sensors are usually characterized by their *Logarithmic Sensitivity* A, which describes the sensor capability of transforming a small temperature increase in a significant resistivity variation. This parameter is defined as (appendix B.1):

$$A = \left| \frac{\mathrm{d} \ln R(T)}{\mathrm{d} \ln T} \right| \tag{3.15}$$

The value of the sensitivity is typically in the range $(1 \div 10)$ for STs and in the range $(10^2 \div 10^3)$ for TESs.

3.4.1 Semiconductor Thermistor

This type of sensor are intrinsically slow so that they are sensitive mainly to thermal phonons. For these reasons they could give information about system in thermal equilibrium and work as temperature sensors.

Normally the semiconductor thermistors consist of Ge or Si small crystal with a doped region. A technique used for fabricating such devices in order to lead an uniform dopant distributions down to the atomic level is the *Neutron Transmutation Doping* (NTD). In this approach all wafers are irradiated at a nuclear reactor with thermal neutrons for the duration of 4 hours[154]. This procedure leads the formation of a homogeneous distribution of p-type dopant. The compensation level $K = N_{\mathrm{A}}/N_{\mathrm{D}}$ between donor and acceptor atoms can be controlled by changing the flux of the neutron irradiation, thus tuning different behavior in the sensor.

A doped semiconductor near absolute zero can behave whether as insulator or a metal, according to the number of dopant atoms planted, which trim the conduction mechanism. In fact, if this number is greater than the critical concentration N_c the

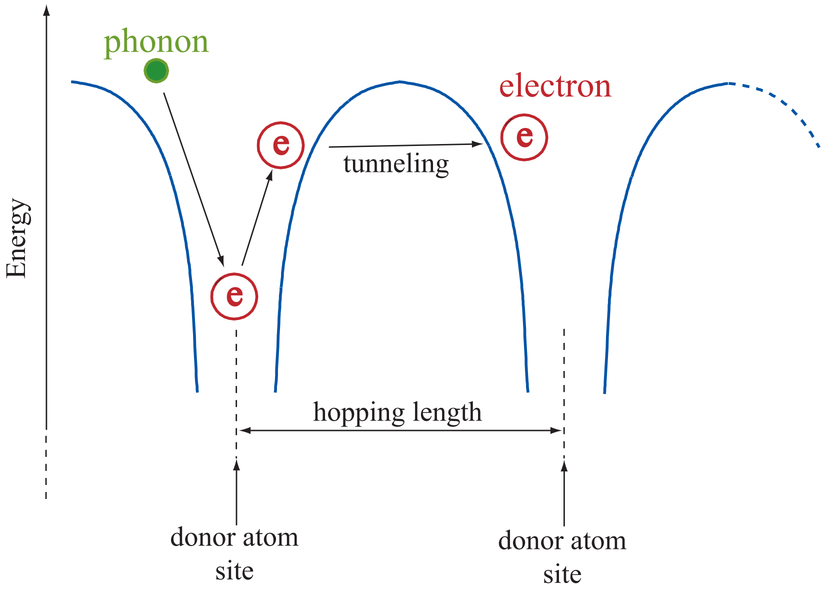

Figure 3.4: Representation of the hopping conduction mechanism.

devices has a metallic behavior. The region near this concentration is called *metal-insulator transition region* (MIT)[155].

At temperature $T < 10\text{K}$, the conduction mechanism is due to the migration of charge carries from an impurity site to another. When the donor concentration is increased, the wave function of the external electron of the donor atom overlaps with the external electron wave function of the neighboring atoms. In this situation the electrons are not localized and the conduction happens by electrons jumping from a donor site to another without using the conduction band. This mechanism is called *hopping mechanism* (figure 3.4). This migration is due to quantum-mechanical tunneling through the potential barrier which separates two dopant sites. This conduction is activated by phonons absorbed into the sensor. The phonon assisted tunneling of localized electrons between different sites depends by *hopping length* (the mean distance between two contiguous sites) which increases with the decreasing temperature.

If $T << 10\text{K}$ and if the doping concentration is slightly lower than N_c the resistivity is strongly dependent on the temperature. So, in order to obtain optimized phonon sensors, one chose to operate semiconductor thermistor slightly below the MIT region. Under these conditions the main electric conduction mechanism is the *Variable Range Hopping* (VRH)[156] belongs to Sir N. F. Mott. Here the carriers can migrate also in far sites if their energy levels are located in a narrow range around the Fermi energy. For a semiconductor the electron phase-space density near the Fermi level is related to the compensation level K adjusted in the doping phase.

In the case of VRH the resistivity depends on the temperature in the following way:

$$\rho(T) = \rho_0 \, \mathrm{e}^{\left(\frac{T_0}{T}\right)^\gamma} \quad \text{with} \quad \gamma = \frac{1}{d+1} \tag{3.16}$$

where ρ_0 and T_0 are parameters depending on the doping concentration, and where d is the dimensionality of the phase space of the system. For a three-dimensional system, considering the Mott Model, one has $d = 3$ and $\gamma = 1/4$. For larger values of K the Coulomb repulsion among the electrons leads to the formation of a gap (called *Coulomb gap*) in the phase-space density near the Fermi level. In this case the dimensionality decreases and γ becomes 1/2[157].

Starting from eq. 3.16, the sensitivity parameter A for a NTD thermistor takes the following form (appendix B.1):

$$A = \left| \frac{\mathrm{d} \ln R(T)}{\mathrm{d}T} \right| = \gamma \left(\frac{T_0}{T} \right)^\gamma \tag{3.17}$$

3.4.2 Transition edge sensors

A transition-edge sensor is a thermometer made from a superconducting film operated near its transition temperature T_c. They are intrinsically fast, and so they can detect athermal phonons. The incident phonons are absorbed directly and the temperature of the electron system in the film raise. If the detector is biased in its superconducting-to-normal transition, this energy deposition results in a macroscopic resistance change. A typical example of a resistance-temperature curve for a TES is shown in figure 3.5(a). Typically, each TES is inductively coupled to its own SQUID (*Superconducting QUantum Interference Device*) channel (figure 3.5(a)) to amplify and read out these resistance (and corresponding current) changes.

The detector time constant can reach a value around 100 μs and, consequently, this kind of sensor allows a reasonable counting rate. The theoretical resolution for a TES calorimeter in the non-saturation regime can be approximated as:

$$\Delta E \simeq 2.355 \sqrt{4 k_B T_c E_{\text{sat}}} \tag{3.18}$$

where E_{sat} is the saturation energy. Since the lower the saturation energy, the lower the E_{sat}, one would like to operate at the lowest saturation energy possible (and also at the lowest critical temperature).

3.5 Detector operation

Taking into account bolometers with semiconductor thermistor as phonon sensor, in order to obtain the best performances a proper biasing circuit is needed.As it shown in figure 3.6(a), the bias current $I_{\text{bol}} = I_{\text{BIAS}}$ is supplied by means of a voltage generator

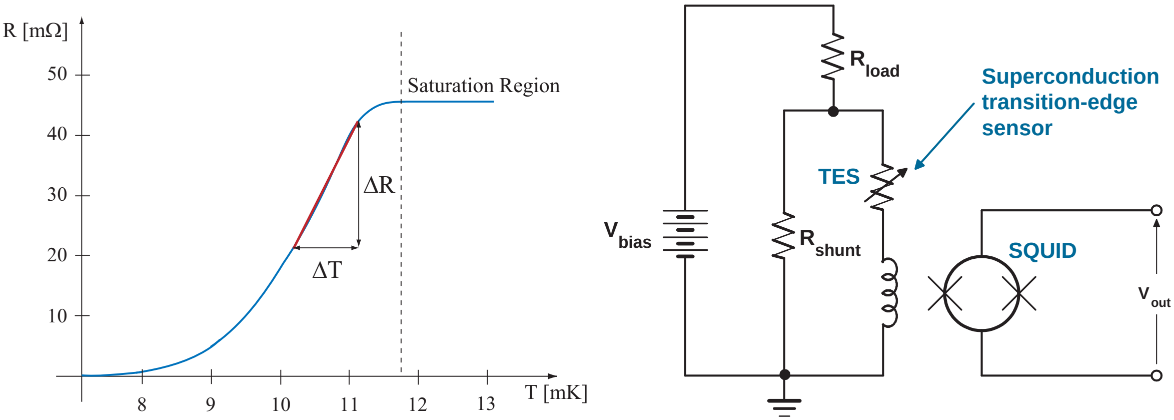

(a) Resistance of a W-TES sensor as function of the temperature. Before the saturation region there are zones with linear response.

(b) Electrical bias circuit and read-out system for a superconductive transition-edge sensor. The voltage variation across the sensor is recorded through the SQUID input coil.

Figure 3.5: Example of thin-film tungsten (W) TES device.

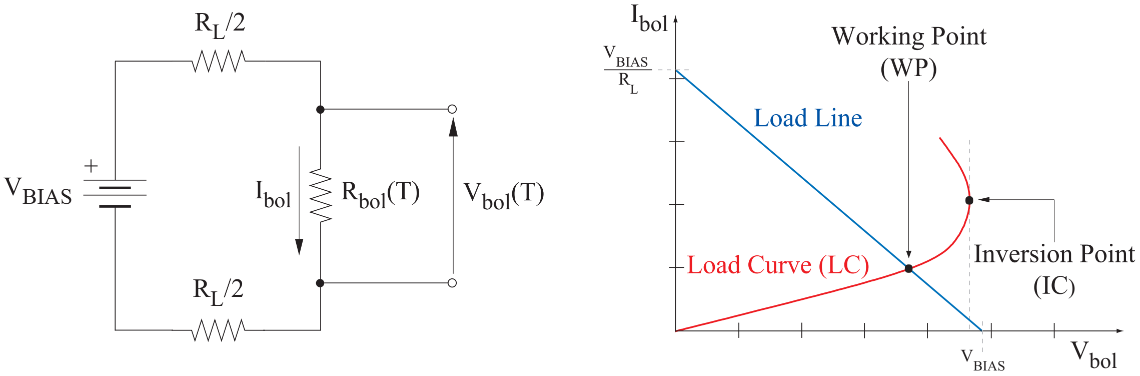

(a) Electric scheme of the biasing system used for the read-out of a thermistor. If $R_{\mathrm{L}} >> R_{\mathrm{bol}}$ the thermistor biasing system (V_{BIAS} plus R_{L}) can be modeled as an ideal current generator, therefore the current I_{bol} turns out to be independent on the value of R_{bol}.

(b) Typical load curve of a thermistor. The working point is the intersection of the current-voltage characteristic with the load line $V_{\mathrm{bol}} = V_{\mathrm{BIAS}} - I_{\mathrm{bol}} R_{\mathrm{L}}$.

Figure 3.6: Thermistor biasing technique.

closed on a load resistor R_{L} in series with the thermistor R_{bol}, whose resistance is negligible in comparison to R_{L} ($R_{\mathrm{L}} >> R_{\mathrm{bol}}$).
Fixed a working point by forcing a bias current (figure 3.6(b)), across the thermistor there is a voltage drop $V_{\mathrm{bol}}(T) = I_{\mathrm{BIAS}}R_{\mathrm{bol}}(T)$. This voltage drop causes a power dissipation $P = I_{\mathrm{BIAS}}V_{\mathrm{bol}}$ with a consequent temperature raise. At this point the thermistor resistance decreases until the electrical power dissipation becomes equal to the thermal power absorbed from the detector by the heat sink. Now a thermal equilibrium is reached and the absorber temperature is give by

$$T_b = T_0 + \frac{P}{G} \tag{3.19}$$

where is G the thermal conductance between the detector and the heat sink and T_0 is the temperature of this last one. This phenomenon makes the *V-I characteristic* curve (also named *volt-amperometric characteristic* or *load curves*) deviate from the linearity and, above a certain value bias current, leads to a non-ohmic behavior. This behavior is very usual in bolometric technique and is often referred to as *Electrothermal Feedback* (figure 3.7(a)). For a given bias current the static resistance is simply the ratio $V_{\mathrm{bol}}/I_{\mathrm{bol}}$ while the *dynamic resistance* is the tangent at the V-I curve in the point (V_{bol} , I_{bol}). If the current bias is further increase at a certain point the dynamic resistance crosses the so called *inversion point* (IP), here first it vanishes and then becomes negative.

The intersection of the load curve with the load line imposed by the biasing system (figure 3.7(a)) determines the working point (WP) of the sensor. Usually this is chosen before the inversion point in such a way that the signal amplitude (*Maximum Amplitude Point*, MAP) or the signal-to-noise ratio (*Optimum Working Point*, OWP) is maximum.

By a combined fit to a set of load curves measured at different base temperatures is possible evaluate the thermistor intrinsic parameter (R_0, T_0 e γ), as it shown in figure 3.7(b).

3.5.1 Signal amplitude

If one considers the monolithic model (figure 3.1(b)), in first approximation the thermal pulse produced by an energy release into the absorber have the following characteristic (figure 3.8):

1) **rise time**: if the thermalization time is assumed negligible, it can be considered instantaneous. For a TeO_2 absorber mass of 760 g the rise time is in the range $t_r = (40 \div 80)$ ms;

2) **fall time** it assumes an exponential decay where the time constant depend on the physical characteristics of the individual detector ($\tau = C/G$). For a TeO_2 absorber mass of 760 g the fall time is in the range $t_f = (130 \div 700)$ ms.

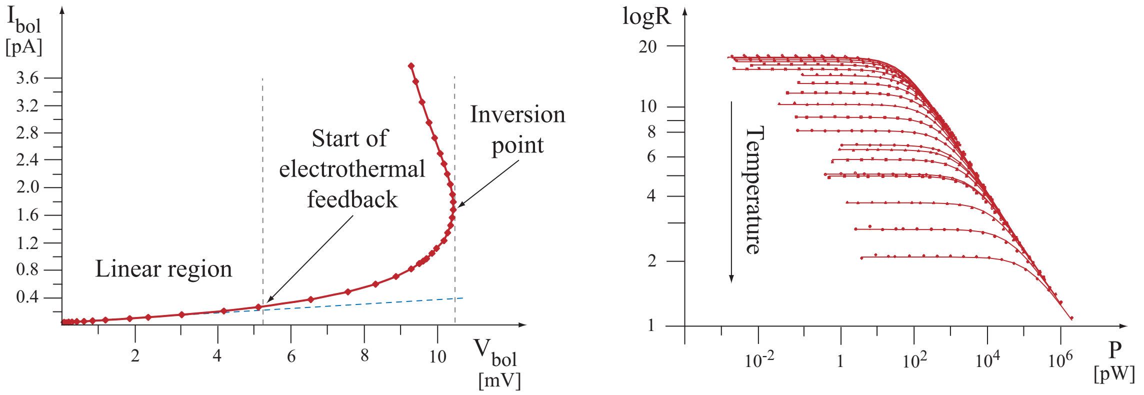

(a) Load curve (V-I) for a semiconductor thermistor @$T_0 = 8$ mK.

(b) Power-Resistance (P-R) characteristic curves of a semiconductor thermistor at different base temperatures.

Figure 3.7: Characteristic curves of a typical NTD Thermistor.

Typically the decay time turns out to be larger than the rise time by an order of magnitude.

The relationship between the electrical pulse height ΔV and the energy deposition ΔE can be obtained using the following partial derivation:

$$\mathrm{d}V_{\mathrm{bol}} = \frac{\partial V_{\mathrm{bol}}}{\partial R_{\mathrm{bol}}}\,\mathrm{d}R_{\mathrm{bol}} = \frac{\partial V_{\mathrm{bol}}}{\partial R_{\mathrm{bol}}}\,\frac{\partial R_{\mathrm{bol}}}{\partial T}\,\mathrm{d}T \tag{3.20}$$

Considering the biasing circuit shown in figure figure 3.6(b) and the equations 3.16 3.17, and assuming $R_{\mathrm{L}} >> R_{\mathrm{bol}}$, one obtains:

$$\Delta V_{\mathrm{bol}} = \mathrm{const}\cdot\frac{A\sqrt{P\cdot R_{\mathrm{bol}}}}{C}\,\Delta E \tag{3.21}$$

where T is the temperature of the detector, C is the heat capacity of the absorber and P is the power dissipated in the thermistor R_{bol} by Joule Effect (for more details see appendix B.2). This expression vanishes in the limit $P \to \infty$ and in the limit $C \to \infty$. An energy deposition of 1 MeV into a $\mathrm{TeO_2}$ absorber typically produces a temperature increase of $\Delta T = 7\cdot 10^{-5}$ K with a related voltage drop variation of $\Delta V_{\mathrm{bol}} = (100 \div 200)\ \mu$V. The best working point (V_{bol} , I_{bol}) maximizes the voltage drop variation or its signal-to-noise ration.

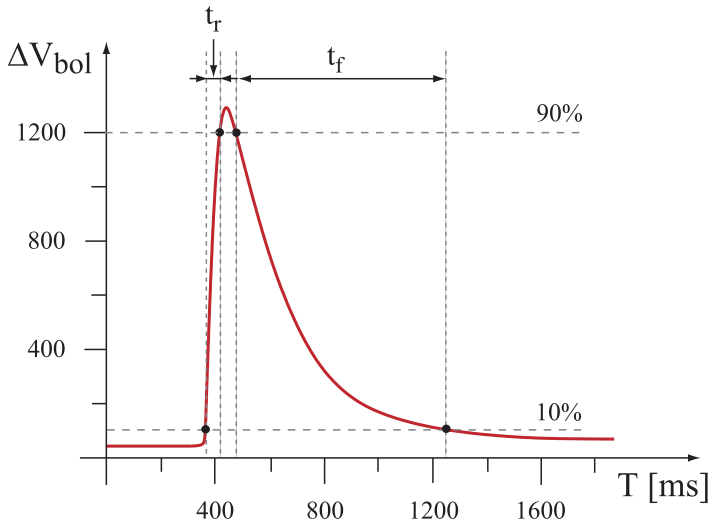

Figure 3.8: Typical pulses coming from the absorber crystals. The rise time is the difference between the time when the signal crosses a low threshold (10% of step height) to the time when the signal crosses the high threshold (90% of step height).

3.5.2 Detector noise

The energy resolution of a bolometric detector is limited by the noise sources. These sources can be classified in two main categories:

1) **intrinsic noise**: it's strictly dependent on the physical characteristic of the absorber and of the sensor. This is a unavoidable source of noise and gives the reachable theoretical limit for the energy resolution (ΔE_{MAX});

2) **extrinsic noise**: it accounts for all the noise sources dependent on the experimental set-up. In this category are included the sources due the cryogenics system, the sources due the electronics read-out, the electromagnetic interferences and the mechanical microphonic noise. This kind of noise dominates the energy resolution of the low temperature experiments.

The two main contributions at the intrinsic noise are the following:

1) **Johnson-Nyquist noise**: considering the semiconductor thermistors as a resistor, the *Johnson-Nyquist noise* (or *thermal noise*) is the electronic white noise generated by the thermal agitation of the charge carriers inside the device at equilibrium, which happens regardless of any applied voltage. For a typical value of resistance $R_{\text{bol}} = (50 \div 100)$ MΩ, working at a temperature $T = 12$ mK, the spectrum noise density is given by:

$$\sqrt{\overline{e_{\text{bol}}^2}} = \sqrt{\langle e_{\text{bol}}^2(t)\rangle_t} = \sqrt{4k_B T R_{\text{bol}}} \simeq 10^{-8}\,\frac{\text{V}}{\text{Hz}} \tag{3.22}$$

As it shown in figure 3.6(b) the sensor is biased using a load resistor that is, in general, at room temperature ($T_\mathrm{L} \simeq 300$ K). One could take into account the Johnson noise leads to this resistor on the thermistor, this contribution is given by:

$$\sqrt{\overline{e^2_\mathrm{det}}} = \sqrt{\overline{e^2_\mathrm{L}}} \left(\frac{R_\mathrm{bol}}{R_\mathrm{L} + R_\mathrm{bol}} \right) = \sqrt{4k_B T_\mathrm{L} R_\mathrm{L}} \, \frac{R_\mathrm{bol}}{R_\mathrm{L} + R_\mathrm{bol}} \tag{3.23}$$

and comparing this contribution with the thermistor one:

$$\frac{\sqrt{\overline{e^2_\mathrm{det}}}}{\sqrt{\overline{e^2_\mathrm{bol}}}} = \frac{\sqrt{\overline{e^2_\mathrm{L}}}}{\sqrt{\overline{e^2_\mathrm{bol}}}} \left(\frac{R_\mathrm{bol}}{R_\mathrm{L} + R_\mathrm{bol}} \right) \simeq \sqrt{\frac{4k_B T_\mathrm{L} R_\mathrm{L}}{4k_B T R_\mathrm{bol}}} \left(\frac{R_\mathrm{bol}}{R_\mathrm{L}} \right) = \sqrt{\frac{R_\mathrm{bol}}{R_\mathrm{L}} \frac{T_\mathrm{L}}{T}} \tag{3.24}$$

Therefore the detector contribution is dominant and it's mandatory to reduce it as much as possible choosing a large enough

2) **Thermodynamic noise**: it is due to the statistical fluctuations of the number of phonons exchanged between the heat sink and the thermistor (as previously said in the section 3.3.2). This phenomenon limits the intrinsic energy resolution, according to the equation 3.14, in the range $\Delta E = (10 \div 100)$ eV. In addition, considering the monolithic model, a detailed calculation of noise due to the intrinsic thermodynamic noise shows that the real energy resolution is the theoretical multiplied to a dimensionless factor ξ.

$$\Delta E = 2.35\xi \, \sqrt{F k_b C(T) T^2} \tag{3.25}$$

The ξ value depends on the details of the temperature sensor, of the thermal conductance and of the temperature dependences of the heat capacity. By means of a proper optimization it's possible to made this of the order of the unity.

Part II

Tellurium Double Beta Decay

Chapter 4

CUORE experiment

4.1 Introduction

The next generation of experiments for the double-beta decay search should be able to observe the phenomenon and measure the effective Majorana mass of the electron neutrino, $|\langle m_\nu \rangle|$, which would provide a measure of the neutrino mass scale. In particular they should be able to explore the inverted hierarchy neutrino mass region. This aim corresponds to a sensitivity in $|\langle m_\nu \rangle|$ better than 50 meV.

The use of bolometers as rare events detectors and in particular for the double beta decay research, has been first suggested by Professor E. Fiorini in 1984[143]. Under his guidance the Milano WIG Group (*Weak Interactions Group*), during the past twenty years, have developed bolometric detectors, of increasing mass, made of *tellurium dioxide* (TeO_2, also called *paratellurite*).

CUORE (*Cryogenic Underground Observatory for Rare Events*[158, 159]) will be the last step of this research line: with its total mass of about 741 Kg it will be the largest cryogenic detector operated so far. The preliminary step performed (table 4.1), in order to achieve this goal, are (in chronological order): a single crystal of 334 g[160] (riv.0), an array of four crystal with a mass of 340 g each[161] (array.4), a tower-like array of 340 g crystal[162, 163, 115, 116] (MiDBD) and, at last, a CUORE-like tower composed by 62 crystal with a total mass of 41.5 Kg (the running experiments CUORICINO). These experimental activity was carried out in the underground location offered by the *Laboratori Nazionali del Gran Sasso* (LNGS) of INFN (*Istituto Nazionale di Fisica Nucleare*).

The CUORE detector will consist of an array of 988 TeO_2 bolometers arranged in a cylindrical configuration of 19 towers each one composed by 52 $5 \times 5 \times 5$ cm^3 crystals. Each tower will have four columns and each column will be composed by 13 crystal. Its total mass will be about 18 times that of CUORICINO; this will allow CUORE to achieve the sensitivity required for the next generation of $0\nu\beta\beta$ experiments.

The excellent performance of the $5 \times 5 \times 5$ cm^3 crystals to be used in CUORE was already proved with the pilot experiment CUORICINO[166, 167, 168, 169, 164, 165].

	$\mathbf{N_c}$	**Mass** [g/each]	**Live Time** $[\mathrm{h} \cdot \mathbf{N_c}]$	$\mathbf{T^{0\nu}_{1/2}}$ [years]	**Bkg** [c/KeV/Kg/y]	$\mathbf{\Delta E_{FWHM}}$ [KeV]	**Ref.**
Riv.0	1	340	9234	$1.8 \cdot 10^{22}$	4.4 ± 0.3	$9 \div 15$	[160]
Array.4	4	340	3096.8	$3.3 \cdot 10^{22}$	$\simeq 4$	$\leqq 12$	[161]
MiDBD	8^{*}	340	4537	$5.6 \cdot 10^{22}$	–	$4 \div 10$	[162]
	20	340	94335.3	$2.1 \cdot 10^{23}$	0.33 ± 0.11	$5 \div 15$	[163]
CUORICINO	44	790	408466.31	$3.0 \cdot 10^{24}$	0.18 ± 0.01	8	[164, 165]
	14	330	116810.54		0.20 ± 0.04	12	
	$4^{\dagger}$	330	20866.22		0.40 ± 0.11	22	

Table 4.1: List of TeO_2-experiments performed from 1993 to the nowadays by the Milano Weak Interactions Group. The detectors were calibrated by a combined radioactive source of ^{238}U and ^{232}Th. The FWHM energy resolutions are measured at the 2615 KeV ^{208}Tl line. The half life limit is given at a confidence level 90%. The CUORICINO live time is equivalent to 55+415 days per crystals.

$\mathbf{N_c}$ is the total number of TeO_2 crystals.

*In the first phase only 8 channels were acquired.

†Two crystals are enriched to 82.3% in ^{128}Te and two are enriched to 75% in ^{130}Te.

Reproducibility was tested, the pulses amplitude is in agreement with the thermal model and the full width at half maximum (FWHM) was $\simeq$ 1 KeV for low energy gamma peaks and $\simeq$ 8 KeV at the 2615 KeV background γ-ray line from the thorium chain[167].

4.2 The location

CUORE will be located in the underground *Hall A* of the The *Laboratori Nazionali del Gran Sasso* (LNGS, L'Aquila, Italy). These laboratories are situated at 150 Km North-East of Rome and are excavated aside the 10 km highway tunnel passing under the Gran Sasso mountain. The altitude is 963 m and the average dolomitic rock cover is 1400 m (or 3700 m.w.e.) This rock, in addition of being a natural shield against cosmic radiation, is entitled to good radiopurity conditions, compared to similar underground physics sites. Table 4.2) shows the environmental background components (neutrons, gammas and muons) measured in the LNGS compared with other european underground laboratories.

The LNGS are a facility especially designed and excavated for underground physics. The underground laboratory comprises three experimental halls (named A, B and C) with a variable length around 100 m and height above 18 m for an overall volume exceeding 180000 m^3. Experimental setups are situated in the halls or in the net of service tunnels that complete the structure (figure 4.1).

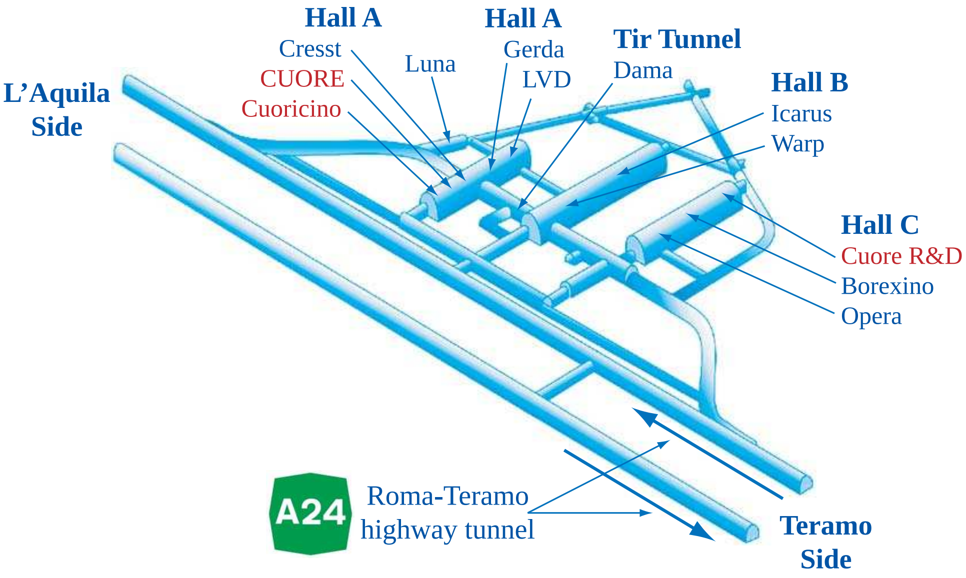

Figure 4.1: Laboratori Nazionali del Gran Sasso, map of the underground experimental halls.

Muon			
Location	**m.w.e.**	Φ_μ $[\mathrm{cm}^{-2} \cdot \mathrm{s}^{-1}]$	**Ref.**
LNGS[a]	3800	$(1.19 \pm 0.05) \cdot 10^{-6} \cdot \mathrm{sr}^{-1}$	[170, 171]
LSM[b]	4800	$(5.14 \pm 0.39) \cdot 10^{-9}$	[172]
IUS[c]	2805	$(4.09 \pm 0.08 \pm 0.13) \cdot 10^{-8}$	[173]
LSC[d]	2500	$(3.94 \pm 0.05 \pm 0.40) \cdot 10^{-7}$	[174]
CUPP[e]	3960	$(1.10 \pm 0.10) \cdot 10^{-8}$	[175]

Gamma					
Location	**m.w.e.**	**Mean Activity** $[\gamma \cdot \mathrm{cm}^{-2} \cdot \mathrm{s}^{-1}]$			**Ref.**
		^{40}K	^{238}U	^{232}Th	
LNGS[a]	3800	$\simeq 1$ (for the whole natural chain)			[176]
IUS[c]	2805	(1130 ± 200) ppm	(67 ± 6) ppb	(127 ± 10) ppb	[177]
LSC[d]	2500	(0.33 ± 0.20)	(0.71 ± 0.12)	(0.85 ± 0.07)	[174]

Neutron				
Location	**m.w.e.**	**Neutron Energy** $\mathrm{E_n}$ **[MeV]**	**Neutron Flux** Φ_n $[10^{-6} \mathrm{n} \cdot \mathrm{cm}^{-2}] \cdot \mathrm{s}^{-1}$	**Ref.**
LNGS[a]	3800	HALL A: Thermal Neutron	1.08 ± 0.02	[178]
		HALL A: $E_\mathrm{n} > 2.5$ MeV	0.23 ± 0.07	[178]
		HALL C: 1 MeV $< E_\mathrm{n} <$ 10 MeV	0.42 ± 0.12	[179]
LSM[b]	4800	Thermal Neutron	1.60 ± 0.10	[180, 181]
		2 MeV $< E_\mathrm{n} <$ 6 MeV	4.00 ± 1.00	[180]
IUS[c]	2805	$E_\mathrm{n} > 0.5$ MeV	$1.72 \pm 0.61 \pm 0.38$	[182]

[a] Laboratori Nazionali del Gran Sasso.
[b] Laboratoire Souterrain de Modane.
[c] Institute of Underground Science, Boulby Mine.
[d] Laboratorio subterraneo de Canfranc.
[e] Centre for Underground Physics in Pyhäsalmi.

Table 4.2: Measurement of environmental activity at the ILIAS Underground laboratories. ILIAS is an european network-project that groups the most important Underground laboratories and Gravitational Waves observatories in Europe.

4.3 CUORE bolometers

In this section it will presented an overview of the configuration adopted for the CUORE bolometers. Their main important parts are: the double beta decay source, the energy absorber and the sensor.

4.3.1 The Double Beta Decay source: ^{130}Te

As shown previously the bolometric technique offer a freedom in the choice of double beta candidates isotope (table 2.2). The only requirement is the following: the chosen candidate nucleus must be part of a crystalline structure with good thermal and mechanicals properties.

The isotope 130 of the tellurium, chosen for the past WIG experiments and also chosen for CUORICINO and CUORE, is a good candidate for testing the neutrinoless DBD in a isotope different from ^{76}Ge and, at the same time, with a competitive sensitive to obtain crosschecked information and to prove the consistency of the Majorana-neutrino hypothesis. The decay searched is:

$$^{130}\mathrm{Te} \;\rightarrow\; ^{130}\mathrm{Xe} + 2e^{-} \quad \Rightarrow \quad Q = (2530.3 \pm 2.0)\ \mathrm{KeV}\ [60] \tag{4.1}$$

The main features of this choice are the following:

1) **Isotopic Abundance**: the sensitivity of a DBD experiment is proportional to the square root of the number of nuclei under control i.e. to the square root of the detector's mass. Since it's impossible to increase easily the mass of some order of magnitude, it is very important to choose an isotope with an high isotopic abundance without expensive enrichment procedure. As shown in table 2.2, the isotope ^{130}Te is an optimal choice since its isotopic content in natural tellurium is i.a = 34.50%[60].

2) **Transition energy**: the Q-value of $\beta\beta-$decay is very important parameter because its relation with the natural radioactivity background. The Q-value of ^{130}Te is $Q = (2530.3 \pm 2.0)$ KeV, this value is located in a clean energy windows between the photo-electric peak and the Compton edge of the 2615 KeV line of ^{208}Tl, and out of the background induced by ^{238}U.

3) **Phase space**: the parameter $G^{0\nu}$ is the element of phase space of the transition. This represents the pure kinematic contribution of the decay process. For a $\beta\beta-$decay one has $G^{0\nu} \propto Q^{5}$, so the higher is the Q-value, the bigger is the probability for the decay to occur. The $\beta\beta$ Q-value for ^{130}Te is reasonable high.

4) **Nuclear dynamics**: as shown in the previous chapters, the life time for $0\nu\beta\beta$ is inversely proportional with the matrix elements $|M^{0\nu}|^2$ by means of the *nuclear structure factor* F_N defined as:

$$F_N = G^{0\nu}\left|M^{0\nu}\right|^2 \quad \text{and} \quad T^{0\nu}_{1/2} = \left[F_N \left(\frac{|\langle m_\nu \rangle|}{m_e} \right)^2 \right]^{-1} \tag{4.2}$$

The nuclear matrix elements are dominated by the nuclear dynamics. Their values are model dependent and different from one nuclide to another. In most of the nuclear models used to compute the matrix elements (for example RQRPA and QRPA methods[72, 73], figure 4.2) the nuclear structure factor of ^{130}Te is more favorable than that of ^{76}Ge (table 4.3)).

Nuclear transition	g_A	M_{GT}^{exp} [MeV^{-1}]	$\langle M^{0\nu}\rangle$		$\varepsilon_{exp.}$	$T_{1/2}^{0\nu}$ ($\langle m_{\beta\beta}\rangle$ = 50 meV) [yrs]
			RQRPA	QRPA		
$^{76}Ge \rightarrow {}^{76}Se$	1.25	0.15 ± 0.006	3.92(0.12)	4.51(0.17)	± 0.05	$0.86^{+0.08}_{-0.07}\ 10^{27}$
	1.00	0.23 ± 0.01	3.46(0.13)	3.83(0.14)	± 0.06	$1.10^{+0.13}_{-0.11}\ 10^{27}$
$^{82}Se \rightarrow {}^{82}Kr$	1.25	0.10 ± 0.009	3.49(0.13)	4.02(0.15)	± 0.08	$2.44^{+0.32}_{-0.26}\ 10^{26}$
	1.00	0.16 ± 0.008	2.91(0.09)	3.29(0.12)	± 0.08	$3.50^{+0.46}_{-0.38}\ 10^{26}$
$^{96}Zr \rightarrow {}^{96}Mo$	1.25	$0.11^{+0.03}_{-0.06}$	1.20(0.14)	1.12(0.03)	$^{+0.12}_{-0.23}$	$0.98^{+1.1}_{-0.31}\ 10^{27}$
	1.00	$0.17^{+0.05}_{-0.1}$	1.12(0.11)	1.21(0.07)	$^{+0.12}_{-0.25}$	$1.12^{+1.3}_{-0.35}\ 10^{27}$
$^{100}Mo \rightarrow {}^{100}Ru$	1.25	0.22 ± 0.01	2.78(0.19)	3.34(0.19)	± 0.02	$2.37^{+0.41}_{-0.32}\ 10^{26}$
	1.00	0.34 ± 0.015	2.34(0.12)	2.71(0.14)	± 0.02	$3.33^{+0.47}_{-0.39}\ 10^{26}$
$^{116}Cd \rightarrow {}^{116}Sn$	1.25	0.12 ± 0.006	2.42(0.16)	2.74(0.19)	± 0.02	$2.86^{+0.50}_{-0.39}\ 10^{26}$
	1.00	0.19 ± 0.009	1.96(0.13)	2.18(0.16)	± 0.02	$4.39^{+0.77}_{-0.61}\ 10^{26}$
$^{128}Te \rightarrow {}^{128}Xe$	1.25	0.034 ± 0.012	3.23(0.12)	3.64(0.13)	± 0.09	$4.53^{+0.64}_{-0.53}\ 10^{27}$
	1.00	0.053 ± 0.02	2.54(0.08)	2.85(0.08)	± 0.10	$7.35^{+1.1}_{-0.88}\ 10^{27}$
$^{130}Te \rightarrow {}^{130}Xe$	1.25	$0.036^{+0.03}_{-0.009}$	2.95(0.12)	3.26(0.12)	$^{+0.26}_{-0.08}$	$2.16^{+0.33}_{-0.46}\ 10^{26}$
	1.00	$0.056^{+0.05}_{-0.15}$	2.34(0.07)	2.59(0.06)	$^{+0.27}_{-0.08}$	$3.42^{+0.51}_{-0.83}\ 10^{26}$
$^{136}Xe \rightarrow {}^{136}Ba$	1.25	0.030	1.97(0.13)	2.11(0.11)		$4.55^{+0.68}_{-0.56}\ 10^{26}$
	1.00	0.045	1.59 (0.09)	1.70 (0.07)		$6.38^{+1.12}_{-0.91}\ 10^{26}$
	1.25	0	1.67(0.13)	1.78(0.11)		$7.00^{+0.84}_{-0.71}\ 10^{26}$
	1.00	0	1.26 (0.09)	1.35 (0.07)		$1.11^{+0.17}_{-0.14}\ 10^{27}$
$^{150}Nd \rightarrow {}^{150}Sm$	1.25	$0.07^{+0.009}_{-0.03}$	4.16(0.16)	4.74(0.20)	$^{+0.06}_{-0.19}$	$2.23^{+0.41}_{-0.21}\ 10^{25}$
	1.00	$0.11^{+0.014}_{-0.05}$	3.30(0.16)	3.72(0.20)	$^{+0.06}_{-0.19}$	$3.55^{+0.87}_{-0.42}\ 10^{25}$

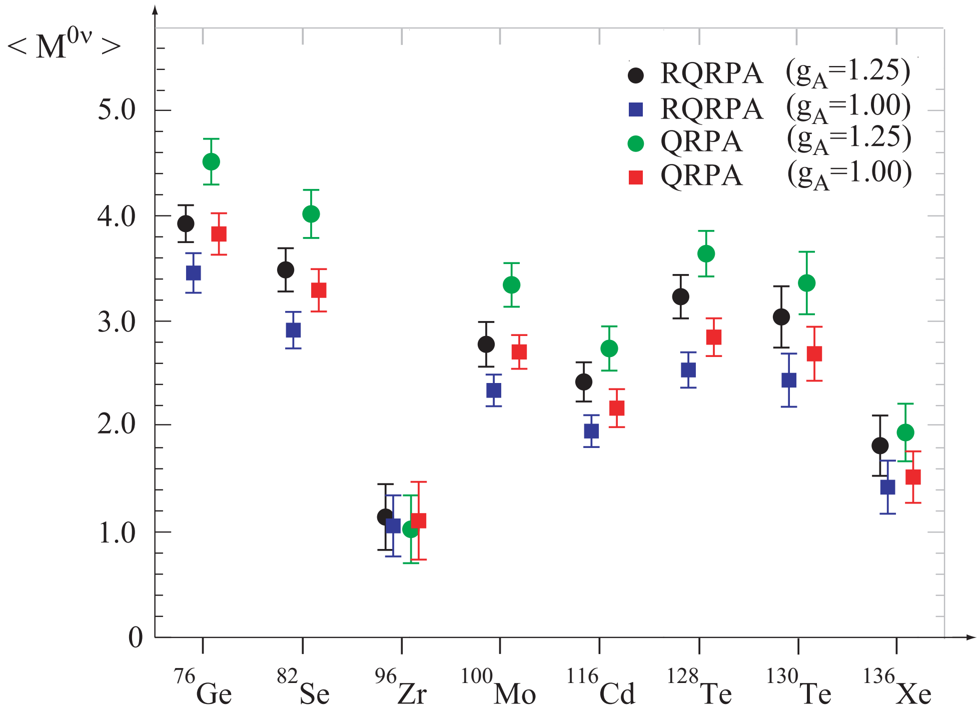

Figure 4.2: Average $0\nu\beta\beta$ nuclear matrix elements $< M^{0\nu} >$ and their variance evaluated in the RQRPA and QRPA[72, 73].

Parent Isotope	F_N $[y^{-1}]$	$Q_{\beta\beta}$ [KeV]
^{48}Ca	$(5.4^{+3.0}_{-1.4}) \cdot 10^{-14}$	4274.0
^{76}Ge	$(7.3 \pm 0.6) \cdot 10^{-14}$	2039.0
^{82}Se	$(1.7^{+0.4}_{-0.3}) \cdot 10^{-13}$	2995.5
^{100}Mo	$(5.00 \pm 0.15) \cdot 10^{-13}$	3035.0
^{116}Cd	$(1.3^{+0.7}_{-0.3}) \cdot 10^{-13}$	2809.0
^{130}Te	$(4.2 \pm 0.5) \cdot 10^{-13}$	2530.3
^{136}Xe	$(2.8 \pm 0.4) \cdot 10^{-14}$	2462.0
^{150}Nd	$(5.7^{+1.0}_{-0.7}) \cdot 10^{-14}$	3367.7

Table 4.3: The most popular parent isotopes, their average nuclear structure factors and the $0\nu\beta\beta$-decay energy[60].

4.3.2 The energy absorber: TeO_2

The WIG group decided to use ^{130}Te in dioxide form (TeO_2). The choice of using TeO_2 crystal (figure 4.3) instead pure Te crystal was motivated by the useful properties of the first one.

1) **Debye temperature**: the θ_D of the tellurium dioxide is higher than of pure Te and so, at the same temperature, the former has a lower specific heat and thus higher pulses can be achieved[183]. Moreover TeO_2 crystals, being dielectric and diamagnetic material, have only the lattice contribution to the specific heat, the others are negligible.

2) **Mechanical properties**: pure Te has poor mechanical properties and breaks after few thermal cycle. Differently large crystal of TeO_2 can be grown with excellent mechanical properties.

3) **Compound quality and mass**: the tellurium dioxide mass is dominated by tellurium, this means that it's possible to work with a large quantity Te (about 80%). Moreover the radiopurity obtained is high: $R < 1$ pg/g both for ^{232}Th and ^{238}U.

Taking into account these consideration it's possible to see that the isotope ^{130}Te in form of TeO_2 crystals it is a very good available choice with moderate cost and good features for rare events research.

4.3.3 The sensor

The sensor used for CUORICINO are NTD-Ge thermistor working in the *variable range hopping* conduction regime with Coulomb gap.

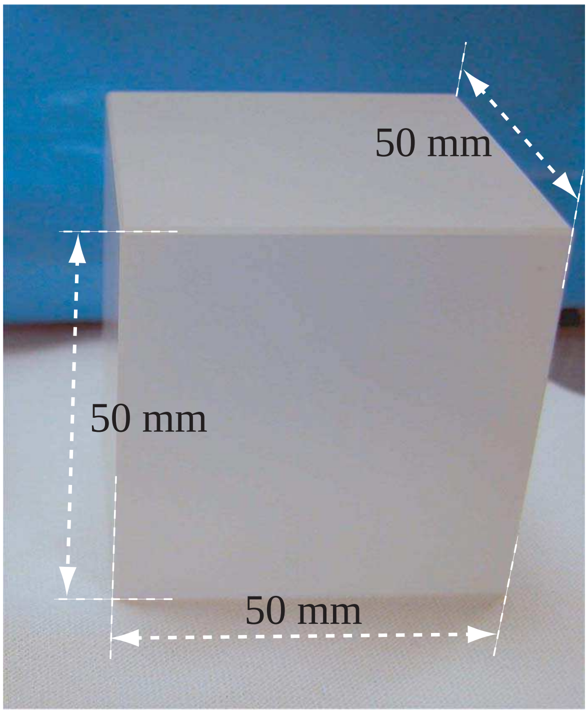

Figure 4.3: Example of $5 \times 5 \times 5\ \mathrm{cm}^2$ TeO_2 crystal. The crystal are produced by Shanghai Institute of Ceramics, Chinese Academy of Sciences SICCAS. The single crystal are grown using the Bridgman technique

As described in the section 3.4.1 this kind of devices are able to convert the thermal pulse into an electrical signal thanks to the temperature dependence of its resistivity. The resistance behavior (figure 4.4) follows the relation:

$$\rho(T) = \rho_0\ \mathrm{e}^{\left(\frac{T_0}{T}\right)^\gamma} \quad \Rightarrow \quad R = \rho(T) \cdot \frac{l}{S} = R_0\ \mathrm{e}^{\left(\frac{T_0}{T}\right)^\gamma} \tag{4.3}$$

where the parameter R_0 depends on the sensor geometry (l is the distances between the electrical contacts where the wires are bound and S is the area of the pad where the contacts are made), ρ_0 the intrinsic electric resistivity and $\gamma = 1/2$ (critical concentration in the MIT region and working temperature lower than 1 °K).

The CUORICINO thermistors have been developed and produced by a group [1] leaded by E. Haller, using a reactor[2]. The Neutron Transmutation Doped Germanium is produced by irradiating an ultrapure germanium crystal by means of a flux composed by thermal neutrons ($E_n \simeq 0.025$ eV), epithermal neutrons ($E_n \simeq (0.025 \div 1)$ eV) and fast neutrons ($E_n > 1$ eV). Ge nuclei capture the thermal and epithermal neutrons and form various radioactive Ge isotope, which subsequently decay into As, Ge and

---

[1] composed by people from *Lawrence Berkeley National Laboratory* (LBNL) and *University of California Berkeley Department of Material Science*

[2] University of Missouri-Columbia and Massachusetts Institute of Technology reactors

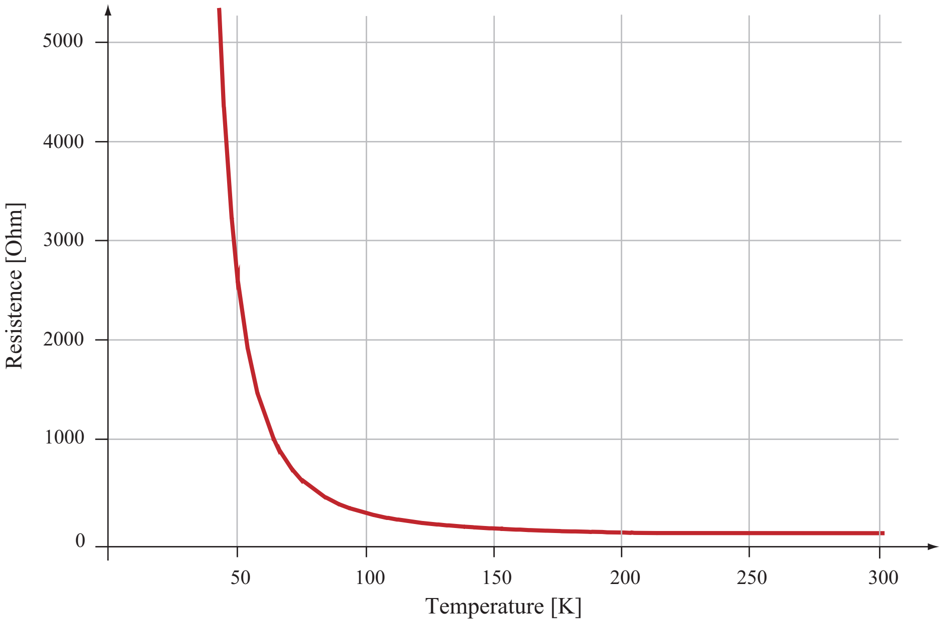

Figure 4.4: Resistance of a NTD-Ge thermistor as a function of temperature.

Ga. The occurring reactions are the following:

$$\left\{\begin{array}{llll} {}^{70}\mathrm{Ge}(i.a. = 21\%) + n \;\rightarrow\; {}^{71}\mathrm{Ge} + \gamma & [\sigma_T = (3.43 \pm 0.17)\ \mathrm{b}] & \\ & [\sigma_E = 1.5\ \mathrm{b}] & \text{Acceptor} \\ {}^{71}\mathrm{Ge} + e^- \;\rightarrow\; {}^{71}\mathrm{Ga} + \nu_e & [\tau_{1/2} = 11.4\ \mathrm{d}] & \end{array}\right.$$

$$\left\{\begin{array}{llll} {}^{74}\mathrm{Ge}(i.a. = 36\%) + n \;\rightarrow\; {}^{75}\mathrm{Ge} + \gamma & [\sigma_T = (0.51 \pm 0.08)\ \mathrm{b}] & \\ & [\sigma_E = (1.0 \pm 0.2)\ \mathrm{b}] & \text{Donor} \\ {}^{75}\mathrm{Ge} \;\rightarrow\; {}^{75}\mathrm{As} + e^- + \bar{\nu}_e & [\tau_{1/2} = 83\ \mathrm{min}] & \end{array}\right.$$

$$\left\{\begin{array}{llll} {}^{76}\mathrm{Ge}(i.a. = 7.4\%) + n \;\rightarrow\; {}^{77}\mathrm{Ge} + \gamma & [\sigma_T = (0.160 \pm 0.0014)\ \mathrm{b}] & \\ & [\sigma_E = (2.00 \pm 0.35)\ \mathrm{b}] & \text{Double} \\ {}^{77}\mathrm{Ge} \;\rightarrow\; {}^{77}\mathrm{As} + e^- + \bar{\nu}_e & [\tau_{1/2} = 11.3\ \mathrm{h}] & \text{Donor} \\ {}^{77}\mathrm{As} \;\rightarrow\; {}^{77}\mathrm{Se} + e^- + \bar{\nu}_e & [\tau_{1/2} = 38.8\ \mathrm{h}] & \end{array}\right. \tag{4.4}$$

where σ_T and σ_E are, respectively, the thermal and epithermal, neutron cross-section. The most important aspect is that ^{70}Ge transmutes into Ga, an acceptor, and that ^{74}Ge transmutes into As, a donor, the primary active dopant in NTD-Ge. The dopant concentration is given by:

$$N_{\text{dopant}} = m \cdot \text{i.a.}\, \frac{\mathcal{N}_{\mathcal{A}}(\sigma_T \Phi_T + \sigma_E \Phi_E)}{M}\, t \qquad \begin{cases} m: & \text{wafer mass} \\ \text{i.a}: & \text{isotopic abundance} \\ M: & \text{molar mass of the} \\ & \text{target isotope} \\ \Phi_T: & \text{flux of the} \\ & \text{thermal neutrons} \\ \Phi_E: & \text{flux of the} \\ & \text{epithermal neutrons} \\ t: & \text{irradiation time} \end{cases} \tag{4.5}$$

By means of this procedure it's possible to obtain a dopant concentrations per neutron unit flux as follow[184]:

$$\begin{cases} \text{Ga} = 2.94 \cdot 10^{-2}\text{cm}^{-3} & \text{per neutron/cm}^2\text{/s} \\ \\ \text{As} = 8.37 \cdot 10^{-3}\text{cm}^{-3} & \text{per neutron/cm}^2\text{/s} \end{cases} \tag{4.6}$$

The intrinsic parameters R_0, T_0 and γ must be experimentally measured for each thermistor (as described in [185]). In the case of CUORICINO the characterization process was done at the INFN cryogenic laboratories of Milano and Firenze (see tables 4.4). The series #31, used in CUORICINO, have the best parameter values according with the detector requirements.

Up to now, the current mounting procedure (CUORICINO-like) provides that the NTDs are first bonded and then glued on the crystals. The order is constrained by the position of the golden-pads that provide electrical contact to the wires: in fact the pads are deposited on the opposite large sides of each thermistor by ion implantation and gold coating along the whole surface (figure 4.5(a)). The current operation of bonding and gluing can sometimes lead to the breakage of wires; moreover, it slows down the whole assembly process and affects its reproducibility.

For CUORE a possible simplification could be obtained if the gold pads are set on the upper face of the thermistors. In this way, the order of the assembly procedure can be inverted by making wire-bonding the last step. This could lead, in principle, to a simpler, faster and more reliable wiring. Such thermistors are called *Flat-pack* NTDs (figure 4.5(b)).

A preliminary set of this kind of thermistors are currently under test at the cryogenics laboratory of Como. The goal is to obtain Flat-pack thermistors with the same characteristics of the #31 CUORICINO series.

NTD Label	$\mathbf{R_0}[\Omega]$	$\mathbf{T_0}$ [°K]	γ
B31_3A	7.2639	3.3840	0.5
B31_3B	8.8157	3.7485	0.5
B31_3C	7.4606	3.4111	0.5
B31_3D	6.8294	3.3709	0.5
B31_3E	8.4670	3.5887	0.5
B31_3F	8.7392	3.3927	0.5
B31_3G	5.6102	3.2202	0.5
B31_3H	7.5310	3.4469	0.5
B31_3I	7.8025	3.4108	0.5
B31_3J	7.7662	3.3002	0.5
B31_3K	7.0633	3.3074	0.5
B31_3L	8.7439	3.3264	0.5
B31_3M	8.8996	3.2432	0.5
B31_3N	9.0574	3.3792	0.5
B31_3O	8.3850	3.1776	0.5
B31_3P	8.8738	3.1168	0.5
B31_3Q	5.0797	3.1612	0.5
B31_3R	7.6408	3.1991	0.5
B31_3S	8.1979	3.2235	0.5
B31_3T	7.0348	3.3846	0.5
B31_3U	7.4667	3.2897	0.5
B31_3V	6.3431	3.4101	0.5
B31_3W	7.6356	3.4346	0.5
B31_3Z	6.5470	3.3568	0.5
B31_4A	7.0414	3.6111	0.5
B31_4B	7.8019	3.3666	0.5
B31_4C	7.7159	3.2975	0.5
B31_4D	6.1891	3.1647	0.5
B31_4E	8.6275	2.9761	0.5
B31_4F	6.3581	3.3016	0.5
B31_4G	10.248	3.6859	0.5
B31_4H	9.2200	3.3479	0.5
B31_L1	1.7939	2.8924	0.5
B31_L2	1.7601	3.0418	0.5
B31_L3	1.6830	2.9918	0.5
B31_L4	1.5834	2.9589	0.5
B31_L5	1.3865	3.2459	0.5
B31_L6	1.2776	3.2965	0.5
B31_M1	2.8365	2.9544	0.5
B31_M2	2.4525	3.0613	0.5
H31_1A	7.1374	3.2955	0.5
H31_1B	7.3534	3.3651	0.5
H31_1C	7.2339	3.2874	0.5
H31_1D	7.3362	3.3046	0.5
H31_S1	0.8378	2.9550	0.5
H31_S2	0.8216	2.9110	0.5
H31_S3	0.8150	2.9810	0.5
H31_F1	0.5137	2.9160	0.5
H31_F2	0.5605	2.8790	0.5
H31_L1	1,5250	2,8650	0.5
H31_L2	1.4770	2.9500	0.5
H31_L5	1.2000	3.2400	0.5
H31_L6	1.1700	3.4000	0.5
H31_L7	1.1300	3.4200	0.5
H31_L8	1.1500	3.3900	0.5
H31_L9	1.1200	3.4100	0.5
H31_L10	1.1200	3.3700	0.5
H31_L11	1.1600	3.3700	0.5
H31_L12	1.1600	3.2000	0.5
H31_L13	1.1700	3.2300	0.5
H31_L14	1.1800	3.3800	0.5
H31_L15	1.1300	3.3200	0.5
H31_L17	1.2100	3.3600	0.5

Table 4.4: Example of a set of NTD-Germanium thermistors characterized for the CUORICINO experiments. The values are taken from the Milano-Como Thermistor Data-Base. In the case of the #31 series the T_0 is around 3 °K, for a logarithmic sensitivity A in the range between 7 and 10.

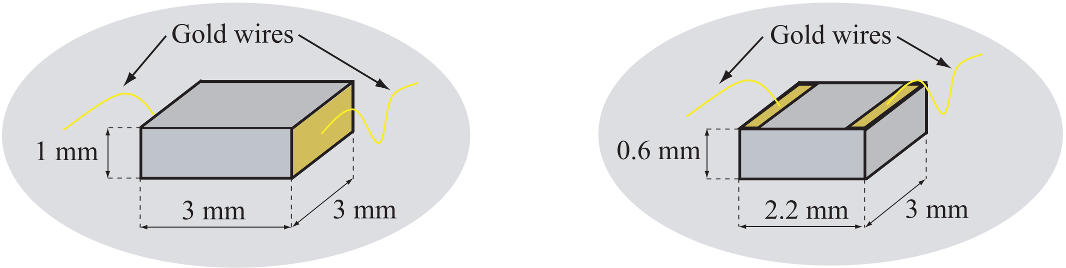

(a) Series #31 $3 \times 3 \times 1$ mm^3 Ge thermistors. The 50 μm gold wires are bonded to the gold-pads of the device sides.

(b) Flat-pack NTDs, the gold-pads are on the top of the device. This solution allows a frontal bonding also when the thermistor is already glued to the crystal.

Figure 4.5: Comparison between the old and the new possible solution.

4.4 The modular structure

The CUORE detector comprises 988 TeO_2 bolometers grouped in 247 modules of 4 bolometers each. Each module is called *Single Module* (SM). The bolometers are arranged in 19 towers of 52 crystal each (*super module*), or in a stack 13 single module high. The towers are assembled in a cylindrical structure as shown in the figures 4.8 and 4.9.

4.4.1 The single module

The single module is the elementary unit of the TeO_2 array detectors. The main goal of this unit is to secure the different parts of the every floor in order to prevent power dissipation caused by friction caused, in its turn, by unavoidable vibrations. The only constraint come from the need to use only clean materials reducing the amount of radioactive contaminants on the surfaces facing the detectors.

The fundamental components of the SM are: the crystal absorber (section 4.3.2), the NTD thermistor (section 4.3.3), the heater, the PTFE[3] supports and, at last, the copper structure (OFHC copper, *Oxygen-Free High Conductivity*).

1) **The bolometer**: each single module is composed by four TeO_2 bolometers. The NTD germanium thermistors are glued to the each crystal by nine spots of Araldit® rapid epoxy deposited over the crystal surface by means of an array of metal pins (figure 4.6). The height of these spots is $h_{\text{spot}} = 50\ \mu$m and their

---

[3] polytetrafluoroethylene is a synthetic fluoropolymer. PTFE is most well known through its trademark brand name Teflon®.

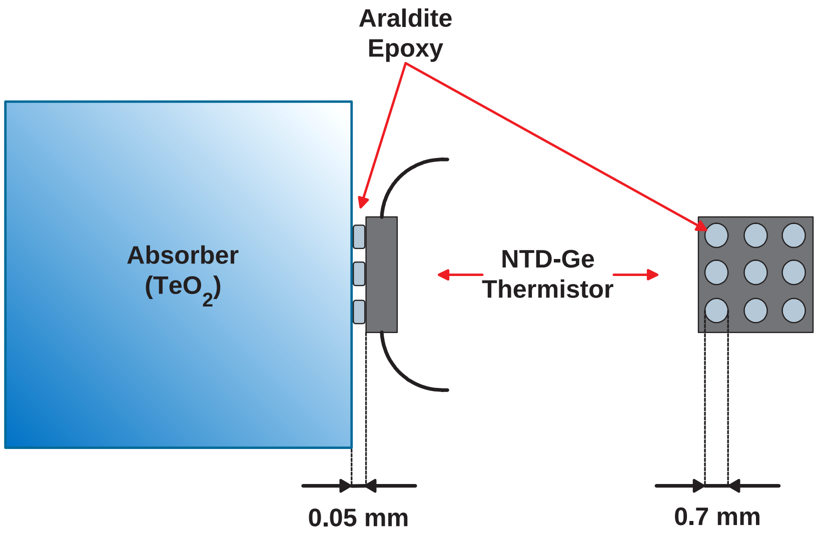

Figure 4.6: The NTD germanium thermistors are glued to the each crystal by nine spots of Araldit® rapid.

diameter it is in the range $D_{\text{spot}} = (0.4 \div 0.7)$ mm. The gluing procedure was already tested and used for both MiDBD[145, 186] and CUORICINO mounting process and, currently, it is characterized by an reasonable level of reliability and reproducibility. Anyway CUORE needs an higher level of automation.

The heat conductance of the epoxy spots was measured at the INFN cryogenic laboratories of Milano and the phenomenological relation for its temperature dependence was found to be $C(T) \simeq 1.6 \cdot 10^{-4} T^3$ W/T per spot[187].

2) **The heater**: Every crystal has its own *heater*. These devices are used as Joule heaters to inject a periodically a fixed energy in the crystal in order to monitor the thermal gain during the measurement and correct its variations off-line. Thanks to this procedure it's possible to stabilize the bolometers response. As in the case of the thermistors, they are glued to the crystal by means of few spots of Araldit® epoxy.

   The heaters are silicon chips with a heavily doped structure that produce a resistance between 100 to 300 KΩ. The resistance value is selectable through four metal pads present on the top side of the chip. The excitation signal is provided using two 50 μm gold wire bonded to two of these pads and the resistance value depends on the length present between the two pads chosen.

   The heaters are driven by means of a dedicated electronics board (section 7.4). The CUORE series are produced by cutting Si-wafer at ITC-irst Center (Trento, Italy).

3) **The copper structure**: the copper structure is a frame used to secure rigidly

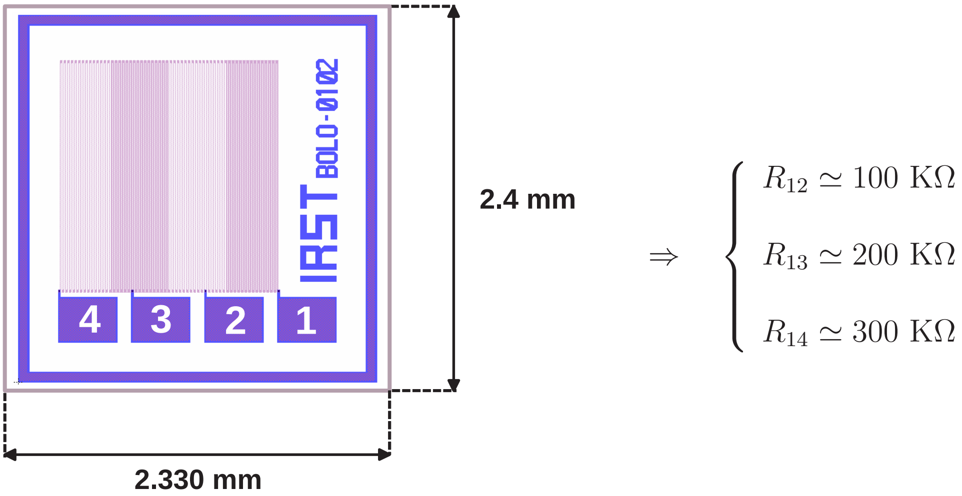

Figure 4.7: Thermal heater chip, top view. The resistance depends on the path length between the chosen metal pads.

the crystals. The copper frame is composed by two part (top and bottom) joined by means of four cylindrical supports (figure 4.9). These frames are connected to each other and with the *mixing chamber* of a dilution refrigerator that provides the base low temperature ($T_\mathrm{b} \simeq 10$ mK) to operate the bolometers. The single frame is shared by two single module, the top frame of one module coincides with the bottom frame of the module above.

Copper has a thermal conductance and specific heat high enough to be ideal heat sink, furthermore it has excellent mechanical properties. The copper structure of the entire detector constitutes the heat sink; being in thermal contact with the coldest point (*mixing chamber*) of the dilution refrigerator.

4) **The Teflon supports**: each crystal is held to the copper frame by means of PTFE supports. Copper guarantees a rigid structure without frictions between the different elements while the PTFE provides an elastic but tight holding of the crystal (figure 4.9). Thus, adopting this solution, it is possible to prevent the differential thermal contractions that could break the crystal or leave them too loose.

The behavior of the single module (detector+PTFE+Cu frames) is determined by the differential thermal contraction of the different components between room and base temperature. While copper and crystals contraction is of the order of 0.1% the contractions of PTFE are about 2%. The length of the critical dimensions have been calculated in a way that, at base temperature (T_b), the crystal cannot move independently to the frame.

The final tests on the CUORE-*single-module* indicate that, when the system is cooled down, the PTFE supports held the crystals tightly without breaking them while, at room temperature, the PTFEs are keeping the crystals in place without applying any force.

OFHC copper and PTFEs will be treated separately with acid (nitric acid, HNO_3) to remove any possible surface contamination. Moreover the copper will be covered by a polyethylene foil with thickness greater than 60 μm in order to absorb the α-particle emitted from a possible residual surface contamination. The penetration depth of an α particle, for example emitted by a ^{210}Po ($T_{1/2} = 138.376$ days and $E_\alpha = 5.407$ MeV), in the polyethylene is $l_{\mathrm{depth}} \simeq 20$ μm so for having an optimal absorption the thickness must be greater than $3l_{\mathrm{depth}} = 60$ μm. The arrays will be assembled in a underground clean room using box with a N_2 atmosphere to avoid radon (Rn) contamination.

4.4.2 From the super module to the entire detector

The CUORE *super module* is a tower-like structure composed of thirteen single modules. As said in the previous section, the single modules of the each tower are connected together by means of a shared copper frame avoiding the use of additional copper supports (CUORICINO mounting). This solution is intended to reduce the amount of copper present in the final structure in order to minimize the background due the surface contamination. In the CUORE design the lateral copper bars, that held the modules and present in CUORICINO, are eliminated. The structure is held together only via the copper columns. Each column has a threaded hole on the tops and ends with a screw. In this way the columns of one module are screwed directly on the columns of the module immediately below.

Thanks to this compact design there is no more separation between the different single modules inside the tower because they are all connected together. The super module must be assembled in sequence starting from the bottom to the top.

The 19 super modules of CUORE will be independently hooked and suspended to a large cylindrical copper plate (84 cm of diameter, figure 4.8), thermally connected to the mixing chamber of the dilution refrigerator. The plate, and the overall arrays, will be suspended from the upper part of the cryostat by a vertical ropes (springy-pendulum suspension, figure 4.10) to decouple the detector from the vibrations of the dilution refrigerator. Each rope is composed by several part of Kevlar®49[4] with a final support made of copper connected to the copper plate. Each part is thermalized. The detector and the plate are surrounded by a cylindrical copper shield, at 10 mK, connected to the mixing chamber plate.

---

[4] Kevlar is the DuPont Company's registered trademark for a light, strong synthetic fiber created in 1965. The Kevlar grade (49) describe the tensile characteristics of the material.

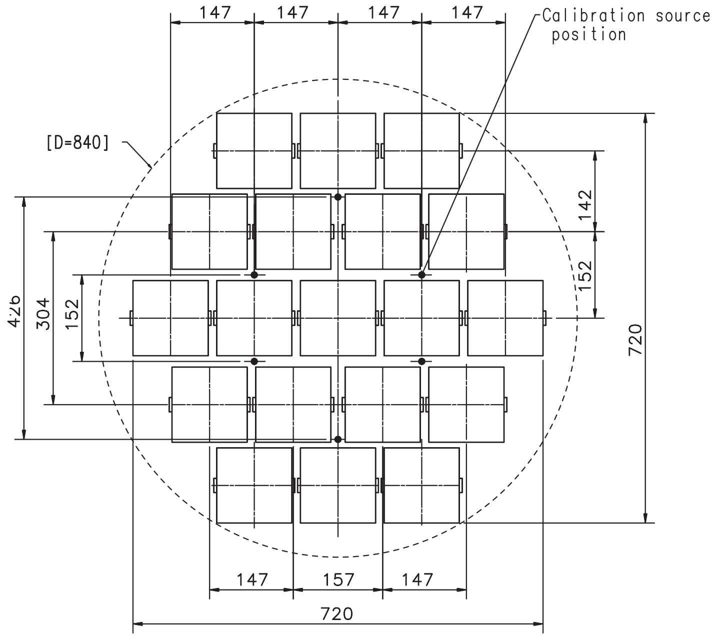

Figure 4.8: Top view of the suspension copper plate. The all towers (super modules) are suspended from a plate connected to the upper cryostat flange by means of vertical springy-ropes.

4.5 The cryogenics setup

The CUORE bolometers will operate at temperatures between 7 and 10 mK. This will require an extremely powerful *dilution refrigerator* (DR). At these temperatures, the cooling power of a DR varies approximately as T^2. The detector and the coldest part of the refrigerator receive some parasitic power from three main sources: the heat transfer of the residual helium gas in the *Inner Vacuum Chamber* (IVC) and the power radiated from the 10 mK shield facing the detector and from vibrational energy. The estimated value is about 1 μW @7 mK, using reasonable values for the residual gas pressure and achievable surface quality for radiation transfer. The resulting estimate for the radiation contribution was negligible.

The total mass to be cooled, including the detector support copper structure and the radioactivity lead shielding (300 K, 40 K, 4 K, 600 mK, 50 mK, and 10 mK) is of about 4-tons: refrigerators with the required characteristics are technically feasible as demonstrated by the cryogenic gravitational wave antennas[188, 189, 190]. CUORE will utilize a similar system to that of the *Nautilus* Collaboration that cools a 2-ton gravitational antenna[191, 192]. That system experienced a parasitic power of 10 μW from unknown sources. The CUORE detector will be cooled by a ^{3}He/^{4}He refrigerator with a cooling power of 3 mW @120 mK. Refrigerators with the required characteristics are technically feasible. One example is the DRS-3000 DR model constructed by the Kamerling Onnes Laboratory (Leiden, Netherlands).

The cryogenics setup used for CUORICINO, and also used in the past for the MiDBD experiment, consist of a *conventional* ^{3}He/^{4}He *Dilution Refrigerator* (appendix A.1) having powers of 1000 μW at 100 mK (Oxford®1000[193]). In this type of refrigerators

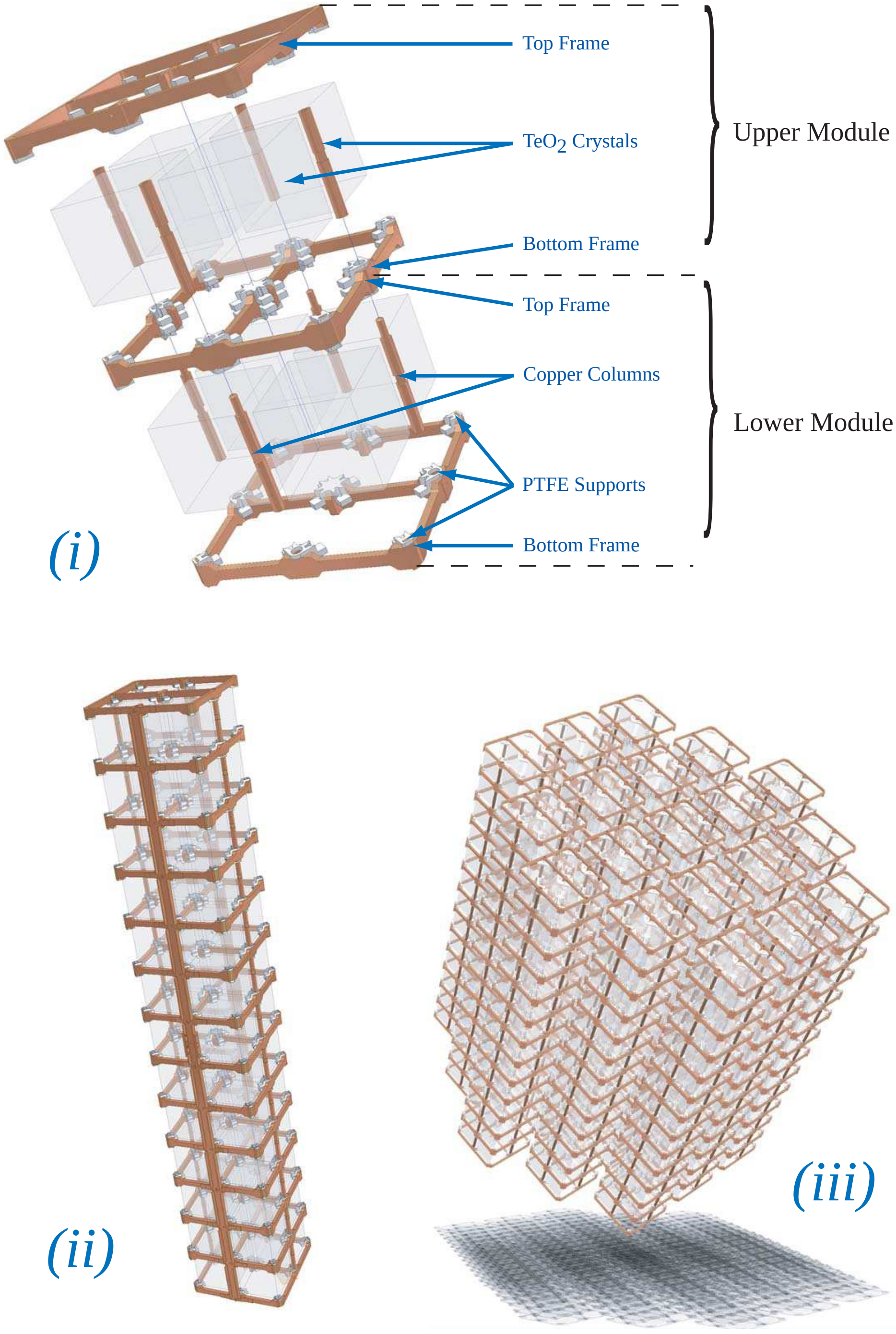

Figure 4.9: The CUORE modular structure. *(i)* two contiguous *Single Modules*. Each frame is shared between two consecutive single modules. The copper columns join the two frames to fasten rigidly the crystals. *(ii)* The super module tower, 13 single modules are held together. *(iii)* the CUORE entire detector (cylindrical-shaped) built of 19 super modules.

any variation of the Main Bath level produces small changes on the mixture flow and, therefore, on the refrigerator cooling power. These changes are harmful for the stability of the bolometers output and could spoil the offline *stabilization procedure* used to adjust the baseline drift due to the temperature variations. These problems could be even more serious in the CUORE cryogenics system, due to the much larger boil-off of the cryostat

An alternative solution to keep the 4 K temperature constant for the whole duration of the measurement is based on a commercial devices called *Pulse Tube Cryocooler* (PTC or PT and also *Pulse Tube Refrigerator*, PTR, for more details se appendix A.2). This type of cryocoolers are specially developed for applications where the object to be cooled is extremely sensitive to vibrations. The absence of moving parts in the pulse tube cold head diminishes the influence of most of the disturbances at the cooler-detector interface. The combination of one or more PTRs with a ^{3}He/^{4}He dilution unit allows to reach temperature below 10 mK.

The CUORE refrigerator (figure 4.10) will use an appropriate number of Pulse Tubes. From a preliminary analysis it is expected that the cooling power of 3+2 *Pulse Tubes PT415* from Cryomech®should be enough (two for redundancy). The aim is to remove the Main Bath boil-off getting rid of the cryogenic fluids.

4.5.1 Shielding requirements

As usual for rare events experiments, the structure of the detector and the cryogenics system must be realized using low radioactive contamination materials. The design of the effective shields, specially those directly surrounding the detector, is a very crucial point to reach the sensitivity goal of CUORE.

As for CUORICINO, the dilution refrigerator will be constructed with materials specially selected for low levels of radioactivity. Nevertheless, these levels might be higher than can be tolerated by the sensitivity requirements. For these reasons a lead shielding system is needed. Part of the bulk lead shielding will be placed inside of the cryostat (*inner shield*), and part outside (*outer shield*). The main parts are the following (figure 4.11):

1) A lead shield inside the cryostat will cancel the contributions to the background level due to the construction materials of the external part. It consists of a lateral and bottom a layer, 6 cm, thick made of ultra-low background lead that constitute a wall surrounding the bottom and the sides of the detector array. This layer, probably, will be composed by two sub-layer: the inner sub-layer will be Roman lead whose ^{210}Pb activity was measured to be less than 4 mBq/Kg[194], whereas the outer sub-layer will be modern low activity lead (16 Bq/Kg of ^{210}Pb).

2) The top of the detector array will be protected by a Pb layer of 30 cm thickness, facing the detector support plate. As in the case of the lateral shield, this layer will be composed by two sub-layer: the internal one made by Roman lead whereas

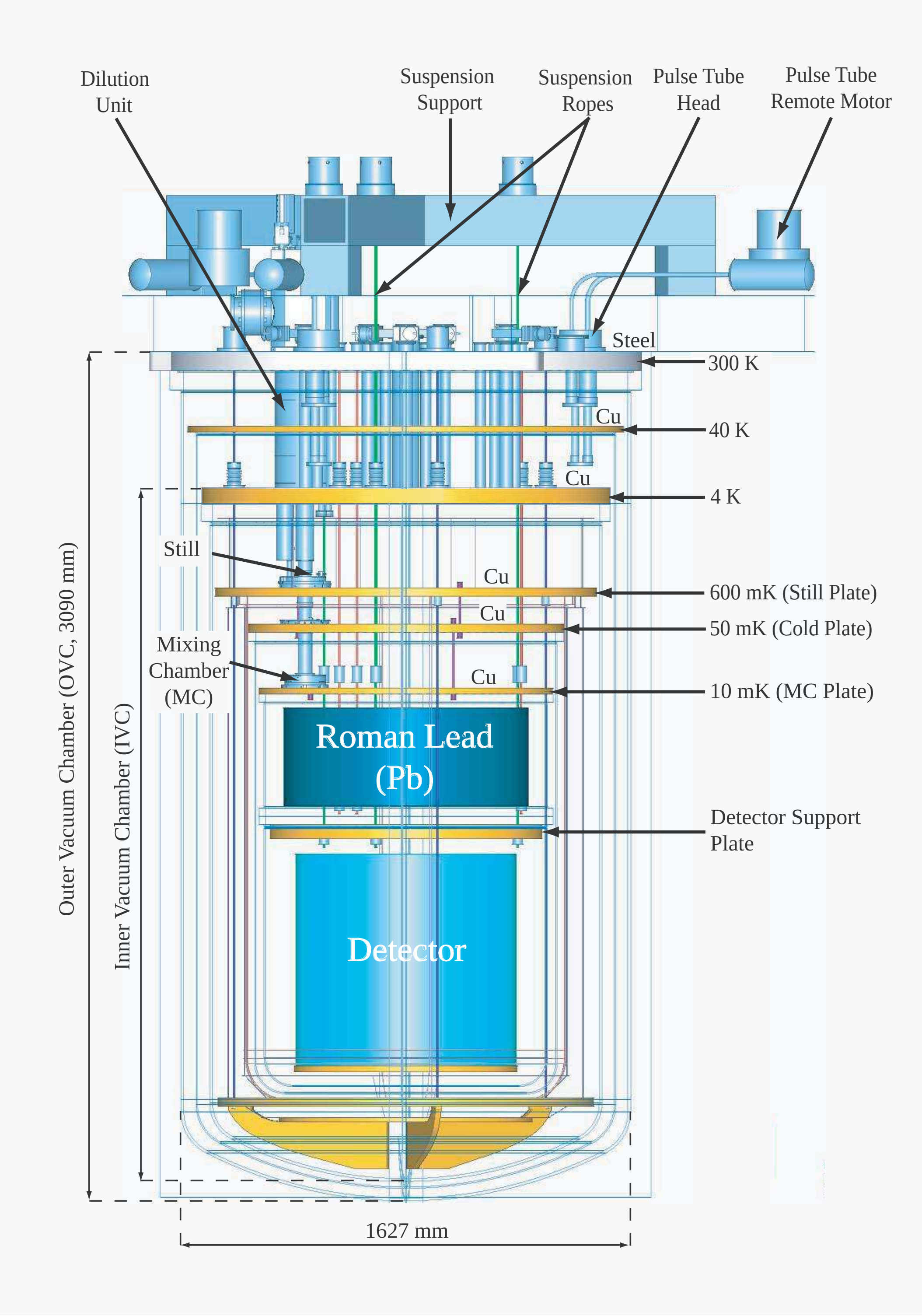

Figure 4.10: CUORE cryostat. The Pulse-Tube-assisted solution is a novel type of mechanical cooling system consisting of a compressor, a rotary valve and a cold head. A PT cooler exhibits extremely low vibration performance not reached by conventional Gifford-McMahon or Stirling coolers.

the more external made by modern lead. This top shield will be placed inside the Mixing Chamber but thermalized with the 50 mK plate (Cold Plate).

3) Another layer of lead, ring shaped 30 cm thick, will be placed inside the IVC directly on the top face of the 600 mK plate (Still Plate). This shield is needed to cover the unprotected space between the lateral shield and the top shield. It will be constructed from low activity lead of 16 Bq/Kg of ^{210}Pb.

4) Finally, outside the dewar, there will be a 25 cm thicknesses of lead with octagonal shape. The lead shield will be surrounded with a 18 cm thick box of polyethylene with a 2 cm thick gap filled with boric acid ($B(OH)_3$). The polyethylene is used to thermalize the fast neutron while the boron atoms capture the thermal neutrons.

The entire dewar, detector, and shields will be hermetically sealed in a radon-box to exclude radon. It will be flushed constantly with dry nitrogen. Moreover the whole system will be enclosed in a Faraday cage to exclude electromagnetic disturbances that also constitute a source of background. The addition of a muon veto surrounding the entire structure will be also considered.

4.6 The Hut

After the approval of CUORE by the Gran Sasso Scientific Committee its final location just near the CRESST installation has been decided (figure 4.1). The entire CUORE setup will be installed inside a proper building which will have to guarantee room for all the setup parts (cryogenics, electronics, shielding), for a controlled area to be used during assembling procedures (clean room) and for all normal monitoring activities (counting room).

The CUORE hut will be divided in three levels.

1) **Ground floor**: On the ground level will be placed the pumps and the compressors for the Pulse-Tube-assisted solution liquefiers. A platform of reinforced concrete, with a central aperture of about 3 m diameter, will also be placed. In this aperture a lifting platform, able to raise at least 80 tons, will be realized with four mechanical jacks, driven by by one electrical motor simultaneously. The radioactivity shielding will be placed on the lifting platform; in this way it will be easy to pull down the shieldings whenever is necessary to open the cryostat.

2) **First floor**: the first level will consist of two separated sections: a clean room, where all the CUORE detector parts will be assembled and stored, and a control room for the cryostat.

3) **Second floor**: also the second level will be separated in two sections. The first one, containing the top of the cryostat, the support structure and the front-end

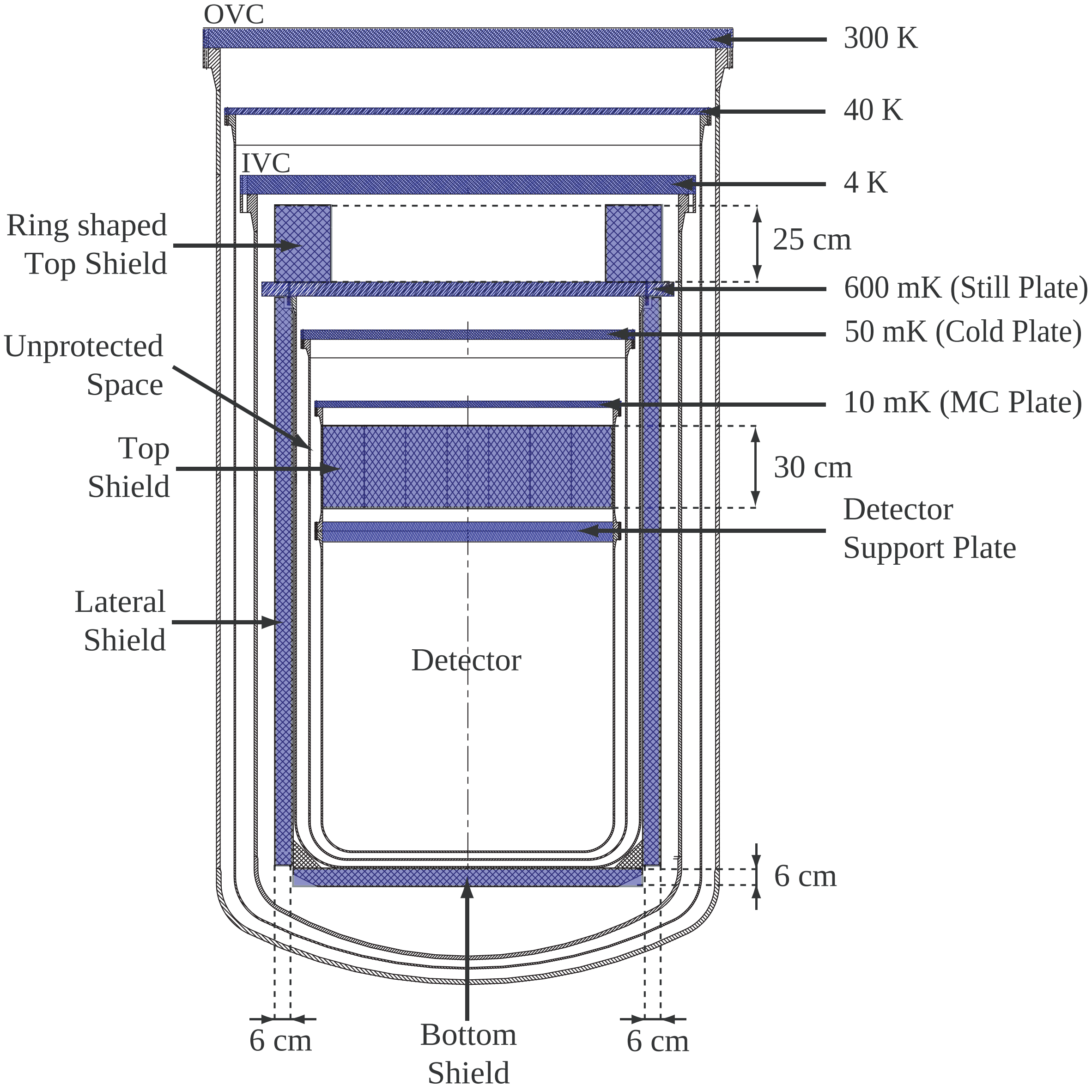

Figure 4.11: Shielding system inside the the cryostat.

electronics crates, will be surrounded by a Faraday cage. The second will be used for the data acquisition system and for the counting room.

4.7 **CUORE** performances

In **CUORICINO** the background in the $0\nu\beta\beta$ region (2530.3 KeV for the ^{130}Te) is improved by a factor 1.5 with respect to the one measured in **MiDBD**. The goal of **CUORE** is to achieve a background rate in the range of $(0.01 \div 0.001)$ counts/KeV/Kg/y with an energy thresholds of 5 KeV and energy resolutions lower than 1 KeV at the 46 KeV line of ^{210}Pb.

4.7.1 Background interpretation

In order to understand the **CUORICINO** background the possible sources are:

1) Bulk an surface contaminations of the construction materials from ^{238}U, ^{232}Th and the ^{40}K, ^{210}Pb isotopes. This is the main contribution expected. Bulk contaminants are present the cryostat structure (cryostat radiation shields), in the heavy structures close to the detectors (the copper mounting structure of the array, the Roman-lead box and the disks on the top of the array) and from the detectors themselves (the TeO_2 crystals). Surface contaminations contribute to the background when they are localized on the crystals or on the copper mounting structure directly facing them. The goal of CUORE is to reduce the surface contribution by a factor at least 20 with respect to this evaluation, obtaining a background coming from surfaces of about $3 \cdot 10^{-3}$ counts/keV/kg/y.

2) Bulk contaminations construction materials due cosmogenics activation. This phenomena is produced by cosmic rays when the crystals are above ground during fabrication and shipping of the crystals from the factory to the underground laboratory. The radionuclei that contribute to background through their β^- decay are the long living ^{60}Co isotope and, with minor contribution, the isotopes ^{110}Ag and ^{124}Sb. On the basis of the present knowledge of the cosmic rays production rates, a possible time schedule for the crystal growth and shipping to Gran Sasso has been studied that can guarantee the required low level of ^{60}Co.

3) Neutron and muon flux (table 4.2) in the Gran Sasso Laboratories. The depth of the **LNGS** (3800 m.w.e) reduces the muon flux down to $2 \cdot 10^{-8}$ cm^{-2}s^{-1}. The environmental neutron flux is due to muons interacting in the rocks and in the **CUORE** external lead shield. These contributions are negligible if compared with the background level due to the radioactive contaminations in the detector's materials.

4) Gamma ray flux (table 4.2) from natural radioactivity in the Gran Sasso Laboratories. A preliminary evaluation of the influence of the environmental γ resulted in a negligible contribution for the $0\nu\beta\beta$ region.

The expected threshold and resolution (5 KeV and lower than 1 KeV severally) were obtained in some test measurements carried out at LNGS *Hall C facility* according with the CUORE R&D program[195, 196]. More details about the CUORICINO background interpretation and about the CUORE background reducing program will be given in the following dedicated chapters.

A more complete and detailed study of the background rates from external sources for CUORE is underway and will be used for the optimization of shieldings and a possible muon veto.

4.7.2 Double beta decay prospects

The main scientific goal of the CUORE detector is the search for the neutrinoless double-beta decay of the ^{130}Te isotope contained in the (natural) TeO_2 crystals. As said in the previous chapters a $0\nu\beta\beta$-decay experiment is characterized by its sensitivity defined as follow:

$$S^{0\nu\beta\beta} = \ln 2 \cdot \epsilon \cdot \frac{\text{i.a.}}{A}\sqrt{\frac{M \cdot t}{B \cdot \Gamma}} \tag{4.7}$$

In the case of a $5 \times 5 \times 5$ cm^3 TeO_2 bolometers with detector efficiency $\epsilon = 0.86$ one has

$$S^{0\nu\beta\beta} = 7.59 \cdot 10^{23}\sqrt{\frac{M \cdot t}{B \cdot \Gamma}} \tag{4.8}$$

where M is the crystal mass in Kg, B is the background in counts per KeV per year and per Kg of detector mass, and t is the live-time. Assuming a background of $B = 0.01$ counts/keV/kg/y and two different energy resolution one obtains:

$$\begin{cases} \Gamma(2.5 \text{ MeV}) = 5 \text{ KeV} & \Rightarrow \quad 9.4 \cdot 10^{25}\sqrt{t} \text{ years} \\ \Gamma(2.5 \text{ MeV}) = 10 \text{ KeV} & \Rightarrow \quad 6.5 \cdot 10^{25}\sqrt{t} \text{ years} \end{cases} \tag{4.9}$$

Considering the better resolution, t years of statistics would provide an effective neutrino mass in the range:

$$|\langle m_\nu \rangle| = (0.036 \div 0.2) \cdot t^{-\frac{1}{4}} \text{ eV} \tag{4.10}$$

according to QRPA model. If successful, the CUORE R&D program could provide a value of $B = 0.001$ c/keV/kg/y and, thus, a detection sensitivity of:

$$\begin{cases} \Gamma(2.5\ \mathrm{MeV}) = 5\ \mathrm{KeV} & \Rightarrow \quad 2.96 \cdot 10^{26}\sqrt{t}\ \text{years} \\ \\ \Gamma(2.5\ \mathrm{MeV}) = 10\ \mathrm{KeV} & \Rightarrow \quad 2.1 \cdot 10^{26}\sqrt{t}\ \text{years} \end{cases} \tag{4.11}$$

and

$$|\langle m_\nu \rangle| = (0.02 \div 0.11) \cdot t^{-\frac{1}{4}}\ \mathrm{eV} \tag{4.12}$$

For an exposure of 5 years, the corresponding $|\langle m_\nu \rangle|$ bounds would range from 8 meV to 45 meV depending on the nuclear matrix element calculations.

Chapter 5

The pilot experiment: CUORICINO

In this chapter it will be discussed the CUORICINO experiment. In particular it will be illustrated the detector behavior, the most recent results and the background interpretation. These information, together with the detector modelling described in the previous chapters, are the starting point of my Ph.D works, as it will illustrated in the next chapters.

5.1 Introduction

The CUORICINO array was built during the second half of the year 2002 and is running at the LNGS since 2003. This experiment represents the first step of the bolometric technique toward a large scale experiment and it has been a unique test bench for the next experiment CUORE. Its good results and performances have demonstrated the feasibility of a large bolometric array of $Te0_2$ crystals in a tower-like structure.

CUORICINO crystals are arranged in a CUORE-like tower made by 13 plane[166, 167]. The single module is similar to the CUORE one (section 4.4.1) but not identical. In this old configuration two contiguous single modules don't share the same frames seeing that they have their own top and bottom frame. Comparing this solution with the one designed for CUORE results that the copper amount is almost the double

The tower structure is as follows: each of the upper 10 planes and the lowest one consists of four TeO_2 crystals of natural isotopic abundance of $5 \times 5 \times 5$ cm^3, while the 11th and 12th planes have nine, $3 \times 3 \times 6$ cm^3 crystals. In the $3 \times 3 \times 6$cm^3 planes the central crystal is fully surrounded by the nearest neighbors. The smaller crystals are of natural isotopic abundance except for four. Two of them are enriched to 82.3% in ^{128}Te and two are enriched to 75% in ^{130}Te. All crystals were grown with pre-tested low radioactivity material by the Shanghai Institute of Ceramics (SICCAS) and shipped to Italy by sea to minimize the activation by cosmic ray interactions. They were lapped with specially selected low contamination polishing compound. All these operations, as well as the mounting of the tower, were carried out in a nitrogen atmosphere glove box in a clean room. The mechanical structure is made of OFHC Copper and Teflon®, and both were previously tested to be sure that measurable radioactive contaminations were minimal and consistent with the required detector sensitivity.

The array was cooled down to approximately 8 mK, with a temperature spread of $\simeq 1$ mK among the different detectors, by a *conventional* ^{3}He/^{4}He *Dilution Refrigerator* (appendix A.1) having powers of 1000 μW at 100 mK (Oxford®1000[193]). The tower is mechanically decoupled from the cryostat, to avoid heating due to vibrations, by means if a a steel spring fixed to the 50 mK plate of the refrigerator. The temperature stabilization of the tower is made by means of a thermistor and a heater glued on it. An electronic channel is used for a feedback system[197].

The entire set-up is shielded with two layers of lead of 10 cm minimum thickness each. The outer one is made of common low radioactivity lead, the inner layer of special lead with a measured content of (16 ± 4) Bq/kg in ^{210}Pb. The electrolytic copper of the refrigerator thermal shields provides an additional shield with a minimum thickness of 2 cm. An external 10 cm layer of borated polyethylene was installed to reduce the background due to environmental neutrons.

The detector is shielded against the intrinsic radioactive contamination of the dilution unit materials by an internal layer of 10 cm of Roman lead (^{210}Pb activity < 4 Bq/kg[194]), located inside the cryostat immediately above the tower of the array. The background from the activity in the lateral thermal shields of the dilution refrigerator is reduced by a lateral internal shield of Roman lead that is 1.2 cm thick. The refrigerator is surrounded by a Plexiglas® anti-radon box flushed with clean N_2 from a liquid nitrogen evaporator, and is also enclosed in a Faraday cage to eliminate electromagnetic interference.

A routine calibration is performed using two wires of thoriated tungsten inserted inside the external lead shield in immediate contact with the outer vacuum chamber (OVC) of the dilution refrigerator. This calibration, normally lasting one to two days, is performed at the beginning and end of each run, which lasts for approximately two/three weeks. The more intense gamma-ray peaks visible in the calibration spectra are used to make the spectra linear. The γ-ray lines used are those at: 511, 583, 911, 968, 1588, and 2615 KeV, and the single escape peak of the 2615 KeV gamma ray at 2104 KeV. The resulting amplitude versus energy relationship is fitted to the calibration data, and all pulse amplitudes are converted into energies. These calibration data are also used to determine the energy resolution of each bolometer.

5.2 Neutrinoless double beta decay results

CUORICINO measurements began since 2003. Excluding two long interruption and several short stops required for the refrigerator maintenance, the duty cycle of the experiment proved to be satisfactory although a not negligible large fraction of the live time is spent in calibration ($\simeq 10\%$). The data-taking is divided in two runs: run #1 and run #2 (table 5.1).

	$5\times5\times5$ cm^3	$3\times3\times6$ cm^3	$3\times3\times6$ cm^3 enriched
Statistics run #1 [kg(^{130}Te)· y]	3.41	0.34	0.05
Statistics run #2 [kg(^{130}Te)· y]	33.43	4.06	0.74
FWHM run #1 [keV]	9.2	14	24
FWHM run #2 [keV]	6.3	10	20
Background run #1 [c/keV/kg/y]	0.18±0.04	0.22±0.13	0.52±0.52
Background run #2 [c/keV/kg/y]	0.18±0.01	0.18±0.03	0.37±0.11
^{130}Te i.a.	33.8%	33.8%	75%
$0\nu\beta\beta$ efficiency	86.3%	84.5%	84.5%

Table 5.1: Summary information concerning the six spectra used for $0\nu\beta\beta$ study. In the upper part of the table the exposure, the FWHM (as fitted with a symmetric gaussian plus a linear background) and the $0\nu\beta\beta$ background counting rate ($2510-2550$ keV window) corresponding to the three kind of detectors is reported. In the lower part of the table the isotopic abundance of ^{130}Te in the crystals (i.a.) and the $0\nu\beta\beta$ efficiency (geometric efficiency computed through a GEANT4 MonteCarlo simulation).

The average FWHM resolutions measured for the complete data set are[164]:

$$\Delta E_{\mathrm{FWHM}} = \begin{cases} 8\ \mathrm{KeV} & \text{for the } 5\times5\times5\ \mathrm{cm}^3 \text{ crystals} \\ \\ 12\ \mathrm{Kev} & \text{for the } 3\times3\times6\ \mathrm{cm}^3 \text{ crystals} \end{cases} \tag{5.1}$$

Both these values are measured on the ^{208}Tl gamma line at 2615 KeV.

No deterioration of the FWHM is observed when summing long measurements and all the detectors together. The statistics collected up to May 2006 for the $0\nu\beta\beta$ measurement corresponds to 8.38 Kg(^{130}Te)y and it is fully analyzed. Other about 3 Kg(^{130}Te)y collected during 2006 will be added soon to the total statistic. The $0\nu\beta\beta$ of ^{130}Te peak should appear as a gaussian line at about 2530 KeV in the anti-coincidence spectrum. No evidence indicating the neutrinoless double-beta decay is found in the analyzed data. The best fit yields a negative result (figure 5.1) for the maximum number of candidate $0\nu\beta\beta$ events (-13.9 ± 8.7 counts). By applying a *maximum likelihood procedure*[198, 199] we obtain a 90% lower limit for the lifetime set to[1][164]:

$$T^{0\nu}_{1/2} \geq \left(3.0\cdot10^{24}\right)\ \mathrm{y}\ \Rightarrow\ |\langle m_\nu\rangle| = (0.19 \div 0.60)\ \mathrm{eV} \tag{5.2}$$

The value of the effective neutrino mass depends on the nuclear model used (see table 5.2).

5.3 Background analysis

This is one of the most important topic in view of CUORE. In fact the main R&D activity of the collaboration is the background reduction program, that is also main

---

[1] the last published value is $T^{0\nu}_{1/2} \geq (1.8\cdot10^{24})$ y $\Rightarrow$ $|\langle m_\nu\rangle| = (0.2 \div 1.1)$ eV [167]

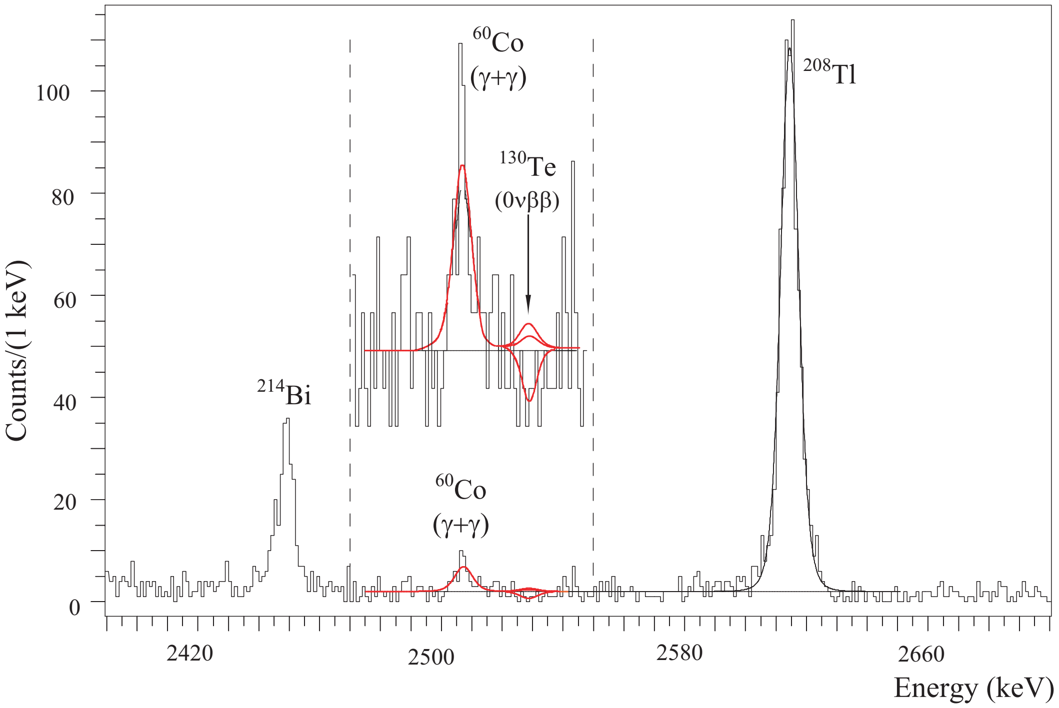

Figure 5.1: Spectrum of the sum of the two electron energies in the region of neutrinoless double beta decay. One can clearly see the peaks at 2447 and 2615 KeV from the decays of ^{214}Bi and ^{208}Tl, plus a small peak at 2505 KeV due to the sum of the two lines of ^{60}Co. The background counting rates in the double-beta decay region are (0.18 ± 0.01) and (0.20 ± 0.04) counts/kg/keV/year, for the $5 \times 5 \times 5$ cm^3 and $3 \times 3 \times 6$ cm^3 respectively.

.

part of this Ph.D work. The motivation and strategies of this activity will be described in the next two chapters.

In figures 5.3 and 5.4 it is shown the background measured by $5 \times 5 \times 5$ cm^3 crystals in CUORICINO[165, 169]. Each figure contains two histogram: the former is the spectrum of events collected operating the CUORICINO array in anti-coincidence (therefore selecting events where just one crystal is hit within the time coincidence window of about 50 ms), whereas the latter spectrum is obtained operating the array in coincidence (selecting events where two and only two crystals are contemporary hit.) In both cases the energy spectra collected by each single (independent) detector of the array are summed together to produce the *sum energy spectra* plotted in the two figures.

The capability of operating the detectors in anti-coincidence in CUORICINO is not much relevant (see figure 5.5) but in the tight-packed structure of CUORE it will play a fundamental role in background reduction. However the differences between coincidence and anti coincidence spectra important informations concerning the background origin and location are obtained as it will be clear in the next section.

As shown in figure 5.3 the 2615 KeV ^{208}Tl line splits the CUORICINO measured background in two regions: the left side of the line and its right side.

Reference	Authors	Method	$\langle m_\nu \rangle$ [eV]
[72, 73]	Rodin *et al.*, 2007	using $2\nu\beta\beta - decay$ to fix g_{pp}	0.46
[85]	Staudt *et al.*, 1992	pairing (Bohn)	0.19
[86]	Pantis *et al.*, 1996	no p-n pairing	0.52
[87]	Vogel *et al.*, 1986		0.47
[88]	Civitarese *et al.*, 1987		0.42
[89]	Tomoda, 1991		0.42
[90]	Barbero *et al.*, 1999		0.33
[91]	Šimkovic *et al.* 1999	pn-RQRPA	0.68
[70]	Suhonen *et al.*, 1992		0.64
[92]	Muto *et al.*, 1989		0.39
[93]	Stoica *et al.*, 2001		0.60
[71]	Faessler *et al.*, 1998		0.55
[68]	Engel *et al.*, 1989	seniority	0.29
[94]	Aunola *et al.*, 1998	Woods-Saxon	0.41
[69]	Caurier *et al.*, 2007	Nuclear Shell Model	0.58

Table 5.2: Updated values of $\langle m_\nu \rangle$ corresponding to $T^{0\nu}_{1/2}(^{130}\text{Te}) = 3.0 \cdot 10^{24}$ y[164].

1) **Left side: bulk contribution and the 3 - 4 continuum**
The ^{208}Tl line is the highest natural γ line due to environmental contamination and appears as one possible contribution (through Compton events) to the $0\nu\beta\beta$ background. The other two peaks are the 2448 KeV, due to ^{214}Bi, and the 2505 KeV sum line due to the interaction, in the same crystal, of the two γ's contemporary emitted by ^{60}Co in its beta decay. Both peaks have an energy definitely too low to give any contribution to the background in the investigated regions.

2) **Right side: the flat continuum between 3 and 4 MeV**
The background measured on the right side of the ^{208}Tl line is ascribed mainly to the degraded alphas coming from ^{238}U and ^{232}Th radioactive chains and due to surface contamination of the crystals or of the inert material facing them. This continuum clearly extends below the ^{208}Tl line thus participating to the neutrinoless-$\beta\beta$ background counting rate (figures 5.2 and 5.3).

The ^{208}Tl line depends from contaminations relatively far from detector, as proved by the reduced intensity of the low energy gamma lines coming from the ^{232}Th chain. A possible guess for these sources are, probably, some thermal shields or the superinsulation.

While the heavy shielding foreseen for CUORE will guarantee a deep reduction of the γ background (^{208}Tl contribution), for the α background (that comes only from the very

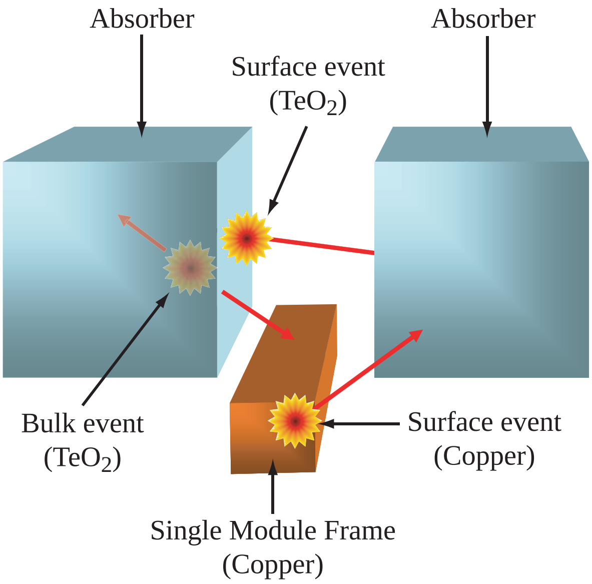

Figure 5.2: Sketch of events due to surface contamination of the crystals or of the inert material facing them (copper).

inner part of the detector) only a severe control of bulk and surface contaminations can guarantee the fulfillment of the sensitivity requirements. In order to do that a correct identification and localization of the sources of the continuous α background is mandatory.

5.4 Background interpretation

The Alpha peaks position and their shape, in the bolometers spectra, give strong indication on the location of the contamination:

1) **sharp gaussian** peaks: if the energy corresponds to the transition energy of the decay ($\alpha + recoil$) they indicate contamination in the crystal bulk whereas if the energy corresponds to the alpha energy indicate contamination in an extremely thin surface layer (at crystals surface or on the inert material surface facing the crystal

2) **asymmetric long-tailed** peaks: they are due to thick contamination in the crystal surfaces.

3) **flat continuum**: a bulk or a deep surface contamination of an inert material facing the detector should produce just a continuum without any α peak.

When the background is dominated by α particles a coincidence between two crystals is produced only if the α emitter is on the surface of one crystal and the α, or the recoiling nucleus, exits from one crystal and enters into one other. In this case the analysis of the coincidence events in the array and the study of gamma peaks are very useful to understand the background origin.

In CUORICINO (figure 5.3) most of the peaks appearing in the region above 4 MeV are ascribed to ^{238}U and ^{232}Th surface contamination of the crystals. Indeed these peaks are visible in both coincidence and anti-coincidence spectra, moreover they have a large low energy tail that once more is (as discussed) a prove that the contamination is at the crystal surface. Four peaks do not belong to this category:

- the α peak centered at 3200 KeV. It is ascribed to an internal contamination of the TeO_2 crystals in the long living isotope ^{190}Pt: indeed the shape of the peak is gaussian (no low energy tail) and no peak appears in the coincidence spectrum, the energy of the peak is compatible with the transition energy of ^{190}Pt. The contamination is probably due to inclusions of fragments of the Pt crucible used in TeO_2 crystal growth.
- the α peak centered at 4080 KeV. It grows on the low energy tail of a surface contamination peak but it is attributed to a bulk contamination in ^{232}Th;
- the α peak centered at 5304 KeV. It is centered at the α (and not α+recoil) emitted by ^{210}Po. The peak is stable in time and is therefore attributed to a ^{210}Pb contamination[2]. The position of the peak indicates that the contamination has to be on a very thin layer (much thinner than the ^{238}U crystal surface contamination described above) either on the crystal surface or on the mounting surface. From the coincidence spectra and scatter plots it is then possible to conclude that at least part (probably not all) of the peak has to be due to a contamination of the crystal surface. If this is the case also part of the 5.4 MeV peak has to be attributed to a such contamination.
- the α+recoil peak centered at 5404 KeV. It has an intensity clearly decreasing with time in agreement with ^{210}Po half-life. The ^{210}Po contamination, usually observed in recently grown TeO_2 crystals, is ascribed to a bulk contamination (no coincidences are observed). Part of the peak is however attributed to the ^{238}U and ^{210}Pb surface contamination discussed above. When CUORICINO was started the 5.4 MeV peak was by far dominated by the bulk contamination ^{210}Pb peak (with an intensity as high as 0.2 count/h/crystal), now the peak has a much reduced intensity (0.03 count/h/crystal) where the ^{210}Pb contamination seems to dominate.

The small amount of coincidences in the 3-4 MeV range as well as the extrapolation (based on Monte Carlo simulations) of the counts attributable to crystal surface contaminations, indicate that a large fraction of the flat continuum between 3 and 4 MeV

---

[2] ^{210}Pb has a half-life of 22 years while that of ^{210}Po is 138 days

has its source outside the crystals. Degraded α could come either form surface or bulk contamination of the mounting components, however the reduced rate of low (hundred KeV) energy gamma peaks allow to exclude that this continuum could be due to U and Th bulk contaminations of copper mounting. Excluding important contribution from the bulk contamination of the small parts of the detector (thermistors, heaters, bonding wires, PTFE parts and so on) on the basis of the radioactive measurements made before the construction of CUORICINO and excluding neutrons on the basis of both Monte Carlo simulation and experimental results (MiDBD experiment didn't see any change in the $0\nu\beta\beta$ background rate when the borated polyethylene shield was mounted) we have concluded that most of the background measured by CUORICINO should come from crystal and copper surfaces.

5.5 Motivation for further R&D activity

The solution of this puzzle is one of the main activity of the CUORE collaboration, in fact only the background reduction can improve the sensitivity to reach the desired level. This is the goal of the CUORE-*background reduction program*; an R&D activity located at the LNGS Hall C facility. This program consists in the development of methods to control and reduce the radioactive background in the $0\nu\beta\beta$ region. As I will illustrate in the next chapter the research line of this program is the main activity of my Ph.D work.

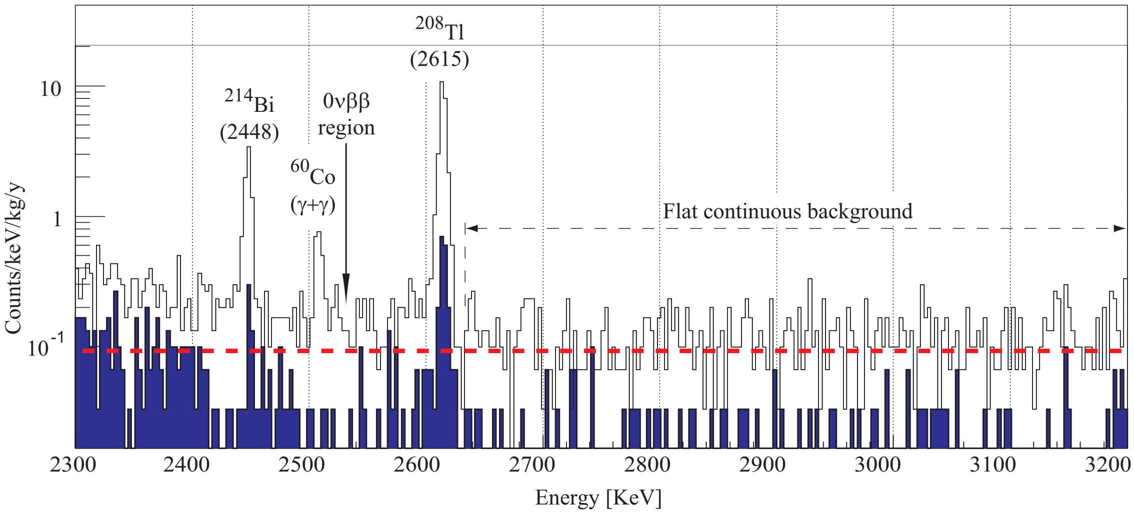

Figure 5.3: CUORICINO background in the $0\nu\beta\beta$ region[165]. the black line refers to the anti-coincidence events spectrum (only one detector hit) the blue filled histogram refers to coincidence events (two detectors contemporary hit). The $0\nu\beta\beta$ decay should appear as a gaussian peak in the anticoincidence spectrum at 2530 KeV (without any corresponding line in the coincidence spectrum). Above the 2615 KeV line a flat continuous background, attributed to degraded alpha particles, is visible. The 2448 KeV ^{214}Bi, the 2505 KeV ^{60}Co and the 2615 KeV ^{208}Tl line are clearly visible.

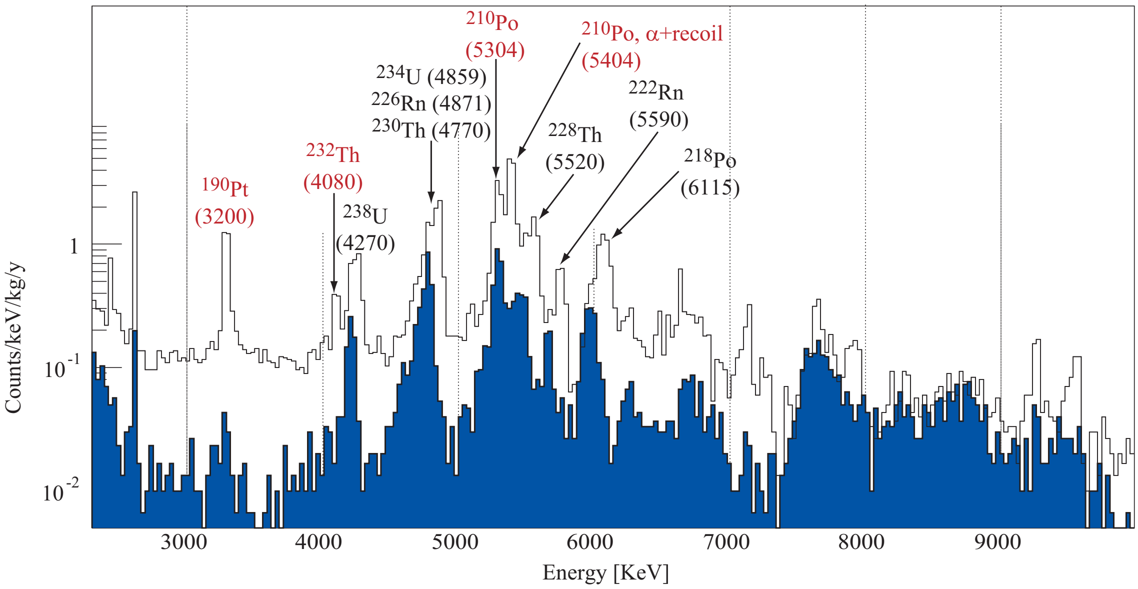

Figure 5.4: CUORICINO background above 2.3 MeV[165]. The black line refers to the anticoincidence events spectrum, the blue filled histogram refers to coincidence events. Most of the peaks appearing in the region above 4 MeV are ascribed to ^{238}U and ^{232}Th surface contamination of the crystals. In the anticoincidence spectrum the peaks have their high energy side centered at the transition energy of the decay (α+recoil completely contained in the crystal) and have a long, low energy tail (either or recoil exit from the crystal depositing part of its energy outside).

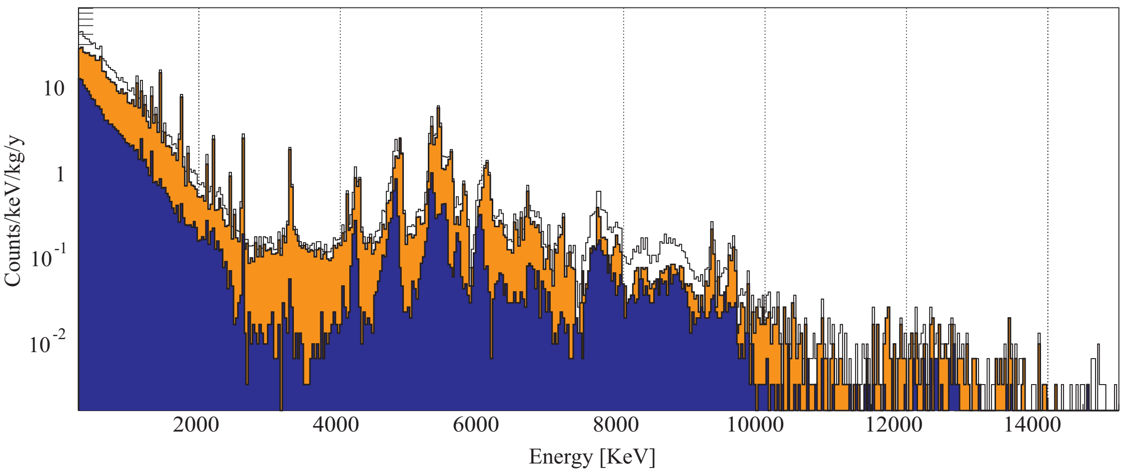

Figure 5.5: CUORICINO background[165]. Black line: total spectrum (all the events are counted), orange filled: anticoincidence spectrum (one detector contemporary hit), blue filled histogram refers to coincidence events (two detectors hit per event). While in CUORICINO the fraction of coincidence events is relatively small in CUORE the large mass and the high granularity of the array will allow to have a relevant reduction of the counting rate by applying an anticoincidence cut

Chapter 6

CUORE background reducing program

6.1 Introduction

My Ph.D activity was dedicated to the development of solution to reduce the background in the double beta decay region of the 130-tellurium (between the line of the ^{208}Tl and its Compton edge). This is one of the main research activity in view of CUORE, in fact, once fixed the mass of the detector, the only tunable parameter available to increase the neutrinoless sensitivity (eq. 2.23) is the background B.

The main background sources can be labeled in two categories:

1) **Internal Background Sources** (IBS): radioactive contaminations that are inside the lead shield and cannot be suppressed using any kind of further shielding, being very near the detector or on the detector itself.

2) **External Background Sources** (EBS): radioactivity due to sources external to the detector. The EBS reduction development is focused on the shielding against external radiation (lead for gammas, polyethylene with boric acid, or borated polyethylene, for neutrons) and on the flagging of very high energy cosmic rays (muon veto).

My activity is concentrated on the study of the internal background. Starting from the experimental evidences, the origin of the background was suggested to be due to degraded alpha particles coming from decays near the surfaces (surface-alpha background). Two different processes are considered: alpha decays on the crystal surface, and alpha particles escaped from the surface of some other component of the detector (copper frames) impinging on the crystal. In the first case the alpha particle releases part of its energy in the absorber and then escapes and releases the remaining energy on a different part of the detector (another crystal, the holder, the external shields and so on). In the second process the alpha particle hits the crystal coming from a different source and having already lost part of its energy in the source material. The lost energy is not fixed values but depends on the depth of the source in the source material.

As pointed out previously the best candidates for the role of source of this background are copper and TeO_2 crystals, because they are by far the most abundant materials inside the detector. The main goal of the activities performed at the Hall C facility is to reduce the surface contamination of the crystals and copper frames and, at the same time, to investigate, if needed, possible further background sources. With this intent, in these three years, two R&D lines were followed: the study of the surface contaminations and the study of the possible *exotic sources* (crystal cracks or relaxation process inside Teflon® supports). In the first R&D line two main solutions were devised in order to reduce possible surface contamination:

1) improvement of the quality of the copper and TeO_2 crystal surface treatment (copper cleaning, crystal surface etching and polishing, radioclean polyethylene film covering);

2) development of bolometers able to identify events originated at the detector surface (SSB, *Surface Sensitive Bolometers*).

The second R&D line was based on the hypothesis that the background sources are not degraded alpha particles but more *exotic effects*. These high energy pulses could arise from mechanical adjustments of the PTFE (already observed in other bolometric detectors at lower energy[200]). Another possibility is that these energy releases are originated from radioactive decays inside the PTFE. To exclude these *exotic possibilities* we have performed two tests using copper-beryllium supports (clamps) instead of the usual PTFE.

In this chapter I will describe the strategies and the experimental solutions adopted in order to achieve the goals of these two research activities.

6.2 The Hall C R&D facility

All the experimental R&D activity described was performed in the Hall C facility. The cryogenic setup (figure 6.1) consists of an Oxford® dilution refrigerator (appendix A.1, [193]) with a power of 200μ W at 100 mK.

Inside the cryostat a special damping system (mechanical filter) reduces the contribution of incoming vibrations to noise[201]. In fact the main sources of TP noise[195] (*thermophononic noise*) are the vibrations of the overall cryogenic set-up, so that the friction between absorber and PFTE supports determines sudden heat release or undesired temperature fluctuations. The large spread of harmonic frequencies which are involved in this phenomenon implies a noise spectrum that has a $1/f$ roll-off, and is therefore particularly annoying for bolometers, which have very low characteristic frequencies. That is why the damping system which mechanically decouple the detectors from the cryogenic set-up is so important.

The dumping system is a double stage harmonic oscillator (figures 6.1, 6.2 and 6.8) that can accommodate different type of detectors.

1) The first stage consists of 14 kg disk made of lead (with a diameter of 17 cm and a height of 5.5 cm) framed inside a copper structure. It is mechanically anchored to the cryostat by means of three 4 cm long stainless steel wires, that are connected to the lead through three harmonic stainless steel strips. These strips can slightly bend, resulting in a longitudinal intrinsic oscillation with the frequency of about 7 Hz. The choice of the lead was imposed also by radioactivity reasons, since a 5.5 cm thickness of ancient roman lead[194], that is free of ^{210}Pb, acts as a good radioactive shield against the entire dilution unit components.

2) The second damping stage is realized by hanging the detector box to the above mentioned Cu frame of the lead, through a stainless steel spring and a copper bar. The longitudinal intrinsic oscillation frequency of this second stage is about 3 Hz. The thermal link between the detectors and the cryostat is ensured by two Cu (99.999%) thin strips of 50 μm thickness (*thermalization strips*) linking the Mixing Chamber to the copper structure of the first stage, and by a second pair of strips linking the first stage to the detector box.

Two different detectors have been realized for test purposes: the RAD detector (*Radioactivity Array Detector*, figure 6.2) and the CAW detector (*CUORE Assembling Working group tower*, figure 6.8). The former was specially built for background studies, the latter for technical studies regarding the crystal mounting system for CUORE. Both these detectors have been employed in these years to check background achievements and further investigate background sources.

6.3 The RAD detector

The *Radioactivity Array Detector* (or RAD, figure 6.2) was built at the LNGS at the end of summer 2004 using ultrapure materials. The RAD consists in a 2-plane array made of eight $5 \times 5 \times 5$ cm^3 TeO$_2$ crystals, with a structure almost identical to that of CUORICINO (two CUORICINO-single module). Often half of the crystals is provided with a second thermistor for redundancy. The temperature of the detector's copper holder is stabilized via a heater and a feedback circuit[197].

A nice feature of the RAD is that it can be mounted inside the Hall C cryostat, as a standalone system, together with other detectors housed in an independent mounting structure. In this way it is possible to exploit the Hall C facility simultaneously for different CUORE measurements (for example the *Scintillating Bolometers* R&D activity).

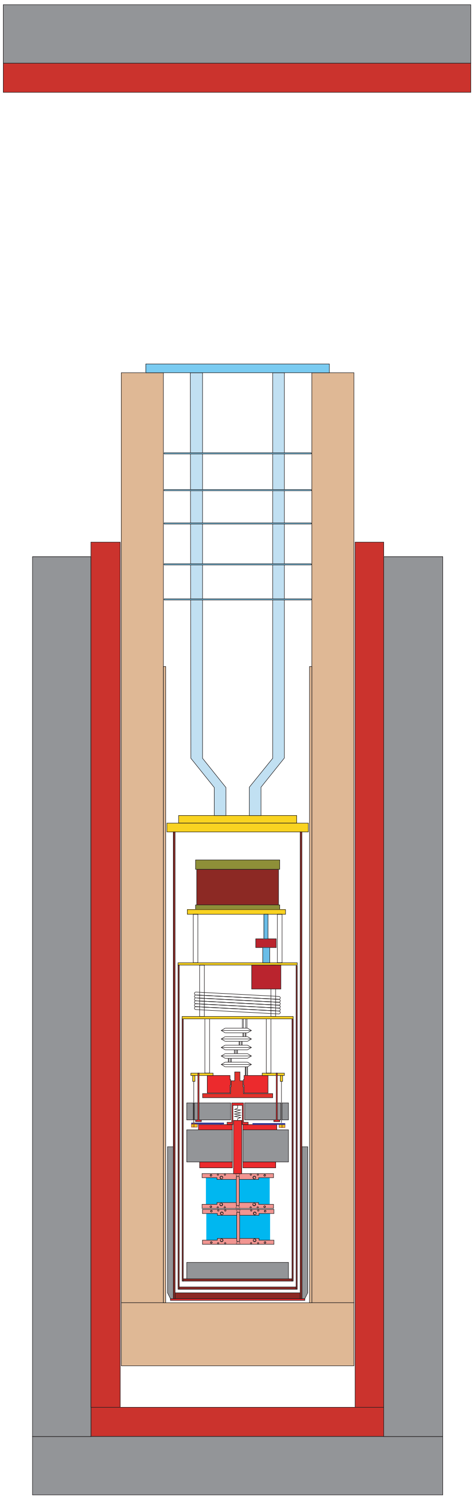

Figure 6.1: The Hall C cryostat.

The observed shape of the background and the rate of coincidence events of the CUORICINO detector indicate the presence of events coming from the crystal surface. The number of these events is not compatible with the measured bulk contamination coming from the ^{238}U and ^{232}Th radioactive chains. This means that if the contribution of degraded alpha particles is the dominant one, there is an excess of contaminants near the surface of the crystals. This is reasonable since the crystals were cut and polished and lapped after being grown. Similar considerations can be done for copper bulk and surface contaminations. For these reasons the collaboration developed a procedure of surface cleaning. As it will be illustrated in the next sections, this procedure was used to built the RAD detectors.

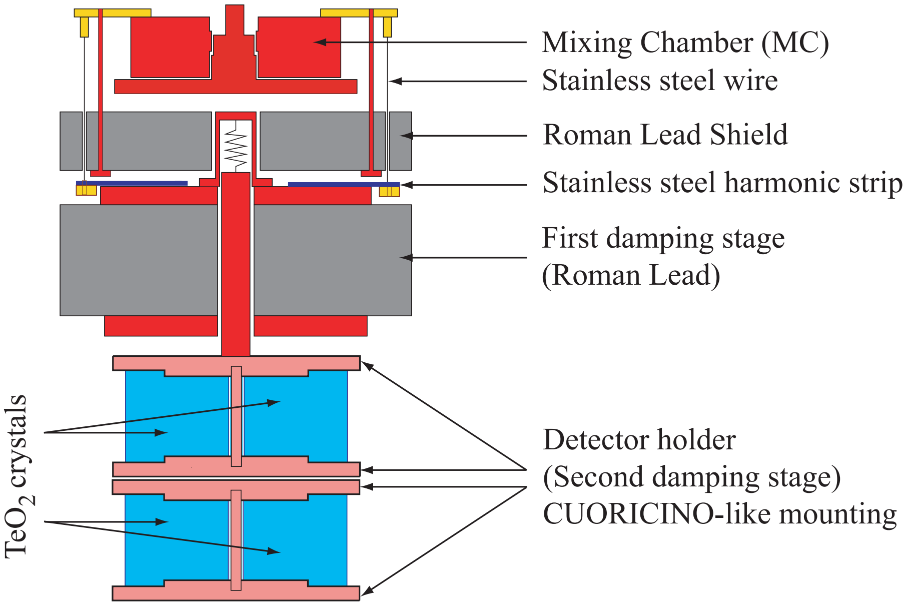

Figure 6.2: Sketch of the RAD detector coupled with the damping system.

From the end of summer 2004 to nowadays six tests were performed (from RAD1 to RAD6) with the following purposes:

- RAD1: test the surface cleaning procedure;
- RAD2: measure the background contribution coming from the so-called *small part* of the detector (PTFE supports, the NTD-Ge thermistor, the Si-heater, the gold bonding wires and finally glue and pins);

- RAD3: test on alpha-background suppression adding a complete polyethylene coverage on the copper faced to the crystals;
- RAD4: check the neutron contribution to the background adding a shield installed around the set-up;
- RAD5: measure of the background contribution coming from possible *exotic sources* removing the Teflon® and replacing it with phosphorus-bronze[1] supports. This measurement is also labelled as Clamps1
- RAD6: measure of the background contribution coming from possible *exotic sources* using covered-phosphorus-bronze supports (Clamps2).

6.3.1 The RAD1 run

The preparation of the first run based on the RAD array started in June 2004. The purpose of this run was to try to change completely approach with respect to surface cleaning, trying to use only few radioclean materials minimizing the procedure. To achieve this, two important rules were followed in the construction:

1) only radiopure cleaning materials (acids, lapping powders and so on) have been used.
2) any kind of contact between unclean materials and the detector parts, or cleaning materials, have been avoided.

Each material was selected and measured during the past two years in the Gran Sasso National Laboratory facilities using different techniques : the *High Purity Germanium* (HPGe[2]) detectors and the *Inductively Coupled Plasma Mass Spectrometry* (ICPMS[3]) facility.

The crystal surface cleaning procedure was the following. The first step was to chemically etch the crystals in a ultrapure nitric acid (HNO_3) solution. The chosen molarity was 4 and the time of etching was about 4 hours at room temperature. After the etching crystals were rinsed with water and dried with nitrogen. The mean etched

---

[1] Phosphorus-bronze is an alloy of copper with 3.5 to 10% of tin (96%Cu and 4%Sn) and a significant phosphorus content of up to 1%.

[2] High-Purity Germanium belong to the class of Intrinsic Semiconductor Detectors and find widespread application in γ-ray spectroscopy. HPGe systems are characterized by a truly high energy resolution thanks to the maximum thickness of the depletion region (or active volume). Besides, HPGe show the much greater operational convenience: whereas common Germanium detectors must be continuously maintained at low temperature, HPGe detectors are allowed to warm to room temperature between uses.

[3] Inductively Coupled Plasma Mass Spectrometry is a type of mass spectrometry that is highly sensitive and capable of the determination of a range of metals and several non-metals at concentrations below one part in 10^{12}

surface was $\simeq 9.4$ μm. The second step consisted in lapping all the crystal surface using a rougher lapping pad (a Nylon pad of 10 μm from Buehler®) together with a finer lapping powder (silicon dioxide, SiO_2, particle size from 1.3 to 2 μm). The percentage of SiO_2 chosen was $(40 \div 60)\%$ of water (in weight). Tacking into account the different behavior of the hard and soft faces, in order to remove the same amount of surface an appropriate time was chosen: 20 minutes for the hard faces and 5-20 minutes for the soft ones. The mean lapped surface was $\simeq 11$ μm.

The copper cleaning was divided into three steps:

1) **Rough cleaning**
   This step is developed to remove the dirty left on the copper surface during the machining (finger prints, machining lubricant and so on). The best way to remove external materials is to wash the copper in ultrasonic bath with some soap. The procedure was carried out by:

   (a) washing the copper in ultrasonic bath with ultrapure water (18 MΩ/cm) and 5% of micro 90 basic soap at the temperature of 40°C for 1 hour;

   (b) rinsing with ultrapure water;

   (c) washing in ultrasonic bath with ultrapure water and 5% of Elma 60 acid soap at the temperature of about 40°C for half an hour;

   (d) rinsing with ultrapure water;

   (e) passivation with a solution of 10% citric ($C_6H_80_7$) acid at 60°C for 1 hour. This is essential to prevent the copper oxidation. During that process, in fact, other kind of air contamination could be trapped on the surface;

   (f) drying with alcohol and clean room papers.

2) **Etching**
   In order to eliminate any contamination potentially implanted during the machining, a layer of copper has been removed from the surface. This second step was carried out by:

   (a) Etching in a solution of 0.5 molar super-pure nitric acid in ultrasonic bath at 40°C for half an hour;

   (b) Rinsing with ultrapure water;

   (c) Passivation with a solution of 10% citric acid at 60°C for 1 hour;

   (d) Rinsing with ultrapure water;

   (e) Drying with nitrogen.

   The mean etched surface of copper after this treatment was $\simeq 5$ μm.

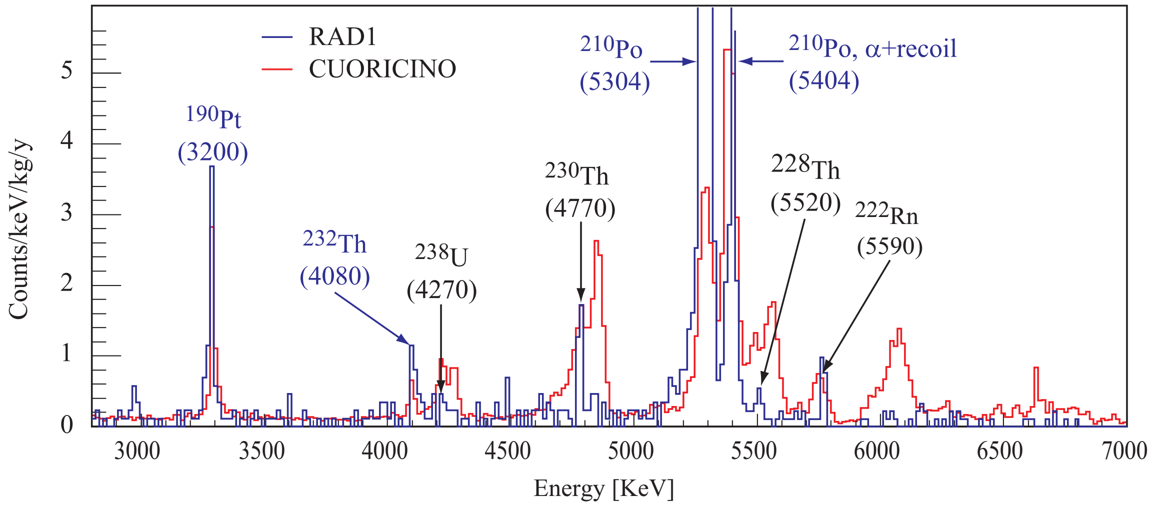

Figure 6.3: CUORICINO background (red line) compared with RAD1 (blue line): the disappearance of crystal surface contamination peaks (visible in CUORICINO spectra as large asymmetric peaks) is evident. The only peak that remain in RAD1 are the doublet of ^{210}Po and the gaussian sharp peaks ascribed to a bulk contamination of the crystals in long living ^{232}Th isotopes (to a level of about 10^{-13} g/g).

3) **Electroerosion**
At the end, the copper electroerosion completes the removal of material from the surface and, at the same time, applies the final passivation to the frames. The advantage of this technique is that, using the appropriate electrolyte, this method is very simple and can be completely controlled. After the electroerosion each piece was rinsed with ultrapure water an passivated again in a citric acid solution with O_2 bubbling. Then the pieces were rinsed again with water, dried only with nitrogen and enclosed in plastic bags filled with nitrogen.

Once the preparation was completed, the detectors was cooled down inside the Hall C experimental facility in late August of 2004. The data are divided into four runs that differ one from another by minor changes in the stabilization system. An external 10 cm lead shield was added between Run I and Run II. Each run consists in a set of data with a calibration to linearize the spectrum. The total measurement time (background data taking) was about 1688 hours acquired during 3.5 months.

The result of RAD1 was quite successful from the point of view of crystal cleaning (figure 6.3): the TeO_2 surface contamination in ^{238}U and ^{232}Th was drastically reduced as proved by the disappearance of the ^{238}U and ^{232}Th alpha peaks. The extremely low background reached so far allowed us for the first time to disentangle the bulk vs. surface contamination of the crystals: once the large spread peaks due to surface contamination disappeared the gaussian sharp peaks of the internal contamination of TeO_2 were visible. Apparently the crystals are contaminated in Th isotopes (^{232}Th in secular equilibrium and long living ^{230}Th isotope belonging to the ^{238}U chain) while no evidence of U contamination in secular equilibrium is obtained.

The only other alpha peaks visible in RAD1 are the two 5.3 and 5.4 peaks due to ^{210}Po decay (as discussed usually the contamination is not in ^{210}Po that has a very short lifetime but in its father ^{210}Pb, for more details see section 5.4). When compared to CUORICINO the intensity of these two lines results to be: comparable in the case of the line due to the deposition of the entire transition energy (α+recoil= 5.4 MeV), 3 times higher in the case of the line due to the deposition of the only alpha particle energy (5.3 MeV). Finally, despite the strong reduction of the ^{238}U and ^{232}Th crystal contamination, no improvement is observed in the flat background spanning the 3-4 MeV region.

6.3.2 The RAD2 run

Starting from the results of the RAD1 test, the RAD2 was intended to test the background contribution coming from the so-called *small parts* of the detector. In fact, the detector is not made only by the TeO_2 crystals and the copper structure but also by small parts like the PTFE supports, the NTD-Ge thermistor, the Si-heater, the gold bonding wires and, finally, glue and pins.

The thermistors can be rejected as a background source, since radioactive contaminations coming from the surface must release at least part of their energy inside the thermistor and this energy release will generate a very fast and very wide pulse signal on the thermistor[4].

To reject the other components a test was prepared in the following way. The top and bottom plates of the copper mounting structure were covered with samples of these small parts. These were: a PTFE slab covering the top plate (facing 4 crystals), a set of heaters facing two crystals on the bottom plane (169 heater for each crystal) and a set of gold wires facing the other two crystals on the bottom plane. In this way, the amount of PTFE, heater and gold wires seen by the interested crystal, was increased, in comparison to with CUORICINO and the RAD1, by a factor respectively of 6, 80 and 169 (table 6.1).

The tower was cooled down in April 2005. The total collected statistics was about 540 hours. This means 1080 hours per detector for heaters and wires (2 detectors each) and 1620 hour per detector for PTFE (3 detectors, one was lost in during the cooling process).

The results of this test were very clear. The 3-4 MeV rates measured proved that the materials used to build the so called *small parts* have a maximum contribution to RAD1 and to CUORICINO background of: heaters 1%, gold wires 3% and PTFE 15%.

---

[4] The heat is released directly on the thermistor without the mediation of the glue spots' conductance. This will lead to shorter rise time (almost negligible). On the other hand the heat is dissipated immediately via the gold wires without passing trough the PTFE supports. This should lead to shorter decay times.

		Volume [mm^3]	**Surface [cm^2]**
PTFE	CUORICINO (Qino)	1544	5
	Rad2 (R2)	7890	30.25
	Ratio (R2/Qino)	5.11	6.05

		Length [cm]	
Wires	CUORICINO (Qino)	8	
	Rad2 (R2)	638	
	Ratio (R2/Qino)	79.75	

		Number	
Heaters	CUORICINO (Qino)	1	
	Rad2 (R2)	169	
	Ratio (R2/Qino)	169	

Table 6.1: Comparison of the amount of material per detector between the Rad2 setup and CUORICINO[196]. Note that while in CUORICINO each detector is exposed to all the samples in Rad2 each detector sees only one sample.

PTFE	**Bulk** [g/g]	**Surface (1 μm)** Bq/cm^2	**Surface (5 μm)** Bq/cm^2
^{232}Th	$6.30 \cdot 10^{-10}$	$3.20 \cdot 10^{-8}$	$5.90 \cdot 10^{-8}$
^{238}U	$3.80 \cdot 10^{-10}$	$1.30 \cdot 10^{-7}$	$1.40 \cdot 10^{-7}$

Si Heaters	**Bulk** [g/g]	**Surface (1 μm)** Bq/cm^2	**Surface (5 μm)** Bq/cm^2
^{232}Th	$2.80 \cdot 10^{-8}$	$1.60 \cdot 10^{-6}$	$3.30 \cdot 10^{-6}$
^{238}U	$1.30 \cdot 10^{-8}$	$8.20 \cdot 10^{-7}$	$7.50 \cdot 10^{-7}$

Golds Wires	**Bulk** [g/g]
^{232}Th	$3.10 \cdot 10^{-7}$
^{238}U	$1.20 \cdot 10^{-6}$

Table 6.2: Contamination values measured for the *Small parts*.

6.3.3 The RAD3 and RAD4 runs

The results of RAD2 maintained open the problem of background reduction. At this point two different hypothesis have been considered:

1) The sources of the contaminations are really degraded alpha particles. Probably, during the cleaning procedure a failure must had happened and thus the main background source is the copper structure.

2) The copper was correctly cleaned and the source of background are not degraded alpha particles but more *exotic effects* (thermal release of the Teflon® support or fracture processes inside the absorber).

A possible test to verify the first hypothesis was to cover all the surface of copper facing the crystals with a radio-clean plastic layer to stop alpha particles eventually escaping from copper. The main advantage of this plastic foil, since it is very thin, is that the bulk and surface contaminations are the same. Thanks to this feature, its contamination can be easily measured by germanium detectors.

Following this idea the only change in the RAD3 with respect to RAD1 was the almost complete coverage of the copper faced to the crystals with a polyethylene film ($\simeq 60\ \mu$m thickness).

The RAD3 was operated at the end of 2005. The result was the dramatic reduction of the 5.3 MeV peak (by more than a factor 3) that has now the same intensity as measured in CUORICINO (figure 6.4). The 5.4 peak on the other hand appears unchanged (proving that it is due to ^{210}Pb and not directly ^{210}Po).

The RAD4 was started at the beginning of year 2006. The detector is the same of RAD3 the only change is in the cryostat external shielding (now including a neutron shield). The new neutron shielding was composed by two parts: an internal layer, facing the detector, made of boron carbide (C_4B) and a more external wall ($\simeq 7$ cm thickness) made of polyethylene. The polyethylene was used to thermalize the fast neutron while the 10-boron atoms captures the thermal neutrons. In order to check the neutron absorption capability of the shield installed for RAD4 measurement we have performed dedicated measurement with an AmBe-neutron source (americium-beryllium, yielding 2200 n/s) both with and without neutron shielding.

The results of RAD4 are completely compatible with those of RAD3. This means that environmental neutrons should not influence appreciably our background counting rate (figure 6.4).

Considering the global analysis RAD3+RAD4 (1893 hours per crystal) the results obtained can be summarized as follows:

- crystal surface contaminations in ^{232}Th and ^{238}U are reduced by a factor 4 ± 2 with respect to CUORICINO;

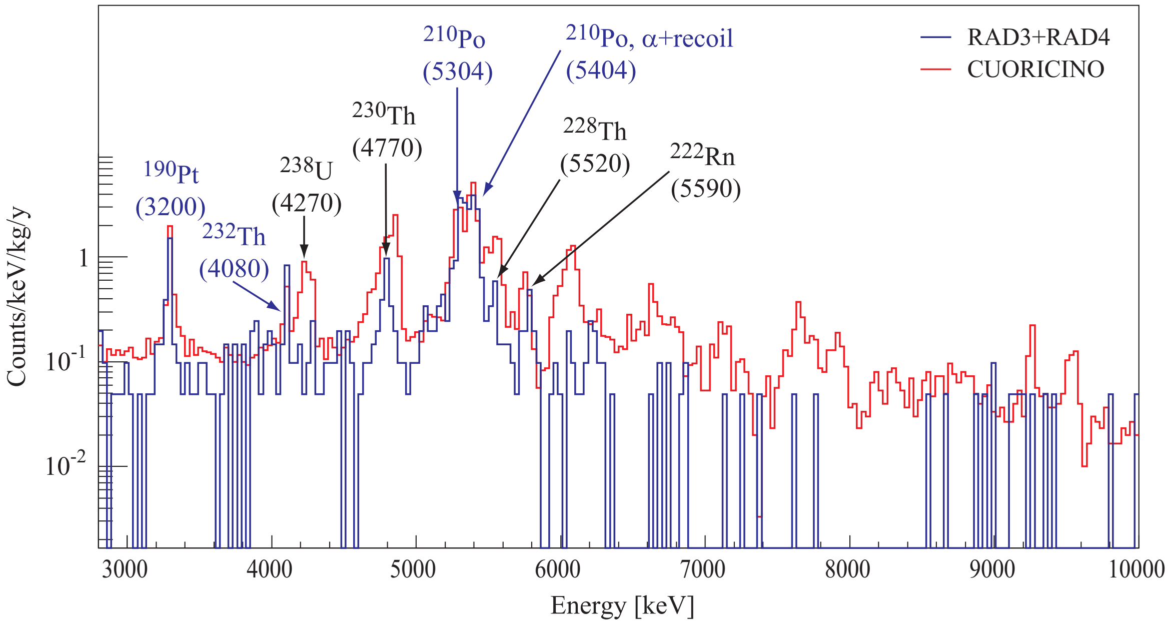

Figure 6.4: CUORICINO background (red line) compared with RAD3+RAD4 (blue line): the 5.3 MeV peak due to ^{210}Po has here a much reduced intensity with respect to that of RAD1, now compatible with CUORICINO. The continuum background between 3 and 4 MeV appears reduced, with respect to CUORICINO, by a factor $(38 \pm 7)\%$.

- crystal bulk contaminations have been measured with a sensitivity much higher than in CUORICINO (where α bulk lines were partially covered by the surface contamination peaks). The results are summarized in table 6.3;

- the 5.4 MeV ^{210}Po peak (α+recoil) is stable in time, therefore can be ascribed to a ^{210}Pb contamination;

- the 5.3 MeV ^{210}Po peak, quite high in RAD1, was due to a contamination of the copper surface and it is efficiently reduced to a level compatible to the CUORICINO one. This result was achieved by means of the polyethylene film used in RAD3 and RAD4. The 5.3 and 5.4 MeV peaks have almost the same intensity and could be both ascribed to the same surface contamination of the crystals;

- the surface treatment plus the polyethylene coverage of the copper have reduced the 3-4 MeV counting rate by a factor 2.0 ± 0.4 (i.e. to (0.06 ± 0.0116) counts/keV/kg/y, to be compared with the (0.12 ± 0.001) counts/keV/kg/y of CUORICINO in the region just above the ^{208}Tl line).

Isotope	Concentration	α-line	Origin	Comments
^{190}Pt	–	3290	–	α-decay on a stable isotope, no γ or β
^{232}Th	$(2 \pm 1) \cdot 10^{-13}$ g/g	4080	^{232}Th	Apparently in secular equilibrium
^{230}Th	$(2 \pm 1) \cdot 10^{-18}$ g/g	4750	^{238}U	Not in secular equilibrium with ^{238}U
^{210}Po	$< 1 \cdot 10^{-5}$ Bq/kg	5407	^{238}U	Not in secular equilibrium with ^{238}U but with ^{210}Pb
^{238}U	$< 2 \cdot 10^{-14}$ g/g	–	^{238}U	Upper limit for ^{238}U in secular equilibrium

Table 6.3: TeO$_2$ bulk contaminations as identified in RAD3+RAD4.

6.3.4 RAD5 and RAD6 runs

After the results coming from the RAD3+RAD4 (reduction of CUORICINO background by 38%) and from the second SSB test (background rate only slightly lower than the CUORICINO one) we decided to investigate possible *exotic sources* responsible for the remaining not-understood background. Starting point of this hypothesis are the previous experience[200] in the CRESST dark matter experiments and the usage of holders made of Teflon® for the all test performed until then.

Teflon® (poly-tetrafluoroethene, PTFE) is a synthetic fluoropolymer (polymer containing atoms of fluorine) characterized by an extremely low coefficient of friction (0.1 or less). Being a polymer, Teflon® is a substance made up of molecules with high molecular mass consisting of many regular repeating structural units or monomers. These long chains of atoms stick together forming bicovalent bonds.

When the Teflon® is cooled down together with the other parts of the detector, it could happen that, due to fast cooling, these chains have no time to set properly. Once the detector reaches the operating temperature, chains would start to arrange releasing heat (thermal release) in the crystal absorber even for a long time. That kind of release would originate impulses whose spectrum, continuum, would increase the background.

In order to investigate this hypothesis, in the RAD set-up we decided to replace the Teflon® support (figures 6.5 and 6.7(a)), typical of the RAD setup, with phosphorus-bronze clamps (figures 6.5, 6.7(b) and 6.7(c)) obtaining a Teflon®-free tower. We chose the phosphorus-bronze alloy in place of the copper beryllium one (CuBe, used in CRESST) which, in preliminary measurements, turned out to be too radioactive. The copper beryllium alloy assures either a lower radioactivity and the proper elasticity necessary to hold the crystals.

The preparation finished in the end of 2006 and the tower was cooled down in January 2007. The measurement time was very short, about 253 hours per crystal. That was due to radioactive contaminations (^{210}Pb) which caused the detectors to show a too high rate (figure 6.6). Under those conditions, it was impossible to make a comparison between Teflon®and phosphorus-bronze. A possible solution was to

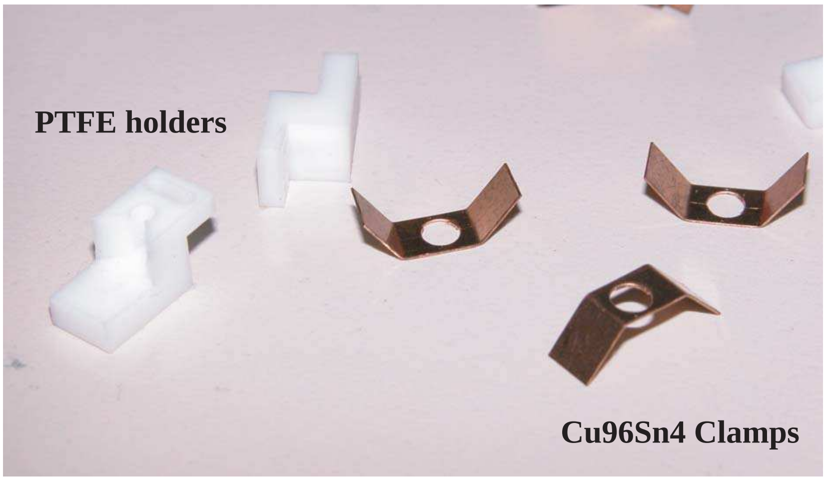

Figure 6.5: Picture of the Cu96Sn4 Clamps used in the RAD5 setup compared with the usual Teflon® supports.

prepare a new run using similar clamps made of the same copper of the frames and treated following the RAD1 cleaning procedure. However, the copper didn't guarantee the required elasticity.

In order to go over this problem we adopted a mixed solution. In fact, for the RAD6, we used the same phosphorus-bronze clamps used in RAD5 but, this time, covered with a copper layer (50 μm thickness). This solution guaranteed both the copper beryllium (clamp core) elasticity and the copper cleaning (clamp surface). In addition, the copper coverage worked as external shield against the contamination inside the copper-beryllium core. The preparation of RAD6 finished in April 2006 and the tower was cooled down in May 2007. To measure the possible radioactive contaminations in the copper coverage, two crystal (B8 and B11) were faced two copper foils (5×5 cm^2), one per crystals, whose thickness was the same of the clamps.

The total measurement time was 411 hours per crystal. The results of RAD6 showed lower contamination than the RAD5 (figure 6.6, No-Copper) but a higher background level if compared to the RAD4 (figure 6.6). Moreover, comparing the spectra of crystals facing the copper foils and of normal crystals (No-Copper), it is clearly visible that the copper used for the clamps coverage have a too high surface contamination probably due to ^{210}Pb. For these reasons it wasn't possible to deduce anything about the *exotic sources* hypothesis.

From the technical point of view, the RAD5+RAD6 proved that the clamps work in the same way of the Teflon® supports. In fact, they provides an elastic but tight holding of the crystal. This means that Teflon®-free study is still possible in future if and only if very clean clamps will be used.

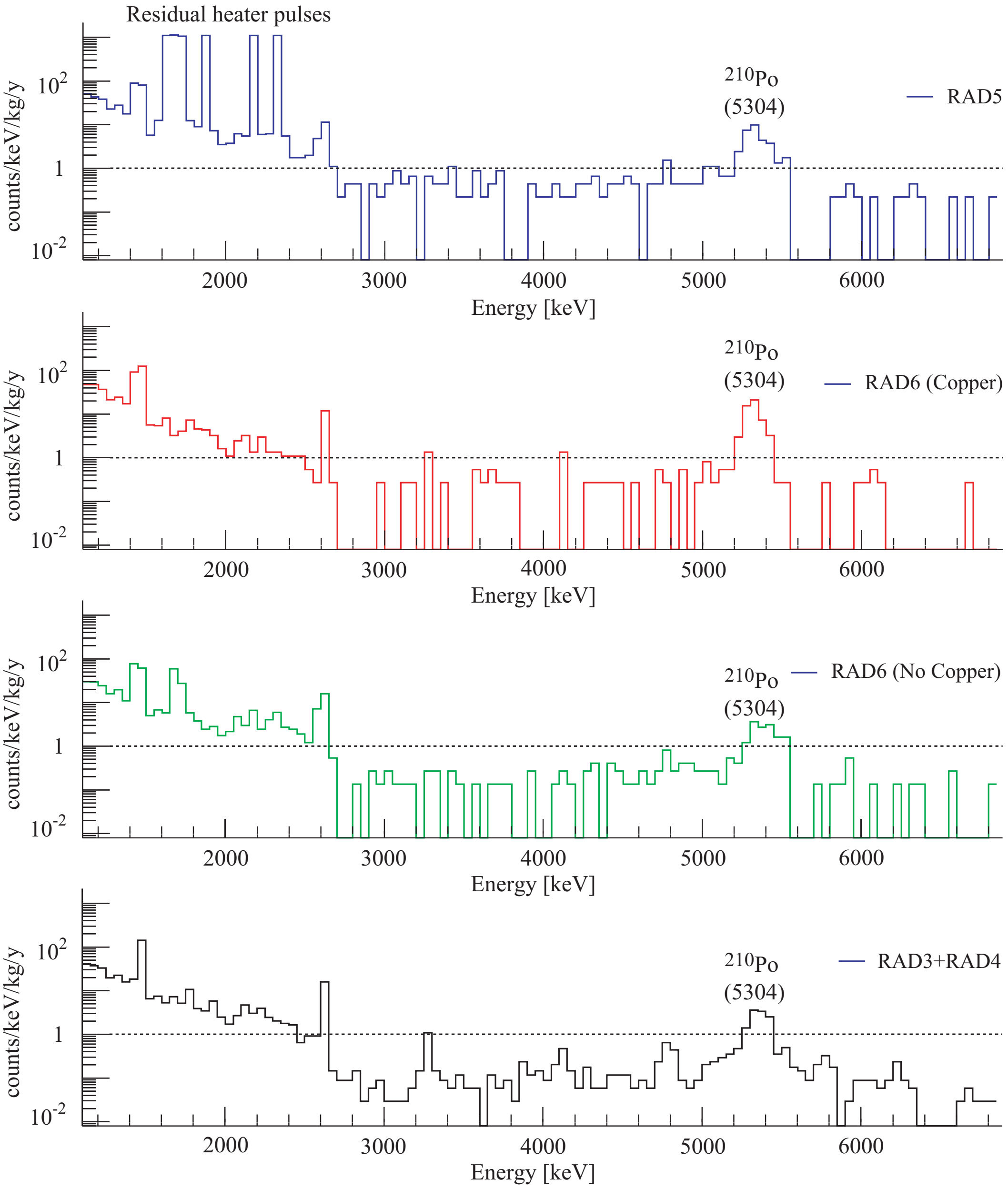

Figure 6.6: RAD5 and RAD6 spectra compared with the RAD3+RAD4 run. In RAD5 (blue) the background counting rate is dominated by the clamps contaminations. In RAD6 the crystals facing the copper foils (red) show an higher peak if compared to the normal ones (green). This is probably due to surface contamination (^{210}Pb) of the copper itself.

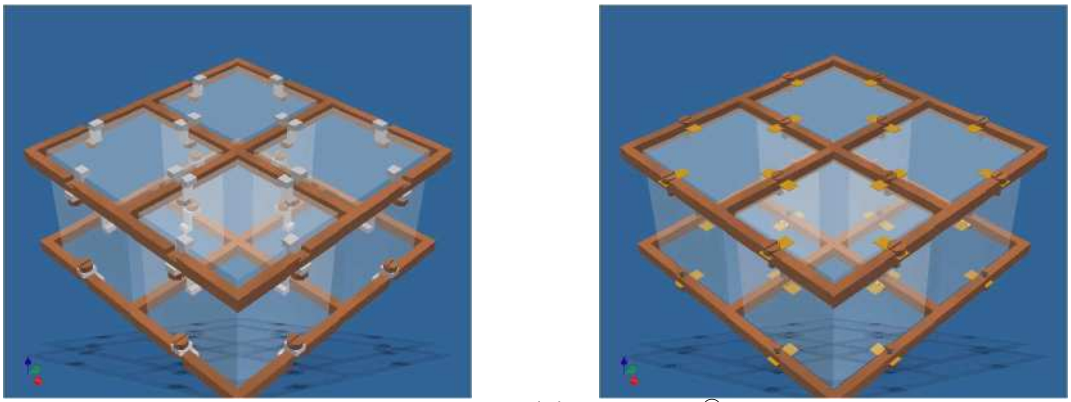

(a) The usual RAD detector. Each crystal is held to the copper frame by means of PTFE supports.

(b) The Teflon®-free RAD detector. Each crystal is held to the copper frame by means of phosphorus-bronze clamps instead PTFE.

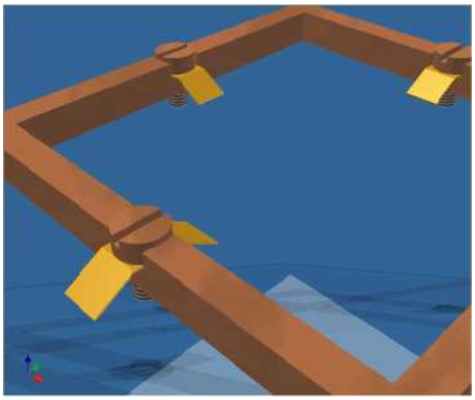

(c) Particular of the phosphorus-bronze clamps used for the RAD5+RAD6 measurements.

Figure 6.7: Comparison between the usual-RAD mounting and the Teflon®-free solution.

6.3.5 The RAD conclusion

With the RAD tests we have proved that, as predicted by the CUORICINO background model (section 5.3), surface contamination of the copper play a relevant role in 3-4 MeV background. This is clearly evident by comparing RAD1 and RAD3+RAD4 counting rates: RAD1 had a rate comparable with CUORICINO while RAD3+RAD4 (the only change was the polyethylene coverage of copper) had a rate lower by a factor 2. In addition the RAD5+RAD6 measurement could not exclude possible not radioactive contribution (*exotic sources*) due to the PTFE supports.

6.4 The CAW detector

The CAW detector is a 3 plane array having a structure a little bit different from that of RAD (and of CUORICINO). This new design is the result of an intense program of optimization of the CUORE detector structure started in 2004, involving all aspects of the single module structure and of its assembly procedure in the final CUORE towers (see section 4.4.1).

The new structure should guarantee a high degree of reproducibility in its mechanical features as well as a simply assembly and a reduced amount of inert material (copper) in between the detectors. Assuming that a large fraction of the background is due to surface contamination of the mounting structure the reduction by about a factor 2 of the copper surface interposed between the detectors is particularly relevant.

The CAW detector is a prototype constructed and successfully tested in 2005 from the technical point of view. At the beginning of 2006 this same array was used for a background test. For CAW1 no particular cleaning procedure was applied while starting from CAW2 we cleaned the set-up with a RAD-like procedure. In fact, the twelve crystals were treated with a surface cleaning procedure similar to the one applied to RAD1 crystals while the copper of the mounting structure was treated as for RAD1 and was covered, as for RAD3, with a polyethylene foil with thickness greater than 60 μm (in order to absorb the α-particle emitted from a possible residual surface contamination).

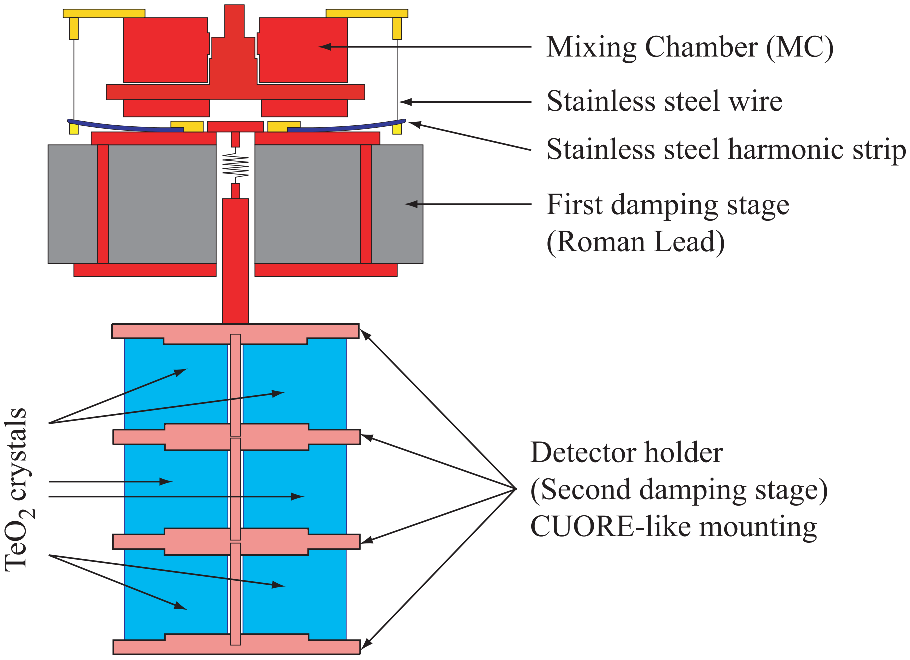

Figure 6.8: The CAW detector.

From the 2005 to nowadays four tests were performed:

- CAW1: the purposes of this measurement were:
    1) test the reproducibility of the new setup (CUORE-like) and test the new PTFE support design (projected to prevent possible low temperature cracks in the crystals);
    2) check the performances of the germanium-SSBs;
    3) check performances and radioactivity of CTI crystals[5].
- CAW2: the purposes of this measurement were:
    1) check the background achievement obtained with RAD3+RAD4 in a different structure and with different crystals;
    2) check the performances of Surface Sensitive Bolometers made of tellurium dioxide instead of germanium;
    3) new check about performances and radioactivity of CTI crystals.
- CCT1: the main purpose was to check the internal and surface contaminations of six new crystals grown with a new procedure and completely processed in China (including etching and lapping).
- CCT2: the purposes of this measurement were:
    1) check the internal and surface contaminations of four new crystals completely processed in China;
    2) check the internal and surface contaminations of the six CCT1-crystals after a further surface treatment at the Gran Sasso Laboratories;
    3) test the new flat-pack thermistors.

6.4.1 Development of surface sensitive elements

The first two CAW measurements at the Hall C facility were closely related to the development and testing of the *Surface Sensitive Bolometer* technique. In fact, an alternative way to reject events due to contaminations in the crystal surfaces and to the part facing the crystal is to develop bolometers able to identify these ones. The basic idea of the method consists in the construction of *Surface Sensitive Bolometers* (SSB) characterized by active shields: six slabs (of Ge or of Si or of TeO_2) operated as bolometers (*Surface Sensitive Elements* or SSE) surround the TeO_2 crystal (Main) creating an active veto[202]. Events generated on the surface of the crystal or of the SSE itself are in this way tagged and rejected.

---

[5] Crystal Technology Incorporated (California, USA) was a possible provider for CUORE detector absorbers.

The implementation of this technique is as follow. For each Main TeO_2 bolometer there are six (one for each face) thin, large-area, auxiliary bolometers that act as active layers (figure 6.9). Each layer will have the same area and shape as the corresponding absorber face and will be separated from it by a sub-millimeter gap, providing a 4π hermetic coverage from external charged particles. On each layer, a NTD-thermistor is attached for temperature reading.

The origin of the events (SSE or Main) can be clearly determined by comparing the amplitude of the pulses from the different detector elements. If an α particle comes from outside the bolometer, it interacts with an active layer releasing there all its energy (*surface event*). As a consequence, the SSE and Main temperatures will rise and there will be a signal on both the layer thermistor and the main one. Because of the small heat capacity of the layer, its thermistor signal will be much higher and faster than that of the main thermistor. On the other hand, an event inside the main crystal (*bulk event*) will lead to pulses with similar amplitudes and shapes on both thermistors (figure 6.9).

This solution has the potentiality to control the problem of the surface radioactivity relying on a technological improvement of the detector rather than on a better cleanness of the employed materials. The main feature of such a detector are that any particle depositing its energy only in the Main, as a $0\nu\beta\beta$ decay event, produces a large particle-induced signal on the main and a small slow thermally induced signal in the SSE (due to temperature rise of the Main).

In order to test the method, several small scale prototype detectors were successfully tested during 2004 at the Cryogenic Laboratory of the Insubria University (Como, Italy). The material used were Ge, TeO2 and Si slabs. Starting from these results we performed two test exploiting the CAW tower. In CAW1 (2005) we implemented one entire tower floor with Si-SSB while, in CAW2 (2006), we used TeO_2-SSB.

While good performances were obtained with both Ge and TeO_2 slabs, Si slabs showed some unexplained features that lead us to consider them less safe than the other two devices. According to these considerations and to the fact that the optimal SSE material should have thermal contraction coefficients as near as possible to the main crystal ones, TeO_2 slabs should be the final choice for a SSB.

6.4.2 The CAW1 run

The experimental setup was prepared with a 12 crystals arranged in three floors of four detectors each (the second biggest TeO_2 mass ever built and operated even to a fourth of CUORICINO).

The twelve crystals used as absorbers came from three different sets each of four crystals. Four crystals were just arrived at that time from the SICCAS company and other four crystals came from the CUORICINO spear detectors. The last four crystals (one floor) were provided by the Crystal Technology Incorporated (CTI, California, USA).

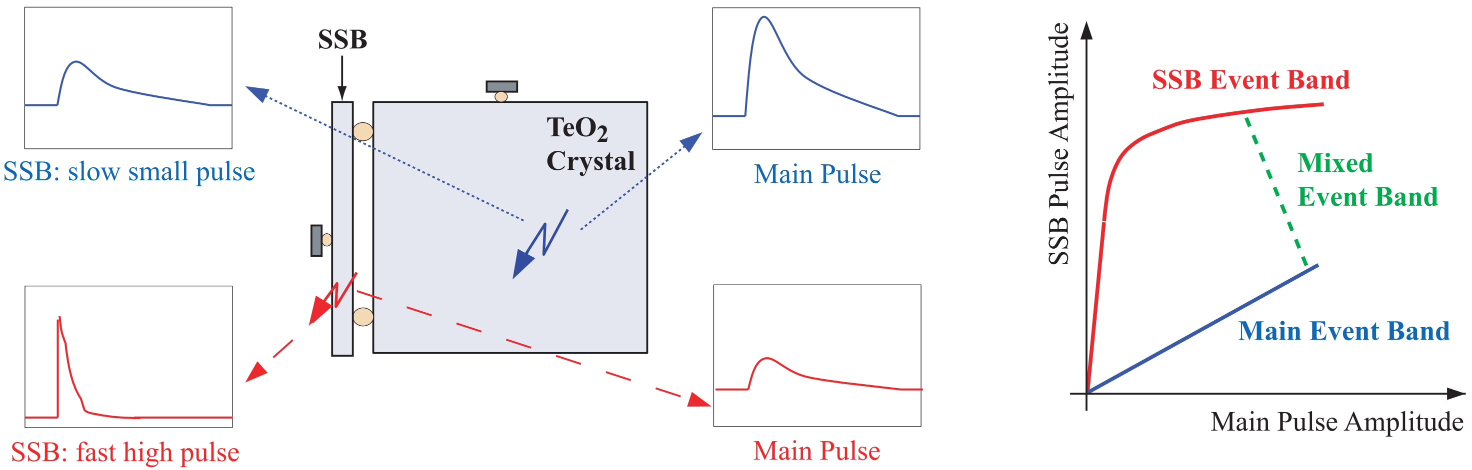

Figure 6.9: The behavior of composite bolometers with respect to a signal produced by interaction in the slab or in the TeO$_2$ crystal. The scatter plot shows the different shapes of the curves drawn by pure SSE events and pure Main ones. The curve originated by a monochromatic alpha sharing its energy between SSE and Main is also shown.

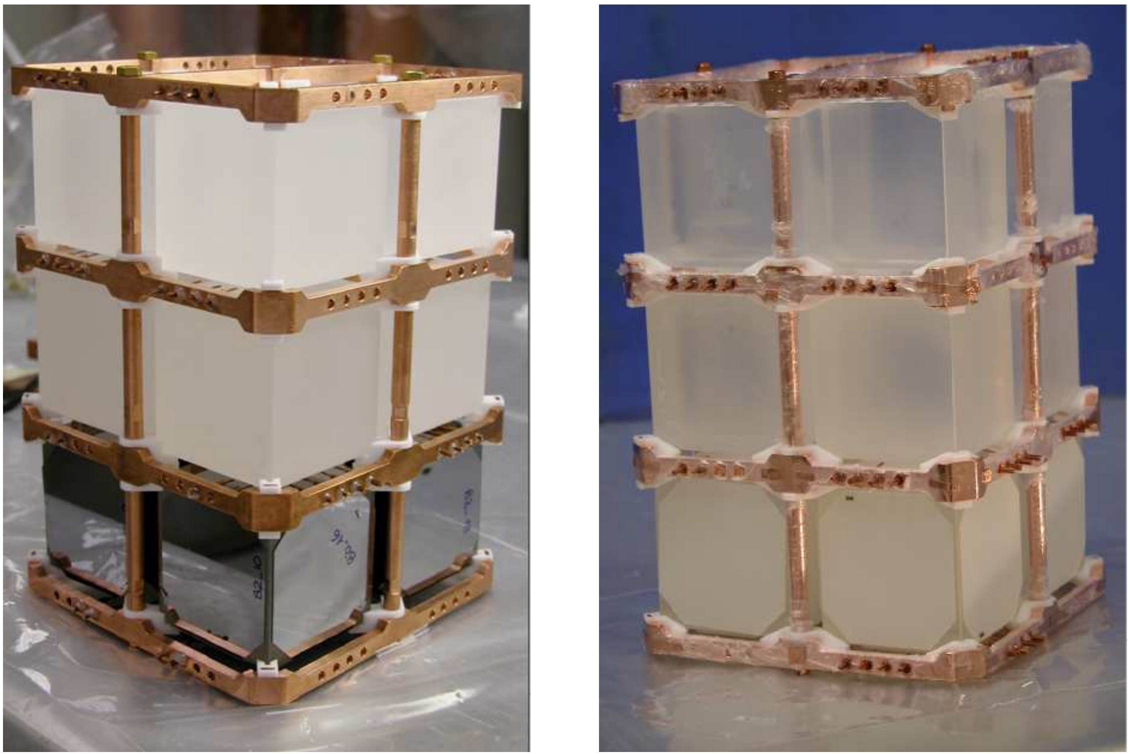

(a) The CAW1 detectors. In the lower floor the Si-SSB detectors are visible. **(b)** The CAW2 detectors. In the lower floor the TeO_2-SSB detectors are visible

Figure 6.10: The two CAW towers during the CAW1 and CAW2 assembling.

On the lower floor of the tower, the four detectors (figure 6.10(a)) were prepared to be a test of Surface Sensitive Bolometers. Due to a delay in the delivery of the TeO_2 slabs the four detectors were realized gluing (with a vacuum grease spot at the center of the slab in order to prevent possible breaks) on each face of the $5 \times 5 \times 5$ cm^3 crystals a Si slab ($50 \times 50 \times 0.3$ mm^3). For three crystals the coverage was not exactly complete (a triangular area near each vertex was not faced by the slab, being then partially covered by the PTFE tips used to held the crystal in the copper frame) while for the fourth of them the Si slabs covered almost completely the crystal and the PTFE tips were positioned on the slab themselves. This crystal was the smallest one.

Each slab was provided with its own NTD-Ge thermistor used to read-out the thermal signal. In order to reduce the readout channels, the six thermistors of the SSEs were connected in parallel. In this way, for each $5 \times 5 \times 5$ cm^3 detector, two channels were read out: the Main (TeO2 crystal absorbed) and the SSEs.

The CAW1 was the first test performed using the CAW tower. From the technical point of view the results obtained showed an easy, fast and standard assembling procedure improving the detector reproducibility and standardization. Furthermore no damage on the crystals occurred with new PTFE supports. For these reasons the collaboration chose this design for CUORE leaving behind the old CUORICINO-like (and RAD-like) structure.

From the physical point of view in particular considering the SSB test, the two detector with smaller dimensions (responsible for the excess noise due to their vibrations) showed a rather poor performance, while for the other two a good energy resolution, compatible with that of the CUORICINO detectors, was measured. Unfortunately during the cooling the electrical connections to the slabs thermistors of one of these detectors were broken, thus only for one detectors the SSE signal could be read-out. A quite long background measurement (520 hours per crystal) was used to understand the behavior of these detectors and to study the rejection efficiency for surface alpha contamination. The detector with complete read-out (Main+SSEs) was used for an extensive study of the main features of the composite bolometer. The two signal coming from the main and from the six SSEs in parallel were acquired with an independent trigger and trigger threshold. Once only signals above the common maximum threshold are considered (equalizing then the thresholds on SSE and Main) only coincident events are observed. The amplitude measured on the Main was calibrated using a gamma source, this provides a correct conversion of the Main pulse amplitude if and only if the considered signal corresponds to a pure interaction in the Main (i.e. the SSE pulse is induced by the thermal heating of the Main). A similar calibration was not possible for signals produced in the SSE due to its small size.

Considering figure 6.11(a), it's easy to recognize three possible case:

1) signals produced by particles interaction in the Main are clearly identified as those belonging to the straight line (Main Band) in the lower part of the plot. These events correspond to small-slow signals in the SSE.

2) signals produced by particle interaction in the SSE belong to the multiple curves (SSE band) identified by a high SSE amplitude and low Main amplitude. We have multiple curves because the six different SSEs are acquired in parallel.

3) when the energy of the particle is shared between the SSE and the Main (surface α-event originating in between the SSE and TeO_2 surface) the signals produced belong to the line connecting the Main Band and the SSE Band.

In figure 6.11(b) it is shown, for the same events, the decay time versus the amplitude as measured on the Main. What is clearly evident is that the events belonging to the Main Band have the usual distribution while events that belong to the SSE Band or to the so called *mixed events* are clearly distinguishable having a much slower decay time. This means that the presence of the slabs thermally connected on the TeO_2 crystal absorber modifies the response of the bolometer in such a way that bulk events are distinguishable from surface events just looking to their decay time (*passive effect*, the glued layers operate as signal-shape modifiers).

This measurement demonstrates therefore the power of this technique in identifying surface events, and opens moreover a new way of using the composite bolometers that

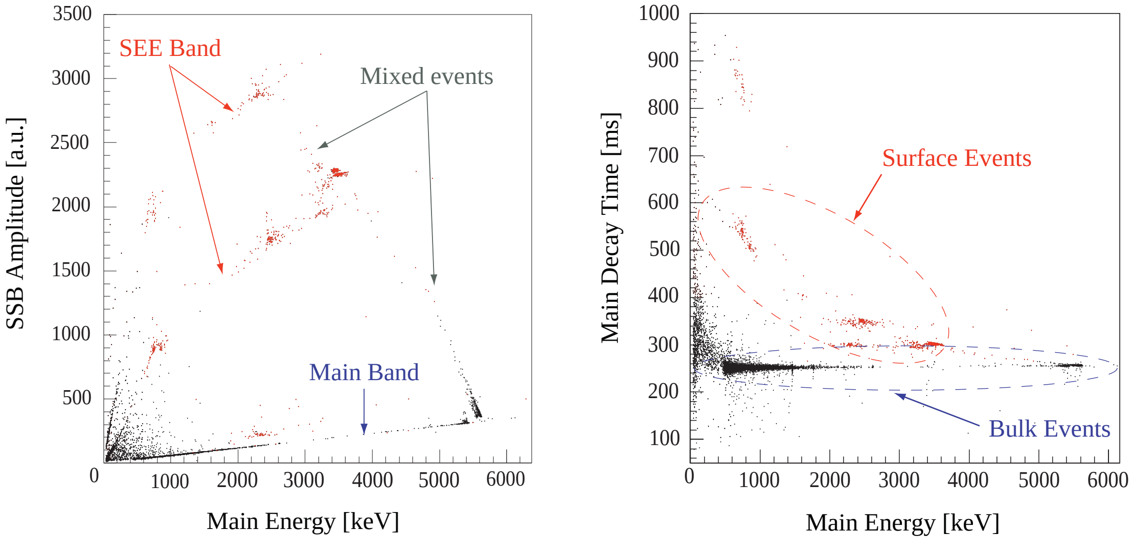

(a) Scatter plot of coincident events as measured by the Main and by the SSEs.

(b) The decay time versus amplitude as measured on the Main.

Figure 6.11: CAW1 scatter plots.

do not require them to be read out. This is particularly important for CUORE because means that SSB could be mounted without increasing the number of thermistors necessary and the number of wires and channels to be biased and read-out.

In this test no cleaning procedure of the detector and mounting system was applied thus the background counting rate was too high. For this reason a quantification of the background reduction obtained by the composite bolometers cannot be obtained, and also the characterization of the CTI crystals was not possible.

As it will be shown in the next section, at the beginning of 2006 a new CAW run with an array of 4 crystals (having this time the correct dimension to fit into the assembly) covered with TeO_2 slabs was constructed using the same cleaning procedure used for the RAD setup.

6.4.3 The CAW2 run

In this second CAW test (figure 6.10(b)) we treated the copper as for RAD1 and we covered it with polyethylene as in RAD3, moreover we treated the twelve crystals with a surface cleaning procedure similar to the one applied to RAD1 crystals.

In the top floor of the tower four CTI $5 \times 5 \times 5$ cm^3 TeO_2 crystals were mounted. These crystals, bought from the Crystal Technology Incorporated (CA, USA), had to be examined since CTI was a possible provider for CUORE detectors. In the middle and bottom floor eight $5 \times 5 \times 5$ cm^3 TeO_2 crystals, bought as usual from SICCAS, were mounted.

Each of the four crystals in the bottom floor were coupled to six TeO_2-SSB. The

SSB slabs were glued with four spot to the main crystal surface and covering almost completely that surface. On two crystals all the SSB were provided with a NTD-Ge thermistor (*active* SSB) while on the other two only one of the six slabs had a sensor (*passive* SSB). In this way it was possible to study the *passive effect* observed in the CAW1 test[6] The middle floor was made up with four crystal, provided by SICCAS, in order to compare the background results with the SSB floor.

The CAW2 was mounted at the beginning of year 2006 and started right after the end of the RAD4 test. The main results obtained were:

1) the CTI crystals show huge ^{210}Po and ^{232}Th contaminations slightly higher that the one typical of the chinese crystals (table 6.4 and figure 6.12). Causes, although still to be understood, could be the initial powder or the crystallization process.

Crystals	**Counting Rate** [counts/hour]
CTI-1	500
CTI-1	90
CTI-1	80
RAD	0.4

Crystals	^{232}**Th Counting Rate** [counts/hour]
CTI	0.0040 ± 0.0010
RAD	0.0019 ± 0.0005

Table 6.4: CTI crystals contaminations. The 5.4 MeV energy (left) and ^{232}Th bulk contaminations are shown compared with the RAD mean values.

2) the RAD3+RAD4 results are confirmed, proving that the surface cleaning procedure of crystals and copper are reproducible (figure 6.13);

3) either active and passive TeO_2 slabs produce a deformation of surface events.

The only uncertainty in this run was the conclusion about the 3-4 MeV flat background source. Considering the two lowest planes (both with chinese crystals, one with SSB and the other without SSB), with SSB perfectly working they would have given a strong indication in favor or against the hypothesis of a copper origin of the background source. Unfortunately one SSB detached from its crystal, for two we lost the electrical contact and finally all the SSB showed an excess alpha surface contamination (figure 6.14). The causes of this contamination are meanly two: the SSBs were cut using contaminated oil and they surfaces were not treated as the $5 \times 5 \times 5$ cm^3 crystals because of the very thin thickness. As a result the rejection capability of SSBs could not be exploited to their best and the data about the background rate measured, being only slightly lower than the one measured by the crystals without SSB, are not enough to draw any conclusion concerning copper.

---

[6] as said previously, the effect of a passive slab is to produce a deformation of pulses originated at the crystal surface and sharing energy between crystal and slab

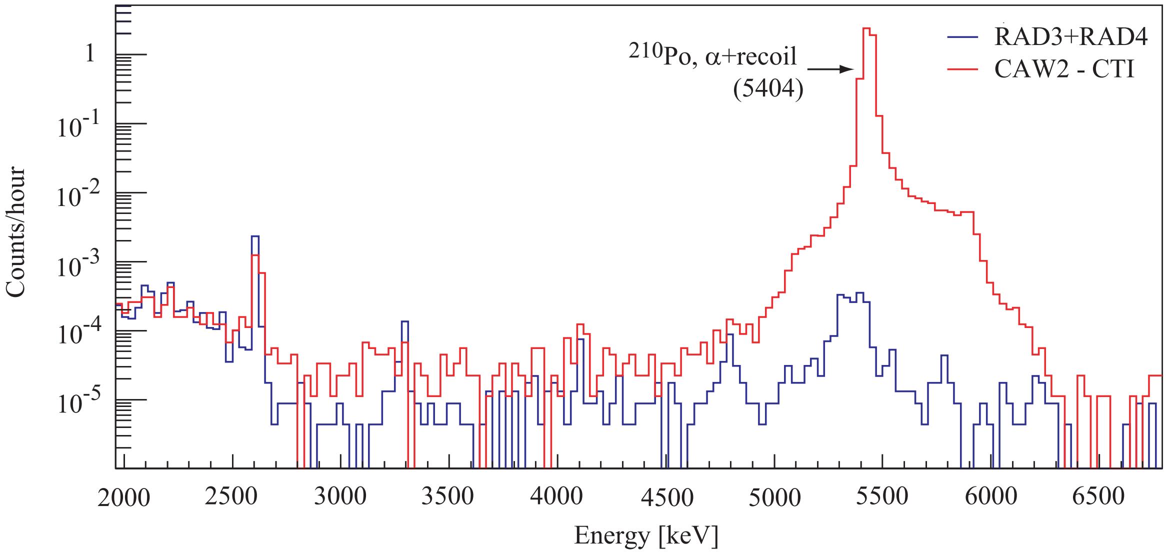

Figure 6.12: CTI floor background compared with RAD3+RAD4. The huge ^{210}Po contamination can be easily visible.

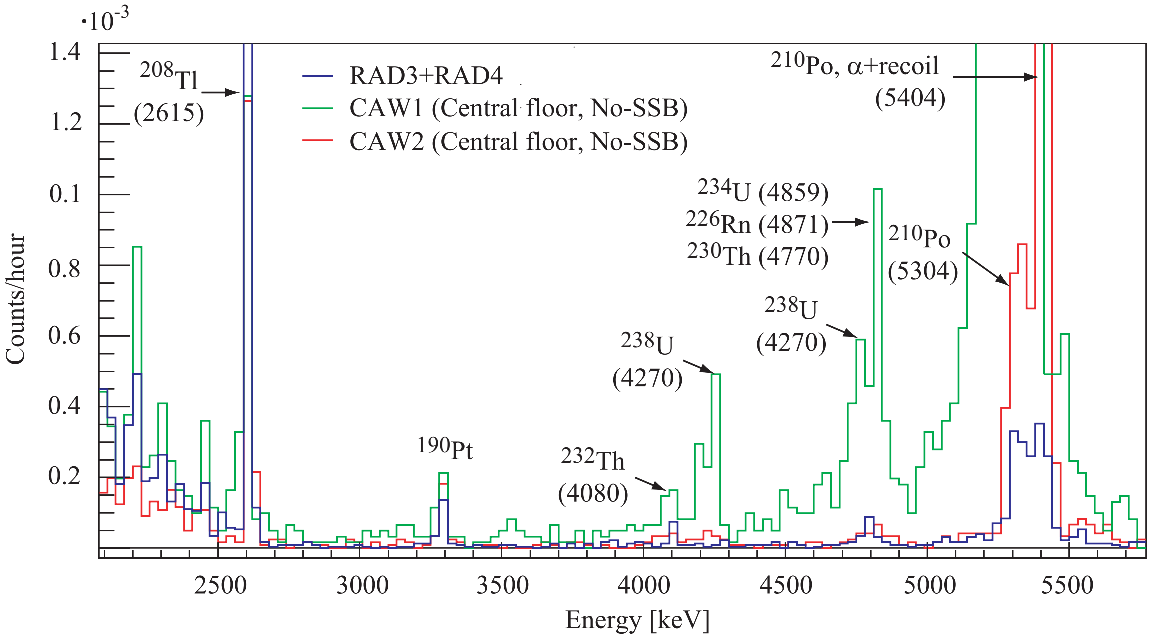

Figure 6.13: CAW2 central floor background compared with the RAD3+RAD4 and with the central floor of CAW1. The spectrum shows that the RAD crystal surface treatment is reproducible, The CAW2 central floor has the same internal contamination measured in RAD3+RAD4.

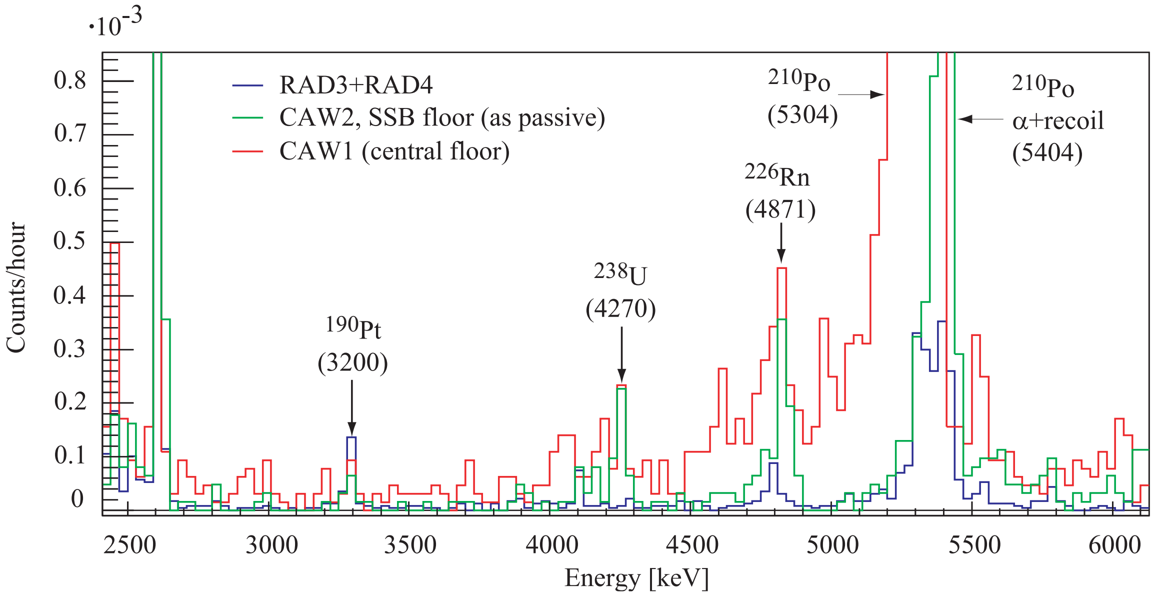

Figure 6.14: SSB floor background compared with RAD3+RAD4 and with previous CAW1 floor without slab. The CAW1-no-slab floor and the CAW2-SSB floor had the same crystals. The background is dominated by alpha particles due to the slab contamination.

Taking into account the results from CAW1 and CAW2 it's clear that a further SSB run will be useful only if we will be able to improve the slab surface radioactivity, the comprehension of decay time method and, finally, the mounting technique.

Detector	**2700 ÷ 3200** [keV]	**Err.** [keV]	**3400 ÷ 3900** [keV]	**Err.** [keV]
RAD3+RAD4	0.06	0.01	0.08	0.02
CAW	0.16	0.04	0.11	0.03
SSB (as passive)	0.11	0.03	0.14	0.03
SSB (as active)	0.03	0.02	0.03	0.02

Table 6.5: CAW2 background compared wight RAD3+RAD4.

6.4.4 The CCT1 run

Up to now, all crystals were produced and optimized through a standard procedure, divided in two phases: first the crystal growing, carried out at the SICCAS then the surface treatments, performed in the clean room of the Gran Sasso Underground Laboratories. The CCT1 test (*Chinese Crystals Test*) was the first performed on crystals completely processed in China. The surface treatment used in China (etching and lapping) is the same successfully optimized at the LNGS and verified with the RAD array.

The main goal of this test was to check bulk and surface contaminations in order to approve the new crystals production and treatment protocol. This protocol (hereafter *new-protocol*) was different from the one adopted for the CUORICINO crystal production (*standard-procedure*, hereafter *old-protocol*). Its aim was to reproduce the CUORICINO crystals performances avoiding old procedure problems (for example, inclusions of platinum fragments due to the crucible used to make it grow). The two protocols are formed by the following processes:

Old-Protocol:

1) Grown with CUORICINO like procedure:
    (a) 80°C dry-up;
    (b) 690°C calcination in platinum crucible;
    (c) first growth in platinum crucible using a standard Bridgman technique;
    (d) ingot selection, ingot grinding, washing, drying and new calcination;
    (e) second growth;
2) first surface treatment in China with dirty chinese aluminium oxide (Al_2O_3) powders;
3) second surface treatment at LNGS: chemical etching with very clean acids (HNO_3 4 molar) and surface polishing following RAD procedure (lapping pad with very clean SiO_2 powder);
4) TeO_2 crystals ready to use.

New-Protocol:

1) three different dry-up and calcination processes tested:
    - A - standard one with 80°C dry-up and 690°C calcination in platinum crucible;
    - B - 600°C calcination without dry-up;
    - C - 240°C dry-up in Teflon®and 690°C calcination in platinum crucible;
2) after the first growth (standard Bridgman in platinum crucible) only a few of the produced ingots are selected ($\simeq 1/3$) in order to reduce the impurity content;
3) ingot selection, ingot grinding, washing, drying and new calcination (after these procedures the powder showed a reduced platinum content);

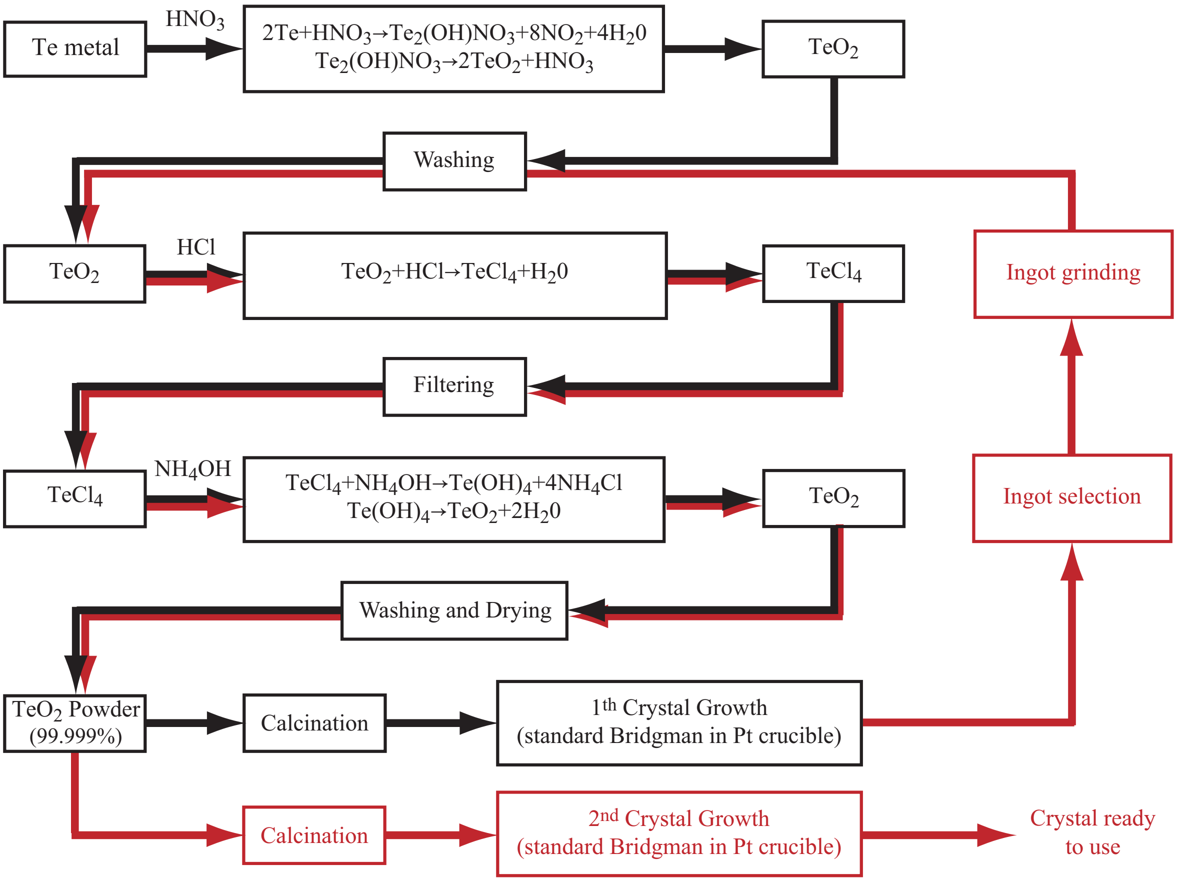

Figure 6.15: TeO_2 powder production.

4) second growth;

5) mechanical treatment:

   (a) washing with water in ultrasonic bath;

   (b) surface lapping with two new Al_2O_3 powders selected for low radioactivity. Two type of powders were selected: big granularity (1 mm lap-off) and small granularity (0.1 mm lap-off) but the small one didn't work properly;

   (c) chemical etching with very clean acids (HNO_3 4 molar) in order to remove the dirty part of the surface;

   (d) polishing with SiO_2 powder (RAD-like), and a new lapping pad ($10 \div 20$ μm lap off).

6) TeO_2 crystals ready to use.

The CCT1 test was carried out using the CAW tower where the copper was covered, as usual, with a polyethylene film. The copper mounting structure was composed by new copper frames realized with *Electrical Discharge Machining* technique (commonly known as EDM machining). Teflon®supports was the usual but, this time, provided by a different company with respect to the past. Six crystals (BA1, BA2, BB1, BB2, BC1, BC2) were fully *chinese* crystals (hereafter *new-style* crystals) grown according to the new protocol) and then treated on surfaces after a chemical etching. These crystals belong the three different series (A, B, C) depending on the preparation of the powders. At first sight they show some yellowish faces instead of the usual white. The remaining six (B63, B64, B65, B66, B68 and B69, already tested in the past) were *old-style* crystals grown as CUORICINO crystals and treated at LNGS. Each of the *new-style* crystals was provided with two sensors while the *old-style* crystals were provided with only one sensor.

The preparation was completed in the last week of July and the tower was cooled down in the first week of August. For the *new-style* crystals all sensors were working while for the *old-style* ones two sensors lost the connection and one was electrically connected but no pulse signal was visible (probably unglued during the cooling down).

From the performances point of view the new crystals appeared to have quite lower pulse amplitudes (despite the quite low temperature of the array) and poorer energy resolution. Such a behavior is not present in the six *old-style* crystals. The study of pulse shape could indicate a correlation between the longer decay constant and the energy resolution.

The background analysis (figure 6.16) shown an excess of counts on the right side of the 2615 keV peak that produces a high value of the $(2.7 \div 3.2)$ keV integral on both *old-style* and *new-style* crystals. The causes have presently no explanation. In the 4-5 MeV region the rate is higher than in the RAD detector, and similar to the rate measured by CUORICINO. The structures appearing in this region of the spectrum look like due to a ^{238}U contamination in the crystal bulk or on crystal surface. Only the coincidence spectrum can distinguish between the two possibilities. In any case the low rate in the coincidence spectra was below what expected if compared to CUORICINO.

The *new-style* crystals showed the usual huge contamination in ^{210}Po, the peak has however an unusual asymmetry that we are not able to explain. Also the *old-style* crystals had a high rate in the polonium region if compared with RAD. This because these crystals was rather recently grown while the RAD ones came from the same batch of CUORICINO crystals. Finally, for the all series no improvement was apparently obtained in the ^{190}Pt crystal contamination.

Because of these problems the data-taking of the CCT1 measurement was very short (about 330 hours per crystal). The causes of these bad performances could be two:

1) **Bulk problem**: in the standardization of the growing procedure, some change was introduced respect with old protocol. Possible Oxygen vacancies could explain the yellowish color and a different heat capacity C of the crystal ($\Delta T = \Delta E/C$);

2) **Surface problem**: the lapping pad used in China came out to be different from

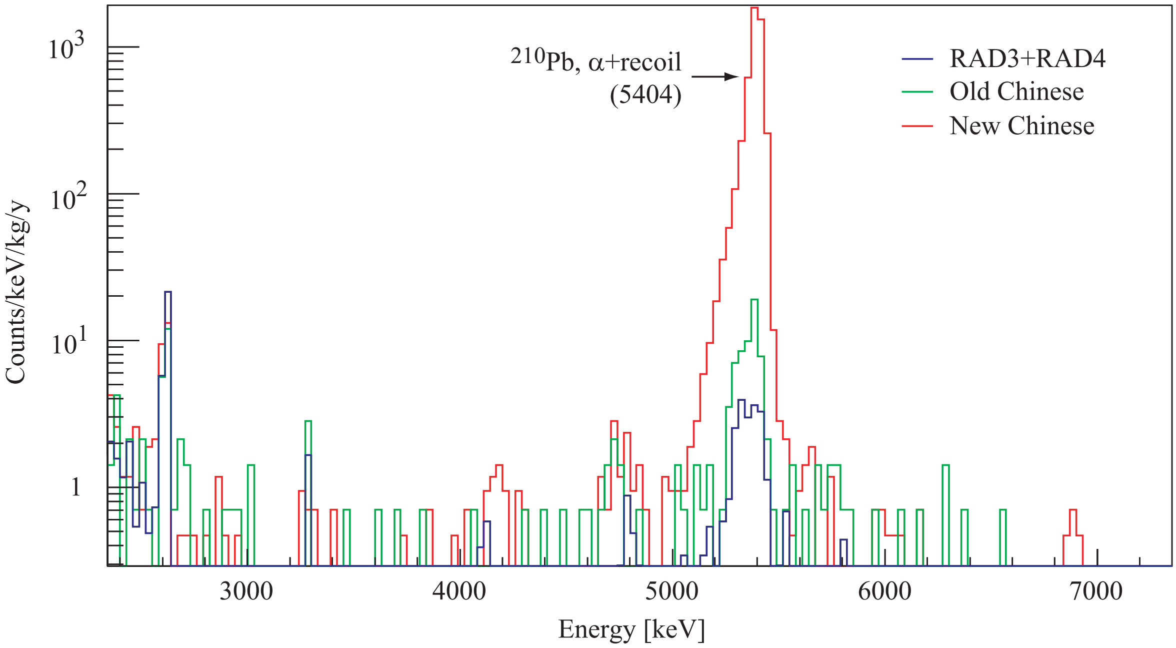

Figure 6.16: RAD background spectrum compared to *new* and *old* style crystals in this run.

> the usual one (black and more soft). The yellowish color can be generate by residuals of the back lapping pad. Moreover possible lack in removing the acid and/or water layer could be left on the crystal by the etching bath. This layer could change the thermal coupling between the thermistor and the crystal. In the past crystals etched but not lapped showed the same behavior.

To check these hypothesis was necessary a new test (CCT2). To achieve this, four new crystals grown with the exact CUORICINO procedure arrived from SICCAS and the six *new-style* crystals was reprocessed with the standard RAD procedure at LNGS clean room. The result of the our treatment was the disappearance of the yellowish surface. This could be a first confirmation to the hypothesis of problems in the surface processing performed in China.

6.4.5 The CCT2 run

As for the case of CCT1, the second CCT test was scheduled to validate the SICCAS protocol production for the CUORE crystals. To achieve this task the main goals of this measurement, still running, are:

1) to check bulk and surface contaminations of four new crystals grown with the *standard procedure* (CUORICINO like) and mechanically treated in China following the RAD procedure.

2) to check the *new-style* crystals (used in CCT1) after a further RAD-like treatment, performed at the LNGS clean room, in order to confirm the suggested *surface hypothesis*.

3) to test and to characterize for the first time the new flat-pack thermistors.

The CCT2 was carried out using the CAW tower with the same frames, PTFE and polyethylene used for the CCT1. The tower is composed by three floor and the involved crystals are the following:

- 2 old crystals, already tested in the past (B64 and B68), grown with the CUORICINO like procedure (*standard-procedure*) and treated at the LNGS following the RAD technique.
- 6 *new-style* crystals (BA1, BA2, BB1, BB2, BC1, BC2), already tested in the CCT1 run, completely processed in China following the *new-protocol* and mechanically reprocessed at the LNGS following the RAD technique.
- 4 new crystals (B71, B72, B73, B74) supposed to be grown with the *standard-procedure* and mechanically treated in China following the RAD procedure (lapping with old chinese powders, chemical etching, polishing with SiO_2 powder and old lapping pad).

All crystals, excluding B64 and B68, are equipped with double thermistor for a double readout. The ex-CCT1 have two classic thermistor (#31 series-like) while the 4 new crystals have one classic thermistor and one new flat-pack.

The preparation was completed in the first week of November and the tower was cooled down in second half of the same month. During the cooling process we have lost 3 sensors over 22 (13.6%) and 2 heaters over 12 (9%). In the case of bolometers provided with one heater and NTD-thermistor this would correspond to 22.6%. In fatc, three sensors of the CCT1 crystals are disconnected (BA2-right, BB1-right and BB2-left) and two crystals, one CCT1 (BA1) and one new (B71), have the heater disconnected. The base temperature in this run is higher than in the previous run (CCT1).

6.4.5.1 Detector performances

After about 1000 hours per crystal, the first results show that the performances of the *new-style* crystals after the RAD-like re-processing are improved. A direct comparison with the CCT1 is not easy to be done since the base temperature of the detectors is this time higher (the average value in CCT2 was $R_{\mathrm{base}} = 37$ MΩ with respect $R_{\mathrm{base}} = 631$ MΩ in CCT1, see tables 6.7 and 6.8). Despite this increase in the working temperature a quite higher pulse response is observed when comparing these crystals in CCT1 ($\Delta V/E = 41$ mV/MeV) and CCT2 ($\Delta V/E = 98$ mV/MeV).

When comparing crystal performances in CCT2 run with CUORICINO one can observe:

1) average resistance at the working point:

$$\begin{aligned} \text{CCT2:}\quad & R_{\text{base}} = (37 \pm 12)\ \text{M}\Omega \\ \text{CUORICINO:}\quad & R_{\text{base}} = (114 \pm 100)\ \text{M}\Omega \end{aligned} \tag{6.1}$$

for CCT2 are considered all the crystals while for CUORICINO only the *big-size* ($5 \times 5 \times 5\text{cm}^3$) from Run#1.

2) average pulse height:

$$\begin{aligned} \text{CCT2:}\quad & \frac{\Delta V}{E} = (112 \pm 76)\ \mu\text{V/MeV} \\ \text{CUORICINO:}\quad & \frac{\Delta V}{E} = (149 \pm 94)\ \mu\text{V/MeV} \end{aligned} \tag{6.2}$$

for CCT2 are excluded the flat-pack thermistors while for CUORICINO only the *big-size* crystals from Run#1 are considered.

3) time constant; *rise time* (t_r) and *fall time* (t_f):

$$\begin{aligned} \text{CCT1}\ \ (\textit{new-style}):\quad & t_r = 43\ \text{ms},\quad t_{f_1} = 166\ \text{ms},\quad t_{f_2} = 1400\ \text{ms} \\ \text{CCT2}\ \ (\textit{new-style}):\quad & t_r = 44\ \text{ms},\quad t_{f_1} = 168\ \text{ms},\quad t_{f_2} = 952\ \text{ms} \\ \text{CCT2}\ \ (\textit{all crystals}):\quad & t_r = 44\ \text{ms},\quad t_{f_1} = 157\ \text{ms},\quad t_{f_2} = 886\ \text{ms} \\ \text{CUORICINO}\ \ :\quad & t_r = 52\ \text{ms},\quad t_{f_1} = 156\ \text{ms},\quad t_{f_2} = 1700\ \text{ms} \end{aligned} \tag{6.3}$$

for CUORICINO only the *big-size* crystals from Run#2 are considered. The *fall time* is fitted using two exponential functions.

Considering the tables 6.7, it is easy to see that the performances of the flat-pack thermistor are worse than that of the classical NTD-thermistor assembled on the same crystal.

6.4.5.2 Detector background

The statistics collected so far in this run (about 1044 hours per crystal) allow us only to make some consideration about the polonium and about the rate in the energy region between 4 and 5 MeV, where the structures due to ^{238}U and ^{232}Th contaminations of the crystals should appear.

Two of the new crystals (B72 and B74) show a very high polonium rate (monochromatic peak at 5.4 MeV), of about 1000 and 2000 count/hour respectively, while the other two (B71 and B73) have a rate of 3.4 and 3.6 count/hour respectively. The analysis performed on the data acquired with the new PXI data acquisition system (see chapter 8) show, for one of these crystals, a rate of polonium pulses that decreases in time quite accordingly to the half life of ^{210}Po. The absence of evidence of ^{210}Bi seems to confirm that the contamination should be ascribed to ^{210}Po, and not to ^{210}Pb. The study of coincidences between B72 and B74 with the facing crystals seems to indicate a bulk origin for these contaminations.

The rates obtained in the different energy regions are shown in tables 6.9 and 6.10. As it can be seen from table 6.10 and figures 6.17 and 6.18, the surface treatment performed on *new-style* crystals, following the RAD procedure, results in a lower counting rate in the ^{238}U and ^{232}Th peak region between 4 and 5 MeV. We need anyway more statistics to get to a safe conclusion about the origin of this contamination. The higher rate in the 6-8 MeV region (table 6.9) shown by the *new-style* crystals in CCT2 run is due to residual heater pulses (pulses not flagged in the analysis).

A surprising high rate is obtained in the 2.7-3.2 MeV region (table 6.6), confirming the indication already noted in the CCT1 run. Given the changes between CCT1 and CCT2 (four crystals are different, all the crystals are in different position and so on) this increased background seems to be due to something external to the crystals (for example the copper mounting structure is a new one). It is however difficult to define which kind of contamination could give rise to such a background shape. The two new crystals (B73, B71) seems to count more in this region, however looking to the distribution of the counts on the single crystals this is not definitely confirmed because of a large spread in the counting rate.The new crystals record a higher rate also below the 2.6 MeV peak (see figure 6.19).

6.4.6 The CCT conclusion

The CCT runs aimed at verifying the quality of crystals and crystal surface treatment on the way to CUORE. The results obtained by comparing the two measurements

1) **Bulk contamination in ^{190}Pt**: either the *new-style* crystals and the new (B71 and B73) crystals shown a contamination compatible with the average value measured in CUORICINO. Possible slight differences in such a contamination are however not easy to be measured given the continuum underlying the peak.

2) **Bulk contaminations**: either in *new-style* crystals and in the new (B71 and B73) crystals, the bulk contamination is not observed. Because of low statistics, only limits can be given on this contamination. With the present sensibility, these limits are certainly comparable to the CUORICINO ones which were already enough for CUORE.

3) **Surface contamination**: for all the crystals the surface contamination is certainly contained below the Cuoricino levels. The peaks observed in the CCT1 run for the *new-style* crystals have disappeared after surface treatment. No significant coincidences are observed, but for a ^{210}Pb surface contamination. Up to now the sensitivity reached in CCT2 is not certainly enough to establish whether the surface contamination level is what needed for CUORE. For such a measurement a statistics higher than the one collected for the RAD is necessary.

4) An **excess rate**: is measured at least in the 2.7 - 3.2 MeV (both in CCT1 and CCT2). The identification of the possible sources of this background require the analysis of both gamma and alpha regions in the different crystals, comparing rates in CCT1 and CCT2 runs. Apparently this excess has nothing to do with crystals, since it is unaffected after crystal treatment and it is observed also in old crystals spectra. Due to the present low statistics and to the usual problems in detectors (for instance the spread in heater peaks positions among the crystals) and due to the many changes that were mandatory introduced in this run, we could also never get an answer for this.

	Crystals	**Rate**
New-style crystals	BA1	18
	BA2	12
	BB1	7
	BB2	10
	BC1	16
	BC2	10
New CUORICINO-like	B71	16
	B72	Not acquired
	B73	24
	B74	Not acquired
Old CUORICINO-batch	B64	5
	B68	13

Table 6.6: Distribution of counts (counts/keV/kg/y) in the 2.7-3.2 MeV region.

New-Style Crystals

Detector	R_{base} [MΩ]		$\Delta V/E$ μV/MeV		FWHM (2615 keV)		FWHM (1460 keV)
	CCT2	CCT1	CCT2	CCT1	CCT2	CCT1	CCT2
BC2_TR	48	258	93.86	31	8	32	6
BC2_TL	36	200	130.76	19	6	58	4
BA2_TR	n.w.	1600	–	99	–	26	–
BA2_TL	76	404	193.38	30	9	49	4.4
BB1_TL	53	535	84.88	42	6	39	3.8
BB1_TR	n.w.	851	–	49	–	35	–
BC1_TL	9	246	20.63	13	13	14	6
BC1_TR	55	1410	93.41	93	28	17	15
BA1_TL	28	607	68.77	35	15	23	14
BA1_TR	24	615	45.85	46	20	21	14
BB2_TL	n.w.	286	–	10	–	18	–
BB2_TR	35	563	152.05	25	8	40	7

New Crystal (CUORICINO like)

Detector	R_{base} [MΩ]		$\Delta V/E$ μV/MeV		FWHM (2615 keV)		FWHM (1460 keV)
	CCT2	CCT1	CCT2	CCT1	CCT2	CCT1	CCT2
B74_TL	62	a.	24	a.		a.	
B74_TR	39	a.	64	a.		a.	
B72_TR	38	a.	200	a.		a.	
B72_TL	6	a.	5	a.		a.	
B73_TR	27	a.	53.11	a.	10	a.	7
B73_TL	24	a.	66.86	a.	7.4	a.	4.8
B71_TR	30	a.	55.4	a.	16	a.	5
B71_TL	42	a.	56.55	a.	6.7	a.	12

Old Crystals (CUORICINO batch)

Detector	R_{base} [MΩ]		$\Delta V/E$ μV/MeV		FWHM (2615 keV)		FWHM (1460 keV)
	CCT2	CCT1	CCT2	CCT1	CCT2	CCT1	CCT2
B64_T	90	843	96.56	204	6.7	8	4
B68_T	133	2538	316.17	564	6.6	7	3.7

Table 6.7: Pulse height and energy resolution for the two different CCT detectors. In blue the values for the flat-pack thermistor are reported.
n.w. = not working, a. = absent.

New-Style Crystals

CCT2					CCT1				
Detector	t_r [ms]	t_{f_1} [ms]	t_{f_2} [ms]	**Ratio**	**Detector**	t_r [ms]	t_{f_1} [ms]	t_{f_2} [ms]	**Ratio**
BC2_TR	41	238	645	0.3	BC2_T1	42	250	1411	0.08
BC2_TL	40	252	655	0.24	BC2_T2	51	291	2168	0.06
BA2_TR	Not Working				BA2_T1	62	63	–	
BA2_TL	49	85	781	0.05	BA2_T2	39	119	2120	0.03
BB1_TL	35	149	839	0.18	BB1_T2	45	135	2159	0.04
BB1_TR	Not Working				BB1_T1	28	120	1733	0.04
BC1_TL	37	123	1370	0.14	BC1_T1	48	149	1072	0.13
BC1_TR	45	107	1069	0.07	BC1_T2	42	94	657	0.05
BA1_TL	51	182	1120	0.17	BA1_T2	46	235	1487	0.14
BA1_TR	55	185	1130	0.24	BA1_T1	48	170	1042	0.08
BB2_TL	Not Working				BB2_T2	43	167	282	0.04
BB2_TR	43	199	961	0.13	BB2_T1	41	142	1871	0.03

New Crystal (CUORICINO like)

CCT2				
Detector	t_r [ms]	t_{f_1} [ms]	t_{f_2} [ms]	**Ratio**
B74_TL	39	181	794	0.16
B74_TR	41	188	882	0.13
B72_TR	31	143	572	0.08
B72_TL	57	157	708	0.35
B73_TR	38	197	789	0.20
B73_TL	43	182	773	0.26
B71_TR	40	125	744	0.18
B71_TL	61	96	715	0.08

Old Crystals (CUORICINO batch)

CCT2					CCT1				
Detector	t_r [ms]	t_{f_1} [ms]	t_{f_2} [ms]	**Ratio**	**Detector**	t_r [ms]	t_{f_1} [ms]	t_{f_2} [ms]	**Ratio**
B64_T	28	84	1169	0.11	B64_T	79	108	1292	0.04
B68_T	36	110	1129	0.07	B68_T	60	71	1058	0.02

Table 6.8: Rise and decay constants. In the table the results obtained in the CCT2 (left) and CCT1 (right) measurements are compared.

CUORICINO							
Analysis	**Detector**	**Continuum**		**^{190}Pt**		**Continuum**	
		2700-3200	**Err.**	**3200-3400**	**Err.**	**3400-3900**	**Err.**
Anticoincidence	CUORICINO	0.12	0.00	0.52	0.01	0.12	0.00
Multiplicity 2	CUORICINO	0.01	0.00	0.02	0.00	0.01	0.00
RAD							
Anticoincidence	RAD	0.06	0.01	0.37	0.05	0.08	0.02
Multiplicity 2	RAD	0.02	0.01	0.04	0.02	0.01	0.01
CCT1							
Anticoincidence	New-style	0.30	0.06	0.39	0.11	0.16	0.04
Multiplicity 2	New-style	0.05	0.02	–	–	0.01	0.01
Anticoincidence	Old (B64, B68)	0.30	0.10	0.34	0.17	0.14	0.07
Multiplicity 2	Old (B64, B68)	–	–	–	–	–	–
CCT2							
Anticoincidence	New-style	0.27	0.03	0.48	0.07	0.15	0.02
Multiplicity 2	New-style	0.02	0.01	0.04	0.02	0.01	0.01
Anticoincidence	New (B73, B71)	0.43	0.07	0.51	0.12	0.19	0.05
Multiplicity 2	New (B73, B71)	0.01	0.01	0.03	0.03	0.01	0.01
Anticoincidence	Old (B64, B68)	0.19	0.05	0.27	0.08	0.10	0.03
Multiplicity 2	Old (B64, B68)	0.02	0.02	–	–	0.01	0.01

Table 6.9: Counting rates (counts/keV/kg/y) in the energy region between 3 and 4 MeV.

CUORICINO							
Analysis	**Detector**	**U and Th peaks**		**^{210}Po peak**		**U and Th peaks**	
		4000-5000	**Err.**	**5000-6000**	**Err.**	**6000-8000**	**Err.**
Single	CUORICINO	0.52	0.00	0.96	0.01	0.20	0.00
Multiplicity 2	CUORICINO	0.10	0.00	0.18	0.00	0.07	0.00
RAD							
Single	RAD	0.17	0.02	0.73	0.03	0.03	0.00
Multiplicity 2	RAD	0.01	0.00	0.15	0.01	0.01	0.00
CCT1							
Single	New-style	0.63	0.06	142.00	0.89	0.12	0.02
Multiplicity 2	New-style	0.03	0.01	1.17	0.08	0.02	0.01
Anticoincidence	Old (B64, B68)	0.30	0.07	2.39	0.20	0.07	0.02
Multiplicity 2	Old (B64, B68)	0.02	0.02	0.03	0.02	0.01	0.01
CCT2							
Anticoincidence	New-style	0.24	0.02	76.8	0.37	0.96	0.03
Multiplicity 2	New-style	0.03	0.01	1.16	0.05	6.18	0.07
Anticoincidence	New (B73, B71)	0.35	0.04	39.7	0.46	0.03	0.01
Multiplicity 2	New (B73, B71)	0.02	0.01	0.49	0.05	0	0
Anticoincidence	Old (B64, B68)	0.23	0.03	2.06	0.11	0.03	0.01
Multiplicity 2	Old (B64, B68)	0.02	0.01	0.12	0.03	0.01	0.01

Table 6.10: Counting rates (counts/keV/kg/y) in the alpha region above 4 MeV.

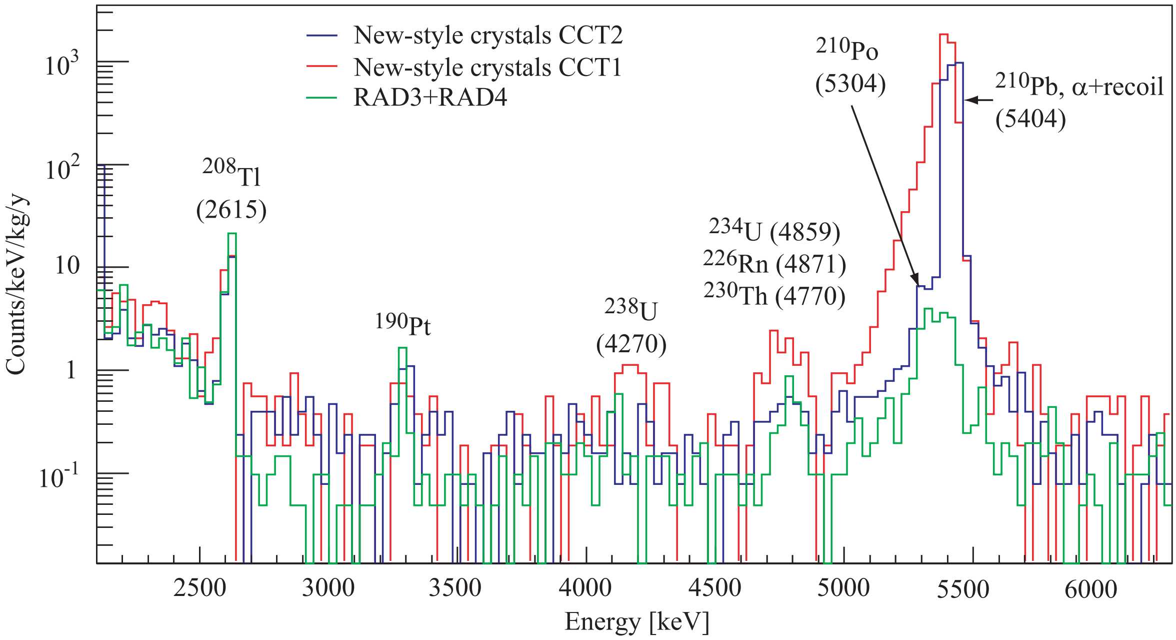

Figure 6.17: Comparison among RAD (green line), *new-style* as arrived from China (CCT1, red line) and *new-style* after surface treatment (CCT2, blue line).

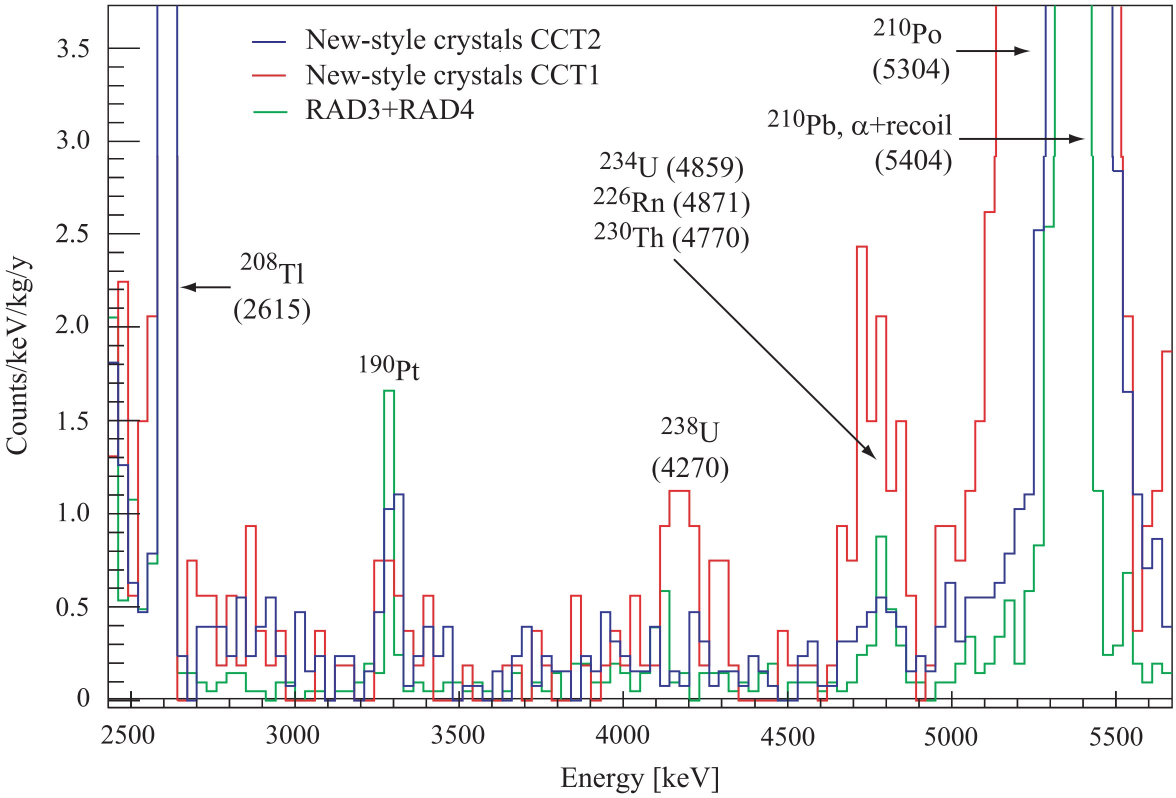

Figure 6.18: Comparison among RAD (green line), *new-style* as arrived from China (CCT1, red line) and *new-style* after surface treatment (CCT2, blue line): zoom in the alpha region. The ^{190}Pt peak is clearly visible. The reduction of ^{238}U peaks the *new-style* crystals (at about 4.2 and 4.7 MeV) is evident.

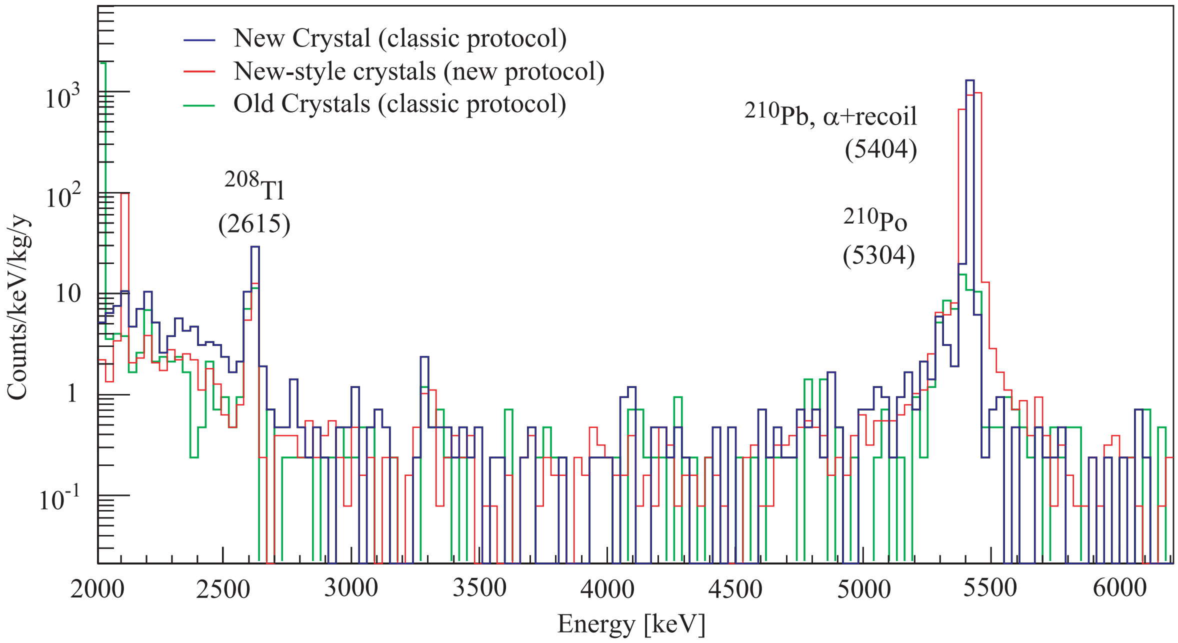

Figure 6.19: CCT2 background. Comparison of the new crystals (B73 and B71, the two with low ^{210}Po contaminations) background (blue line) with new-style (red line) and old crystals (B64 and B68, green line).

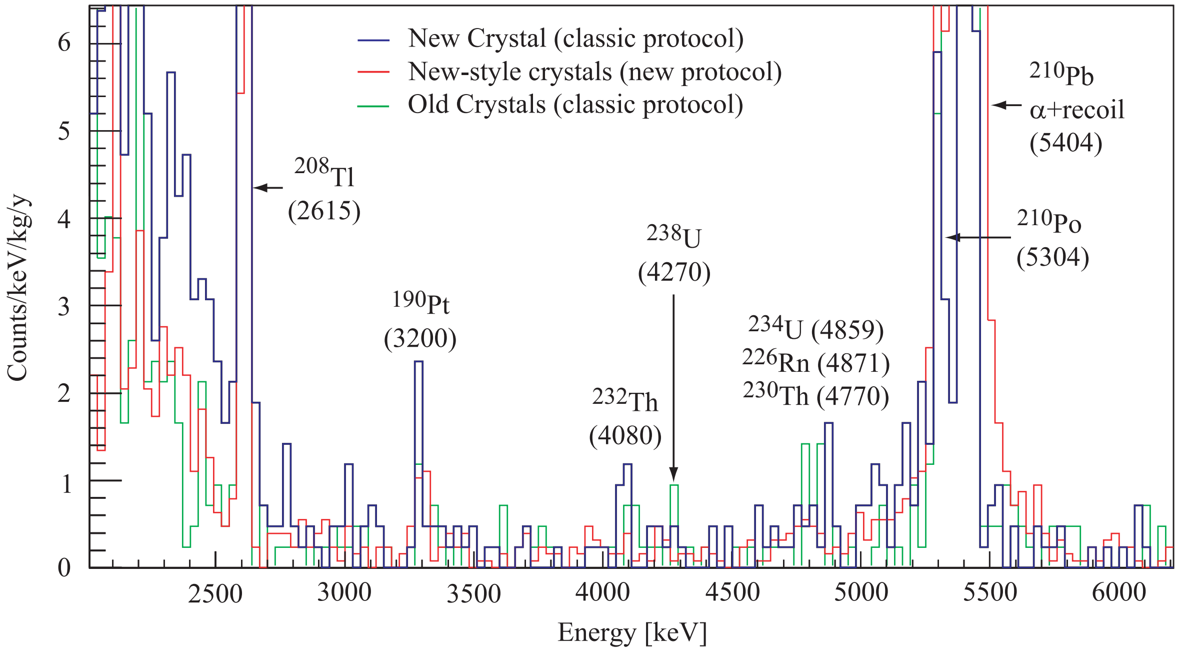

Figure 6.20: CCT2 background: zoom in the alpha region.

PART III

TECHNICAL ASPECTS

Chapter 7

CUORICINO/CUORE electronics

7.1 Introduction

Although CUORE will have more channels respect to CUORICINO, the design of their electronics will be very close each other. Due to this, modifications needed to upgrade the system of CUORICINO to that of CUORE are already defined.

The electronics of CUORE/CUORICINO[203, 204, 205, 139] is composed by four main parts:

1) **Front-End Boards**, these furnish a bias current to the NTD thermistor and receive and process the resulting signal-bearing voltage.

2) **Bessel Boards**, these filter the signal in order to get a better signal to noise ratio.

3) **Pulser Boards**, these boards are used to allow a continuous stabilization of the energy conversion gain of the whole detector.

4) **Voltage Supply**, this is a system composed of many supply voltage boards guarantees very stable and low noise ±10V line.

The design of the electronics system should satisfy many specifications, the four major issues can be summarized as follow:

1) The entire system and, in particular the biasing and the pre-amplifier circuitries should be characterized by a small noise contribution especially in the frequency band of the detector signal (from one to few tens of Hertz).

2) It should accommodate the broad spread of manufacturing characteristics that are typical for each bolometer/thermistor module. For example the optimal current bias it's different for every channel and ranges from 150 pA pA to 300 pA. Without a tuning the signal amplitude could exhibit a corresponding spread that could exceed the full dynamic of the acquisition system.

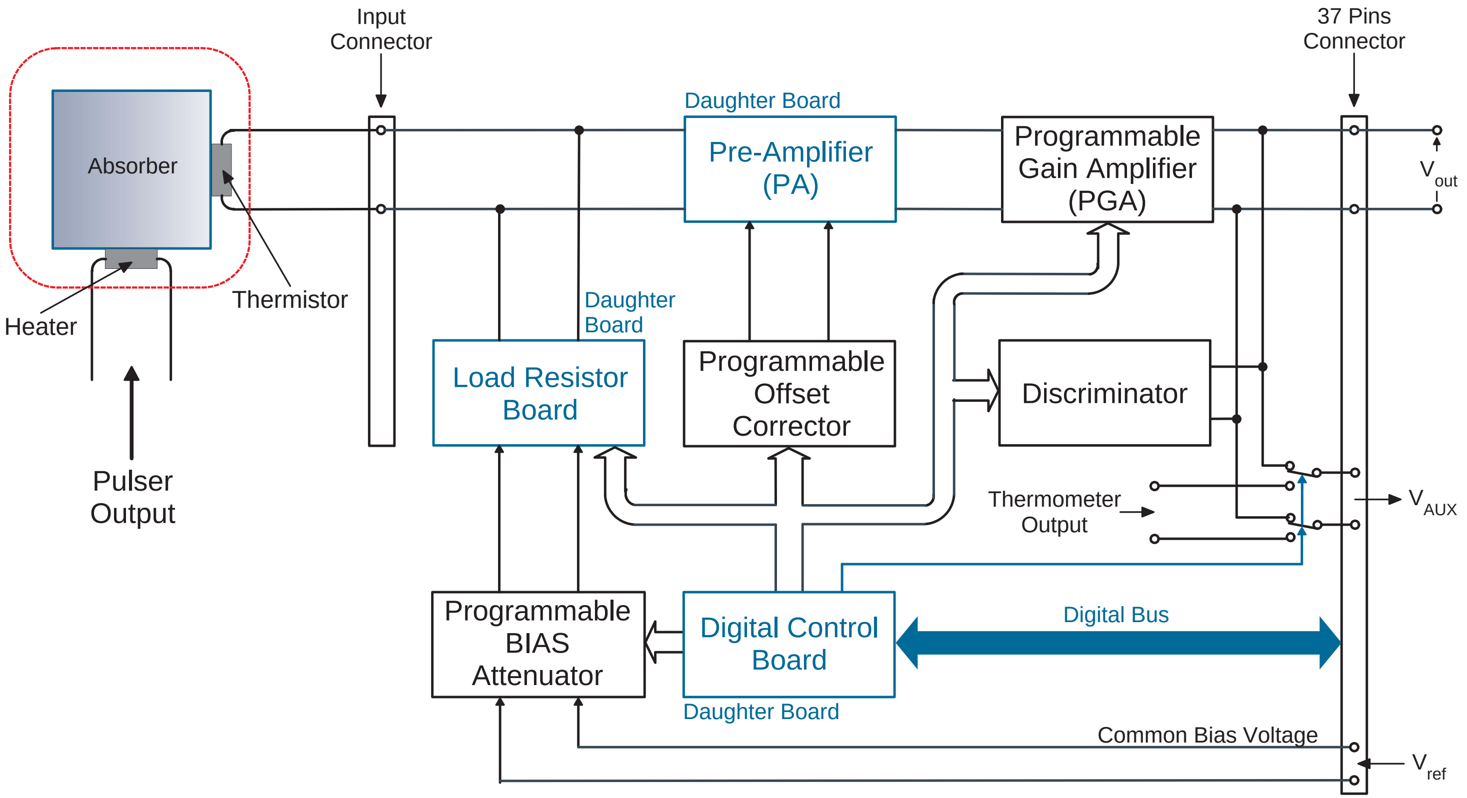

Figure 7.1: Schematic of one channel of the two present on each CUORICINO main board (MB).

3) It should enable measurement *in situ* of the bolometer characteristics (load curves, optimum working point and so on).

4) The design should incorporate a high level of remote programmability in order to avoid mechanical interventions in the vicinity of the detector during the measurements.

This chapter presents a brief discussion of the circuitries able to address these issues and presently used for the CUORICINO

7.2 Front-End Board

The signal variation across the NTD thermistor (consequence of the particle interactions with the absorber) is in the order of $\Delta V_{\mathrm{Th}} = (100 \div 200)\ \mu\mathrm{V}$. It's clear that to obtain an acquirable dynamic signal an amplification is needed. This amplification is provided by the Front-End board[203] (figure 7.1).

The Front-End board (also called Main Board) is used to amplify the voltage variation across the NTD thermistor. Each board includes two complete analog channels and their associated logic circuitries. It also has its own digital logic section, which communicates with the remote control and customizes the parameters of the associated analog section. The logic section is implemented as a daughter card of the Main Board (MB). The preamplifier portion of the analog section and the load resistor system are also on daughter cards. A single input connector at the rear of the MB serves both channels.

A Front-End crate accommodates 15 Front-End boards and, for CUORE, 33 crates will be needed for a total of $N_{\mathrm{TOT}} = 33 \cdot 15 \cdot 2 = 990$ channels. Each crate also accommodates a very stable low-noise voltage supply/reference to service all the cards present inside it[206].

The single blocks that constitute each board are described in the following sections.

7.2.1 The load resistor and the biasing systems

As described in the previous chapters, the NTD thermistor converts the thermal signal into a voltage signal. As shown in figure 7.2, the bias current for the thermistor is sourced through a pair of low-noise large value *thick-film* 27 GΩ resistors manufactured by SIEGERT Electronic©. These resistors are accommodated in a specific daughter board. They have been selected for their $1/f$ noise when biased at the current levels required by the detectors[207]. V_{b1} and V_{b2} are the voltage delivered by the programmable bias attenuator. The circuit in input to the preamplifier is in a differential configuration in order to suppress possible common effects like the adjacent channel crosstalk and like the microphonic noise induced by wire vibration.

The load resistor daughter card also accommodates a pair of 6.8 GΩ resistors. By means of a bistable relay it's possible to connect this pair in parallel with the 27 GΩ resistors with the purpose to allow the I-V characterization of the thermistor *in situ*. The total load resistor switches from $R_\mathrm{L} = 2 \cdot 27 = 54$ GΩ to $R_\mathrm{L} = 2 \cdot (6.8//27) \simeq 10.9$ GΩ.

The large spread in bolometer operating point, between 150 pA to 300 pA, requires that the bias current of each channel must be individually adjusted. In addition the I-V characteristic of the bolometer must be explored over a large range[208]. For these reasons each channel includes a dual programmable attenuator which produce the dual bias voltage as an adjustable fraction of a common reference voltage. The circuit is a 5-bit R-2R ladder network with optical isolation from its digital commands. The voltages V_b1 and V_b2 can be set by the following law:

$$V_\mathrm{b1} = -V_\mathrm{b1} = \frac{n}{2^5} \cdot \frac{V_\mathrm{ref}^{+} - V_\mathrm{ref}^{-}}{2} \tag{7.1}$$

where V_ref^{+} and V_ref^{-} are derived from an Agilent Technologies© 6627A system power supply, common to all modules. The quantity $|V_\mathrm{ref}^{+} - V_\mathrm{ref}^{-}|$ may be set as high as 60 V and n can be any integer value in the range from 0 to 2^5. The values of the two voltages V_b1 and V_b2 can be set remotely. The programmable bias attenuator also provides the additional feature of inverting the polarity of the bias voltage (polarity selector, figure 7.2). This feature is very useful since by reversing the bias during the DC characterization it's possible to avoid the common effects (leakage currents and offset voltages) introduced by the electronics.

The maximum calculated deviation of the bias attenuator circuit from an ideal R-2R ladder is $\simeq 5\%$. The noise measured between the outputs node is 28 nV/$\sqrt{\mathrm{Hz}}$ at 1 Hz, which is negligible compared with 20 nV/$\sqrt{\mathrm{Hz}}$, the thermal noise of the 27 GΩ resistors[204].

7.2.2 The pre-amplifier

The design of the preamplifier must satisfy four main requirements:

1) It must be a voltage amplifier configuration that allows floating inputs which make biasing naturally compatible with DC coupling.

2) It must be in differential configuration. Compared with a single-sided configuration the amplifier noise is doubled but the microphonic noise, originating in the leads that connect the preamplifier with the bolometer, and inter-channel crosstalk can be largely suppressed.

3) It must minimize the noise in the frequency interval from 1 Hz to a few tens Hz (the bandwidth of the acquired bolometer). The CUORICINO preamplifier

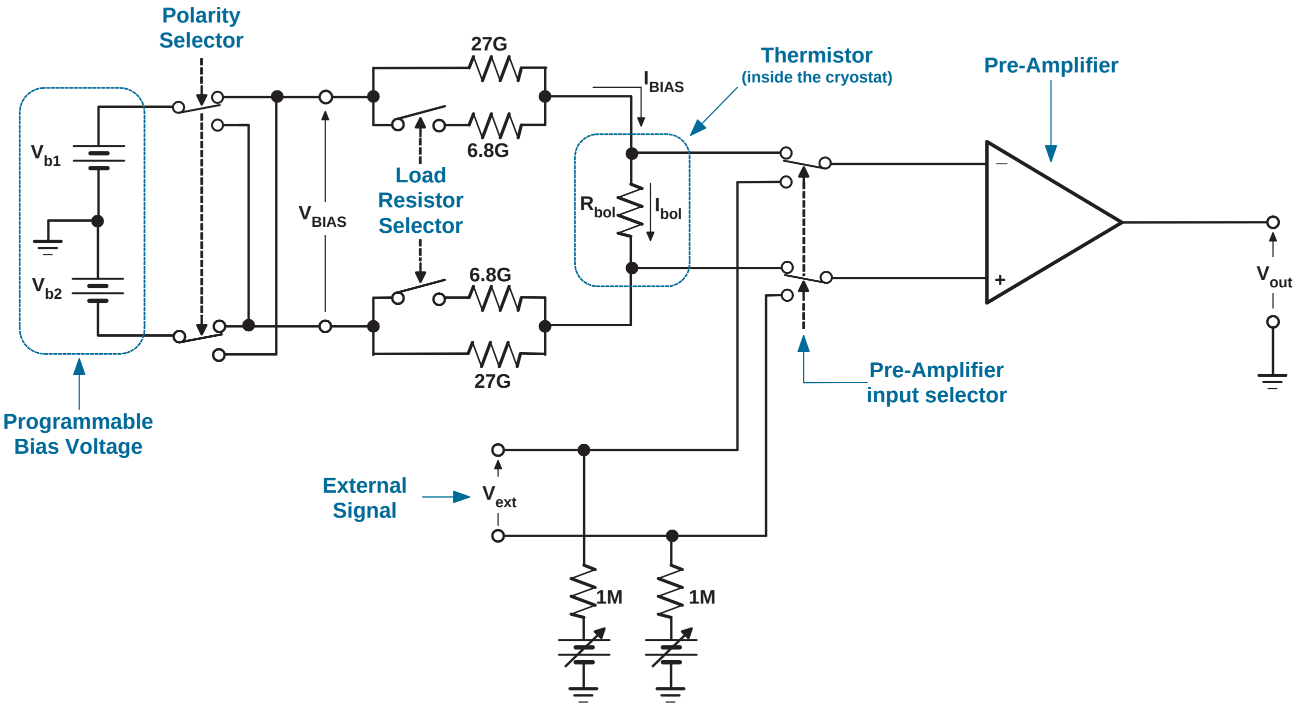

Figure 7.2: Configuration options at the preamplifier input.

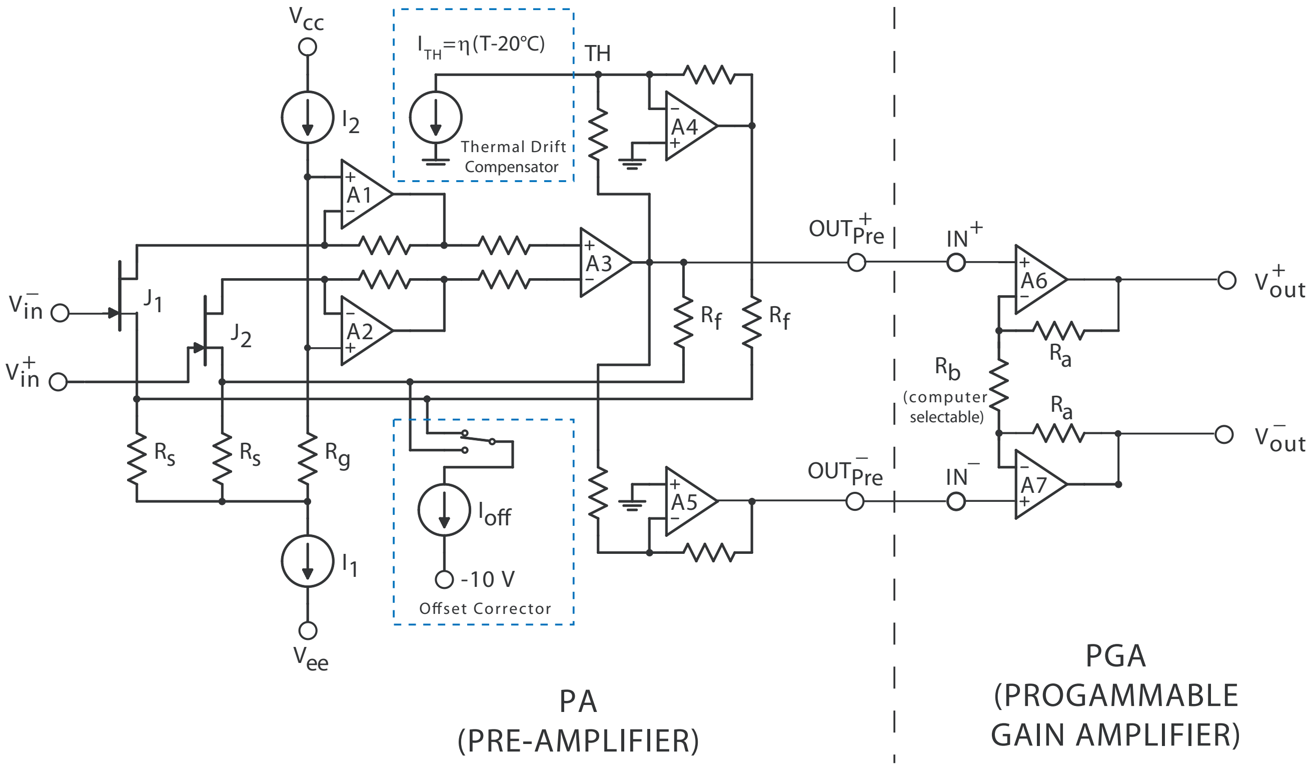

Figure 7.3: Schematics of the preamplifier (PA) and the programmable gain amplifier (PGA).

is characterized by a voltage noise of 3 $\mathrm{nV}/\sqrt{\mathrm{Hz}}$ that becomes 4 $\mathrm{nV}/\sqrt{\mathrm{Hz}}$ at 1 Hz[158].

4) It must cover the thermal instability that could drift the bolometer baseline. A special circuit, based on a diode that serves as a thermometer, is developed to maintain the drift below 0.2 μV/°C.

The core of the design is the JFET pair J_1 and J_2 (figure 7.3), which accepts the differential input. Appropriate biasing of these input JFETs can optimize parallel and series noise. A Small voltage drop between drain and source (V_{DS}) allows having small input noise gate current responsible for the parallel noise, and an adequate level of I_{DS} limits the amount of series noise. The operational amplifiers A_3 and A_4 close the feedback loop and establish the differential gain through the feedback resistor R_{f}. With $R_{\mathrm{f}} = 20\ \mathrm{K}\Omega$ and $R_{\mathrm{s}} = 180\ \Omega$ the gain is:

$$G_{\mathrm{PA}} = 2 \cdot \frac{R_{\mathrm{f}} + R_{\mathrm{s}}}{R_{\mathrm{s}}} \simeq 200\ \frac{\mathrm{V}}{\mathrm{V}} \tag{7.2}$$

The chosen working point for the JFETs is a compromise between an adequate level of gain, noise and power dissipation[204, 139, 158].

$$(V_{\mathrm{DS}},\ I_{\mathrm{DS}}) = (0.8\ \mathrm{V}\ ,\ 1.5\ \mathrm{mA}) \tag{7.3}$$

The input JFETs in the pre-amplifier circuit are not individually compensated for the ambient temperature drift. However, it's possible to deal with this issue by trimming the circuit as a whole. First one operates the circuit in a *temperature-controlled chamber* in order to characterize its thermal response. Then a current proportional to the temperature is injected in the virtual ground labeled TH in the figure 7.3. This current will cancel the measured drift. The sensitive component of the thermal drift compensation circuit is a diode that serves as a thermometer. The component chosen is a PNP transistor BC858, which at a bias of 100 μA has a low frequency noise between 20 and 30 $\mathrm{nV}/\sqrt{\mathrm{Hz}}$[204]. The correction current is given by:

$$\Delta I_{\mathrm{Th}} = \pm\, 2 \cdot \frac{\mathrm{mV}}{{}^{\circ}\mathrm{C}} \cdot \frac{T - T_0}{R_{\mathrm{TH}}} = \eta(T - T_0) \quad \text{with} \quad \eta = \pm\, 2 \cdot \frac{\mathrm{mV}}{R_{\mathrm{TH}}\ {}^{\circ}\mathrm{C}} \tag{7.4}$$

where $T_0 \simeq 20$°C and R_{TH} is the resistance trimmed in the temperature-controlled chamber. The magnitude of the coefficient η is proportional to the value of this resistance, which, essentially converts the junction voltage to a current.

In addition, the pre-amplifier daughter card accommodates an analog thermometer based on the integrated-circuit LM50 (Single-Supply Centigrade Temperature Sensor), which allows the monitoring of the preamplifier temperature remotely via the FE board auxiliary output.

The input offset of the preamplifier is the sum of two contributions: the asymmetry of the input JFETs and, being the bolometer DC coupled, the bias voltage of the NTD thermistor. In situations like these a system for offset trimming is very convenient. The offset corrector designed for the CUORICINO pre-amplifier is able to compensate the input offset from −80 mV to 80 mV under the control of a digital section. The correction current is supplied by means of a circuit based on a 12-bit digital to analog converter DAC8043A. This is less noisy than ordinary DACs because it omits the conventional output buffer (typically very noisy). In order to minimize the low frequency noise due to this converter (proportional to the square of the reference applied voltage) the voltage reference is chosen sufficiently low, but, in this way the DAC8043A swings the output until just 20 mV, i.e. 1/4 of the maximum output excursion. The additional 60 mV are afterwards obtained by injecting in the output node a current provided by two low noise resistors digitally controlled by switches. Through another digitally controlled switch it is possible to invert the polarity of the total correction current.

7.2.3 The programmable gain amplifier

The outputs of the pre-amplifier drive the differential inputs of the programmable gain amplifier, which is the final stage of the analog signal processing chain. This circuit provides a digital choice among several values of gain through the selectable resistance R_b(figures 7.3, 7.4). This resistance is a combination of a set of five resistor obtaining $2^5 = 32$ possible values. The resulting gain takes values from 1 to $\simeq$ 22 V/V for a total gain from 220 to $\simeq$ 5000 V/V. All components used have an adequate low frequency noise behavior.

7.2.4 The digital control board

The main purpose of the *Digital Control Board* (DCB) is the configuration of the parameters that influence the analog signal processing chain. In CUORICINO the communication with the remote controller (generally a personal computer) is performed using a I2C bus (*Inter-Integrated Circuit*). The I2C is a multi-master serial computer bus, invented by Philips©, typically used to connect low-speed peripherals to a motherboard. This serial bus uses only two bidirectional open-drain lines, Serial Data (SDA) and Serial Clock (SCL), pulled up with resistors.

Each channel in the system has a unique address 7-bit length and the remote control communicates with one channel at time. The rudimentary protocol proceeds through four steps: addressing the channel, sending the command, transferring the data and closing the communication. An oscillator based on the NE555 timer chip furnishes a 3.9 KHz clock to the DCB. Since the possible electrical noise originating from the clock is undesirable during the data-taking, the board can shut down the oscillator and the clock runs only when needed.

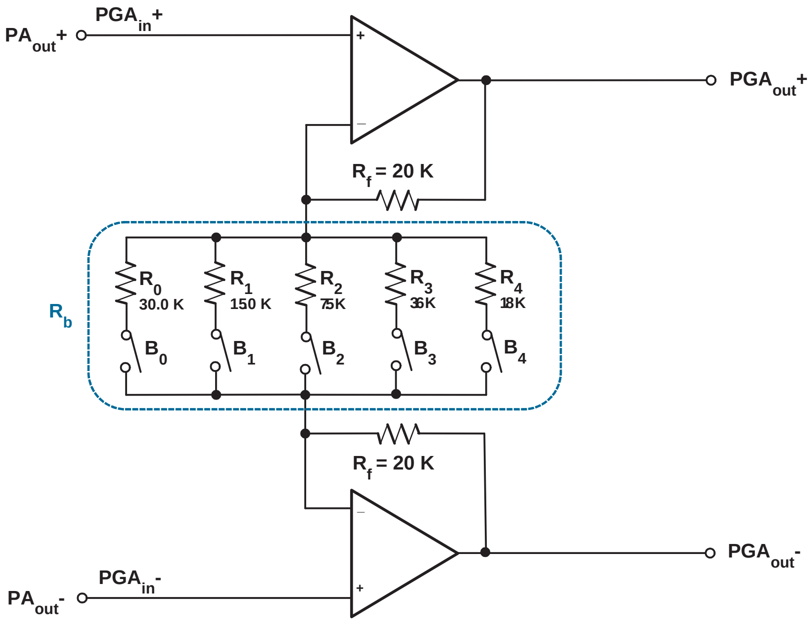

Figure 7.4: The programmable gain amplifier (PGA).

Each FE board has one DCB, which accommodates three Xilinx© XCR3128XL CPLD (*Complex Programmable Logic Device*) with 128 macro-cell[1]. Each single channel has one CPLD for the implementation of the DCB function. The third CPLD is shared by the two channels and manages the communication. A microcontroller (MCU) 8051, powered by Philips©, performs the I2C communications. The CPLDs chosen (Xilinx© XCR3128XL) have two main features. The first is that their outputs can remain active even when the board clock is idle, the second is the low current consumption.

All the programmable parameters of the Front-End board are grouped in six 8-bit registers. It's possible to read/write these registers remotely using the I2C bus by means of the digital control board.

The evolution of the programmable devices since the CUORICINO devices will allow to avoid the use of the CPLDs in favour of much cheaper microcontrollers in CUORE.

7.2.5 The wiring

In CUORICINO the connections from the thermistors to the cable-plug outside the cryostat (where the electronics is plugged) are realized in two steps using a twisted pair of wires. The first step, namely the connection from the thermistors to the cryostat's mixing chamber, is realized by means of twisted wires made of Constantan®[2]. The

---

[1] the macro-cell is an elementary digital building block of a CPLD.

[2] a copper-nickel alloy consisting of 60% Copper and 40% Nickel

second step, namely the connection from the mixing chamber to room temperature, is realized using twisted coaxial cables made of a core of superconductive NbTi alloy, having diameter of 100 μm, surrounded by a Copper-Nickel low resistance alloy. Each twisted pair is isolated by a Teflon® layer and shielded by CuNi shell. Five stages of thermalization are used to cut the thermal conductance of the superconductive cables themselves. These five stages are located respectively at 4.2 K, 1.2 K, 600 mK, 50 mK and 5 mK plates. Each stage is made of a sapphire substrate anchored through a L-shaped copper support attached to the thermalized plate. The side anchored (bottom) is sputtered with gold, the other side (top) has twelve 1 mm wide tracks (gold-platinum), where the superconductive twisted wires are soldered. The total length of the leads is about 5 m.

In CUORE the best choice seems to be the following: the connection between the thermistors and the mixing chamber should be realized via Mylar®[3] strips with serigraphed pairs of wires at a distance of 0.2 mm one from the other and a ground wire at the same distance between each pair. The connections between the mixing chamber to room temperature should be realized by means of ribbon cables. These cables consist of several pairs of twisted Manganin®[4] wires (e.g., 12 pairs) evenly spaced and having the diameter of 100 μm.

7.2.6 The cold electronics

The front-end electronics discuss so far is all at room temperature, for this reason it is called *warm electronics* (WFE). In reality, in the CUORICINO experiment two front-end configurations are being investigated. The former consisting of 38 channel completely operated at room temperature, while the latter consisting of 24 channel characterized by an additional first differential unity gain buffer stage at low temperature (*cold electronics*, CFE). The main reason for these two prototypes is to estimate the effect of the common mode noise (due to microphonism) of the connecting wires on the detector energy resolution at low energy, in order to achieve the maximum possible sensitivity at threshold.

The additional stage is inserted near the 4.2 K plate of the dilution refrigerator, therefore much closer to the detectors. Each cold stage is a differential buffer composed by two Si-JFETs that work in source-follower configuration. The working temperature, fixed by a dedicated heater, is 110 K, optimum value for the silicon. This solution reduces the length of the leads to about 1 m, while the remaining part of the wiring from the cold stage to room temperature is driven by the low impedance of the buffer.

Each cold buffer, together to the load resistors, is located on a board that accommodates 6 channels. A thermally shielded metallic box contains two of such boards. Inside the boxes the boards are suspended by means of nylon wires that have a small

---

[3] biaxially-oriented poly ethylene terephthalate (boPET) polyester film used, typically, in the field of electrical insulation.

[4] trademarked name for an alloy of typically 86% copper, 12% manganese, and 2% nickel

thermal conductance to the heat sink, at 4.2 K.

In CUORE only the warm electronics will be used. The reasons are the following. The more relevant microphonism sources are due to the mechanical friction between the detector and its mounting. Experimentally this type of noise has resulted much greater than that of the connection leads and, moreover, it isn't a common mode. Under these conditions it's clear that the use of a cold buffer stage isn't necessary. This fact will save a factor of two in the number of the connecting leads (two for the readout and two for the biasing in the case of cold stage) reducing the thermal power injection inside the fridge.

7.3 Bessel Board

The acquired bolometer signals are analyzed off-line by optimal filtering algorithms in order to maximize the signal to noise ratio. To obtain an adequate frequency response it is needed an anti-aliasing filter placed at the downstream of the analog signal processing (FE Board).

This filter is an active six-pole Bessel low-pass filter (LPF) which yields a roll-off of 120 db/decade. In order to adapt the bandwidth to every bolometer the cut-off frequency can be adjusted by a remote control between four possible values (8, 12, 16 or 20 Hz). One Bessel module (Bessel Board) accommodates three channels. One Bessel crate accommodates 15 Bessel Board and, for CUORE, $N_{\mathrm{TOT}} = 22 \cdot 15 \cdot 3 = 990$ channels will be needed.

A Bessel filter was chosen (also called *Thomson filter* or *maximally flat time delay filter*) as opposed to Chebyshev or Butterworth filters, so that the wave shape of filtered signals in the passband is preserved. This feature depends on its linear phase response, which produces an excellent pulse response and an almost constant group delay across the entire passband.

A n-order Bessel low-pass filter is characterized by its transfer function:

$$H(s) = \frac{\theta_n(0)}{\theta_n\left(\frac{s}{\omega_0}\right)} \qquad \text{where} \qquad \theta_n(x) = \sum_{k=0}^{n} \frac{(2n-k)!}{(n-k)!k!} \cdot \frac{x^k}{2^{n-k}} \tag{7.5}$$

where $\theta_n(x)$ is a *reverse Bessel polynomial*, from which the filter gets its name, and ω_0 is the cutoff frequency. A six-order filter is generated by a cascade of filtering-cells, where each single cell is a two-order VCVS filter (*Voltage-Controlled Voltage-Source*, figure 7.5(b)[209]). The Voltage-Controlled Voltage-Source, also known simply as a controlled-source filter, is a variation of the *Sallen-And-Key* circuit (figure 7.5(a)). It replace the unity-gain follower with a non-inverting amplifier with a gain greater than one. The high input and the low output impedances, as well as the stable gain of a non-inverting amplifier make it a good approximation for an ideal filter; moreover, the gain is simply tuned through the resistances R_{A} and R_{B}. The transfer function is:

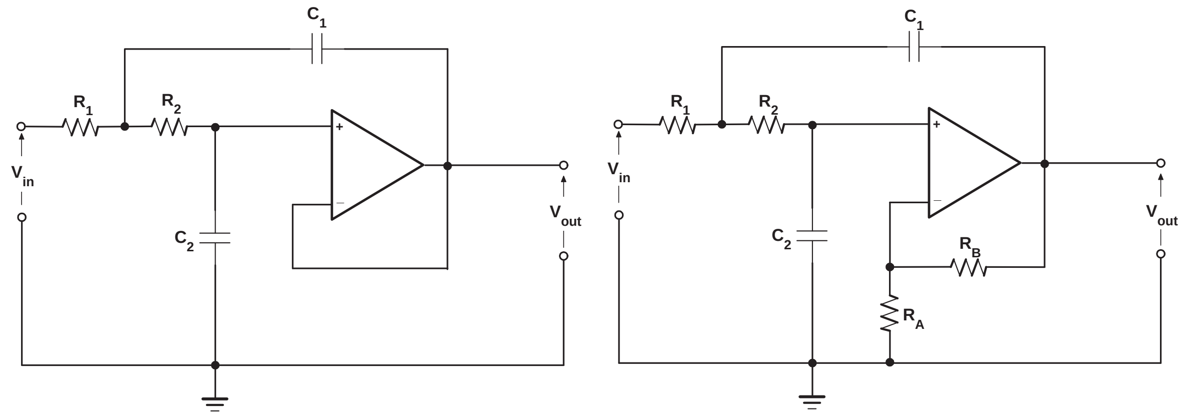

(a) Low Pass Sallen-And-Kelly architecture, the DC gain is unitary ($K = 1$).

(b) VCVS architecture, the DC gain is given by $K = 1 + \dfrac{R_\mathrm{B}}{R_\mathrm{A}}$

Figure 7.5: Active Low Pass Filters

$$H(s) = \frac{K \cdot \dfrac{1}{R_1 R_2 C_1 C_2}}{s^2 + s\left[\dfrac{1}{R_1 C_1} + \dfrac{1}{R_2 C1} + \dfrac{1-K}{R_2 C_2}\right] + \dfrac{1}{R_1 R_2 C_1 C_2}} = \tag{7.6}$$

$$= \frac{K \cdot \omega_0^2}{s^2 + 2\xi s \omega_0 + \omega_0^2} \tag{7.7}$$

where the coefficients ω_0, K and ξ are:

$$\text{the cutoff frequency:} \quad \omega_0 = \frac{1}{\sqrt{R_1 R_2 C_1 C_2}}$$

$$\text{the zero frequency gain:} \quad K = 1 + \frac{R_\mathrm{A}}{R_\mathrm{B}}$$

$$\text{the damping factor:} \quad 2\xi = \frac{1}{Q} = \sqrt{\frac{R_2 C_2}{R_1 C_1}} + \sqrt{\frac{R_1 C_2}{R_2 C_1}} + (1-K)\sqrt{\frac{R_1 C_1}{R_2 C_2}}$$

and where Q is the *quality factor* of the filter. If $R_1 = R_2 = R$ and $C_1 = C_2 = C$ the damping factor results $2\xi = 1 - K$.

To construct a n-pole filter (where n is an even number) one need to cascade $n/2$ 2-pole VCVS filter cells. Within each single cell one use $R_1 = R_2 = R$ and $C_1 = C_2 =$

C. However the RC products for the different cells are different and must be scaled by the normalizing factor f_n (given by a standard design table, for more details see [209]) according to:

$$RC = \frac{1}{2\pi f_0 f_n} \tag{7.8}$$

For each 2-pole cells, once fixed the RC product and the damping factor ξ_i the single gain is given by $K_i = 3 - \xi_i$, with $i = 1, .., n/2$. The gains must be satisfy $K_1 < K_2 < ... < K_{n/2}$ in order to avoid dynamic range problems.

In the case of the CUORICINO Bessel board the values of the resistances R_1 and R_2 (for each single VCVS cell) aren't fixed, but selectable by means of two digitally controlled switch obtaining four possible cut frequency values (8, 12, 16 or 20 Hz). Through another switch is possible to enable or disable the filter. The total gain of the filtering chain is $\simeq 2$.

Each Bessel board accommodates also three analog-trigger circuits, each one AC coupled to the output of the relative anti-aliasing filter channel. The signal generated by the *trigger channel* could be used as an input for the hardware trigger of the data-acquisition system. The gain of the trigger channel is settable remotely to 4.2, 12.5, 21 or 29 V/V. The trigger circuit has a baseline restoration section[210] and an AC compensation network[211] in order to prevent any re-trigger effect that can arise from the presence of any trailing undershoot in the signal excursion. In fact, pulses from bolometers may exhibit trailing undershoots because of the coupling of the inductive part of their dynamic impedance with the shunting parasitic capacitances. The re-trigger compensating network time consants are selectable remotely to 14, 27, 53 or 66 seconds. The final element of the circuit is a two-pole Bessel low-pass filter. The cutoff of this filter tracks the cutoff of the anti-aliasing filter, but is 4 Hz higher in frequency. This features is used in the acquisition installed at the Hall C facility but is not being used in CUORICINO where the trigger is only software. The same will apply to CUORE.

All of the remotely configurable parameters of the Bessel board (anti-aliasing filter and analog trigger) are grouped in a 8-bit programmable register. Two bit for the gain, two bit for the cut frequency, two bit for the re-trigger time constant, one bit for the filter enable and, at the last, a bit flag to indicate if a hardware configuration is loaded. This register could be read/write from a remote control using a I2C bus. The serialization/parallelization of this register and the I2C protocol are implemented by a 128 macro-cell CPLD.

7.4 Pulser Board

In a bolometric experiment the stability of the energy conversion gain is very important. To calibrate, and maintain the calibration, a source of energetic particles cannot be left close to the detector (in order to not increase the radioactive background).

Typically one uses this technique only at the beginning of the measurement, during the measurement another solution is needed[205].

The solution adopted consists in the injection of a short pulse of power to the absorber using a small resistor (*heater*) supplied by an ultra-stable calibrated pulser. The detector array is composed of a tower having 13 floors and the heating resistors of every crystal that stay on a floor are all connected in parallel. The calibration pulse signals are sent in sequence, one floor at a time. In CUORE the layout will be different and the heater resistors that will stay in the same column (each tower has four columns) will be all connected in parallel.

Each pulse has a width much shorter than the detector's signal (the range is between 500 μs and few milliseconds). The bolometers are sensitive to the energy developed across the heating resistor. The parameter of interest is the quantity E_{G} given by:

$$E_{\mathrm{G}} = V_{\mathrm{G}}^2\, t_{\mathrm{w}} \tag{7.9}$$

where V_{G} is the pulse amplitude, t_{w} its width and E_{G} is the energy injected referred to one ohm. The calibration pulse signal should satisfy the following relationship:

$$V_{\mathrm{G}} = \sqrt{e \cdot \frac{R_{\mathrm{H}}}{t_{\mathrm{w}}}\, \alpha U_{\mathrm{C}}} \tag{7.10}$$

where R_{H} is the resistance of the heater (generally in the range from about 50 KΩ to 100 KΩ), e the charge of the electron ($e = 1.6 \cdot 10^{-19}$ C) and U_{C} the wanted calibration energy expressed in eV. The parameter $(1-1/\alpha)$ accounts for any amount of energy lost because of thermal conductive path towards the heat sink due to the heater connecting wires. An example considering an α factor of about 5, $R_{\mathrm{H}} = 100$ KΩ and $t_{\mathrm{w}} = 1$ ms, the amplitude V_{G} can be in the range $(2.8 \div 9)$ mV for energy calibration pulses of $(0.1 \div 1)$ MeV.

The principle of operation of the pulse generator is very simple (figure 7.6). The concept is to deliver a voltage supply by a precised buffered reference to the heater, when needed, through an analog switch. The solution adopted minimizes as much as possible any drift effect that can be added to the system.

The complete pulse generator is split into two parts (figure 7.6). The former, namely the circuitry that generates the analog pulses (*analog-mixed board*), is located on the top of the refrigerator, inside the Faraday's cage; the latter, (*clock-generator card*) is located outside the Faraday's cage. This last part is outside the cage because the precise 10 KHz clock, used to determinate the pulse duration, is always running and could produce electromagnetic interferences if located inside.

The main blocks that compose the analog-mixed board are the following:

- **The V-ref generator**: it's composed of two sub-parts. The first is a precision voltage reference based on the integrated circuit LT®1027, that furnishes a Vref = 5 V voltage. The second is a buffered heavy low pass filter connected

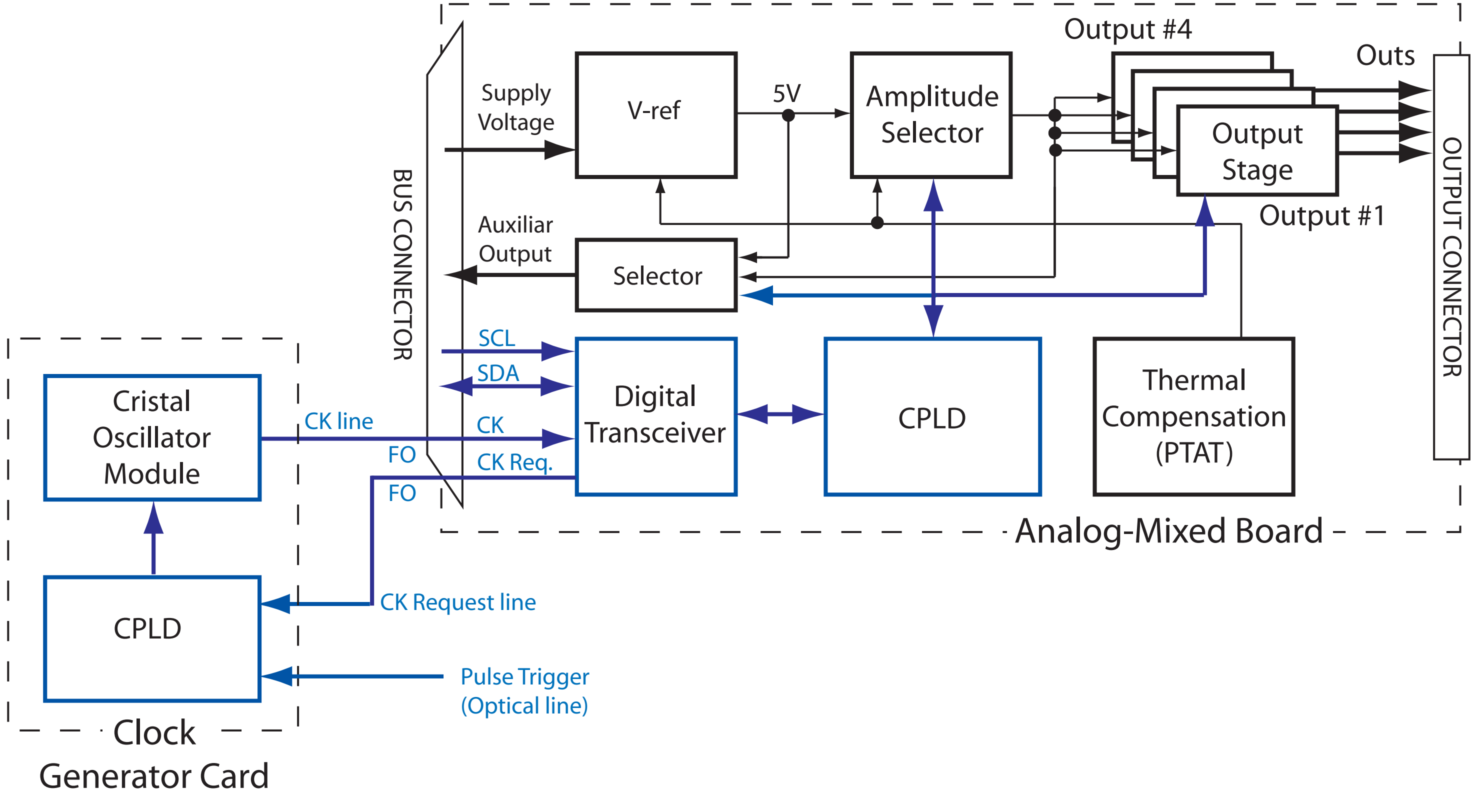

Figure 7.6: Complete schematic of the pulse generator system. The clock generation is remote (clock-generator card) and the communication is via optical fiber link.

at the previous voltage reference with the the intention of suppressing the noise. The trim input of the LT®1027 is used to add a voltage *Proportional To the Absolute Temperature* (PTAT). This voltage allows to compensate the thermal drift (about 2 ppm/°C) of this block .

- **The amplitude selector**: the main part of this block is a very precise and low drift R-2R 12-bit DAC (ADC7545A from National Devices©). The DAC has an input of 5 V voltage furnished by the V-ref generator and produces an output of 2^{12} possible voltage values in the range from 0 to $V\mathrm{ref}(2^{12}-1)/2^{12}$. The DAC output is inverted and buffered by means of two operational amplifiers, where an appropriate PTAT voltage corrects their drift.

- **The output stage**: it is an attenuator that reduces the voltage present at the input to the fraction required to produce the needed calibration power across the heater resistor. Three different attenuation levels are digitally selectable by an analog switch (ADG452 from National Devices©). The resistive attenuation network is realized using very stable and precise resistances and has less than 1 ppm/°C drift.

  In this stage the output pulse is created. In normal conditions of operation (no pulse) the out is a ground potential. This connection to ground is realized only with passive components, avoiding the presence of any possible DC offset. This condition is a very important requirement because any DC offset generates a constant heat injection that may increase the detector's temperature. If a pulse is to be given, the digital control connects the attenuator, controlling two analog switch, to the amplitude selector for the amount of time t_w and the *heater pulse* is created. As soon as the pulse width t_w is elapsed the digital control connects the output to the ground again. The pulse width can be digitally selected from 2^8 different values in the range between 100 μs and 25.5 ms.

  The output stage has four attenuators so one pulse generator system can drive four heaters. The voltage coming from the amplitude selector is multiplexed among these four channels, for this reason is possible to pulse them only one at a time.

- **The thermal compensation**: it consists of an analog thermometer (LM50B from National Semiconductor©) connected to two buffer amplifiers obtaining two voltages of opposite gain proportional to the temperature (PTAT voltages). Thanks to these two voltages it's possible to compensate drifts of any polarity.

- **The digital control**: the core of the digital control unit is a 256-macro-cell CPLD. The communication with the remote controller is via I2C bus using two fiber optic (FO) lines. Inside the CPLD two main blocks are implemented: the *bus manager* and the *board manager*.

> The *bus manager* controls the two FO lines (SDA, SCL) and de-serializes the data line to 8-bit internal bus of the analog-mixed board, or serializes the 8-bit internal parallel bus to the data line. The *board manager* has a double task: it configures the analog-mixed board in the basis of the pattern received remotely and provides the commands for the generation of the analog output pulses.
>
> It needs four 8-bit register to configure the analog-mixed board. The first is used for the determination of the analog pulse width to be generated, the second contains the eight least significant bits of the twelve bits of the DAC. The third register is divided into two equal parts; the least significant nibble coincides to the most significant bits of the DAC, while the most significant nibble coincides to four configuration bits (for example writing these bits it is possible to select the output that must be fired). The last register is divided in four pairs of bits and each pair selects the output attenuation of each of the four channels present on the board. There are only three possible values selectable (1/134, 1/201, 1/401), the remaining code is dedicated to the disconnection of the respective output when selected.

On the analog-mixed board a 500 Hz clock is used for the serial bus communication and for the board setting. It is normally in idle status and is waken up when either SDA or SCL lines change from their idle status. Differently the precise 100 μs clock used for the definition of the analog pulse width is generated on the clock-generator card and transmitted to the analog-mixed board by a clock FO line only when the clock request line is active.

The clock-generator card is based on a crystal oscillator module working at 10 MHz. A 128 macro-cell CPLD is present to provide the communication with the other elements of the system. The clock signal is transmitted using a fiber optic line (*Clock line*) in order to avoid ground loop and/or the conduction of electromagnetic interference inside the Faraday's cage. The CPLD polls the clock request and a *Pulse Trigger* FO line; when both are found active the clock signal is generated and transmitted.

The pulse generation is as follow. The remote system sets the first three bytes on the analog-mixed board. The fourth byte (output attenuation) needs to be set only once, typically at the start of the data taking. If the bit 7 of the third byte is high, the analog-mixed board sets the *Clock request* FO line. When the *Pulse Trigger* FO line is also set by the remote system (for example via a optical line coupled with a photodiode) the clock-generator card sends the 100 μs clock to the analog-mixed board via the *Clock* FO line and the pulse is generate following the parameters set in the configuration registers. When the pulse is generated the analog-mixed board clears the clock request signal, the clock signal generation ceases and the board go in the idle status. When a pulse generation is in progress all the write operations are disable to avoid any errors.

The pulses have a time duration very much shorter than the typical thermal response of the detector[139]. The Joule dissipation from the heater produces heat pulses in the crystal almost indistinguishable from those from γ-rays used as calibration lines. The heater pulses are used to measure (and later correct off line) the gain drifts. The pulses are generated in periodical sequence. In CUORICINO three different pulser amplitudes are used. The first and the last pulse of the sequence are severally characterized by lower and higher energies than the normal pulses (*central pulses*). The central pulses are used to calibrate the detector while the former and the latter are used respectively to correct the threshold stability and to check the effectiveness of the gain stability correction. In CUORICINO, the pulse sequence is produced with a frequency of about one in every 300 seconds, for each of the 62 bolometers. Any variation in the voltage amplitude recorded from the heater pulses indicates that the gain of that bolometer has changed.

Chapter 8

CUORE Data Acquisition System

8.1 Introduction

The second but not less important task of this Ph.D work was the development and testing of the CUORE Data Acquisition System (the so called Apollo suite). In these three years [1] I continually cooperated with the CUORE DAQ Working Group in order to define the best hardware configuration for the data acquisition system of the experiment and to develop the software necessary to operate it.

From the data acquisition point of view, CUORE is an enlarged version of CUORICINO. Despite that the CUORE DAQ will be a completely new system because some features needed in CUORE are absent in CUORICINO. The main missing features are:

1) possibility to perform the pulse coincidences on-line. When one bolometer will trigger the system will be able to acquire also the bolometers related to itself. In this way, for example, it will be possible to perform a first coincidence analysis among the fired crystals and the nearest neighbors (*side-pulses* technique).

2) possibility to use more trigger at the same time. More trigger algorithms could be running simultaneously. This means that as consequence of the trigger strategy used it will possible to divide the acquired events by energy, shape, rise time and so on.

3) capability to interact with the CUORE data base. The most important improvement with respect to the CUORICINO data base is that both the DAQ and the off-line analysis will be able to interact with data base. Possible automatic update will be done by data acquisition system and by analysis jobs while the collected informations will be used directly in the off-line analysis. This is a very important features because in CUORE the event rate will be higher and the amount of information, useful also for the analysis, will be larger.

---

[1] the first one spent at the Genova University and the last two wholly spent ad the Gran Sasso Underground Laboratories

4) possibility to control the CUORE electronics (Front-Ends, Bessels and Pulser) from the data acquisition system via a dedicated process (named `SlowServer`).

5) possibility to have a continuous data-taking. The system will store on disk the triggered data (as usual and then as in CUORICINO) but also the continuous data before triggers. In this way there is no loss of information and it will be possible to re-trigger the data off-line at any time allowing further and different analysis.

6) the data acquired by different channels will be correlated in space and in time and, if necessary, the system will perform a first rough analysis.

Apollo will be an automatic hardware/software system able to acquire signals coming from 988 bolometers, to monitor the detector's status, to correlate it last with the data acquired and, at last, to interface the experiment's electronics. As I will show in the next sections, to achieve either a resolution in agreement with the physics requirements and wide dynamic, the digitizing will be based on a nominal 18-bit ADC (the current CUORICINO acquisition is based on nominal 16-bit ADCs).

At the present day three Apollo prototypes are developed and used. These are severally installed: at the Genova INFN Laboratory (16 channels), at the Gran Sasso Electronics Laboratory (16 channels) and at the Gran Sasso Hall C R&D facility (48 channels). The first two are used to develop, test and debug the system while the latter, installed at the R&D facility during the 2007, is the only one really connected to real bolometers and it's used to perform the final debugging and to acquire real data. Starting from the first months of the 2008 it's scheduled the installation of a new system (80 channels) at the Gran Sasso Hall A cryostat in order to upgrade the CUORICINO data acquisition.

8.2 DAQ requirements

The DAQ system must be designed to read out the signals coming from each crystal. Before reaching the ADC, bolometric signals are amplified and shaped by an electronics chain, as described in previous chapter (section 7.2 and 7.3). The input stage of Data Acquisition system must match the features of the input signals. Moreover it is requested not to spoil the energy resolution of the detector. Below it is illustrated how the system design satisfies these requirements

- **Features of the input signal**: the CUORE/CUORICINO electronics provides pulses well described by the following typical parameters:

  1) differential signal V given by:

  $$V = V^{+} - V^{-} \tag{8.1}$$

  where V^{+} and V^{-} are two single-ended voltage levels of the differential pairs measured with respect to ground.

2) voltage amplitude of the differential signal in the range $(-10 \div 10)$ V;
3) typical *rise time* $(10\% \rightarrow 90\%)$ in the range $t_r = (40 \div 80)$ ms;
4) typical *fall time* $(90\% \rightarrow 10\%)$ in the range $t_f = (130 \div 700)$ ms, therefore larger than the rise time by an order of magnitude.
5) total duration of each pulse around 5 s.

The typical signal shape provided by the electronics chain is shown in figure 8.1.

During the normal data-taking the input voltage V is a positive value in the range $0 < V < +10$ volts while during the thermistors characterization procedure (*Load Curve* and *Optimum Working Point* determination procedures, see section 3.5) it can assume reversed values in order to measure and subtract possible common effect due to asymmetries in the circuitries of the electronics. As a consequence the DAQ system must be able to accept input signal in the range $-10 < V < +10$ volts. The trigger strategy is directly related to the typical event shape.

Since many of CUORE events are expected to involve only one bolometer, the readout must be independent for each channel. In particular all the channels must be *auto-triggering* with a *programmable threshold* on the incoming signal. This feature is required because of the large spread in the bolometer performances, experienced in CUORICINO and expected for CUORE. At the moment various trigger algorithm being taken into account (derivative, Constant Fraction Discrimination and others) but only after exhaustive tests it will possible to select the ones with best performances.

- **Energy resolution**: in CUORICINO the full scale energy is usually around 20 MeV. The energy resolution is limited by non linearity in the calibration curve and by gain instabilities due to drifts on the detector temperature. For the $0\nu\beta\beta$ region the best value reached in CUORICINO is $\simeq 4$ keV at 2.5 MeV. At low energy the resolution can reach also smaller value. In fact, considering the best detector, the measured resolution Γ_{FWHM} around few hundred keV is better than 1 keV. The greater part of the remaining detectors have an energy resolution worst by a factor $(1.5 \div 2)$. The best value corresponds to a root mean square value of:

$$\sigma_E = \frac{\Gamma_{\mathrm{FWHM}}}{2\sqrt{2\ln 2}} = \frac{1}{2.355} \simeq 425 \text{ eV} \tag{8.2}$$

This values must be guaranteed also in CUORE. Considering the full scale range, the energy resolution obtained using a real 16-bit sampling is:

$$\Gamma_{\mathrm{ADC}} = \frac{20}{2^{16}} \text{ MeV} \simeq 300 \text{ eV} \tag{8.3}$$

obtaining a value enough for the the best detectors and adequate for all the others.

- **Sampling rate**: signals coming from the bolometer and filtered by the Bessel Board have a frequency bandwidth from zero to $f_{\max}$ which is the cut frequency of the six-pole filter. As discussed in section 7.3, selectable values for this frequency are 8, 12, 16 and 20 Hz and, considering the CUORICINO case, the typical used value according to the bolometer response is $f_{\max} = 12$ Hz.

  Taking into account these considerations, the least sampling rate for the data acquisition system must be $f_c \geq 2 \cdot f_{\max}$, as follows from the *Nyquist-Shannon sampling theorem*. Moreover each pulse must be sampled for about 5 s in order to get a good measurement of the pulse tail and of the baseline level. The sampling rate will be selectable in the range from zero to 10 KHz and, in accordance with the CUORICINO experience, a typical value could be a sampling rate of 125 Hz for a window long 512 samples ($\Delta T_{\text{acquired}} = 1/f_c \cdot 512 \simeq 4$ s). With these mentioned values the typical event size for one channel is about:

$$\text{Event Size} \quad = \quad f_c \cdot \Delta T_{\text{acquired}} \cdot 16 \text{ bits} = 8192 \text{ bits} = 1 \text{ kbyte} \tag{8.4}$$

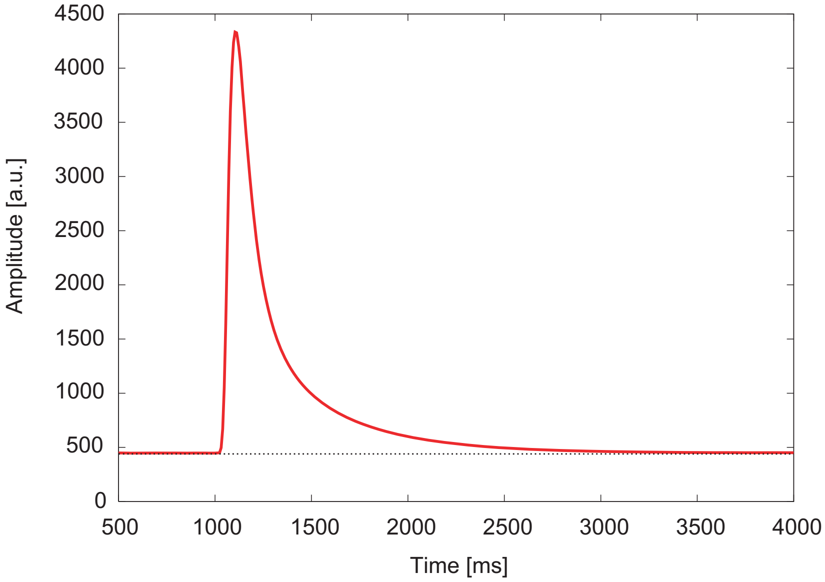

Figure 8.1: Typical bolometric signal after the electronics chain.

8.3 Apollo: the architecture of the system

The CUORE data acquisition apparatus will be a system composed by a set of personal computer, network infrastructure, PCI[2] based interface and some crates housing the digitizing boards. The data acquisition software is custom made. It is developed on `GNU/Linux` environment using the `C++` programming language and it is based on the `ROOT` software package (developed by CERN). The user interface which allows people to interact with the system will be developed exploiting the `ROOT GUI` classes support.

8.3.1 The hardware configuration

The core of the data acquisition is the digitizing board. After a preliminary phase, based on the study of a custom made board, the collaboration decided to adopt a cheaper commercial solution. In order to satisfy the above requirements we chose board from the *National Instruments®* (NI) *M Series devices* (for the specifications see table 8.1). These boards (NI PXI-628x)[3] accommodated a 18-bit ADC and are the highest-resolution multifunction data acquisition devices for the PCI bus produced by NI.

Up to now we adopted and tested two different board: the NI PXI-6281 and the NI PXI-6284. The former devices offer 16 single ended (8 differential) analog input channels and 24 digital I/O lines while the latter offer 32 single ended (16 differential) analog input channel and 48 I/O lines. Both devices contain two 80 MHz, 32-bit counter/timers and support hardware-timed digital I/O at rates up to 10 MHz on 32 lines.

The NI PCI-628x boards are typically accommodate in a dedicated crate and could communicate with a remote control (personal computer) through a PXI-PCI interface composed by a pair of boards: the (NI PXI-8336 on the crate and the NI PCI-8336 on the remote control). The communication between this two boards is performed via fiber-optic cabling.

The number of boards needed to realize the entire system will be $988/8 \simeq 124$ in case of NI PXI-6281 or $988/16 \simeq 62$ in case of NI PXI-6284. The number of crates is not defined yet, it depends on the features of the crate that will be chosen. The available solution are three: the NI PXI-1045 with 18 slots, the NI PXI-1044 with 14 slots and, at last, the NI PXI-1036 with 6 slots.

In any case, each NI crate will be controlled by an associated personal computer (data receiver machine). The setup already installed at the Gran Sasso Hall C R&D facility, and also at the Genova INFN Laboratory, is using the HP ProLiant ML150

---

[2] The *Peripheral Component Interconnect* specifies a computer bus for attaching peripheral devices to a computer motherboard.

[3] PXI, (*PCI eXtensions for Instrumentation*) is a modular instrumentation platform originally introduced in 1997 by National Instruments®. These platforms are used as a basis for building electronic test equipment or automation systems.

	NI PXI-6281	NI PXI-6284
Analog input channels	8 differential 16 single ended	16 differential 32 single ended
ADC resolution	18 bits	18 bits
Maximum sampling frequency per acquired channel	$(500/N_{\mathrm{acq}})\cdot$KSample/s	$(500/N_{\mathrm{acq}})\cdot$KSample/s
Input range	±10 V	±10 V
Input bias current	±10 pA	±10 pA
Input impedance	10 GΩ in parallel with 100 pF	10 GΩ in parallel with 100 pF
Adjacent channels crosstalk	-75 dB @ 100 KHz	-75 dB @ 100 KHz
Non-Adjacent channels crosstalk	-95 dB @ 100 KHz	-95 dB @ 100 KHz
Analog output channels	2	–
Digital I/O channels	24	48
Number of boards needed for CUORE	124	62

Table 8.1: NI PXI-6281/NI PXI-6284 most important specifications. N_{acq} is the total number of acquired channels.

server produced by the *Hewlett-Packard*®Company. Each data reader machine will be connected with the same data processor (another personal computer) devoted to build and to store the events. Another computer is needed to host the server processes (`DaqServer`, `SlowServer` and `MsgLogger`) that controls the data acquisition system.

All computers and all processes are connected with each other via standard network switch. The network infrastructure will be rather simple, with a single switch star-connected to all PCs. Normal 100 Mbit ethernet is probably more than enough for CUORE but it would be easy to implement this structure using 1 Gbit optical link without any architectural modifications.

8.3.2 The data acquisition and control software

The system will consist of few processes distributed on separate hosts and exchanging command and data between them. Each process will carry out a different task under control of the `DaqServer`, the main process, devoted to make the system as a whole body. The *Low Level* interface between the digitizing boards and the system, is developed exploiting the `NI-DAQmx`® library (version 8.0) provided by NI for the `GNU/Linux`

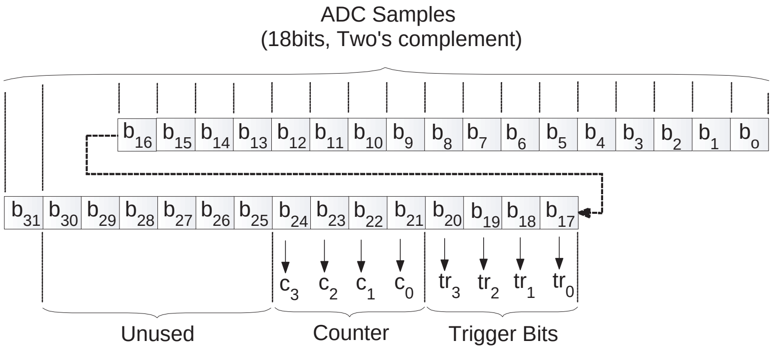

Figure 8.2: Format of the Apollo raw data written on the shared memory by the `DataReader` processes. The stored information consists of 32 bits. The data digitized by the ADC are expressed exploiting 18 bits (from b_0 to b_{16} plus the most significant bit b_{31}) using the *two's complement* for the signed number representations. Four bits (from b_{17} to b_{20}) are used for the trigger flags (at the moment four trigger algorithms are expected to run at the same time) Four bits (from b_{21} to b_{24}) constitutes a 4-bit counter useful to check possible data loss. Six bits (from b_{25} to b_{30}), not used at the present time, could be used in future to any purpose.

environment. Communication between processes on separate hosts, but also on the same host, will be handled via network through a standard TCP/IP *socket communication protocol*[4]. Acquired data will be finally stored on dedicated disks as ASCII files (continuous data-taking) and as `ROOT` files (triggered events).

The following is a brief description of the processes and their functions:

- `DataReader`: this is the first process in the data handling chain. It continuously reads data from all channels defined, and apply triggering and possibly filtering algorithms to the data. At this level the trigger just flag the pulses, without creating the events. All data are then stored into a shared memory segment (one for each channel). The format of the data is shown in figure 8.2. In general there is one `DataReader` process for each DAQ crate.

- `DataSender`: it is a process that simply take date from the shared memory and send it to the `Builder` machine via network (TCP/IP connection). If enabled the `DataSender` can write the *continuous-data* on ASCII files.

- `DataReceiver`: it is a process that collects the data sent by the `DataSender` and fills a shared memory segment that is identical to the one filled by `DataReader` in the crate receiver machine. For each `DataSender` process a corresponding `DataReceiver` process must exist. The couple `DataSender`/`DataReceiver` can be just removed when all the processes are installed in the same machine. As for the `DataSender` also the `DataReceiver` can write the *continuous-data* on ASCII files.

---

[4] an internet socket (or commonly, a socket or network socket), is a communication end-point unique to a machine communicating on an internet protocol-based network.

- `Builder`: this is the process that builds the *event* and write it to `ROOT` files. It reads shared memory segment previously filled by `DataReceiver` searching for trigger flags. When a flag is found the corresponding *event* is built. An *event* is a data unit containing, typically, a triggered pulse, a record of event *infos* and an optional list of nearest neighbor pulses. The `ROOT` files written contains all the information needed the offline analysis.

  The `Builder` is a renaming of the `Diana` process, the reconstruction and analysis software of the CUORE experiment. `Diana` is based on a flexible framework that is basically only capable of running a list of sequences, each of them being a coherent list of modules. A sequence is a list of modules and each module is a piece of code that acts on a single event and compute some quantity (i.e. filtering, fast Fourier transform and so on). The list of modules are defined by a configuration file. This file, through a simple syntax, tell `Diana` (`Builder`) which modules should be run, which modules should be grouped in sequences and which input parameters are to be given to each module. Thanks to this design the `Builder` are able to perform a first on-line analysis on triggered pulses.

- `DaqServer`: as already said, it is the main process of the system. It is in charge of starting the all no-server process, to control the all processes (servers included) and to start and stop DAQ runs. `DaqServer` is controlled by means of socket commands. Even if direct socket communication is possible, in standard conditions users do not have to interact directly with the `DaqServer`: all actions can be done by means of the dedicate GUI that works as a socket client.

- `MsgLogger`: this is the message server. It receives messages from other processes and write them to log files. Moreover `MsgLogger` handle informations about status of running processes; a process can inform the `MsgLogger` about its status or ask to it the status of another running process.

- `ApolloGUI`: this process provides the user interface for the data acquisition system. It works as a socket client and interacts only with the `DaqServer`. The `ApolloGUI` is devoted to enable the user to control the acquisition runs, to choose the different options and parameters, to look at the real time data streaming and the statistics about the run in form of graphs, histograms and tables.

- `SlowServer`: this process is the only one able to interact directly with the electronics crates (Front-Ends, Bessels and Pulsers). Using a standard protocol (I2C at the moment, CAN-bus in future) the `SlowServer` can write and read the configuration registers of the electronics. It is controlled by the `DaqServer` and used, for the *pulse-sequence* generation, by the `PulserCotroller`. During the acquisition runs the writing mode for the Front-End and Bessel crates is disabled.

- `PulserCotroller`: this process is devoted to control the pulser boards during the data taking. Its main task is to generate the calibration *pulse-sequence* during

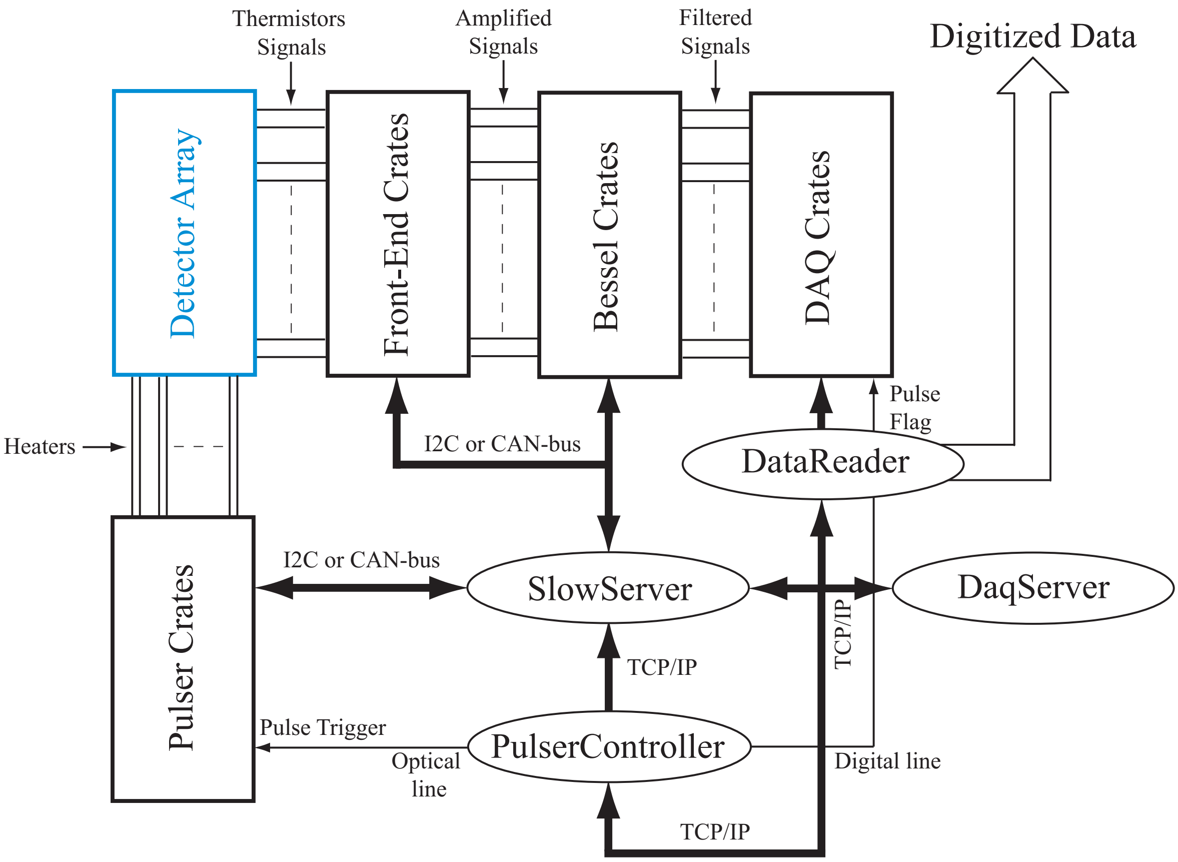

Figure 8.3: Slow control block diagram. The `SlowServer` in the process devoted to configure and to control the CUORE electronics. Working together the `PulserCotroller` process, it generates the calibration pulse-sequences during the data taking.

> the data-taking. The `PulserCotroller` reads the parameters of the sequence channel by channel from the CUORE data base and, exploiting internal timers, drives the pulser boards. The pulse parameters are set through the `SlowServer` while *pulse trigger* is given by means of a fiber optic line that connect the machine where the `PulserCotroller` runs to the pulser crates. At the same time of the trigger the process send a synchronous digital pulse (*pulse-flag*) to a digital input of the DAQ boards in order to flag the event as a *pulser-event*.

All the processes can communicate with the database (`qdb`, the CUORE database). The CUORE database will run on a dedicated server and it will be reachable via standard ethernet networking. The database contains different informations about: the cryostat status, the detectors configuration (crystals, heaters, thermistors), the electronics and the DAQ (address mapping, active channels), the trigger strategy (trigger thresholds and parameters) and parameters related to the runs ended (run type, start date, stop data, hardware configuration, setting used and so on). The data acquisition system can write and read several table of the database. The informations stored in the database can be used directly in the off-line analysis.

8.4 The Hall C setup

During the 2006 two preliminary set-ups, already used, were realized to develop and debug the Apollo system.

The first one, located at the Gran Sasso Electronics laboratory, is composed by one National® crate with one board (16 channels). This set-up is also connected to one electronics crate accommodating six Front-End boards and five Bessel boards. All boards (CUORICINO-like) are interfaced to the personal computer is via I2C line. This set-up is used to debug all the Apollo processes and to develop the `SlowServer`.

Another set-up, located at the Genova INFN Laboratory is composed by one crate with one or more boards, depending on circumstances, a HP ProLiant ML150 server, one personal computer and a crate with two Pulser board. The DAQ crate is controlled through the HP® server while the personal computer is used to interface the DAQ system with the pulser boards. The server and the PC are connected using the standard TCP/IP. This set-up is used to develop and debug the DAQ software directly involved in the data acquisition and, recently, to develop those processes liable to the *pulse-sequence* generation.

The most important set-up developed is the one installed at the Hall C facility during the 2007. This is the first Apollo prototype connected to real bolometers. The main target of this set-up is to check the correct operation of the National® PXI hardware and compare its performance with the usual data acquisition system (Hall C *standard-acquisition*, VXI based[5]). Exploiting a custom *patch-panel*, able to split in two identical copy signals coming from the anti-aliasing filter boards, the system can run at the same time with the standard system (*parallel-acquisition*).

The set-up is composed by one National® crate (NI PXI-1036) with three NI PXI-6284 ADC boards for a total of 48 channel. A HP ProLiant ML150 server controls the crate while a usual personal computer is used to interact with the electronics (only Front-Ends and Bessel Boards).

All the Apollo processes are running on the HP® server except for the `SlowServer` that is running on the PC. The HP ProLiant ML150 server also hosts an instance of the CUORE database. Here informations about the Hall C facility, the detector cooled and about the performed runs are collected. Once selected the hardware configuration (run profile, settings), the two main servers (`SlowServer`, `DaqServer`) get the hardware configuration from the database while, when the user starts or stops the DAQ run (using the `ApolloGUI`), the `DaqServer` write on it different parameters that characterize the run.

---

[5] The VXI bus (*VME eXtensions for Instrumentation*) architecture is an open standard platform for automated test based upon VMEbus based *Versa Module Eurocard*.

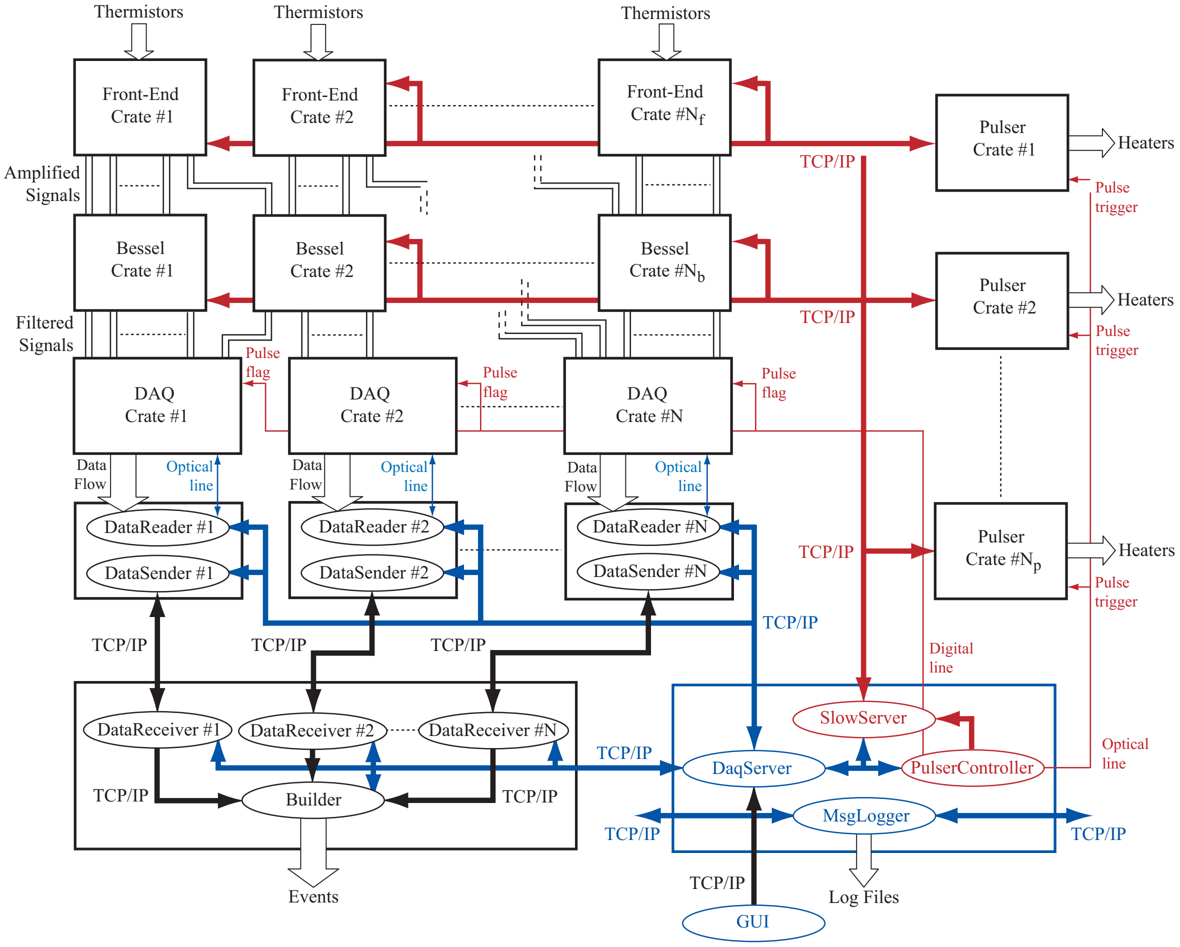

Figure 8.4: Apollo block diagram. Communication between processes is handled via network through a standard TCP/IP *socket communication protocol*. All processes can communicate with the MsgLogger and with the database.

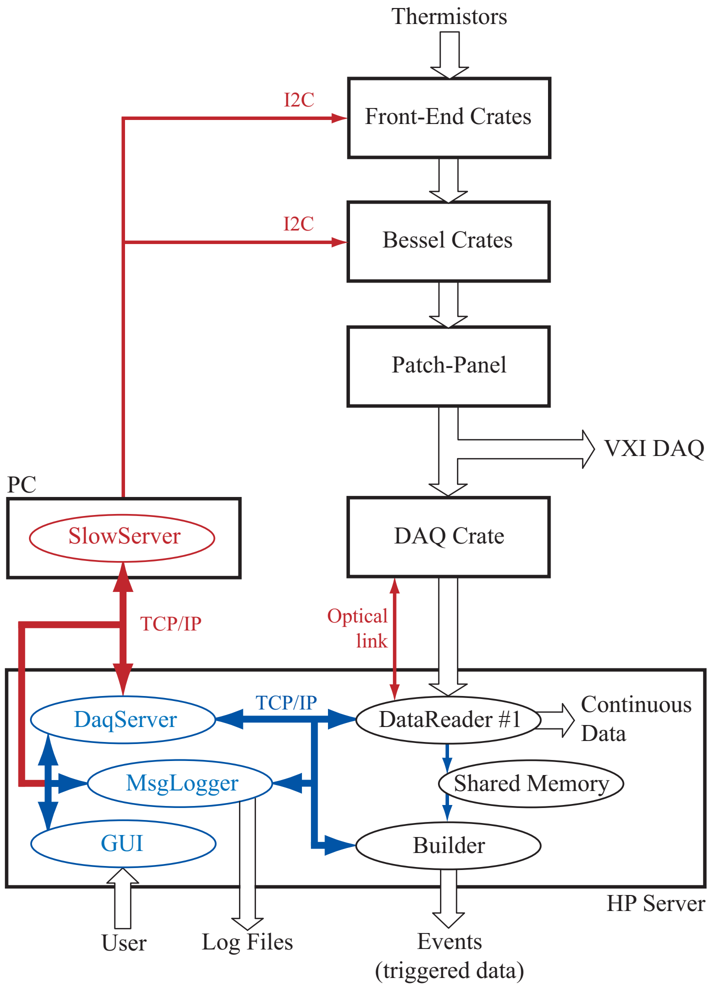

Figure 8.5: Apollo Hall C set-up. All the processes are running on the HP® server except for the `SlowServer` that is running on a dedicated personal computer. The `DataReader` and the `Builder` are running in the same machine, for this reason the two processes `DataSender` and `DataReceiver` are not needed. The `Builder` reads the continuous (flagged) data directly on the shared memory. The communication between the `SlowServer` and the electronics is implemented using the I2C protocol exploiting the parallel port of the personal computer.

In the 2007 three main tests were performed on the Hall C prototype, exploiting the detectors developed for the background studies.

8.4.1 RAD5 DAQ test

This test was the first with acquired signals coming from real bolometric sources. The data taking lasted few days in January and February during the Clamps1 measurement. The main goal was to validate the hardware set-up and debug the Apollo software. The standard VXI and Apollo DAQ systems were running separately and in parallel (but

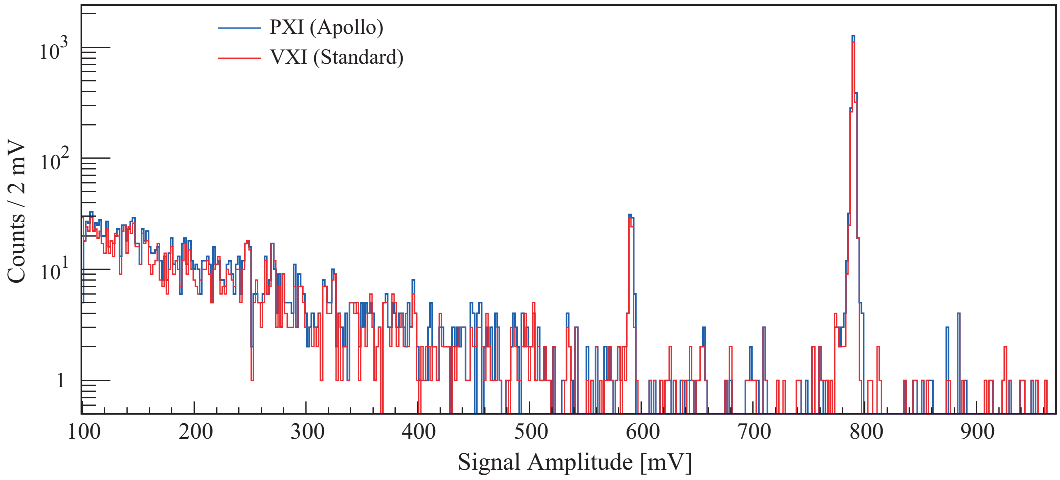

Figure 8.6: Preliminary comparison between VXI and PXI spectra. The spectra were obtained from three days of background measurement when the two systems were running in parallel.

only for eight channels). The signals split, for the eight channels, was realized using a custom metal box with one input (Bessel boards outputs) and two outputs (VXI and PXI inputs). We used a metal box in order to shield cables and connectors from the electromagnetic noise.

Apollo data were continuously saved on ASCII files for offline analysis and/or reprocessing. A first attempt of trigger was running in order to have a complete DAQ chain triggered events (the so called *Diana-event*, saved in `ROOT` file format).

Despite the the brief duration, in this test we obtained very useful feedback from the system. No crashes and no data loss happened. The *derivative trigger* worked properly and the data acquired was consistent with the data acquired by the standard acquisition. Comparing the two spectra (figure 8.6) obtained after three days of background measurement, no evident discrepancy appeared. The two visible peaks have the same counting rate, moreover the triggered pulses have the same shape.

8.4.2 CCT1 DAQ test

After the good results coming from the Clamps1 DAQ test a long data taking was fundamental to finally validate the Apollo system. To fulfill this requirement we exploited the two *Chinese Crystals Test* measurements to perform the first test with the two acquisition systems steadily in parallel. To have a parallel data taking, the system was completed with a patch-panel able to split all the 48 channels of the facility in two identical copy. The second test, the CCT2, is still running.

The CCT1 DAQ test was the first long duration measurement performed with the first prototype of the new acquisition system. The prototype operated with no interruptions for the whole data taking. We acquired 19 channels with a sampling rate

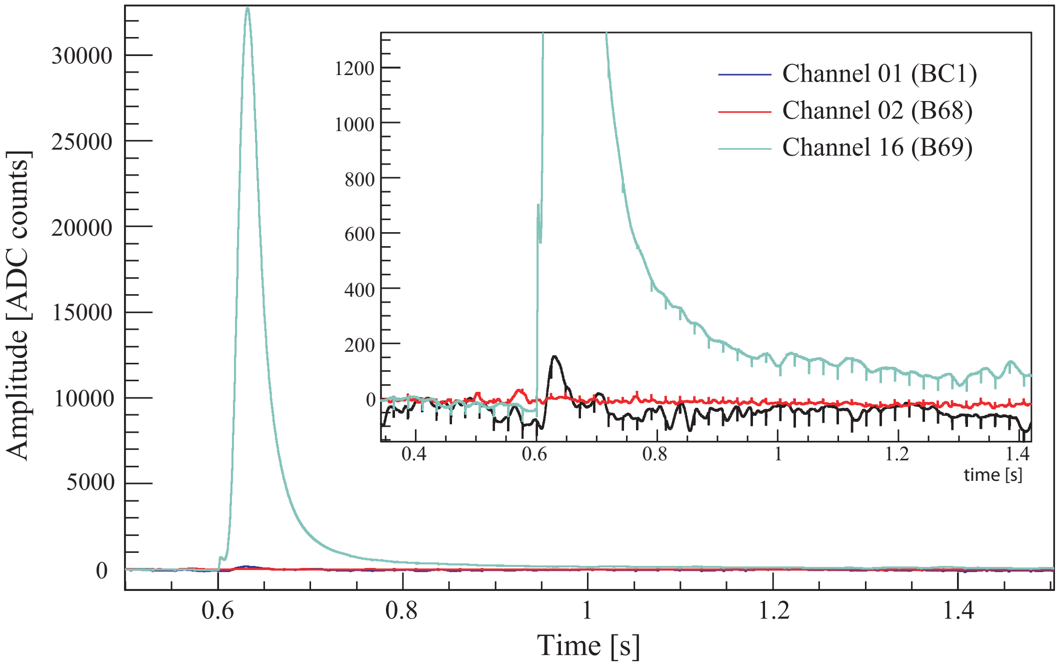

Figure 8.7: Cross-talk measured between the channel 16 (green line) and the two channels 01 (blue line) and 02 (red line). The cross-talk entity measured is smaller than 8%. The small negative spikes present in all the three baseline (and visible in the zoomed timelines) are interferences due to the VXI acquisition. This effect disappeared changing the PXI sampling frequency from 4 kHz to 125 Hz.

of $f_c = 125$ Hz. As usual, the data were continuously saved on ASCII files (about 25 MByte/channel/day) and also in *Diana-event* format on `ROOT`-files. In total, we acquired about one month of background measurements, few days of calibration and few measurements with pulsers set at several different energies.

During the test, the PXI system ran with no crashes and no operational problems. Also the trigger worked properly (figures 8.11 and 8.12). The only one problem was the appearance of some cross-talk[6] in a few channels (figure 8.7). This cross-talk was not inside the detector, because it was not present in VXI data. Moreover it was not coming from the PXI board, because we observed it only on a few channels. This effect was observed also when we acquired non-connected channels. For these reasons we suppose that the cross-talk was produced by bad connection in the patch-panel. Subsequent tests proved this hypothesis. In fact, replacing the connectors that connected the PXI boards with the path-panel with others with screws with a right size, the effect vanished.

---

[6] In electronics, the term cross-talk (XT) refers to any phenomenon by which a signal transmitted on one circuit or channel of a transmission system creates an undesired effect in another circuit or channel.

8.4.3 CCT2 DAQ test

After the good performances came out during the Clamps and CCT1 DAQ tests and understood the cross-talk problem, the collaboration decided to use the Apollo Hall C set-up as an independent acquisition system. The two acquisition are still running in parallel but, since the CCT2 DAQ test is already in progress at the present time, the data acquired with the PXI are analyzed independently with respect the VXI data.

In the CCT2 DAQ test we introduced several improvements in the software. In fact, we improved the system stability, we developed graphical tools to monitor the run in real time and, at last, we improved the *derivative-trigger* algorithms (figures 8.11 and 8.12). The hardware conditions are the same of the previous test except for minor change in the patch-panel in order to solve the cross-talk problem.

The first result obtained from the PXI data analysis was the identification of the new crystals (B72 and B74) high activity as due to a Polonium contamination. This was possible by a comparison between the measured half-life and the theoretical one.

As said in the previous chapter 6, the two crystals B72 and B74 show a very high Polonium contamination rate (monochromatic peak at 5.4 MeV). This rate is too high for the standard acquisition which is not able to trigger the pulses. To solve this problem we decided to re-process the continuous data-taking saved by the Apollo system and, using a *peak-finder* algorithm, we re-triggered off-line the baseline searching the Polonium peaks.

Considering the B72 crystal (figure 8.8), the most contaminated, the Polonium analysis is performed on data acquired in 68 days while each single measurement is performed on a data taking 10 hours long (table 8.2). ^{210}Po is an alpha emitter that has a half-life of 138.376 days[7]. After 68 days, its activity should decrease of about 29%.

In this low level analysis the counting rates are calculated only by removing the periodical pulses which belong to the calibration *pulse-sequence*. All other pulses are left. Considering the first and the last measured values (647 and 463 mHz, respectively) we can calculate the experimental decreasing of the contamination activity. The result is about 28% accordingly with the value (29%) calculated for the ^{210}Po. Moreover, fitting the counting rates trend using the following function:

$$F(x) = p_0 \, \mathrm{e}^{p_1 \cdot x} \tag{8.5}$$

we obtain (figure 8.9):

$$\begin{cases} p_0 = (23400 \pm 75) \text{ counts/10 hours} \\ \\ p_1 = (485.4 \pm 9.5) \cdot 10^{-5} \text{ days}^{-1} \end{cases} \tag{8.6}$$

---

[7] it decays directly to its daughter isotope ^{206}Pb. A milligram of ^{210}Po emits about as many alpha particles per second as 4.5 grams of ^{226}Ra.

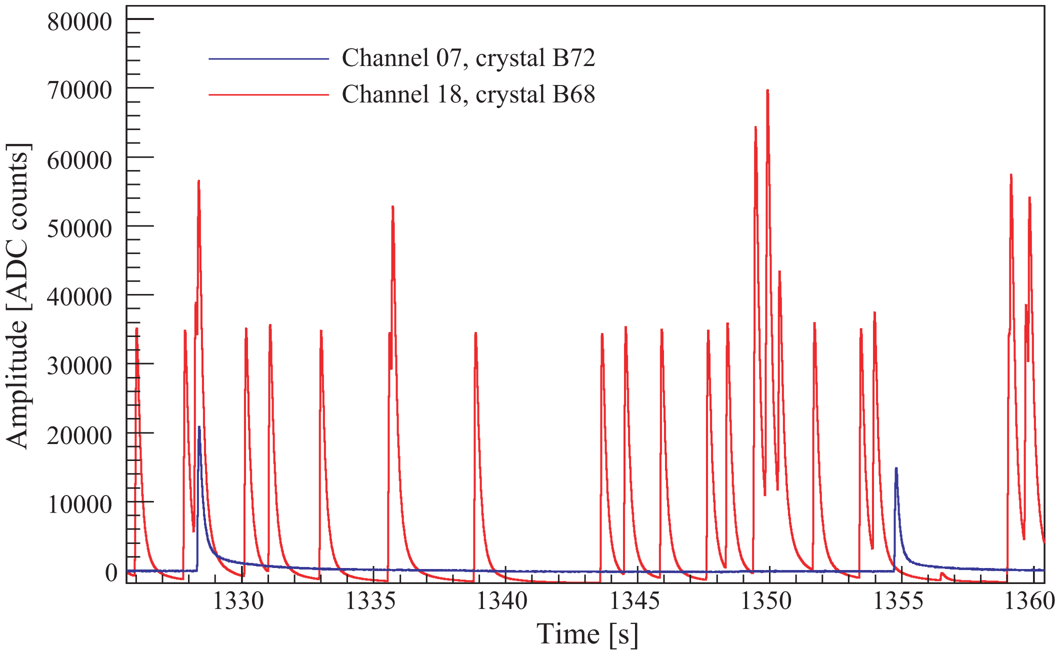

Figure 8.8: Comparison between two channels acquired by the new DAQ system during the CCT2 measurements. The channel 18 show an high rate. Ad said in the chapter 6, this is due to a high ^{210}Po contamination in the crystal B72.

Run Number	**Time** [days]	**Count**	**Rate** [mHz]
174	0	23295	647
177	3	23026	640
181	6	22705	631
188	10	22321	620
202	13.1	21931	609
214	23.9	20944	582
221	36.1	19828	551
223	41.3	19345	537
226	47.2	18357	510
232	60.2	17563	488
236	67.9	16682	463

Table 8.2: Polonium activity measured on the B72 crystal using the Apollo DAQ system. The time is measured from the start of the CCT2 test.

for an experimental half-life of:

$$t_{1/2}^{\mathrm{exp}} = (142.8 \pm 2.8)\ \mathrm{day} \tag{8.7}$$

The value is quite compatible with the Polonium half-life. The overestimate is probably due to the signal pile-up and to the inability of the *peak-finder* to solve pulses in a

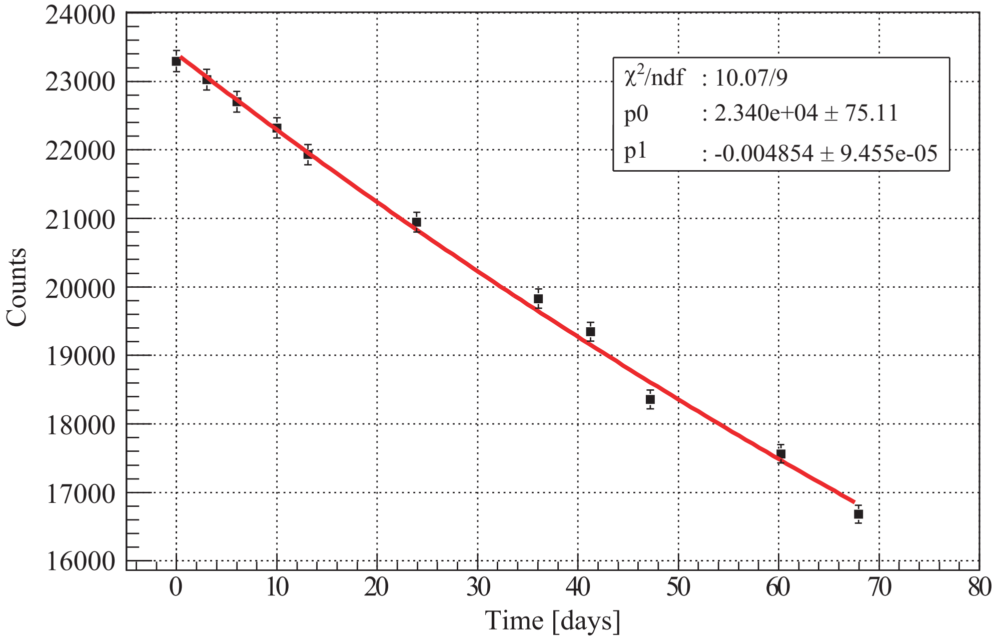

Figure 8.9: Fit of the counting rates measured on the B72 crystal using the Apollo DAQ system. No energy cuts are applied.

distance lower than 70 ms.

A solution to correct the counting consists in an energy calibration of the spectrum: once marked the Polonium alpha-decay peak, it is possible to calibrate (in first linear approximation) and so to obtain the energy spectrum. In this way, for example, all under-energy event can be rejected and, at the same time, an event matching a given energy $E >> 5.4$ MeV, can be ascribed to pile-up effects (this means that such event is considered as *double* in peaks counting).

In this second level analysis we use the 5.4 MeV alpha line to calibrate the acquired spectrum (figure 8.10) and, using a threshold of 4 MeV to reject the too low energy events and thresholds of 7 MeV and 8 MeV to reject pile-up effects, we obtain for the the half-time the values shown in table 8.3.

Except for the threshold of 5 MeV, too close to the 5.4 alpha peak, the calculated values are compatible with the ^{210}Po half-life. This result confirm that the contamination in the two crystal is due to ^{210}Po.

Currently the CCT2 DAQ test is still running. The data are analyzed day by day and the results are continually compared with the standard analysis in order to identify possible anomalies.

The good results achieved by the Hall C prototype convinced the collaboration to update also the CUORICINO acquisition with the new solution. During the 2008 a new set-up will be installed at the Gran Sasso Hall A. This will be the last step of the DAQ

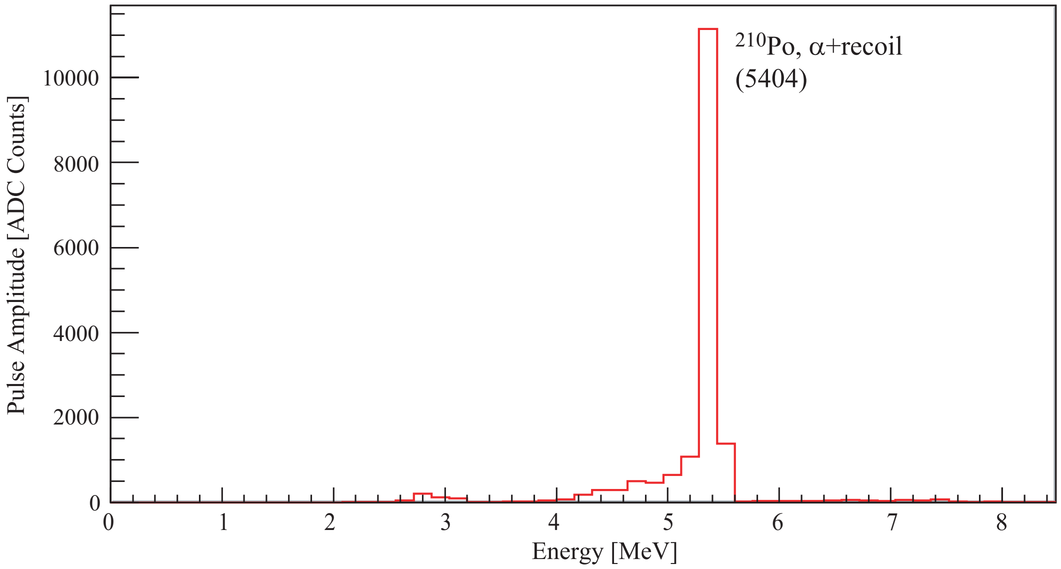

Figure 8.10: Example of spectrum used to calibrate the second level analysis.

Time [days]	**Rate** [mHz]	**Rate** [mHz]	**Rate** [mHz]	**Rate** [mHz]
	(No cuts)	Rejected: $E < 4$ MeV Double: $E > 7$ MeV	Rejected: $E < 4$ MeV Double: $E > 8$ MeV	Rejected: $E < 5$ MeV Double: $E > 8$ MeV
0	647	684	663	574
3	640	679	659	571
6	631	668	647	564
10	620	654	636	554
13.1	609	644	626	547
23.9	582	612	596	523
36.1	551	576	562	495
41.3	537	565	551	487
47.2	510	534	521	462
60.2	488	510	497	444
67.9	463	483	471	423
$\mathbf{t}_{1/2}$ [days]	142.8	136.0	139.0	154.1
$\mathbf{\Delta t}_{1/2}$ [days]	2.8	2.5	2.6	3.4

Table 8.3: Counting rates obtained applying different energy cuts.

development before the realization of the final system.

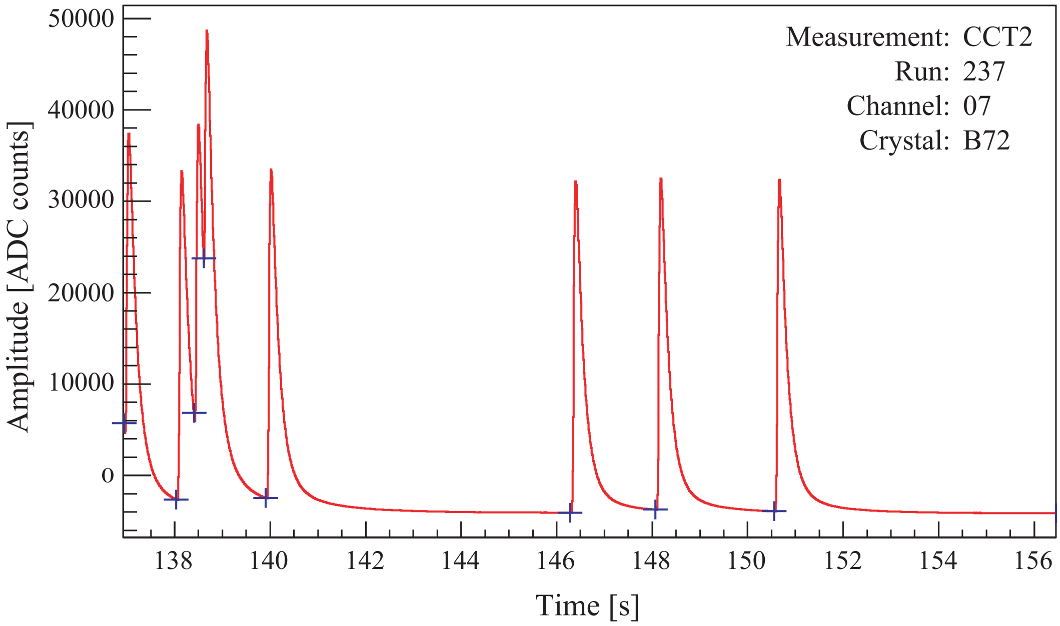

Figure 8.11: Example of baseline acquired during the CCT2 DAQ test. The blue crosses are placed by the trigger. The pulses was triggered using the *derivative trigger* algorithm.

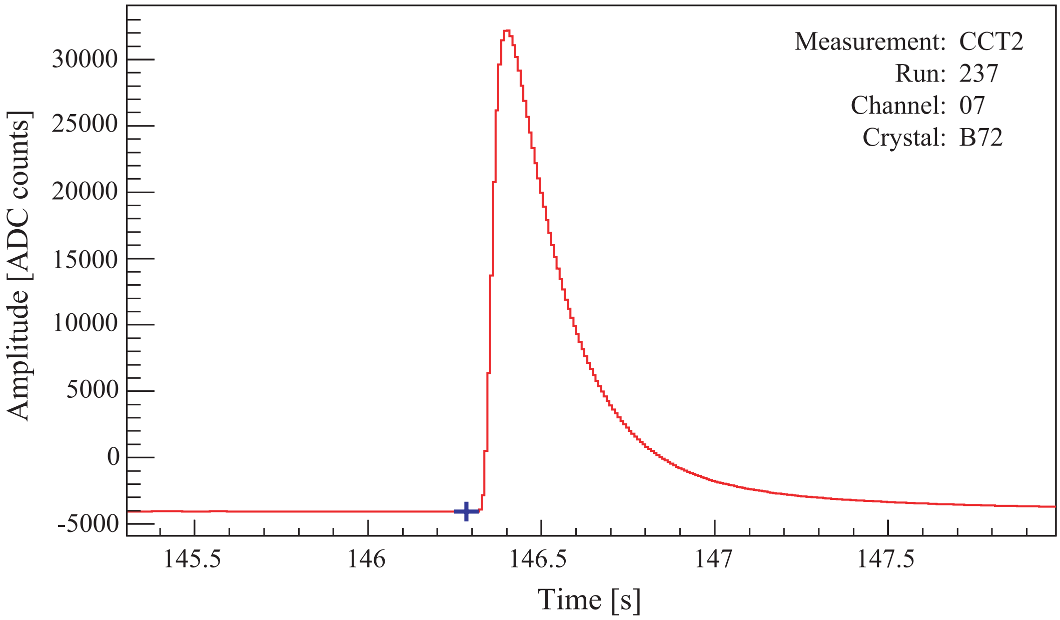

Figure 8.12: Example single pulse acquired during the CCT2 DAQ test.

Conclusion

My Ph.D. activity was focused manly on two tasks: the R&D activity aimed at the reduction of the detector background, and the design and development of the data acquisition system for the CUORE experiment.

Background is the only parameter that can be reduced by orders of magnitude thus allowing a sizeable improvement of the experimental sensitivity. To achieve this goal, during these three years I worked in the CUORE background reducing program, a R&D activity aimed at the study of the CUORICINO background and at developing solutions in order to reduce it. The main result of this activity is the background reduction in the double beta decay region by a factor 38% with respect to CUORICINO. This result shows that we apparently have a technique that can get rid of the ^{238}U and ^{232}Th surface contamination of the crystals, but we have not found a completely satisfactory solution yet for the contaminations responsible of the major fraction of that flat continuous background that extends from 4 MeV down to the $0\nu\beta\beta$ region. However, we have proved that, as predicted by the CUORICINO background model, surface contamination of copper play a relevant role in 3-4 MeV background. This is clearly evident by comparing the data of all performed runs. A possible solution to this puzzle could be to devolop a new copper surface treatment, including the Plasma cleaning.

The second taks of my work was devoted to the development of the data acquisition and control system of the experiment. In 2007 the first prototype of the system was installed at the Hall C facility. The architecture, although obviously somewhat reduced and simplified, are the same that will be adopted forCUORE. The software is identical to the one foreseen for CUORE and its design is such that all future upgrades will be installed in Hall C as well, for validation and tests. This system also includes a brand new slow control system for Front-End, Bessel filter and pulser control boards. The slow control system is completely integrated in the DAQ system, and it is designed to allow the complex functions like the automatic calculation of the load curves and the determination of the optimal working point for the bolometers. These features are already implemented and will be tested in the near future.

Starting from the results obtained from the Hall C DAQ tests a similar set-up will be installed in Hall A in order to upgrade the CUORICINO data acquisition. This system will be also capable of reading out the data produced by a simple muon based on a set of plastic scintillators.

Appendix A

Cryogenics

A.1 Dilution refrigerator

A *Dilution Refrigerator* (DR) is a cryogenic device, originally proposed by H. London in 1951, that could reach temperatures below 10 mK using a mixture of two isotopes of helium: helium-3 and helium-4[212]. The lower temperature reached using this device is about 2 mK achieved by G. Frossati and co-workers at the University of Leiden[213, 214, 215] and by G.R. Pickett and co-workers at Lancaster University[216].

A.1.1 Properties of ^{3}He/^{4}He mixture

Considering the phase diagram shown in figure A.1 when cooled below $T_\lambda = 870$ mK, the mixture undergoes a spontaneous phase separation to form a ^{3}He-rich phase (diluted phase) and a ^{3}He-poor phase (concentrated phase, ^{4}He-rich). The two phases are maintained in liquid-vapor form. Since there is a boundary between both phases, extra energy is required for particles to go from one phase to another. The lighter helium-3 rich fraction floats on top of the heavier helium-4 rich fraction.

The Helium-4 atoms are bosons, and their superfluidity can be understood in terms of the Bose statistics that they obey (*Bose-Einstein condensation*). This superfluid component has zero viscosity, zero entropy, and infinite thermal conductivity, it is often described as a *massive vacuum*. The Helium-4 atoms act as a *quantum solvent* [217, 218]

The dissolved Helium-3 atoms are not in superfluid status (^{3}He becomes superfluid at temperatures below 1 mK in zero magnetic field) and, if $T < \frac{1}{3}T_\mathrm{F}$, it is behaves like a *perfect Fermi-gas*.

Since the ^{3}He vapor pressure is much higher than the ^{4}He vapor pressure, pumping (using, for example, a rotary pump) on the ^{4}He-rich phase it's possible to remove mostly ^{3}He (a move to the left off the equilibrium line in the diagram), destroying the equilibrium. To restore equilibrium, ^{3}He has to cross the phase boundary from the ^{3}He-rich side to the ^{4}He-rich side. However, it needs energy to get past the boundary.

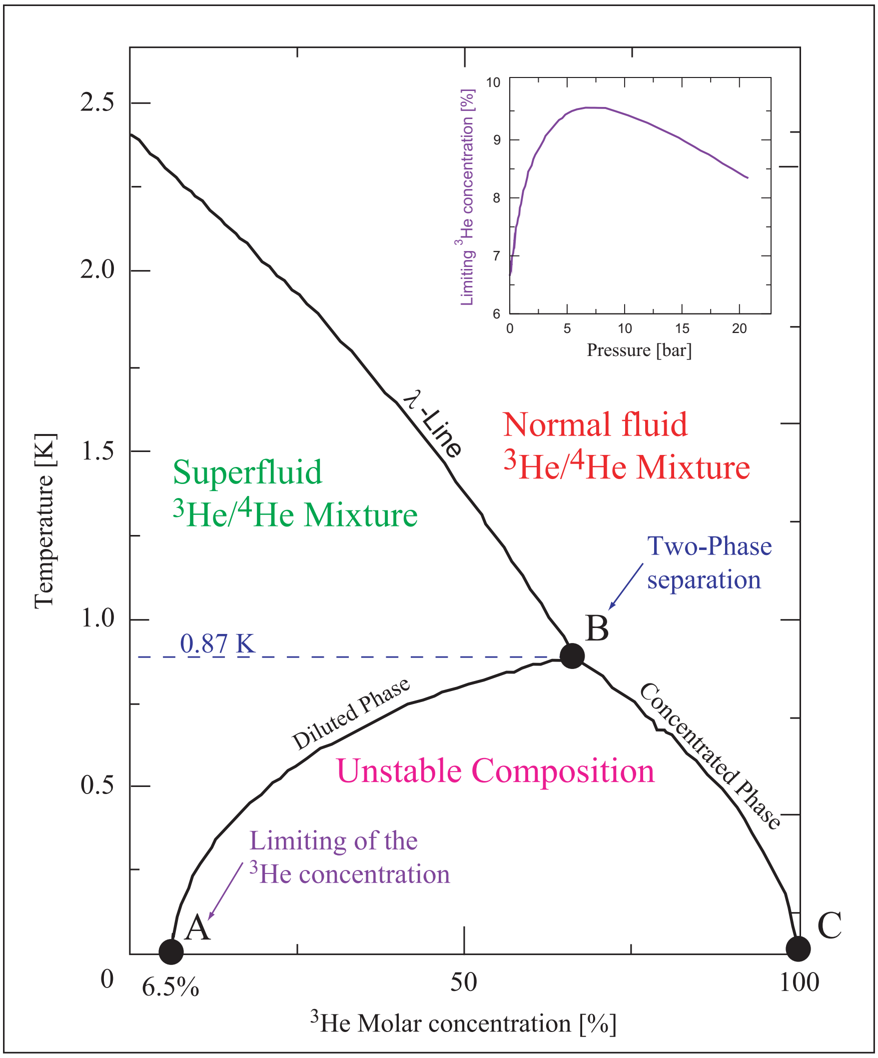

Figure A.1: Phase diagram of ^{3}He/^{4}He mixture as function of the temperature in saturated vapor pressure. The different regions have the following characteristics. *Normal fluid*: behaves like a Newtonian fluid. It has finite viscosity and is the only entropy carrying component in the system. *Superfluid*: zero viscosity, zero entropy, and infinite thermal conductivity. *Coexistence phase*: separation of two phases, the upper rich on ^{3}He, the lower on ^{4}He.

The ^{3}He-rich phase provide the ^{3}He and gets the energy in the form of heat from the surrounding chamber (typically the so called *mixing chamber*), further cooling the mixture. Then the ^{3}He crosses the phase boundary and joins the ^{4}He-rich phase, restoring equilibrium. Finally, the atoms lost by the ^{3}He-rich phase are replenished by a constantly circulating flow of ^{3}He (*recirculating* dilution refrigeration).

If one forces, at constant pressure, a constant number of mols n_3 to pass from the concentrated phase to the diluted one it's possible to obtain the following *heat of mixing*[217]:

$$\dot{Q} = \dot{n}_3 = \Big[H_\mathrm{d}(T) - H_\mathrm{c}(T)\Big] \simeq 84\dot{n}_3 T^2 \qquad \text{(A.1)}$$

where $\dot{n}_3$ is the ^{3}He flow and where the enthalpy of ^{3}He in the dilute phase ($H_\mathrm{d}(T)$) is larger than the enthalpy of ^{3}He in the concentrated phase $H_\mathrm{c}(T)$. The cooling results according to the enthalpy difference of the two phases.

A.1.2 The cooling system

To exploit the cooling properties of the ^{3}He/^{4}He mixture is necessary cool down the mixture below the temperature $T_\lambda = 870$ mK, where the phases separation happens. In a dilution refrigerator (figure A.2) this can be obtained by means of four main cooling step[217, 218, 193].

1) **T = 4.2 K**: the dilution unit is dipped in a bath (*Main Bath*, MB) of liquid Helium-4 (LHe) . The Main Bath is thermal isolated from room temperature by the *Outer Vacuum Chamber* (OVC) which contains the super-insulation. Here the mixture ^{3}He/^{4}He is cooled down at the temperature of 4.2 K.

2) **T = 1.3 K**: the second step is realized by an evaporation refrigerator usually called *1K-pot*. The 1K-pot is thermal isolated from the 4.2 K stage by the *Inner Vacuum Chamber* (IVC) and it is filled by means of a capillary put in the main bath. Here the Liquid ^{4}He coming from the main bath condenses. Pumping the vapor above the liquid bath the temperature decreases at 1.3 K (according with the *Clausius-Clapeyron relation*). At the temperature of 1.3 K the mixture get liquid and begins to condense in the dilution unit filling first the *Mixing Chamber* (MC), and then the *Still*. At this stage the liquid mixture is homogeneous.

3) **T < 870 mK**: in order to get phase separation, the temperature must be reduced to below 870 mK (the tri-critical point). The still is the first part with a temperature below 1.3 K. When this is pumped the mixture undergoes an expansion and its temperature cools (according with the *gas equation of state*). When $T < T_\lambda = 870$ mK the dilution can stars. The still is kept at temperature of 600 mK and its task is to cool the incoming ^{3}He before it enters the heat exchangers and the mixing chamber.

4) **T ≃ (4 ÷ 10 mK)**: the dilution process continues and the cooling proceeds, as explained in the previous section, until the heat extraction rate $\dot{Q} = 84\dot{n}_3 T^2$ is balanced by the sum of the various heat inputs which may present.

It is important for the operation of the refrigerator that the ^{3}He concentration and the volume of mixture is chosen correctly, so that the phase boundary is inside the mixing chamber, and the liquid surface is in the still. The concentration of ^{3}He in the mixture is typically between 10% and 20%.

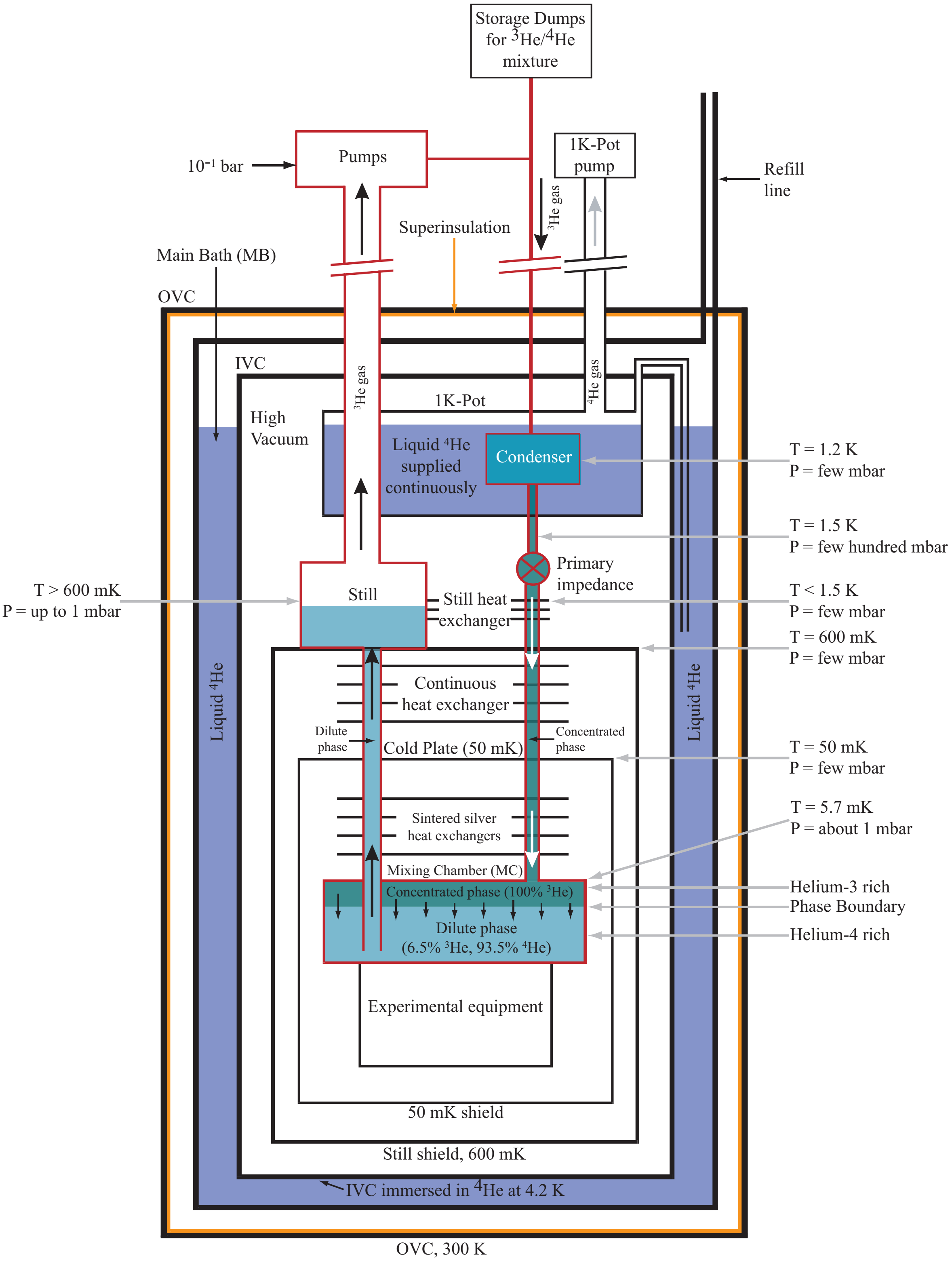

Figure A.2: Schematic diagram of a conventional dilution refrigerator.

A.2 Pulse Tube Cryocooler

The *Pulse Tube Cryocooler* (PTC or PT and also *Pulse Tube Refrigerator*, PTR) is a relatively new type of refrigerator. It was introduced in 1964 by Gifford and Longworth[219]. A significant improvement was made in 1984 by Mikulin *et al.*[220], in 1986 by Radebaugh *et al.*[221] and in 1990 by Zhu *et al.*[222]. In 1994 Matsubara [223] used this technique to reach temperatures below 4 K. By the end of the 1990s, temperatures below 2 K with a three-stage pulse tube had been reached[224].

A pulse-tube refrigerator works by the cyclic compression and expansion of a fixed quantity of gas, usually helium. The essential elements of a pulse-tube refrigerator are shown in figure A.3. Due to heat exchange between gas, regenerator, tube walls, the aftercooler and the two heat exchangers, a temperature difference develops along the tube.

A piston, or a switching valves, generates pressure oscillations in the system and the aftercooler (AC) removes the heat of compression. The function of the regenerator is to store heat, taking it from the gas, when it flows from the compressor to the tube, and reject this heat back to the gas, when the gas flows from the tube to the compressor. The regenerator consists of a porous material with a large heat capacity and a large heat-exchanging surface. After passing the regenerator the gas enters the *pulse tube*, which is just a tube with the heat exchangers CHX and HHX on its two ends. The cold heat exchanger (CHX) is the coldest point of the system. Here the heat is extracted from the load to be cooled. In the tube, the compressible gas oscillates. The hot heat exchanger (HHX) rejects this heat to the surroundings. This last is maintained at ambient temperature. The orifice O is a tunable resistance valve. The buffer volume is a reservoir, the volume of which is typically 10 times larger than the volume of the pulse tube. Gas flows through the orifice due to a pressure difference. The pressure in the buffer is practically constant and close to the average pressure in the pulse tube. The combination of the orifice O and the buffer provides a phase difference between the flow of the gas in the tube and the pressure. The cycle results in net enthalpy flow from the cold end to the hot end thus providing a continuous refrigeration effect.

In well-known coolers as the *Stirling coolers* and the popular *Gifford-McMahon coolers* the gas is compressed and expanded periodically by means of displacers. The Pulse Tube cryocoolers have not displacers and, for this reason, exhibits low vibrations and no electro-magnetic interferences. Furthermore its construction is simpler, cheaper, and more reliable.

The combination of the PTR with a ^{3}He/^{4}He dilution unit allows to reach temperature below 10 mK. A two or more stages PTR cools down the system at about 4 K then a Joule-Thompson expansion condenses the ^{3}He/^{4}He mixture. This solution will be used for the CUORE refrigerator.

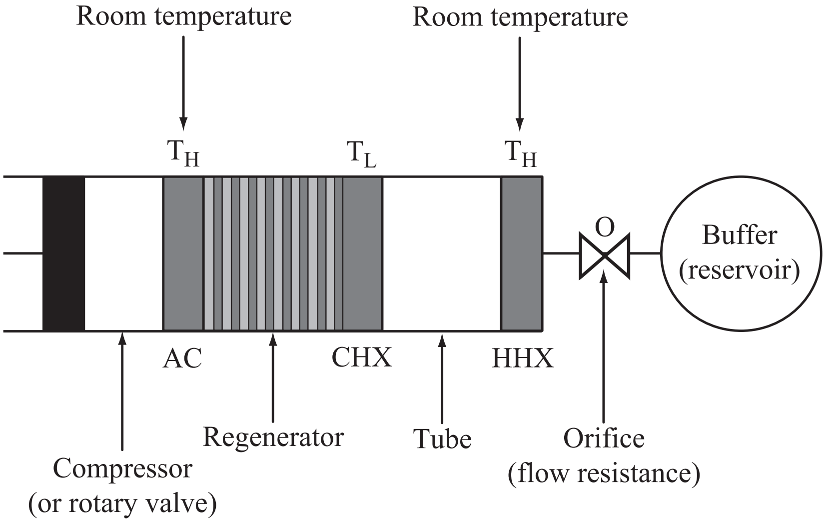

Figure A.3: A schematic representation of a Pulse Tube Refrigerator. From left to right it consists of a compressor (or rotary valve), an aftercooler (AC), a regenerator, a cold heat exchanger (CHX), a pulse tube (tube), a hot heat exchanger (HHX), an orifice (O), and a buffer.

Appendix B

Thermistors and electronics

B.1 Thermistor Logarithmic Sensitivity

The *Logarithmic Sensitivity* of a temperature sensor, like a thermistor, describes its capability of transforming a small temperature increase in a significant resistivity variation. This parameter is defined as follows:

$$A = \left| \frac{\mathrm{d}\ln R(T)}{\mathrm{d}\ln T} \right| \tag{B.1}$$

In the case of an `NTD` thermistor, where the resistivity depends on temperature according to the *hopping* and the *variable range hopping*, one has the following relations:

$$\rho(T) = \rho_0\ \mathrm{e}^{\left(\frac{T_0}{T}\right)^\gamma} \Rightarrow R(T) = \rho(T)\frac{l}{S} = \rho_0 \frac{l}{S}\ \mathrm{e}^{\left(\frac{T_0}{T}\right)^\gamma} = R_0\ \mathrm{e}^{\left(\frac{T_0}{T}\right)^\gamma} \tag{B.2}$$

where ρ_0, T_0 and γ are intrinsic doped-dependent parameters. Replacing this relation in equation B.1 one obtains:

$$\begin{aligned} A &= \left| \frac{\mathrm{d}\ln R(T)}{\mathrm{d}\ln T} \right| = \left| \frac{T}{R(T)} \frac{\mathrm{d}R}{\mathrm{d}T} \right| = \left| \frac{T}{R_0\ \mathrm{e}^{\left(\frac{T_0}{T}\right)^\gamma}} \frac{\mathrm{d}\left[R_0\ \mathrm{e}^{\left(\frac{T_0}{T}\right)^\gamma}\right]}{\mathrm{d}T} \right| = \\ &= \left| \frac{T}{R_0\ \mathrm{e}^{\left(\frac{T_0}{T}\right)^\gamma}} \frac{-\gamma R_0\ \mathrm{e}^{\left(\frac{T_0}{T}\right)^\gamma} \frac{T_0^\gamma}{T^{\gamma+1}}\ \mathrm{d}T}{\mathrm{d}T} \right| = \left| -\gamma \frac{T T_0^\gamma}{T^{\gamma+1}} \right| = \\ &= \gamma \left(\frac{T_0}{T}\right)^\gamma \end{aligned} \tag{B.3}$$

As one can easily see from this last equation (B.3), the Logarithmic Sensitivity depends only on the parameters γ and T_0, intrinsic to the chosen material.

B.2 Thermistor Signal Amplitude

As shown in the section 3.5.1, the relationship between the electrical pulse height ΔV across the thermistor and the energy deposition ΔE it can be obtained using the following partial derivation:

$$\mathrm{d}V_{\mathrm{bol}} = \frac{\partial V_{\mathrm{bol}}}{\partial R_{\mathrm{bol}}}\,\mathrm{d}R_{\mathrm{bol}} = \frac{\partial V_{\mathrm{bol}}}{\partial R_{\mathrm{bol}}}\,\frac{\partial R_{\mathrm{bol}}}{\partial T}\,\mathrm{d}T \tag{B.4}$$

Considering the biasing circuit shown in figure 3.6(a) the working voltage across the thermistor R_{bol} is given by:

$$V_{\mathrm{bol}} = I_{\mathrm{bol}}R_{\mathrm{bol}} = \frac{R_{\mathrm{bol}}}{R_{\mathrm{L}} + R_{\mathrm{bol}}}\,V_{\mathrm{BIAS}} \quad \Rightarrow \quad \frac{\partial V_{\mathrm{bol}}}{\partial R_{\mathrm{bol}}} = \frac{R_{\mathrm{L}}}{(R_{\mathrm{L}} + R_{\mathrm{bol}})^2}\,V_{\mathrm{BIAS}} \tag{B.5}$$

The derivative of the resistance trend (eq. B.2) with respect to the resistance temperature is given by:

$$\frac{\partial R_{\mathrm{bol}}}{\partial T} = R_0\,\mathrm{e}^{\left(\frac{T_0}{T}\right)^{\gamma}}\left[-\gamma\left(\frac{T_0}{T}\right)^{\gamma}\frac{1}{T}\right] = R_{\mathrm{bol}}\frac{A}{T} \tag{B.6}$$

Replacing the relationships B.5 and B.6 in the equation B.4 one obtains:

$$\mathrm{d}V_{\mathrm{bol}} = \frac{R_{\mathrm{L}}R_{\mathrm{bol}}}{(R_{\mathrm{L}} + R_{\mathrm{bol}})^2}\,V_{\mathrm{BIAS}}\,A\frac{\mathrm{d}T}{T} \tag{B.7}$$

Now, considering the square root of the power dissipated in the thermistor by Joule Effect one gets:

$$\sqrt{P} = \sqrt{I_{\mathrm{bol}}V_{\mathrm{bol}}} = I_{\mathrm{bol}}\sqrt{R_{\mathrm{bol}}} = \frac{V_{\mathrm{BIAS}}}{R_{\mathrm{L}} + R_{\mathrm{bol}}}\,\sqrt{R_{\mathrm{bol}}} \quad \Rightarrow \quad \frac{\sqrt{P}}{\sqrt{R_{\mathrm{bol}}}} = \frac{V_{\mathrm{BIAS}}}{R_{\mathrm{L}} + R_{\mathrm{bol}}} \tag{B.8}$$

replacing this last relation in the relation B.7, and considering at the initial time ($t = 0$) $\mathrm{d}T = \mathrm{d}E/C$ (section 3.2, eq. 3.1), one obtains:

$$\mathrm{d}V_{\mathrm{bol}} = \frac{R_{\mathrm{L}}}{R_{\mathrm{L}} + R_{\mathrm{bol}}} \sqrt{P} \, \frac{R_{\mathrm{bol}}}{\sqrt{R_{\mathrm{bol}}}} \, A \frac{\mathrm{d}T}{T} = \frac{R_{\mathrm{L}}}{R_{\mathrm{L}} + R_{\mathrm{bol}}} \, \frac{A\sqrt{P R_{\mathrm{bol}}}}{C} \, \mathrm{d}E \tag{B.9}$$

Since $R_{\mathrm{L}} >> R_{\mathrm{bol}}$, the final expression becomes:

$$\mathrm{d}V_{\mathrm{bol}} = \sqrt{P} \, \frac{R_{\mathrm{bol}}}{\sqrt{R_{\mathrm{bol}}}} \, A \frac{\mathrm{d}T}{T} = \frac{A\sqrt{P R_{\mathrm{bol}}}}{C} \, \mathrm{d}E \tag{B.10}$$

List of Figures

References

[1] E. Fermi, "Versuch einer Theorie der β-Strahlen," *Zeitschrift für Physik A Hadrons and Nuclei*, vol. 88, pp. 161–177, 1935. 5

[2] H. Bethe and R. E. Peierls, "The neutrino," *Nature*, vol. 133, pp. 532–533 and 689–690, 1934. 5

[3] K. C. Wang, "A Suggestion on the Detection of the Neutrino," *Physical Review*, vol. 61, p. 97, 1942. 5

[4] C. L. Cowan, F. Reines, F. B. Harrison, H. W. Kruse, and A. D. McGuire, "Detection of the free neutrino: A Confirmation," *Science*, vol. 124, pp. 103–104, 1956. 5

[5] F. Reines, "The neutrino: from poltergeist to particle," *Reviews of Modern Physics*, vol. 68, pp. 317–327, 1996. 5

[6] T. D. Lee and C. N. Yang, "Parity Nonconservation and a Two-Component Theory of the Neutrino," *Physical Review*, vol. 105, pp. 1671–1675, 1957. 5

[7] M. Goldhaber, L. Grodzins, and A. W. Sunyar, "Evidence for Circular Polarization of Bremsstrahlung Produced by Beta Rays," *Physical Review*, vol. 106, pp. 826–828, 1957. 5

[8] B. Pontecorvo, "Mesonium and antimesonium," *Sovietic Physics - Journal of Experimental and Theoretical Physics*, vol. 6, p. 429, 1957. 5, 9

[9] B. Pontecorvo, "Inverse beta processes and nonconservation of lepton charge," *Sovietic Physics - Journal of Experimental and Theoretical Physics*, vol. 7, pp. 172–173, 1958. 5, 9

[10] G. Danby, J.-M. Gaillard, K. Goulianos, L. M. Lederman, N. Mistry, M. Schwartz, and J. Steinberger, "Observation of High-Energy Neutrino Reactions and the Existence of Two Kinds of Neutrinos," *Physical Review Letters*, vol. 9, pp. 36–44, 1962. 5

[11] M. L. Perl *et al.*, "Evidence for anomalous lepton production in $e^+ - e^-$ annihilation," *Physical Review Letters*, vol. 35, pp. 1489–1492, 1975. 6

[12] K. Kodama *et al.*, "Observation of tau-neutrino interactions," *Physics Letters B*, vol. 504, pp. 218–224, 2001. `hep-ex/0012035v1`. 6

[13] J. N. Abdurashitov *et al.*, "Measurement of the solar neutrino capture rate with gallium metal," *Physical Review C*, vol. 60, p. 055801, 1999. `astro-ph/9907113v2`. 6

[14] J. N. Abdurashitov *et al.*, "Measurement of the Solar Neutrino Capture Rate by SAGE and Implications for Neutrino Oscillations in Vacuum," *Physical Review Letters*, vol. 83, pp. 4686–4689, 1999. `astro-ph/9907131v2`. 6

[15] P. Anselmann *et al.*, "Solar neutrinos observed by GALLEX at Gran Sasso," *Physics Letters B*, vol. 285, pp. 376–389, 1992. 6

[16] P. Anselmann *et al.*, "Implications of the GALLEX determination of the solar neutrino flux," *Physics Letters B*, vol. 285, pp. 390–397, 1992. 6

[17] W. Hampel *et al.*, "Final results of the ^{51}Cr neutrino source experiments in GALLEX," *Physics Letters B*, vol. 420, pp. 114–126, 1992. 6

[18] M. Altmann *et al.*, "GNO solar neutrino observations: results for GNO I," *Physics Letters B*, vol. 490, pp. 16–26, 2000. `hep-ex/0006034v1`. 6

[19] M. Altmann *et al.*, "Complete results for five years of GNO solar neutrino observations," *Physics Letters B*, vol. 616, pp. 174–190, 2005. `hep-ex/0504037v1`. 6

[20] Y. Fukuda *et al.*, "Evidence for Oscillation of Atmospheric Neutrinos," *Physical Review Letters*, vol. 81, pp. 1562–1567, 1998. `hep-ex/9807003v2`. 6

[21] Y. Fukuda *et al.*, "Study of the atmospheric neutrino flux in the multi-Gev energy range," *Physics Letters B*, vol. 436, pp. 33–41, 1998. `hep-ex/9805006v3`. 6

[22] Y. Fukuda *et al.*, "Measurement of the Flux and Zenith-Angle Distribution of Upward Throughgoing Muons by Super-Kamiokande," *Physical Review Letters*, vol. 82, pp. 2644–2648, 1999. `hep-ex/9812014v2`. 6

[23] S. P. Mikheyev and A. Y. Smirnov, "Resonant neutrino oscillations in matter," *Progress in Particle and Nuclear Physics*, vol. 23, pp. 41–136, 1989. 6

[24] L. Wolfenstein, "Neutrino oscillations in matter," *Physical Review D*, vol. 17, p. 2369, 1978. 6

[25] Q. R. Ahmad *et al.*, "Direct Evidence for Neutrino Flavor Transformation from Neutral-Current Interactions in the Sudbury Neutrino Observatory," *Physical Review Letters*, vol. 89, p. 011301, 2002. 6

[26] K. Eguchi *et al.*, "First Results from KamLAND: Evidence for Reactor Antineutrino Disappearance," *Physical Review Letters*, vol. 90, p. 021802, 2003. `hep-ex/0212021v1`. 7

[27] T. Araki *et al.*, "Measurement of Neutrino Oscillation with KamLAND: Evidence of Spectral Distortion," *Physical Review Letters*, vol. 94, p. 081801, 2005. `hep-ex/0406035v3`. 7

[28] A. I. Belesev *et al.*, "Results of the troitsk experiment on the search for the electron antineutrino rest mass in tritium beta-decay," *Physics Letters B*, vol. 350, pp. 263–272, 1995. 7

[29] V. M. Lobashev *et al.*, "Direct search for mass of neutrino and anomaly in the tritium beta-spectrum," *Physics Letters B*, vol. 460, pp. 227–235, 1999. 7

[30] C. Kraus *et al.*, "Final results from phase II of the Mainz neutrino mass searchin tritium β decay," *The European Physical Journal C*, vol. 40, pp. 447–468, 2005. 7

[31] A. Osipowicz *et al.*, "Katrin: A next generation tritium beta decay experiment with sub-ev sensitivity for the electron neutrino mass," 2001. `hep-ex/0109033v1`. 7

[32] S. M. Bilenky and S. T. Petcov, "Massive neutrinos and neutrino oscillations," *Reviews of Modern Physics*, vol. 59, pp. 671–754, 1987. 7

[33] P. Langacker, "Neutrino physics," 1995. `hep-ph/9503327v1`. 7

[34] A. Strumia and F. Vissani, "Neutrino masses and mixings and.," 2006. IFUP-TH/2004-1, `hep-ph/0606054v2`. 7, 25, 34

[35] R. N. Mohapatra *et al.*, "Theory of neutrinos," 2004. `hep-ph/0412099v2`. 7

[36] R. N. Mohapatra and G. Senjanović, "Neutrino masses and mixings in gauge models with spontaneous parity violation," *Physical Review D*, vol. 23, pp. 165–180, 1981. 7, 9

[37] B. Kayser and R. E. Shrock, "Distinguishing between Dirac and Majorana neutrinos in neutral-current reactions," *Physics Letters B*, vol. 112, pp. 137–142, 1982. 8

[38] L. F. Li and F. Wilczek, "Physical processes involving Majorana neutrinos," *Physical Review D*, vol. 25, pp. 143–148, 1982. 9

[39] Z. Maki, M. Nakagawa, and S. Sakata, "Remarks on the unified model of elementary particles," *Progress of Theoretical Physics*, vol. 28, pp. 870–880, 1962. 9

[40] N. Cabibbo, "Unitary symmetry and leptonic decays," *Physical Review Letters*, vol. 10, pp. 531–533, 1963. 10

[41] M. Kobayashi and T. Maskawa, "CP Violation in the Renormalizable Theory of Weak Interaction," *Progress of Theoretical Physics*, vol. 49, pp. 652–657, 1973. 10

[42] L. L. Chau and W. Y. Keung, "Comments on the Parametrization of the Kobayashi-Maskawa Matrix," *Phys. Rev. Lett.*, vol. 53, pp. 1802–1805, 1984. 10

[43] G. Altarelli and F. Feruglio, "Neutrino masses and mixings: A theoretical perspective," 1999. CERN-TH/99-129, DFPD-99/TH/21, `hep-ph/9905536v3`. 10

[44] M. C. Gonzalez-Garcia and Y. Nir, "Developments in neutrino physics," *Reviews of Modern Physics*, vol. 75, pp. 345–402, 2003. CERN-TH/2002-021, WIS/08/02-Feb-DPP, `hep-ph/0202058v3`. 10

[45] M. Honda, Y. Kao, N. Okamura, and T. Takeuchi, "A simple parameterization of matter effects on neutrino oscillations," 2006. OCHA-PP-252, YITP-05-52, VPI-IPPAP-06-01, `hep-ph/0602115v1`. 11

[46] C. Giunti, "Absolute neutrino masses," *Acta Physica Polonica B*, vol. 36, pp. 3215–3226, 2005. `hep-ph/0511131v1`. 12

[47] M. Maltoni, T. Schwetz, M. A. Tortola, and J. W. F. Valle, "Status of global fits to neutrino oscillations," *New Journal of Physics*, p. 122, 2004. IFIC/04-19, TUM-HEP-548/04, YITP-SB-04-29, `hep-ph/0405172v6`, updated in 2007. 13, 24

[48] M. Geoppert-Mayer, "Double Beta-Disintegration," *Physical Review*, vol. 48, pp. 512–516, 1935. 15

[49] E. Majorana, "Theory of the Symmetry of Electrons and Positrons," *Nuovo Cimento*, vol. 14, pp. 171–184, 1937. 15

[50] G. Racah, "On the symmetry of particle and antiparticle," *Nuovo Cimento*, vol. 14, pp. 322–328, 1937. 15, 19

[51] W. H. Furry, "On Transition Probabilities in Double Beta-Disintegration," *Physical Review*, vol. 56, pp. 1184–1193, 1939. 15

[52] E. L. Fireman, "A Measurement of the Half-Life of Double Beta-Decay from ${}_{50}\mathrm{Sn}^{124}$," *Physical Review*, vol. 75, pp. 323–324, 1949. 15

[53] M. G. Inghram and J. H. Reynolds, "Double Beta-Decay of Te^{130}," *Physical Review*, vol. 78, pp. 822–823, 1950. 15

[54] N. Takaoka and K. Ogata, "The half-life of Te-130 double beta-decay," *Zeitschrift für Naturforschung A*, vol. 21, pp. 84–90, 1966. 15

[55] T. Kirsten, O. A. Schaeffer, E. Norton, and R. W. Stoenner, "Experimental Evidence for the Double-Beta Decay of Te^{130}," *Physical Review Letter*, vol. 20, pp. 1300–1303, 1968. 15

[56] C. S. Wu, E. Ambler, R. W. Hayward, D. D. Hoppes, and R. P. Hudson, "Experimental Test of Parity Conservation in Beta Decay," *Physical Review*, vol. 105, pp. 1413–1415, 1957. 16

[57] E. Fiorini, A. Pullia, G. Bertolini, F. Cappellani, and G. Restelli, "A search for lepton non-conservation in double beta decay with a germanium detector," *Physics Letters B*, vol. 25, pp. 602–603, 1967. 16

[58] J. Basdevant, J. Rich, and M. Michael, *Fundamentals in Nuclear Physics: From Nuclear Structure to Cosmology*. Springer, 1st ed., June 2005. ISBN: 0-38701-672-4. 16, 17

[59] P. J. Siemens and A. S. Jensen, *Elements Of Nuclei: Many-body Physics With The Strong Interaction*. Westview Press, 1st ed., May 1994. ISBN: 0-20162-731-0. 17

[60] K. Zuber, "Summary of the Workshop on: Matrix elements for Neutrinoless Double Beta Decay," *IPPP/05/56, DCPT/05/114*, pp. 1–20, 2005. `nucl-ex/0511009`. 19, 63, 65

[61] H. Kluge, K. Blaum, F. Herfurth, and W. Quint, "Atomic and Nuclear Physics with Stored Particles in Ion Traps," *Physica Scripta T*, vol. 104, pp. 167–177, 2003. 19

[62] F. Boehm and P. Vogel, *Physics of Massive Neutrinos*. Cambridge University Press, 2nd ed., June 2000. ISBN: 0-521-42849-1. 19

[63] S. R. Elliott, A. A. Hahn, and M. K. Moe, "Direct evidence for two-neutrino double-beta decay in ^{82}Se," *Physical Review Letter*, vol. 59, pp. 2020–2023, 1987. 19

[64] Y. G. Zdesenko, F. A. Danevich, and V. I. Tretyak, "Has neutrinoless double β decay of ^{76}Ge been really observed?," *Physics Letters B*, vol. 456, pp. 206–215, 2002. 19

[65] H. Ejiri, "Double Beta Decays and Neutrino Masses," *Progress in Particle and Nuclear Physics*, vol. 48, pp. 185–200, 2002. 19

[66] D. O. Caldwell, *Current Aspects of Neutrino Physics*. Springer, 1st ed., September 2001. ISBN: 3-540-41002-3. 20

[67] M. Doi, T. Kotani, and E. Takasugi, "Role Of The Nucleon Recoil Term in the Neutrinoless Double Beta Decay," *Physics Letters B*, vol. 158, p. 164, 1985. 22, 26

[68] J. Engel and P. Vogel, "Double beta decay in the generalized-seniority scheme," *Physics Letters B*, vol. 225, pp. 5–9, 1989. 22, 28, 87

[69] E. Caurier, F. Nowacki, and A. Poves, "Nuclear structure aspects of the neutrinoless double beta Decay," *To appear in European Journal of Physics*, 2007. `0709.0277v1 [nucl-th]`, Proceedings of the 4th-ILIAS meeting, Chambery 2007. 23, 87

[70] J. Suhonen, O. Civitarese, and A. Faessler, "Description of the $0^+ \rightarrow 0^+$ neutrinoless double-beta decay transition in ^{76}ge Particle-number-projected quasiparticle random phase approximation," *Nuclear Physics A*, vol. 543, pp. 645–660, 1992. 23, 28, 87

[71] A. Faessler and F. Simkovic, "Double beta decay," *Journal of Physics G: Nuclear and Particle Physics*, vol. 24, pp. 2139–2178, 1998. 23, 28, 87

[72] V. A. Rodin, A. Faessler, F. Šimkovic, and P. Vogel, "Assessment of uncertainties in QRPA $o\nu\beta\beta$-decay nuclear matrix elements," *Nuclear Physics A*, vol. 766, pp. 107–131, 2006. `nucl-th/0503063v3`. 23, 27, 63, 64, 87

[73] V. A. Rodin, A. Faessler, F. Šimkovic, and P. Vogel, "Erratum: Assessment of uncertainties in QRPA $o\nu\beta\beta$-decay nuclear matrix elements," 2007. `0706.4304v1 [nucl-th]`. 23, 27, 63, 64, 87

[74] Q. R. Ahmad *et al.*, "Measurement of day and night neutrino energy spectra at SNO and constraints on neutrino mixing parameters," *Physical Review Letters*, vol. 89, p. 011302, 2002. `nucl-ex/0204009v2`. 24

[75] A. Strumia and F. Vissani, "Neutrino oscillations and signals in β and $0\nu\beta\beta$ experiments," *Nuclear Physics B*, vol. 637, pp. 345–377, 2002. 25

[76] A. Strumia and F. Vissani, "Addendum to: Neutrino oscillations and signals in β and $0\nu\beta\beta$ experiments," *Nuclear Physics B*, vol. 659, pp. 359–362, 2003. 25

[77] A. Nucciotti, "Double beta decay: experiments and theory review," 2007. `0707.2216v3 [nucl-ex]`. 25

[78] A. Lewis and S. Bridle, "Cosmological parameters from CMB and other data: A Monte Carlo approach," *Physical Review D*, vol. 66, p. 103511, 2002. 25

[79] M. Tegmark *et al.*, "Cosmological parameters from SDSS and WMAP," *Physical Review D*, vol. 69, p. 103501, 2004. 25

[80] P. Crotty, J. Lesgourgues, and S. Pastor, "Current cosmological bounds on neutrino masses and relativistic relics," *Physical Review D*, vol. 69, p. 123007, 2004. 25

[81] O. Elgaroy and O. Lahav, "Neutrino masses from cosmological probes," *New Journal of Physics*, vol. 7, p. 61, 2005. `hep-ph/0412075v2`. 25

[82] V. Barger, S. L. Glashow, D. Marfatia, and K. Whisnant, "Neutrinoless double beta decay can constrain neutrino dark matter," *Phys. Lett. B*, vol. 532, pp. 15–18, 2002. MADPH-02-1254, AMES-HET-02-01, `hep-ph/0201262v2`. 25

[83] S. R. Elliott and P. Vogel, "Double Beta Decay," *Annual Review of Nuclear & Particle Science*, vol. 52, pp. 15–151, 2002. `hep-ph/0202264v1`. 26, 27

[84] M. Kortelainen and J. Suhonen, "Nuclear matrix elements of neutrinoless double beta decay with improved short-range correlations," *Physical Review C*, vol. 76, p. 024315, 2007. `0708.0115 [nucl-th]`. 27

[85] A. Staudt, T. T. S. Kuo, and H. V. Klapdor-Kleingrothaus, "$\beta\beta$ decay of ^{128}Te, ^{130}Te, and ^{76}Ge with renormalized effective interactions derived from Paris and Bonn potentials," *Physical Review C*, vol. 46, pp. 871–883, 1992. 28, 34, 87

[86] G. Pantis, F. Šimkovic, J. D. Vergados, and A. Faessler, "Neutrinoless double beta decay within the quasiparticle random-phase approximation with proton-neutron pairing," *Physical Review C*, vol. 53, pp. 695–707, 1996. 28, 87

[87] P. Vogel and M. R. Zirnbauer, "Suppression of the two-neutrino double-beta decay by nuclear-structure effects," *Physical Review Letters*, vol. 57, pp. 3148–3151, 1986. 28, 87

[88] O. Civitaresea and J. Suhonenb, "Extracting information on the $0\nu\beta\beta$ decays from the $2\nu\beta\beta$ decays," *Nuclear Physics A*, vol. 761, pp. 313–332, 2005. 28, 87

[89] T. Tomoda, "Double beta decay," *Reports on Progress in Physics*, vol. 54, pp. 53–126, 1991. 28, 87

[90] C. Barberoa, F. Krmpoti, A. Marianoa, and D. Tadi, "Nuclear moments for the neutrinoless double beta decay II," *Nuclear Physics A*, vol. 650, pp. 485–497, 1999. 28, 87

[91] F. Šimkovic, G. Pantis, J. D. Vergados, and A. Faessler, "Additional nucleon current contributions to neutrinoless double β decay," *Physical Review C*, vol. 60, p. 055502, 1999. 28, 87

[92] K. Muto, E. Bender, and H. V. Klapdor, "Proton-neutron quasiparticle RPA and charge-changing transitions," *Zeitschrift für Physik A Hadrons and Nuclei*, vol. 333, pp. 125–129, 1989. 28, 87

[93] S. Stoica and H. V. Klapdor-Kleingrothaus, "Neutrinoless double-β-decay matrix elements within the second quasirandom phase approximation method," *Physical Review C*, vol. 63, p. 064304, 2001. 28, 87

[94] M. Aunola and J. Suhonen, "Mean-field effects on neutrinoless double beta decay," *Nuclear Physics A*, vol. 643, pp. 207–221, 1998. 28, 87

[95] V. A. Rodin, A. Faessler, F. Šimkovic, and P. Vogel, "On the uncertainty in the 0nu beta beta decay nuclear matrix elements," *Phys. Rev. C*, vol. 68, p. 044302, 2003. `nucl-th/0305005v1`. 28

[96] W. C. Haxton and G. J. Stephenson, "Double beta decay," *Progress in Particle and Nuclear Physics*, vol. 12, pp. 409–479, 1984. 28

[97] E. Caurier, F. Nowacki, A. Poves, and J. Retamosa, "Shell model studies of the double beta decays of ^{76}Ge, ^{82}Se, and ^{136}Xe," *Physical Review Letters*, vol. 77, pp. 1954–1957, 1996. 28

[98] J. G. Hirsch *et al.*, "Double-beta decay to excited states in ^{150}Nd," *Nuclear Physics A*, vol. 589, pp. 445–459, 1995. 28

[99] M. K. Moe, "Experimental review of double beta decay," *Nuclear Physics - Proceedings Supplements*, vol. 19, pp. 158–176, 1991. 29

[100] H. V. Klapdor-Kleingrothaus *et al.*, "Search for neutrinoless double beta decay with enriched Ge-76 1990-2003: HEIDELBERG-MOSCOW experiment," 2004. `hep-ph/0404062v1`. 31, 38

[101] H. V. Klapdor-Kleingrothaus, I. V. Krivosheina, A. Dietz, and O. Chkvorets, "Search for neutrinoless double beta decay with enriched Ge-76 in Gran Sasso 1990-2003," *Physics Letters B*, vol. 586, pp. 198–212, 2004. `hep-ph/0404088v1`. 31, 38

[102] C. E. Aalseth *et al.*, "The IGEX Ge-76 neutrinoless double-beta decay experiment: Prospects for next generation experiments," *Physical Review D*, vol. 65, p. 092007, 2002. `hep-ex/0202026v1`. 31

[103] C. E. Aalseth *et al.*, "Recent results of the IGEX Ge-76 double-beta decay experiment," *Physics of Atomic Nuclei*, vol. 63, pp. 1225–1228, 2000. 31

[104] H. V. Klapdor-Kleingrothaus, A. Dietz, I. V. Krivosheina, and O. Chkvorets, “Data acquisition and analysis of the Ge-76 double beta experiment in Gran Sasso 1990-2003,” *Nuclear Instruments and Methods in Physics Research Section A*, vol. 522, pp. 371–406, 2004. `hep-ph/0403018v2`. 31

[105] H. V. Klapdor-Kleingrothaus, A. Dietz, H. L. Harney, and I. V. Krivosheina, “Evidence for neutrinoless double beta decay,” *Modern Physics Letters A*, vol. 16, pp. 2409–2420, 2001. `hep-ph/0201231v1`. 31

[106] C. E. Aalseth *et al.*, “Comment on ’Evidence for neutrinoless double beta decay’,” *Modern Physics Letters A*, vol. 17, pp. 1475–1478, 2002. `hep-ex/0202018v3`. 31

[107] H. L. Harney, “Reply to the ’comment on Evidence for neutrinoless double beta decay’,” 2001. `hep-ph/0205293v1`. 31

[108] H. V. Klapdor-Kleingrothaus, “Reply to a ’comment of article Evidence for neutrinoless double beta decay’,” 2002. `hep-ph/0205228v2`. 31

[109] H. V. Klapdor-Kleingrothaus, A. Dietz, and I. V. Krivosheina, “Status of evidence for neutrinoless double beta decay,” *Foundations of Physics*, vol. 32, pp. 1181–1223, 2002. `hep-ph/0302248v1`. 31

[110] H. V. Klapdor-Kleingrothaus, “First evidence for neutrinoless double beta decay - and world status of double beta experiments,” 2005. `hep-ph/0512263v1`. 31

[111] R. Arnold *et al.*, “Study of 2beta-decay of Mo-100 and Se-82 using the NEMO3 detector,” *JETP Letters*, vol. 80, pp. 377–381, 2004. `hep-ex/0410021v1`. 32

[112] A. S. Barabash, “NEMO-3 double beta decay experiment: Lastest results,” 2006. Proceedings of the XXXIII International Conference on High Energy Physics, Moscow (Russia), July 2006, `hep-ex/0610025v1`. 32, 38

[113] H. Ejiri *et al.*, “Limits on the Majorana neutrino mass and right-handed weak currents by neutrinoless double beta decay of Mo-100,” *Physical Review C*, vol. 63, p. 065501, 2001. 33

[114] F. A. Danevich *et al.*, “Search for 2β decay of cadmium and tungsten isotopes: Final results of the Solotvina experiment,” *Physical Review C*, vol. 68, p. 035501, 2003. 33, 38

[115] C. Arnaboldi *et al.*, “A calorimetric search on double beta decay of ^{130}Te,” *Physics Letters B*, vol. 557, pp. 167–175, 2002. 33, 59

[116] A. Alessandrello *et al.*, “New experimental results on double beta decay of Te-130,” *Physics Letters B*, vol. 486, pp. 13–21, 2000. 33, 59

[117] R. Luescher *et al.*, “Search for $\beta\beta$ decay in ^{136}xe: new results from the Gotthard experiment,” *Physics Letters B*, vol. 434, pp. 407–414, 1998. 33

[118] R. Bernabei *et al.*, “Investigation of beta beta decay modes in Xe-134 and Xe-136,” *Physics Letters B*, vol. 546, pp. 23–28, 2002. 33, 38

[119] R. Hazama *et al.*, “Challenge on Ca-48 enrichment for candles double beta decay experiment,” 2007. `0710.3840v1 [nucl-ex]`. To appear in the proceedings of 6th Rencontres du Vietnam: Challenges in Particle Astrophysics, Hanoi, Vietnam, 6-12 Aug 2006. 35

[120] T. Kishimoto, “CANDLES for the study of ^{48}Ca double beta decay and low radioactivity CaF2 crystals,” 2006. talk at 2nd Topical Workshop in Low Radioactivity Techniques (LRT2006), Aussosis (France), October 1-4, 2006. 35, 38

[121] R. Gaitskell *et al.*, “White paper on the majorana zero-neutrino double-beta decay experiment,” 2003. `nucl-ex/0311013v1`. 35, 38

[122] H. V. Klapdor-Kleingrothaus, L. Baudis, G. Heusser, B. Majorovits, and H. Pas, “GENIUS: A supersensitive germanium detector system for rare events,” 1999. `hep-ph/9910205v4`. Prepared for 2nd International Conference Physics Beyond the Standard Model, Tegernsee, Germany, 6-12 Jun 1999. 35

[123] H. V. Klapdor-Kleingrothaus, O. Chkvorez, I. V. Krivosheina, H. Strecker, and C. Tomei, “Genius test-facility started operation in gran sasso: With first ten kg of naked germanium detectors in liquid nitrogen,” *Nuclear Instruments and Methods in Physics Research Section A*, vol. 511, pp. 341–346, 2003. `hep-ph/0309170v1`. 35

[124] Y. G. Zdesenko, O. A. Ponkratenko, and V. I. Tretyak, “High sensitivity GEM experiment on 2beta decay of Ge-76,” *Journal of Physics G*, vol. 27, p. 2129, 2001. `nucl-ex/0106021v1`. 35

[125] I. Abt *et al.*, “A new Ge-76 double beta decay experiment at LNGS,” 2004. `hep-ex/0404039v1`. 36, 38

[126] H. Ejiri, J. Engel, R. Hazama, P. Krastev, N. Kudomi, and R. G. H. Robertson, “Spectroscopy of double-beta and inverse-beta decays from ^{100}mo for neutrinos,” *Physical Review Letters*, vol. 85, pp. 2917–2920, 2000. 36, 38

[127] H. Nakamura *et al.*, “Multi-layer scintillation detector for the moon double beta decay experiment: Scintillation photon responses studied by a prototype detector MOON-1,” 2006. `nucl-ex/0609008v2`. 36, 38

[128] K. Zuber, “COBRA: Double beta decay searches using CdTe detectors,” *Physics Letters B*, vol. 519, pp. 1–7, 2001. `nucl-ex/0105018v1`. 36

[129] T. Bloxham *et al.*, “First results on double beta decay modes of Cd, Te and Zn isotopes with the COBRA experiment,” *Physical Review C*, vol. 76, p. 025501, 2007. `0707.2756v1 [nucl-ex]`. 36

[130] G. Bellini *et al.*, “High sensitivity 2beta decay study of Cd-116 and Mo100 with the BOREXINO counting test facility (CAMEO project),” *The European Physical Journal C*, vol. 19, pp. 43–55, 2001. INFN/BE-00/03, `nucl-ex/0007012v1`. 36, 38

[131] K. Wamba, “Exo: The enriched xenon observatory for double beta decay,” 2002. `hep-ph/0210186v1`. 37, 38

[132] F. LePort *et al.*, “A liquid xenon ionization chamber in an all-fluoropolymer vessel,” *Nuclear Instruments and Methods in Physics Research Section A*, vol. 578, pp. 409–420, 2007. `physics/0611183v1`. 37

[133] Y. Suzuki, “Future solar neutrino experiments,” *Nuclear Physics Proceedings Supplements*, vol. 143, pp. 27–34, 2005. 37

[134] S. Soldner-Rembold, “Search for neutrinoless double beta decay with nemo 3 and supernemo,” 2007. `0710.4156v1 [hep-ex]`. 37, 38

[135] I. Ogawa *et al.*, “Search for neutrino-less double beta decay of Ca-48 by CaF-2 scintillator,” *Nuclear Physics A*, vol. 730, pp. 215–223, 2004. 38

[136] C. Bucci, “CUORE: Cryogenic Underground Observatory for Rare Events,” 2007. Talk at LAUNCH Workshop, Heidelberg (Germany), 21-22 March 2007. 38

[137] A. S. De Silva, M. K. Moe, M. A. Nelson, and M. A. Vient, “Double beta decays of Mo-100 and Nd-150,” *Physical Review C*, vol. 56, pp. 2451–2467, 1997. UCI-Neutrino 97-10, `nucl-ex/9706005v1`. 38

[138] F. A. Danevich *et al.*, “Quest for double beta decay of ^{160}gd and Ce isotopes,” *Nuclear Physics A*, vol. 694, pp. 375–391, 2001. 38

[139] C. Arnaboldi *et al.*, “CUORE: A Cryogenic Underground Observatory for Rare Events,” *Nuclear Instruments and Methods in Physics Research Sec.A*, vol. 518, pp. 775–798, 2004. `hep-ex/0212053v1`. 38, 135, 141, 151

[140] N. Ishihara *et al.*, “A separation method of 0ν- and 2ν-events in double beta decay experiments with DCBA,” *Nuclear Instruments and Methods in Physics Research Section A*, vol. 443, pp. 101–107, 2000. 38

[141] S. Simom, “Application of Low Temperature Calorimetry to Radioactive Measurements,” *Nature*, vol. 135, p. 763, 1935. 39

[142] D. H. Andrews, R. D. Fowler, and M. C. Williams, “The Effect of Alpha-particles on a Superconductor,” *Physical Review Series II*, vol. 135, pp. 154–155, 1949. 39

[143] E. Fiorini and T. O. Niinikoski, “Low Temperature Calorimetry For Rare Decays,” *Nuclear Instruments and Methods in Physics Research Sec.A*, vol. 224, p. 83, 1984. 39, 59

[144] F. Gatti *et al.*, “Proceedings of the 10th International Workshop on Low Temperature Detectors,” *Nuclear Instruments and Methods in Physics Research Section A*, vol. 520, pp. 1–685, 2004. 39

[145] A. Alessandrello *et al.*, “A massive thermal detector for alpha and gamma spectroscopy,” *Nuclear Instruments and Methods in Physics Research Section A*, vol. 440, pp. 397–402, 2000. 40, 71

[146] J. D. Patterson and B. C. Baley, *Solid-State Physics, Introduction to the Theory.* Springer, 1st ed., Jannary 2007. ISBN: 3-540-24115-9. 42

[147] Y. B. Levinson, “Nonequilibrium Phonons in Nonmetallic Crystals,” *Modern Problems in Condensed Matter Sciences*, vol. 16, pp. 91–143, 1986. ISBN: 0-444-86989-1. 44

[148] B. Taylor, H. J. Maris, and C. Elbaum, “Phonon Focusing in Solids,” *Physical Review Letters*, vol. 23, pp. 416–419, 1969. 45

[149] N. E. Booth, B. Cabrera, and E. Fiorini, “Low-Temperature Particle Detectors,” *Annual Review of Nuclear & Particle Science*, vol. 46, pp. 471–532, 1996. 45

[150] N. W. Ashcroft and N. D. Mermin, *Solid State Physics.* Brooks Cole, 1st ed., January 1976. ISBN: 0-030-83993-9. 46

[151] G. F. Knoll, *Radiation Detection and Measurement.* Wiley, 3rd ed., January 2000. ISBN: 0-471-07338-5. 46, 47

[152] U. Fano, “On the Theory of Ionization Yield of Radiations in Different Substances,” *Physical Review*, vol. 70, pp. 44–52, 1946. 47

[153] C. A. Klein, “Bandgap Dependence and Related Features of Radiation Ionization Energies in Semiconductors,” *Journal of Applied Physics*, vol. 39, pp. 2029–2038, 1968. 47

[154] K. M. Itoh et al., “Neutron transmutation doping of isotopically engineered Ge,” *Applied Physics Letters*, vol. 64, pp. 2121–2123, 1994. 48

[155] A. Miller and E. Abrahams, "Impurity conduction at low concentrations," *Physical Review*, vol. 120, pp. 745–755, 1960. 49

[156] N. F. Mott and J. H. Davies, "Metalinsulator transition in doped semiconductors," *Philosophical Magazine B*, vol. 42, pp. 845–858, 1980. 49

[157] V. D. Nguyen, V. L. Nguyen, and D. T. Dang, "Variable range hopping in the Coulomb gap and gate screening in two dimensions," *Physics Letters A*, vol. 349, pp. 404–410, 2006. 50

[158] CUORE Collaboration, "CUORE: A Cryogenic Underground Observatory For Rare Events," 2005. `hep-ex/0501010v1`. 59, 138, 141

[159] A. Alessandrello *et al.*, "A cryogenic underground observatory for rare events: CUORE, an update," *Physics of Atomic Nuclei*, vol. 66, pp. 452–457, 2003. `hep-ex/0201038v2`. 59

[160] A. Alessandrello *et al.*, "A new search for neutrinoless beta beta decay with a thermal detector," *Physics Letters B*, vol. 335, pp. 519–525, 1994. 59, 60

[161] A. Alessandrello *et al.*, "Improvements in ^{130}Te double beta decay search with cryogenic TeO$_2$ array detectors," *Nuclear Physics B - Proceedings Supplements*, vol. 48, pp. 238–240, 1996. 59, 60

[162] A. Alessandrello *et al.*, "Preliminary results on double beta decay of Te-130 with an array of twenty cryogenic detectors," *Physics Letters B*, vol. 433, pp. 156–162, 1998. 59, 60

[163] A. Alessandrello *et al.*, "A calorimetric search on double beta decay of ^{130}Te," *Physics Letters B*, vol. 78, pp. 167–175, 035502. 59, 60

[164] C. Arnaboldi *et al.*, "Results from a search for the $0\nu\beta\beta-$decay of ^{130}Te," *Physical Review C*, vol. 78, p. 035502, 2008. `0802.3439 [hep-ex]`. 59, 60, 85, 87

[165] F. Alessandria *et al.*, "CUORICINO and CUORE," *LNGS annual report*, vol. 1, pp. 33–52, 2007. LNGS/EXP-02/07. 59, 60, 86, 91, 92

[166] C. Arnaboldi *et al.*, "First results on neutrinoless double beta decay of ^{130}Te with the calorimetric CUORICINO experiment," *Physics Letters B*, vol. 584, pp. 260–268, 2004. 59, 83

[167] C. Arnaboldi *et al.*, "New limit on the neutrinoless $\beta\beta$ decay of ^{130}Te," *Physical Review Letters*, vol. 95, p. 142501, 2005. `hep-ex/0501034v1`. 59, 61, 83, 85

[168] A. Alessandrello *et al.*, "The first step toward CUORE: Cuoricino, a thermal detector array to search for rare events," *Nuclear Physics B, Proceedings Supplements*, vol. 87, pp. 78–80, 2000. 59

[169] F. Alessandria *et al.*, "CUORICINO and CUORE. Neutrinoless double beta decay searches with low temperature detectors," *LNGS annual report*, vol. 1, pp. 17–38, 2006. LNGS/EXP-03/06. 59, 86

[170] S. P. Ahlen *et al.*, "Study of penetrating cosmic ray muons and search for large scale anisotropies at the Gran Sasso Laboratory," *Physics Letters B*, vol. 249, pp. 149–156, 1990. 62

[171] S. P. Ahlen *et al.*, "Muon astronomy with the macro detector," *The Astrophysical Journal*, vol. 412, pp. 301–311, 1993. 62

[172] L. Chabert, *Etude du bruit de fond neutron induit par les muons dans l'expérience EDELWEISS-II*. PhD thesis, Université Claude Bernard Lyon-I, 2004. 62

[173] M. Robinson *et al.*, "Measurements of muon flux at 1070 m vertical depth in the Boulby underground laboratory," *Nuclear Instruments and Methods in Physics Research Section A*, vol. 511, pp. 347–353, 2003. 62

[174] G. Luzón *et al.*, "Characterization of the Canfranc Underground Laboratory: status and future plans," *The Identification of Dark Matter*, vol. 554, pp. 514–519, 2006. Proceedings of the Sixth International Workshop, Rhodes, Greece 11-16 September 2006. 62

[175] T. Enqvist *et al.*, "Measurements of muon flux in the Pyhäsalmi underground laboratory," *Nuclear Instruments and Methods in Physics Research Section A*, vol. 554, pp. 286–290, 2005. 62

[176] C. Arpesellam, "Background measurements at Gran Sasso Laboratory," *Nuclear Physics B, Proceedings Supplements*, vol. 28, pp. 420–424, 1992. 62

[177] P. Smith *et al.*, "Simulation studies of neutron shielding, calibration and veto systems for gaseous dark matter detectors," *Astroparticle Physics*, vol. 22, pp. 409–420, 2005. 62

[178] P. Belli *et al.*, "Deep Underground Neutron Flux Measurement With Large Bf-3 Counters," *Il Nuovo Cimento A*, vol. 101, pp. 959–966, 1989. 62

[179] F. Arneodo *et al.*, "Neutron background measurements in the Hall C of the Gran Sasso Laboratory," *Il Nuovo Cimento A*, vol. 112, pp. 819–831, 1999. 62

[180] V. Chazal *et al.*, "Neutron background measurements in the Underground Laboratory of Modane," *Astroparticle Physics*, vol. 9, pp. 163–172, 1998. 62

[181] S. Fiorucci *et al.*, "Identification of backgrounds in the EDELWEISS-I dark matter search experiment," *Astroparticle Physics*, vol. 28, pp. 143–153, 2007. `astro-ph/0610821v2`. 62

[182] E. Tziaferi *et al.*, "First measurement of low intensity fast neutron background from rock at the Boulby Underground Laboratory," *Astroparticle Physics*, vol. 27, pp. 326–338, 2007. 62

[183] M. Barucci, C. Brofferio, A. Giuliani, E. Gottardi, I. Peroni, and G. Ventura, "Measurement of Low Temperature Specific Heat of Crystalline TeO_2 for the Optimization of Bolometric Detectors," *Journal of Low Temperature Physics*, vol. 123, pp. 303–314, 2001. 65

[184] E. E. Haller, "Advanced far-infrared detectors," *Infrared Physics &Technology*, vol. 35, pp. 127–146, 1994. 68

[185] A. Alessandrello *et al.*, "Heat capacity of low temperature Ge- and Si-calorimeters and optimazation of As-implanted silicon thermistors," *Nuclear Instruments and Methods in Physics Research Section A*, vol. 263, pp. 233–236, 1988. 68

[186] C. Arnaboldi *et al.*, "A calorimetric search on double beta decay of ^{130}Te," *Physics Letters B*, vol. 557, pp. 167–175, 2003. 71

[187] M. Pedretti. *et al.*, "Measurement of thermal properties for modeling and optimization of large mass bolometers," *Physica B*, vol. 329, pp. 1614–1615, 2003. 71

[188] M. Bassan, E. Coccia, N. Menci, and I. Modena, "Numerical model for cooling a gravitational wave detector below 1K," *Cryogenics*, vol. 31, pp. 147–152, 1991. 74

[189] A. de Waard *et al.*, "Cooling down miniGRAIL to milli-Kelvin temperatures," *Classical and Quantum Gravity*, vol. 21, pp. S465–S471, 2004. 74

[190] S. R. Furtado and O. D. Aguiar, "Fast cooling techniques for gravitational wave antennas," *Classical and Quantum Gravity*, vol. 19, pp. 1973–1978, 2002. 74

[191] P. Astone *et al.*, "First Cooling Below 0.1K of the New Gravitational-Wave Antenna Nautilus of the Rome Group," *Europhysics Letters*, vol. 16, pp. 231–235, 1991. 74

[192] P. Astone *et al.*, "The gravitational wave detector NAUTILUS operating at T=0.1K," *Astroparticle Physics*, vol. 3, pp. 231–243, 1997. 74

[193] N. H. Balshaw, *Practical Cryogenics, An Introduction to Laboratory Cryogenics.* Oxford Instruments Superconductivity Limited, 1st ed., 1987. 74, 84, 94, 177

[194] A. Alessandrello *et al.*, "Measurements of internal radioactive contamination in samples of Roman lead to be used in experiments on rare events," *Nuclear Instruments and Methods in Physics Research Section B*, vol. 142, pp. 163–172, 1998. 76, 84, 95

[195] S. Pirro *et al.*, “Present status of MI-BETA cryogenic experiment and preliminary results for CUORICINO,” *Nuclear Instruments and Methods in Physics Research Section A.*, vol. 444, pp. 71–76, 2000. 81, 94

[196] P. Gorla, *Optimization of the CUORE detector performance.* PhD thesis, Universitá Degli Studi di Milano Bicocca, 2005. 81, 102

[197] C. Arnaboldi *et al.*, “The temperature stabilization system of CUORICINO: An array of macro bolometers,” *IEEE Transactions On Nuclear Science*, vol. 52, pp. 1630–163, 2005. 84, 95

[198] S. Baker and R. D. Cousins, “Clarification of the use of CHIsquare and likelihood functions in fits to histograms,” *Nuclear Instruments and Methods in Physics Research*, vol. 221, pp. 437–442, 1984. 85

[199] R. M. Barnett *et al.*, “Review of particle physics. particle data group,” *Physical Review D*, vol. 54, pp. 1–720, 1996. 85

[200] J. Astrom *et al.*, “Fracture processes studied in CRESST,” *Nuclear Instruments and Methods in Physics Research Section A.*, vol. 559, pp. 754–756, 2006. 94, 105

[201] S. Pirro, “Further developments in mechanical decoupling of large thermal detectors,” *Nuclear Instruments and Methods in Physics Research Section A*, vol. 559, pp. 672–674, 2006. 94

[202] L. Foggetta, A. Giuliani, C. Nones, M. Pedretti, and S. Sangiorgio, “Surface-sensitive macrobolometers for the identification of external charged particles,” *Applied Physics Letters*, vol. 86, p. 134106, 2005. 110

[203] C. Arnaboldi *et al.*, “The front-end readout for CUORICINO, an array of macro-bolometers and MIBETA, an array of μ-bolometers,” *Nuclear Instruments and Methods in Physics Research Sec.A*, vol. 520, pp. 578–580, 2004. 135, 137

[204] C. Arnaboldi *et al.*, “The Programmable Front-End System for CUORICINO, An Array of Large-Mass Bolometers,” *IEEE Transactions On Nuclear Science*, vol. 49, pp. 2440–2447, 2002. 135, 138, 141

[205] C. Arnaboldi, G. Pessina, and E. Previtali, “A programmable calibrating pulse generator with multi-outputs and very high stability,” *IEEE Transactions On Nuclear Science*, vol. 50, pp. 979–986, 2003. 135, 148

[206] G. Pessina, “Low-noise, low drift, high precision linear bipolar (±10 V) voltage supply/reference for cryogenic front-end apparatus,” *Review of Scientific Instruments*, vol. 70, pp. 3473–3478, 1999. 137

[207] C. Arnaboldi *et al.*, “Low-Frequency Noise Characterization of Very Large Value Resistors,” *IEEE Transactions On Nuclear Science*, vol. 49, pp. 1808–1813, 2002. 137

[208] A. Alessandrello *et al.*, “Measuring thermistor resistance with very low d.c. power dissipation,” *Cryogenics*, vol. 37, pp. 27–31, 1997. 138

[209] P. Horowitz and W. Hill, *The Art of Electronics*. Cambridge University Press, 2nd ed., July 1989. ISBN: 0-521-37095-7. 145, 147

[210] G. Pessina and A. Fascilla, “A self-buffered DC baseline restorer with quasi-ideal behavior,” *Nuclear Instruments and Methods in Physics Research Sec.A*, vol. 437, pp. 557–559, 1999. 147

[211] G. Pessina and C. Arnaboldi, “A very simple baseline restorer for nuclear applications,” *Nuclear Instruments and Methods in Physics Research Sec.A*, vol. 512, pp. 129–135, 2003. 147

[212] J. Wilks, *Properties of Liquid and Solid Helium*. Oxford University Press, 1st ed., July 1987. ISBN: 0-198-51245-7. 175

[213] G. Frossati, “Obtaining ultralow temperatures by dilution of ^{3}he in ^{4}he,” *Journal de Physique*, vol. 39 C6, pp. 1578–1589, 1978. 175

[214] G. Frossati, “Experimental techniques: Methods for cooling below 300 mk,” *Journal of Low Temperature Physics*, vol. 87, pp. 595–633, 1992. 175

[215] G. A. Vermeulen and G. Frossati, “Powerful dilution refrigerator for use in the study of polarized liquid ^{3}he and nuclear cooling,” *Cryogenics*, vol. 27, pp. 139–147, 1987. 175

[216] D. J. Cousins *et al.*, “An Advanced Dilution Refrigerator Designed for the New lancaster Microkelvin Facility,” *Journal of Low Temperature Physics*, vol. 114, pp. 547–570, 1999. 175

[217] F. Pobell, *Matter and Methods at Low Temperatures*. Springer, 2nd ed., November 2001. ISBN: 0-521-42849-1. 175, 176, 177

[218] D. Betts, *An Introduction to Millikelvin Technology*. Cambridge University Press, 1st ed., August 2005. ISBN: 0-521-01817-X. 175, 177

[219] W. E. Gifford and R. C. Longsworth, “Pulse-tube refrigeration,” *Journal of Engineering for Industry-Transactions of the ASME*, vol. 84, pp. 264–268, 1964. 179

[220] E. I. Mikulin, A. A. Tarasov, and M. P. Shkrebyonock, “Low temperature expansion pulse tubes,” *Advances in Cryogenic Engineering*, vol. 29, pp. 629–637, 1984. 179

[221] R. Radebaugh, J. Zimmerman, D. R. Smith, and B. Louie, “A comparison of three types of pulse tube refrigerators: New methods for reaching 60K,” *Advances in Cryogenic Engineering*, vol. 31, pp. 779–789, 1986. 179

[222] S. Zhu, P. Wu, and Z. Chen, “Double inlet pulse tube refrigerators: an important improvement,” *Cryogenics*, vol. 30, pp. 514–520, 1990. 179

[223] Y. Matsubara and J. L. Gao, “Novel configuration of three-stage pulse tube refrigerator for temperatures below 4K,” *Cryogenics*, vol. 34, pp. 259–262, 1994. 179

[224] M. Y. Xu, A. T. A. M. de Waele, and Y. L. Ju, “A pulse tube refrigerator below 2K,” *Cryogenics*, vol. 39, pp. 865–869, 1999. 179